On the formation of massive stars : a numerical approach

Raphaël Mignon-Risse

UNIVERSITÉ DE PARIS
ÉCOLE DOCTORALE STEP'UP, 560
LABORATOIRE ASTROPHYSIQUE INSTRUMENTATION MODÉLISATION

THÈSE

en vue d'obtenir le grade de

Docteur de l'Université de Paris

Spécialité : Physique de l'Univers

On the formation of massive stars: a numerical approach

Par RAPHAËL MIGNON-RISSE

Dirigée par Matthias GONZÁLEZ

Présentée et soutenue publiquement le 21/09/2020

Devant un jury composé de :

M.	Dominique AUBERT	Professeur, Université de Strasbourg, Rapporteur
M.	Fabien CASSE	Professeur, Université de Paris, Président
M.	Matthias GONZÁLEZ	Maître de conférences HDR, Université de Paris, Directeur de thèse
Mme	Frédérique MOTTE	Chercheuse, CNRS, Rapporteuse
M.	Pascal TREMBLIN	Chercheur CEA HDR, CEA Saclay, Examinateur

Résumé

La compréhension de la formation des étoiles est un des défis fondamentaux de l'astronomie moderne. En effet, c'est un rouage indispensable de la machine complexe que constitue le milieu interstellaire. Celui-ci est le terrain de jeu de nombreux processus physiques et chimiques, où cohabitent champ magnétique, champ de rayonnement, turbulence, rayons cosmiques... La formation stellaire se déroule dans les nuages moléculaires et permet, par effondrement gravitationnel puis réactions de fusion nucléaire, de convertir le gaz environnant, initialement composé princalement d'hydrogène et d'hélium, en éléments plus lourds que l'on appellera métaux, par simplicité. Les étoiles massives (plus de huit masses solaires, notées $M_\odot$), lorsqu'elles explosent en supernovæ, restituent ce gaz enrichi en métaux au milieu interstellaire. Les étoiles massives se caractérisent par leur luminosité et leur température de surface très élevées, qui induisent notamment une grande pression de radiation et un rayonnement ionisant. Le sujet de cette thèse porte sur la formation de ces astres.

Les étoiles massives sont moins nombreuses que les étoiles de faible masse. Pour en observer un même nombre, il faut donc observer des régions du ciel plus lointaines. Elles se forment dans des régions denses, ce qui rend les observations difficiles. Ainsi, les contraintes observationnelles sont faibles quant à leur processus de formation, contrairement aux étoiles de faible masse. Les simulations numériques sont donc un outil indispensable à la compréhension de ce problème. Parmi les nombreuses questions qui entourent ce sujet, nous avons tenté de répondre à trois en particulier : comment les étoiles massives acquièrent-elles leur masse durant la phase principale d'accrétion de matière ? Quel est le mécanisme à l'origine des éjections de matière que l'on observe ? Quels processus sont responsables de la formation de systèmes multiples plutôt que de systèmes unitaires ? Commençons par résumer les avancées théoriques majeures qui ont été faites sur ces questions.

A symétrie sphérique, il est impossible de former une étoile de plus de $40\,M_\odot$, alors que l'on en observe de plus de $100\,M_\odot$. En effet, les réactions nucléaires commencent au sein de la proto-étoile alors qu'elle est toujours dans la phase d'accrétion. Conséquence de sa luminosité déjà élevée, sa force radiative, qui est répulsive, est plus grande que la force gravitationnelle qui attire le gaz, et l'accrétion s'arrête ; c'est ce que l'on appelle la barrière radiative. Ce problème a justifié que la majorité des développements dans ce domaine ont concerné le transfert radiatif. Heureusement, des simulations numériques multi-dimensionnelles ont mis en évidence l'accrétion par un disque, tandis que la pression radiative est libérée perpendiculairement au disque, vers les régions transparentes. Ce mécanisme a permis d'atteindre des masses supérieures à $100\,M_\odot$, cohérentes avec les observations. De plus, la pression radiative entraîne la formation de cavités radiatives. Celles-ci seraient instables aux instabilités de Rayleigh-Taylor radiatives, et cela permettrait d'accréter de la matière sur l'étoile également, en plus du disque d'accrétion. Ces travaux numériques ont été réalisés avec de l'hydrodynamique radiative, négligeant le champ magnétique. Les développements récents ont consisté à traiter le rayonnement du milieu ambiant (émanant du disque par exemple) et rayonnement stellaire, appelé parfois irradiation, avec des méthodes de transfert radiatif différentes. En effet, ces rayonnements diffèrent par leur fréquence (ultraviolet pour l'irradiation, infrarouge pour

le rayonnement ambiant) et l'opacité du milieu qu'ils traversent (principalement transparent pour le premier, opaque pour le second). L'implémentation d'une telle méthode dans un code haute-performance représente la majeure partie de ce travail de thèse.

Le code utilisé lors de cette thèse, RAMSES, se caractérise par une grille spatiale dont la résolution peut être adaptée selon les critères de l'utilisateur, cette technique est appelée Raffinement Adaptatif de Maillage (AMR). RAMSES propose des modèles sous-maille, appelés *particules puits*, pour simuler la formation d'étoiles, leur capacité à accréter le gaz et leur rétroaction, ce qui le rend idéalement adapté pour étudier la formation stellaire. Il inclut aussi de nombreux modules physiques, dont de la Magnéto-HydroDynamique (MHD) non-idéale, que n'ont pas les codes utilisés dans les simulations précédentes. Le module de transfert radiatif utilisé jusqu'à présent, basé sur la méthode de Diffusion à Flux Limité (FLD), est particulièrement adapté au rayonnement ambiant lorsque le milieu est opaque, mais pas à l'irradiation. Le principal travail que j'ai réalisé durant cette thèse porte sur le couplage entre ce module et un module de transfert radiatif plus avancé (et coûteux) utilisé jusqu'à présent en cosmologie, afin de traiter l'irradiation, dans une approche que l'on appellera *hybride*. Ce second module s'appuie sur la méthode M1, qui est adaptée aux champs de rayonnement fortement anisotropes. J'ai donc validé cette méthode hybride via des tests sans hydrodynamique consistant à calculer la température d'un disque irradié par une étoile. Ce problème n'ayant pas de solution analytique, j'ai comparé mes résultats avec ceux de codes de transfert radiatif Monte-Carlo, résolvant exactement l'équation du transfert, pour évaluer le gain en précision que nous apporte cette méthode. Ce gain est d'autant plus élevé que le disque est peu opaque, et la zone d'ombre au sein du disque, où peu de rayonnement pénètre, est devenue visible. D'autre part, la force radiative, responsable des cavités radiatives, était sous-estimée d'un facteur cent car le couplage gaz-rayonnement est fortement dépendant de la fréquence du rayonnement. La méthode hybride permet de mieux prendre en compte cette dépendance spectrale à l'égard du rayonnement stellaire. Après la validation de cette méthode, j'ai donc entrepris de l'appliquer à la formation d'étoiles massives afin de répondre aux questions citées précédemment.

J'ai tout d'abord utilisé des simulations numériques d'hydrodynamique radiative modélisant l'effondrement d'un cœur massif pré-stellaire afin d'étudier l'impact de la méthode de transfert radiatif hybride, en comparaison à la méthode FLD et à la littérature. Mes résultats montrent que les cavités radiatives sont plus étendues qu'avec la méthode FLD, du fait de la force radiative plus importante, et le taux d'accrétion légèrement plus faible car le disque protège le flot d'accrétion contre ce rayonnement stellaire. J'ai ensuite employé l'AMR pour que l'interface des cavités soit à la résolution maximale. Aucune instabilité de Rayleigh-Taylor n'est apparue car le gaz est advecté au travers de cette interface trop rapidement pour qu'elles aient le temps de se développer. Cela constitue à ce jour la première preuve de leur absence, à résolution égale avec les travaux de la littérature, à méthode de transfert radiatif comparable et fondée sur des arguments théoriques. Le mécanisme conforté par ces simulations est celui de l'accrétion par un disque uniquement. Cette application a permis de valider la méthode hybride dans un contexte dynamique.

En marge de ce travail, nous avons entrepris une collaboration avec le groupe de Formation des Etoiles Massives de l'Université de Tübingen, afin de comparer la capacité de nos codes respectifs quant à la modélisation de la fragmentation des disques d'accrétion, et dont les résultats préliminaires sont présentés ici. En effet, la fragmentation des disques pourrait être cruciale pour la formation de systèmes multiples, qui sont plus fréquents que dans le cas des étoiles de faible masse. Il est nécessaire de résoudre certaines échelles physiques caractéristiques : l'échelle de hauteur hydrostatique du disque, et la longueur de Jeans, pour éviter la fragmentation *artificielle* qui affecte la multiplicité du système par l'introduction de particules puits, ainsi que la structure du disque et donc l'accrétion.

Pour aller plus loin, nous avons relaxé l'hypothèse d'absence de champ magnétique que

nous avions invoquée jusqu'alors. Tandis que la force radiative était sous-estimée avant l'utilisation de la méthode hybride, la force de Lorentz était surestimée dans le cadre de la MHD idéale, car le champ magnétique est accumulé à mesure que le gaz s'effondre. La MHD non-idéale (ici, la diffusion ambipolaire, *i.e.* la friction entre les ions et les neutres) offre une solution à ce problème avec la diffusion du champ magnétique dans les zones de forte densité, notamment le disque d'accrétion. Ainsi, à l'aide des premières simulations mondiales de formation d'étoiles massives incluant une méthode d'irradiation et la MHD non-idéale, nous avons pu interroger de manière non biaisée le mécanisme à l'origine des éjections. Nous avons obtenu des éjections bien plus étendues spatialement et collimatées qu'en l'absence de champ magnétique. La force de Lorentz domine la force radiative, excepté à proximité de la proto-étoile massive. Le mécanisme de lancement des éjections est une *tour magnétique* due au gradient de pression magnétique, conséquence de l'enroulement des lignes de champ dans le cœur en effondrement. En revanche, cette expérience numérique n'a pas permis d'obtenir des résultats convergents (en terme de résolution) sur les jets magnéto-centrifuges qui sont susceptibles de se produire car ils nécessitent une résolution bien supérieure et donc des expériences numériques dédiées. Ces mêmes simulations ont mis en évidence le freinage magnétique, responsable de réduire la taille du disque d'un facteur $\sim$10 par rapport au cas non magnétique, et déjà observé dans le cadre de la formation des étoiles de faible masse. En incluant un champ de vitesse initial turbulent dont nous avons fait varier l'amplitude, nous avons obtenu une variété de rayons de disques et de multiplicités, permettant de reproduire les disparités dans les contraintes observationnelles actuelles. Finalement, nous nous sommes intéressés aux propriétés de ces éjections que l'on peut directement comparer aux données observationnelles, telles que leur angle d'ouverture.

Dans ces travaux de thèse, nous avons ainsi implémenté le couplage entre deux modules de transfert radiatif dans le code RAMSES afin de traiter l'irradiation avec une méthode plus adaptée au rayonnement anisotrope. Nous avons mis en évidence le caractère multi-physique de la formation des étoiles massives, avec en particulier la nécessité de tenir compte des effets de MHD non idéale en plus de l'irradiation. Nos résultats semblent indiquer une forte continuité dans les mécanismes d'accrétion et d'éjection entre les étoiles de faible masse et les étoiles massives, en accord avec les observations. Ils se limitent toutefois aux phases précédant la formation de régions HII par le rayonnement ionisant stellaire. De même, nous avons supposé des conditions initiales ne tenant pas (ou peu) en compte de forts effets d'environnement tels que le suggèrent les modèles à plus grande échelle. Le présent travail constitue cependant une étape essentielle en direction de ces modèles globaux.

Abstract

Understanding the formation of low- and high-mass stars is a fundamental challenge of modern astronomy. They form from the collapse of gravitationally-unstable cores, in the interstellar medium which is nothing but simple to model: energies of gravity, turbulence, magnetic fields, radiation, and cosmic-rays are close to equipartition. Hence, numerical simulations are of a great help in studying star formation. In this work, we have focused on the formation of massive stars, which are very luminous and power a strong radiative force which can, in a simple unidimensional view, stop further accretion of material. Multi-dimensional simulations and particular treatment of stellar radiation are two main ingredients. In that view, the main task of the present thesis has been the numerical coupling between two radiative transfer methods. With this new tool, we have focused on three axes: the mechanisms of accretion, of ejection, and the formation of multiple stellar systems.

The very heart of this thesis has been the numerical coupling between two radiative transfer methods into the RAMSES code (Teyssier, 2002), and its validation through pure radiative transfer benchmark tests. Then, we have applied this method in a radiation-hydrodynamical context of a massive pre-stellar core collapse. We have shown that the radiative force is enhanced, in comparison to the previous method used, ending up in the formation of larger radiative cavities and slightly less accretion. More importantly, we have tested the presence and accretion via radiative Rayleigh-Taylor instabilities at the border of these cavities, whose existence was an active debate in the community. We have shown their absence in our simulations to be of physical, rather than numerical, origin.

In an on-going side-project carried in collaboration with A. Oliva and R. Kuiper (Univ. of Tübingen), we have led a comparison study between our respective codes, when it comes to modelling accretion disk fragmentation and subsequent formation of multiple stellar systems. With a Cartesian grid (instead of their spherical grid), our results show the formation of a binary or triple system, while they obtained a single star. When a multiple system is sufficiently dominated in mass by a single object, our codes show correct agreement on the disk rotation profile and temperature structure.

Finally, we have run original simulations of turbulent magnetized cores with ambipolar diffusion and the newly implemented hybrid radiative transfer method. We have identified the magnetic tower flow as the dominant outflow mechanism, except very close to the massive protostar where radiative force dominates. We have compared these outflow properties to those obtained from observational statistical samples. Our results tend to show a good agreement, provided our initial conditions are representative of the least massive progenitors of high-mass stars, and the collimation is not intrinsic to the outflow mechanism but also depends on environmental factors. Hence, these questions need to be further investigated. We have identified disk-mediated accretion as the only accretion mechanism, with disk sizes significantly smaller than predicted by the radiation-hydrodynamical simulations, and in agreement with recent low-mass star formation results. Eventually, we have questioned the disk-outflow-magnetic fields alignment. Our results are consistent with a random disk-magnetic field alignment and a slightly better outflow-magnetic field alignment, provided the medium is not too turbulent.

Remerciements

Cette thèse a été une quête, une aventure, qui, comme je l'espérais, fut aussi humaine que scientifique. Il est temps de remercier toutes les personnes qui m'ont accompagné, certains au quotidien et d'autres pour en arriver là, six ans après l'instant zéro.

Pour cette raison, je te serai toujours reconnaissant, Frédéric, de m'avoir fait croire de nouveau à un rêve auquel j'avais appris à renoncer. Un grand merci à toi, Peggy, de m'avoir donné ma chance puis montré la beauté de ce métier.

A part ces remerciements hors du temps, je commencerai par Matthias: merci de m'avoir pris en stage il y a trois ans. Tu as réussi à ce que le transfert radiatif et la formation d'étoiles massives éclipsent mon premier amour qu'étaient les microquasars ! J'ai grandement apprécié d'être ton premier thésard (ne serait-ce que pour voir ta HDR !) - j'espère ne pas t'avoir dissuadé d'en avoir d'autres !! Merci d'avoir été là (= Saclay ou P7) au quotidien, jonglant avec tes cours et tes mails pour toujours te rendre disponible. Du scientifique, j'ai beaucoup appris de la rigueur et de la pédagogie. J'ai aussi apprécié nos échanges non-scientifiques, démultipliés pendant cette troisième année.

J'en viens aux membres du DAp. Merci à Lisa et Flo, mes acolytes pendant ces trois ans (team navette), avec qui la pause café de 16h est devenue un rituel, certes plus rare à mesure que la fin approchait (surtout Flo, tellement consciencieuse !). Merci aux thésards du DAp, dont la liste ici ressemblerait à la liste d'auteurs d'un papier LIGO/VIRGO, et en particulier à Théo et Mansour. Fabien, que j'ai rencontré à un arrêt de bus au Royaume-Uni avant ma première conférence internationale, j'ai été ravi que tu puisses revenir à Saclay pendant ma dernière année (légèrement coupée par le Covid !). Anaëlle, pour ton suivi et tes conseils précieux. Jérôme, grâce à qui j'ai pu conserver une activité physique (presque) régulière et avec qui j'ai grandement apprécié discuter (à 10km/h maximum par contre). Pour leur implication dans le soutien aux thésards du DAp, dont j'ai bénéficié, un grand merci à Emeric et Vianney également. Merci à mes cobureaux successifs, Bruno (qui a réponse à tout), Antoine, Gerardo et Anne-Cécile (pour ton fun communicatif), d'avoir donné vie à ce bureau, chacun à votre manière. Merci aux membres du LMPA, Antoine, à la bonne humeur contagieuse, Noé (toujours là pour aider), la Magburst team: Alexis, Raphaël, Mattéo; et Marc-Antoine. Jérôme, qui m'aura converti au flexitarisme (dans un premier temps !) et dont la sensibilité à des causes nobles m'a beaucoup inspiré. En plus de ton calme et de ta gentillesse, tu es un exemple de ce que les chercheurs peuvent apporter à notre société. Merci à Seb Fromang pour tes conseils jusqu'à ton départ pour le LSCE (là aussi, une noble cause !) et bien évidemment pour m'avoir permis de rencontrer Matthias. Patrick, pour tes riches enseignements tous-terrains (MHD, hydro, RAMSES, transfert... climat !) et tes échanges avec Paolo en conférence dignes d'un Nadal-Federer. Thierry, dont le sens physique aiguisé (notamment sur les gradients d'entropie) est inspirant, et pour ta bienveillance en particulier pendant le confinement.

Plus que des collaborateurs, merci à Benoît (mon "deuxième" directeur !) et Joki, les rois du transfert radiatif (mais pas que), pour votre aide, votre disponibilité et vos désormais nombreuses relectures ! Neil, nos chemins se sont croisés brièvement, merci d'avoir malgré tout trouvé le temps de répondre à mes questions (les opacités, toujours elles). Alexis, pour ton aide en particulier quant à mes projets pour la suite, même le week-end. Je remercie les membres de

mon jury, Fabien, Dominique, Frédérique pour m'avoir transmis une sensibilité aux contraintes observationnelles, que j'espère encore faire grandir, et Pascal pour la pertinence des points que tu as soulevés lors de la soutenance et à la lecture du manuscrit.

En s'éloignant un peu de la science et en se rapprochant des bars (attention, les deux sont parfois confondus) : je pense bien évidemment à Amaël et Simon pour nos nombreuses discussions philosophiques/politiques autour d'une (deux?) bière; merci aussi de m'avoir accueilli dans votre bureau en tant que réfugié climatique pendant la canicule. Si l'on peut parler d'une famille astrophysique, merci à Ugo, mon "cousin" de thèse. Merci à Max et toi pour votre accueil chaleureux à Lyon et vos ondes positives. J'ai une pensée pour Fabien le désormais Lillois et mes Nancéiens, à commencer par Bruno et Guillaume, en poursuivant avec la famille : Aurore, Max et Bastien. Cette thèse est pour toi, Dino, dont la vie aura été celle d'une étoile massive. A mes amis d'enfance, de la maternelle au doctorat, pour votre amitié et enfin votre soutien le jour J : Matthieu, Paul (le futur docteur !), Baptiste, Guillaume, Quentin (qui aura dû venir à Saclay pour constater que non, ce n'était pas de l'astrologie) et Julien. Un petit coucou également à Michel, Kenji, Thomas et Tristan.

Ce doctorat n'aurait pas été possible sans mes parents, que je remercie infiniment pour m'avoir transmis la passion de l'astronomie, laissé prendre cette direction et même encouragé; c'est le fruit de votre travail, dont vous pourrez au moins apprécier les premières pages en français ! Merci aussi à mes soeurs, Laura et Fanny, pour votre soutien, et à ma grand-mère.

Enfin, Clau, merci de m'avoir apporté ta lumière, ton amour et ton soutien durant ces trois années (et avant), et très particulièrement lors de la rédaction de ce manuscrit, alors confinés. Un chapitre se clôt et j'ai hâte d'écrire le suivant à tes côtés.

Contents

List of Figures

List of Tables

CHAPTER 1
Introduction

Contents

1.1 Preamble and definitions

IN GALAXIES, the space between celestial objects (from protostars to black holes) is the *InterStellar Medium* (ISM), which is multiphase (ionized, atomic and molecular, McKee & Ostriker 1977), turbulent (see the review by Elmegreen & Scalo 2004), magnetic, with strong variations of density, velocity, gas abundances and temperature. Star formation is one of the steps of the so-called interstellar cycle. It occurs in dense and cold complexes called molecular clouds, which are made of a mixture of gas and dust. Molecular clouds contain denser blobs called *clumps*, which gather matter (gravitationally or because of compression by external forces) until they become massive enough to be gravitationally unstable, at which stage they are qualified as *dense pre-stellar cores*, and collapse onto themselves. Star formation follows this process and turns gas into stars, which form elements heavier than the hydrogen, deuterium and helium - the most abundant elements - already present in the primordial Universe. Stellar radiation and winds affect the interstellar medium properties by injecting kinetic energy and ionizing radiation into it, which can contribute locally to the formation of new clumps as well. At a star's death, a supernova explosion takes place if the star is massive enough and enriches the interstellar medium with all the elements formed during its life. Supernovae and expanding

ionized bubbles trigger new events of star formation. The formation of stars is, indeed, a fundamental brick of the interstellar cycle and an active topic of research due to its importance to understand the ISM as well as the formation of solar systems like ours. It also comes with a number of open questions.

Research in physics has always looked for invariant functions in a quest for general laws, uniqueness, and causality from a common source. It that view, it is natural to study statistical functions such as the distribution of the initial mass of stars. The origin and possible universality of this so-called *Initial Mass Function* (IMF) is a matter of debate and so is its inheritance from the pre-stellar core mass. Likewise, the path from clumps and cores to stars has been deeply studied and is not entirely revealed. In fact, star-forming regions are intrinsically dense and far from us (> 100 pc), hence difficult to observe. Although dust is a minor contributor to the ISM mass, it is its main source of opacity and prevents the observations in the optical range. The development of sub-millimeter and millimeter observatories has played a crucial role in making progess in this area. Moreover, star formation is a non-linear problem. On the one hand, the (magneto-)hydrodynamical equations are non-linear. On the other hand, the timescale for the densest part of the cores to collapse is much shorter than the free-fall time of the lower-density envelope, hence protostars' feedback may affect the environment they accrete from. It is a multi-physics puzzle, since the cores are close to equipartition between thermal, turbulent and magnetic pressures (Mouschovias, 1991). At smaller scales and higher densities, ions and neutrals are decoupled and modelling the magnetic field is a complex problem. This applies to the formation of stars of all masses, but massive stars, *i.e.* $\sim$8 times more massive than our Sun, add a significant ingredient to this: radiation. As we shall see, massive star formation requires the treatment of various physical processes and is motivated by the large impact that massive stars have on their environment.

I will first present the multiple faces of massive stars when it comes to impacting their surrounding, and astrophysical questions they are linked to. This sets the motivations to understand their formation. The state of the art of low-mass star formation is depicted, because it shares many fundamental concepts with our current knowledge of high-mass star formation, which is described next. At the end of this chapter, the reader will find essential theoretical elements which are useful for a full understanding of this problem.

1.2 The central role of massive stars

MASSIVE STARS ($\gtrsim 8\,M_\odot$), are very luminous and have large surface temperatures (spectral-type O- or B-), as shown in left panel of Fig. 1.1. Simple arguments based on the hydrostatic equilibrium can show that a star's luminosity L increases with its mass M as $L \propto M^a$ (with $1 < a < 6$, see *e.g.* Salaris & Cassisi 2005). In fact, they are hotter than their low-mass counterparts, their blackbody spectrum peaks at higher frequency and implies a higher-energy flux. Their feedback affects their environment on various spatial scales. On small scales ($\lesssim 10^4$ AU), radiation pressure can push away the gas and create molecular outflows. On larger scales ($\lesssim 10^6$ AU), their photoionizing flux creates HII regions where the temperature goes from $\lesssim 100$ K to $\sim 10^4$ K. The large associated thermal pressure can cause the dispersal of its host molecular cloud (Ali & Harries, 2019), although high-density filaments could resist it (Watkins et al., 2019). Hereafter, I show how active are massive stars in the interstellar medium and in the Galaxy.

The feedback from massive stars is not only multi-scale, it is also multi-physics. At the end of their intense life (see the left panel of Fig. 1.1, which indicates their lifetime as a function of the mass), massive stars explode into supernovæ. On galactic scales, supernovae are among the main drivers of galaxy evolution (Larson 1974, Dekel & Silk 1986). These extraordinary events eject several solar masses of gas at supersonic speeds which cause heating and momentum in-

jection into the ISM. Their outflows in the form of radiation and winds may also be important in that view (Naab & Ostriker, 2017). Massive stars launch line-driven winds (Castor et al. 1975, Kee & Kuiper 2019) which have a similar impact as radiation pressure locally, although their influence on galactic scales is not clear yet. Despite their small number, they dominate the total stellar radiation (e.g Leitherer et al. 1999 for a synthesis model of feedback from stellar populations). The typical energy of a supernova is $\sim 10^{51}$ erg, but the total radiative energy during the massive star's life is $\sim 10^{53}$ erg, and $\gtrsim 10^{50}$ erg in winds. After their death, the interstellar medium (ISM) is enriched in metals for the next generation of stars (see Nomoto et al. 2013 for a review on the chemical evolution of galaxies). Massive stars may also be major contributors to the total amount of cosmic rays in the ISM according to recent *Fermi* LAT observations in the Cygnus region (Aharonian et al., 2019). Their feedback may regulate or enhance star formation (Rebolledo et al., 2020) by increasing the turbulent motions and therefore the mass at which cores fragment to form stars (see Sect. 1.9). Large dust grains can suffer disruption via radiative torques owing to the strong radiation in a radius of $\sim$2 pc from massive stars and supernovae (Hoang et al., 2018). Hence, massive stars undoubtedly play a central role in the ISM and galaxy evolution.

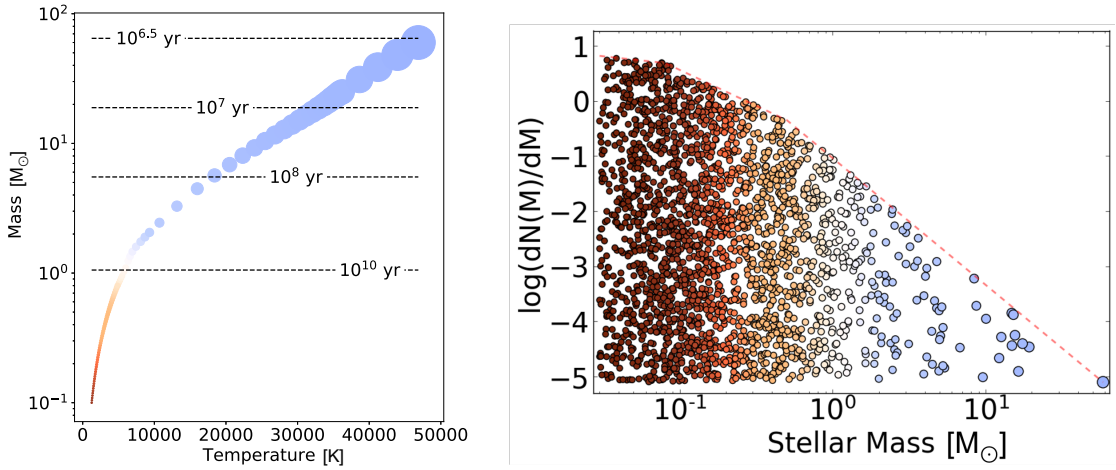

Figure 1.1: Left: Stellar mass-temperature relation. The dashed lines indicate their lifetime, the color of dots their spectral color (hence surface temperature) and the size of dots their luminosity. Right: Initial distribution of the mass of stars (Kroupa, 2001). The number of stars is randomly sampled from this distribution. The dots color gives their spectral color. Credit: plots from https://github.com/keflavich/imf based on stellar evolution models (Ekström et al., 2012).

The formation of massive stars is also at the center of a more general astrophysical question, the origin and the universality (or not) of the *Initial Mass Function* of stars (IMF, see e.g. Salpeter 1955, Kroupa 2001, Chabrier 2005), *i.e.* the number of stars at a given mass as a function of their mass, at birth (right panel of Fig. 1.1). Its origin may be linked to the *Core Mass Function* (CMF). In that view, ground-based (sub)-millimeter surveys of ρ Ophiuchi, Serpens, and Orion B have revealed a resemblance between both distribution functions (Motte et al. 2001, Bontemps et al. 2001), confirmed by Herschel observations in the Aquila and Polaris regions on larger samples (Andre et al., 2010). This would imply that the stellar masses are at least partly determined by the cloud's fragmentation before collapse, with a high ($> 50\%$) efficiency for converting the cloud's gas into stars (Motte et al., 2001). Theoretical works have attempted to explain the (lack of) variations of the IMF by looking at the underlying processes that govern star formation. Some of these studies have focused on large-scale turbulence (Padoan et al., 1997) or addi-

tional local processes such as dust opacity limit, tidal forces from other stars and collapsing envelope properties Hennebelle et al. 2019. A crucial production from this type of works is to predict what should be the typical stellar mass, which is $\sim$0.5 $M_\odot$ in the observational samples, (Kroupa, 2001). In the former case, it is found to be sensitive to the Mach number of the flow and decreases with it (Padoan et al., 1997). In the latter, it is equal to $5-10$ times the characteristic mass set by the opacity limit reached during the collapse phase (first Larson core, Sect. 1.3). Then, the further accretion is impeded by other accreting objects (of similar masses) formed in the turbulence-induced density fluctuations of the envelopes. To sum up, the IMF universality question remains open, both on the theoretical and observational sides, and it is not clear yet whether it is mainly governed by large- or small-scale physics. The high-mass end of the IMF is very sensitive to the scenarii of massive star formation since only a few objects populate it.

The origin of the mass of stars is also linked to another fundamental astrophysical question: is there an upper-mass limit to stars ? A number of studies have contributed to answer this question and revealed stars with a mass much greater than 8 $M_\odot$: up to $\sim$300 $M_\odot$ in the R136 star cluster (Crowther et al., 2010), $\sim$200 $M_\odot$ in the 30 Doradus nebula in the Large Magellanic Cloud (Schneider et al., 2018), $\sim$120 $M_\odot$ in the Arches cluster (Martins et al., 2008). The high masses are not reserved to individual objects: the WR 20a (Wolf-Rayet star, highly variable) binary is believed to contain two $\sim$80 $M_\odot$ stars orbiting each other (Bonanos et al., 2004). Finally, the first generation of stars (so-called Population III) may have hosted very massive stars. Indeed, the absence of metals, that stars would produce afterwards, allows clouds to reach higher masses ($\sim 10^3$ $M_\odot$) before becoming unstable (Bromm et al., 1999) and eventually merge to $\sim 10^4$ $M_\odot$, showing no sign of fragmentation. It may be that these Pop. III stars were therefore quite massive, $\gtrsim$100 $M_\odot$ (Hosokawa et al., 2016), unless a mechanism would stop the accretion. Understanding the formation of present-day massive stars is a mandatory step to tackle the formation of Pop. III stars in the early Universe. The example of WR 20a leads us to the following problem.

When one looks at the solar system, one might be tempted to think that stars form alone. Actually, as in WR 20a, most stars are born in clusters (Lada & Lada 2003, Stahler 2018). The majority of massive stars are part of multiple systems which can contain more than two stellar objects (Eggleton & Tokovinin, 2008). For instance, a system of four OB stars is detected in the Great Carina Nebula (Leung et al., 1979). Statistical studies on these objects have shown that more than 70% of galactic OB stars are in binary associations (Sana et al., 2012), and more than 82% in the southern Milky Way (Chini et al., 2012). In the young and nearby OB association Scorpius OB2 (Sco OB2), the binary fraction is $\gtrsim$ 70% with intermediate-mass ($\sim 4-8$ $M_\odot$) primaries. As a particular case, the three-body interaction leads to the ejection of one companion while the two others come closer to each other. There is a clear trend pointing at a higher fraction of runaways among massive stars (Gies & Bolton, 1986). A recent sample of 250 O-stars led to 69% runaways (Chini et al., 2012) from spectroscopic measures. The typical runaway velocities are $v \simeq 30-40$ km/s, but they can reach much higher values, $v \simeq 500$ km/s (Silva & Napiwotzki, 2011). These runaway stars can be a moving source of ionization for the interstellar medium, and as they leave their birth place they lead to a random distribution of supernovæ in the galaxy. This motivates the need to understand the formation of such multiple systems. A complete theory of massive star formation should account for this multiplicity question but most theoretical works have focused on single objects, due to its complexity and to the various physical processes involved.

Massive stars are, undoubtedly, complex objects whose interactions with their surroundings makes them essential. Despite the necessity to understand massive star formation, there is, to date, no complete theory. In addition of being a theoretical challenge, as I will show, this is also a complex observational task. Massive stars do not live long because of a high nuclear reaction efficiency. They are also fewer in number than low-mass stars, and therefore rare and

statistically located far from us ($>$ 1 kpc, one tenth of the Milky Way radius). They are born in dense regions which offer them a large mass reservoir but also complicate the observer's task (more details in Sect. 1.6). In the next sections I will review the current knowledge on (low-mass) star formation and I will introduce the difficulties encountered when one extends this view to high-mass stars.

1.3 A first step : Low-mass star formation

"The process of star formation and the conditions under which star formation begins have been the subject of much speculation, but so far little if any hard factual knowledge on the subject can be claimed."
Richard Larson, 1968

1.3.1 Theory

Many advances have been made since Richard Larson's PhD thesis (1968). Currently, the formation of low-mass stars ($M_\star \lesssim 8\,M_\odot$) is better understood than that of high-mass stars - although some open questions remain, as I will show later. Here, I briefly review the state of the art to use it as a prerequisite to tackle massive star formation.

Stars form in molecular clouds (composed of a mixture of gas and dust), from the collapse of gravitationally-unstable clumps of higher density than the background gas. The first bricks of the theory mainly rely on calculations of a cloud gravitational collapse (see the equations in Sect. 1.9), both from analytical and numerical approaches. Rotation, magnetic fields and turbulence were first neglected, for the calculations to be tractable, despite their ubiquity in the interstellar medium. The general dynamics of this phenomenon has been studied under simple assumptions, such as spherical symmetry. Among the first hydrodynamical calculations, Penston (1969) and Larson (1969) obtained non-homologous solutions with $\rho \propto r^{-2}$, highlighting the sensitivity to initial and boundary conditions. It has been pointed out later in Shu (1977), who obtained a self-similar solution describing an "inside-out" collapse, starting from an isothermal sphere at rest. In this solution, a rarefaction wave propagates against the collapsing flow at the sound speed. Indeed, the free-fall time depends inversely on the density, so it becomes shorter in the inner, hence denser, part of the cloud (right panel of Fig. 1.2). The free-falling envelope density is given by a power-law $\rho \propto r^{-3/2}$.

Left panel of Fig. 1.2 shows the evolution of the central temperature and density during the collapse, as obtained with numerical simulations (Masunaga & Inutsuka, 2000). The ideal gas approximation for an adiabatic reversible process would state that $T \propto \rho^{\gamma-1}$, thus the slope of the curve is set by the adiabatic index γ. Hence, the collapse dynamics is strongly linked to the microphysics.

Four phases can be distinguished, starting from a pre-stellar core of $\sim$10 K and $\sim 10^{-18}$ g cm^{-3} (H_2 particle density $n \sim 10^6$ cm^{-3}), which is typically a self-gravitating, gravitationally unstable (see Sect. 1.9.1), starless object on the verge to collapse.

- **Isothermal collapse**: the core is unstable to density perturbations and collapses. Its central density increases and is sufficiently low for the energy provided by the collapse to be radiated away. Gas and dust are thermally coupled (Galli et al., 2002) and dust is the main contributor to the total opacity. So far, medium is optically-thin because of the low density. When the central region reaches densities of the order of 10^{-13} g cm^{-3} ($n = 10^{11}$ cm^{-3}) it becomes opaque to its own radiation.
- **Adiabatic contraction**: the core center becomes optically-thick, so the gravitational energy provided cannot be radiated away and the core heats up adiabatically. The central

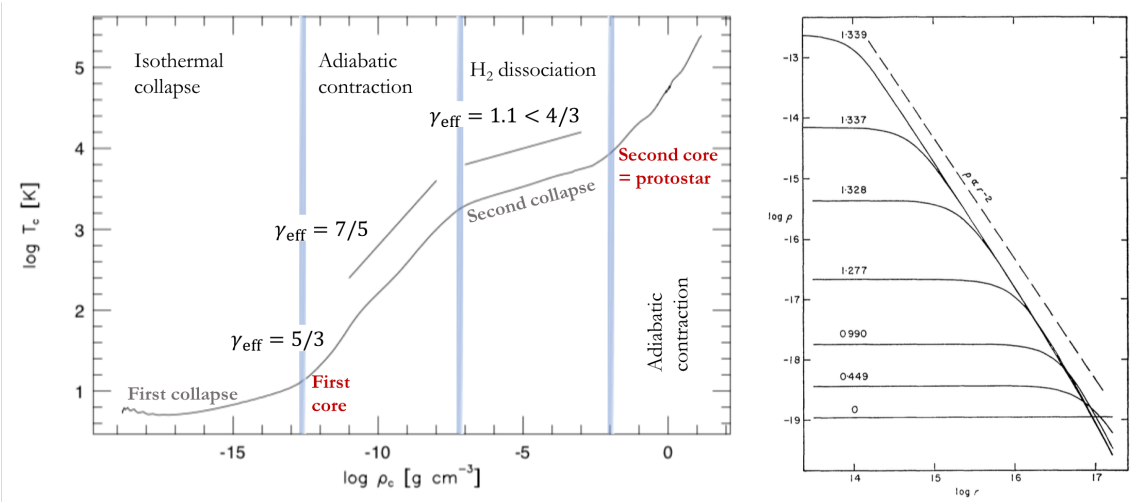

Figure 1.2: Left panel: Evolution of the central temperature and density during a collapse (adapted from the radiation hydrodynamical calculation result from Masunaga & Inutsuka 2000). Four phases can be distinguished (see text). Right panel: Temporal evolution of the cloud radial density profile (Larson, 1969). The profile becomes more sharply peaked with time because the free-fall time is lower in the densest part.

temperature and pressure increase rapidly enough to slow down the collapse. Outside, it remains isothermal and the gas continues to free-fall onto the central region, where it is suddenly stopped and produces a shock front. The central region has a quasi-adiabatic behavior with an effective adiabatic index $\gamma_{\rm eff} = 5/3$ (similar to that of an atom) and is often called the first Larson core, or first hydrostatic core. It has a radius of $\sim 1 - 10$ AU, much larger than a stellar radius. At $\sim$100 K, the rotational degrees of freedom of the hydrogen molecules are excited, and the adiabatic index decreases (the curve flattens) from $\gamma_{\rm eff} = 5/3$ to $\gamma_{\rm eff} = 7/5$.

- **H_2 dissociation**: the core continues to heat up until its central temperature reaches $\sim$2000 K. The H_2 binding energy per molecule is smaller than the thermal energy, which results in H_2 dissociation. Most of the gravitational energy is consumed in this process. The adiabatic index decreases below its critical value (see Sect. 1.9.2) so the core becomes unstable and begins collapsing a second time. The first core lifetime was about 10^3 yr.

- **Adiabatic contraction**: the heating process starts again, and the pressure rises rapidly until the density reaches stellar values and stops the collapse. At the center, a small core is in hydrostatic equilibrium arises. This object is the second Larson core, or second hydrostatic core. It has a radius of about one solar radius and is a protostar.

So far, the main source of energy was gravity. After the temperature exceeds 10^6 K, the core starts burning the deuterium (present in small quantities in the ISM, with abundances $(D/H) \sim 2.5 \times 10^{-5}$, Bruston et al. 1981) via the reaction $\mathrm{p} + \mathrm{d} \rightarrow \gamma + {}^3\mathrm{He}$. The protostar goes through several phases that a few studies have aimed to probe assuming spherical accretion (*e.g.*, Stahler 1988, Hosokawa & Omukai 2009). The protostar evolution depends on its entropy, whose supply varies between different accretion geometries. At a given entropy, there is a unique relation between the star's mass and radius. For instance, a large increase in entropy causes the protostar to bloat up. For low-mass protostars (or, equivalently, low accretion rates, $\dot{M} \lesssim 10^{-5}\,\mathrm{M_\odot.yr^{-1}}$), the heat (entropy) generated by fusion is not transported radiatively due to the high opacities (because of high densities). As a consequence of this sharp entropy profile, convection takes

place in most of the interior and helps bringing new fuel, *i.e.* protons, via internal mixing. This effect is local and does not concern the rest of the protostar, which remains radiative due to low opacities. Progressively, deuterium burning provides entropy and therefore increases the protostar size. Energy production via deuterium fusion is very sensitive to the temperature. An increase of temperature causes more deuterium burning and therefore a higher temperature (and entropy), which bloats the protostar up and lowers the temperature consequently. The temperature is approximately kept constant by this mechanism, the so-called thermostat effect (Stahler 1988), but requires a steady supply of fresh deuterium via convection (step (a) of Fig. 1.3). As the protostar grows, a radiative barrier ("luminosity wave") forms (b) and disables the inward transport of deuterium, while the center depletes it rapidly (c). The interior luminosity declines consequently and the outer shell accumulates deuterium until it reaches its fusion temperature and becomes convective (d). This new rise of entropy causes the swelling of the outer layers. The mass increases, and so does the radius of the radiative barrier, which drives the convection shell outward until the protostar is entirely radiative. As deuterium burning has stopped, the star starts to contract again and this mechanism provides a new source of luminosity. This is considered as the Pre-Main Sequence phase (PMS). There is no thermostat effect anymore so the core reaches higher temperatures as contraction occurs. When the temperature is 10^7 K, the protostar reaches the Zero-Age Main Sequence (ZAMS) as hydrogen fusion begins.

All these processes contribute to the protostar's feedback onto its birth environment and therefore may play a crucial role during its accretion phase. It cannot be straighforwardly extended to high-mass protostars and requires dedicaded studies (Hosokawa & Omukai 2009, Hosokawa et al. 2010), which themselves depend on the accretion scenario. Standard numerical simulations are not coupled to protostellar evolution codes, due to the high computational cost (a few exceptions exist, *e.g.* Kuiper & Yorke 2013). Accounting for protostellar evolution usually involves pre-computed models which indicate the stellar radius and luminosity, at a given accretion rate and stellar mass. It is however important to keep this in mind as being a subgrid physical model and a limitation one would like to alleviate in the future.

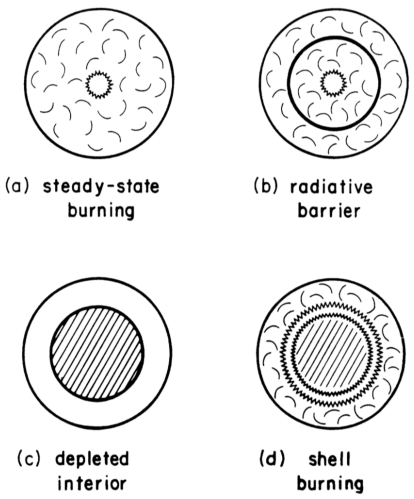

Figure 1.3: Schematic figure of the temporal sequence of a low-mass protostar's interior (Palla & Stahler, 1990).

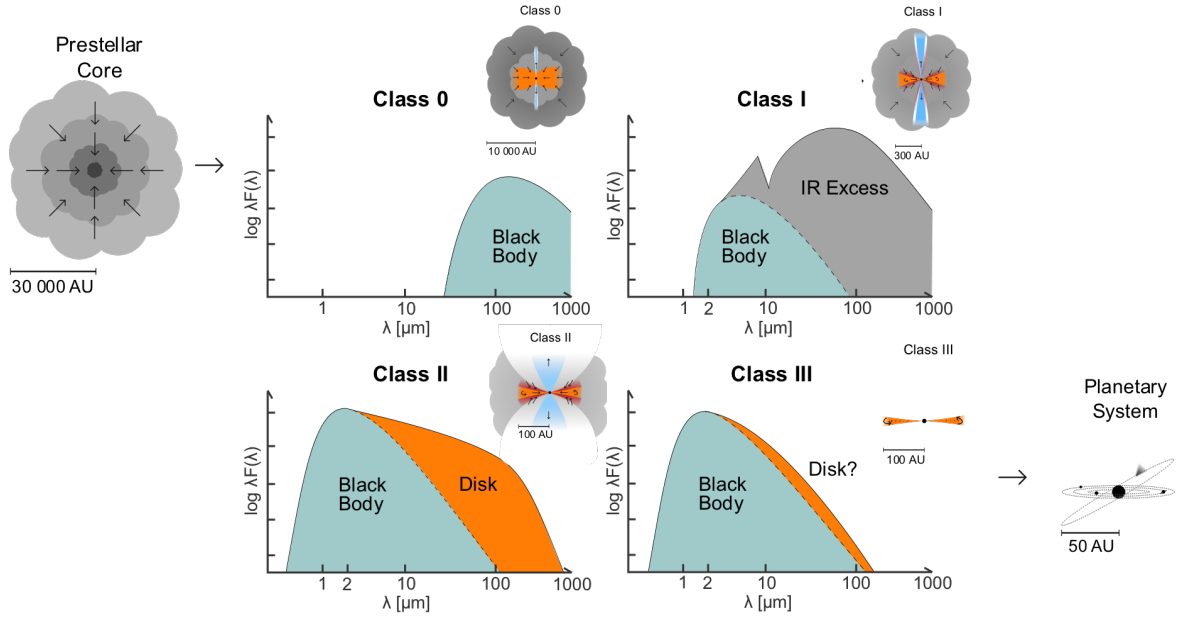

Figure 1.4: Empirical evolutionary sequence of low-mass star formation and corresponding spectral energy distribution, based on Andre (2002). Credits: Magnus Vilhelm Persson.

1.3.2 Empirical evolutionary sequence

After the seminal works of star formation, which covered its theoretical aspect, infrared and sub-millimeter surveys have confirmed the global picture (Shu & Adams 1987, Lada 1987, Andre et al. 1993, Ward-Thompson et al. 1994), notably with the NRAO 11m telescope, the IRAM (1984-) telescope, and the IRAS satellite (1983), respectively. The Spitzer (2003-2020) and Herschel (2009-2013) space telescopes have significantly contributed to advances in this field, due to their sensitivity in this range of wavelengths. The observational evolutionary sequence of low-mass star formation is pictured in Fig. 1.4. It divides the different steps of star formation into classes (Andre, 2002), initially based on the spectral energy distribution (SED) and the observed geometry.

- **Pre-stellar phase**: it is characterized by a pre-stellar core embedded in its parent cloud which emits thermal radiation at low temperature and therefore in sub-millimeter wavelengths. It is cold ($T \sim 10 - 20$ K), dense ($\rho \sim 10^{-20} - 10^{-18}\,\mathrm{g\,cm^{-3}}$, $n \sim 10^{4} - 10^{6}\,\mathrm{cm^{-3}}$), has a size of $\sim 0.01 - 0.1$ pc) and is typically observed via dense tracers like N_2H^+. The collapse theoretical picture I have presented previously would be located between this step and the class 0 object.

- **Class 0**: the newly-formed protostar (second Larson core) accretes material from the collapsing envelope, with $M_\star \ll M_{\mathrm{env}}$: most of the mass remains in the envelope. At this point, the emission is dominated by the surrounding dust, which has absorbed the protostar radiation. The short lifetime of this step ($\sim$ 30 kyr) and the opaque envelope make it difficult to observe. The cloud initial rotation and angular momentum conservation lead to the formation of an accretion disk around the protostar, while outflows pierce through the envelope and escape. This is the main accretion phase. The mechanism at the basis of these outflows is not consensual but it may serve the redistribution of angular momentum, needed for accretion to occur. Two main candidates are disk winds (launched from every disk radius) and "X-winds" (launched at the corotation radius between the

disk and the star magnetosphere) and both are magnetocentrifugal mechanisms (see the review by Pudritz & Ray 2019 and Sect. 1.9.4).

- **Class I**: The protostar is fed by the disk until its mass exceeds the disk mass, this is the end of the main accretion phase, $M_\star > M_{\rm env}$. Both components emit thermal radiation measurable on the SED, mainly the disk in the infrared (hundreds of Kelvins) and the protostar in the UV range (thousands of Kelvins). During this phase, inflow (inferred from the SED fitting) and outflows (visible in the optical or in the infrared, *e.g.* right panel of Fig. 1.7) are taking place simultaneously.

- **Class II**: at the end of the main accretion phase, a significant fraction of the disk mass has been accreted by the central object. The SED is dominated by the protostar emission, which reaches the pre-Main Sequence. The disk can still absorb and re-emit ∼25% of the total luminosity (Adams & Shu, 1986). This configuration remains visible for $\sim$ 1 Myr and is often called a T-Tauri star, as a reference to the first-ever observed object of this type.

- **Class III**: dust grain growth occurs in the (optically-thin) debris disk and eventually leads to planet formation, while the protostar is reaching the Main-Sequence (starting the hydrogen fusion reaction). The disk emission in the SED becomes negligible.

This generally accepted scenario is shady by several open questions, such as the origin of the outflows, the protostellar disk formation and evolution, and the star-disk interaction. In addition, the physics of protoplanetary disks and planet formation is highly-dependent on the previous phases. The general and qualitative picture is, however, supported by both observations and numerical works. Our question of interest is: does it apply to massive stars?

1.4 Towards higher masses: when radiation comes into play

In this section I set the seeds for this thesis by presenting the historical difficulty encountered when trying to explain massive star formation with the previous scenario.

Let us consider a protostar accreting from a spherically-symmetric envelope (1D view, see the top panel of Fig. 1.5). On the one hand, gas is free-falling onto the protostar, accelerated at $a_{\rm grav} = GM_\star/r^2$, where r is the distance to the protostar of mass $M_\star$, and G the gravitational constant. On the other hand, the protostar's radiation exerts a pressure on the inflow, corresponding to a radiative acceleration $a_{\rm rad} = \kappa L_\star/(4\pi r^2 c)$ where $L_\star$ is the protostar's luminosity and c is the speed of light. The medium is composed of gas and dust (∼1% in mass) and its opacity κ is dominated by the dust continuum opacity. At the protostellar densities, gas and dust are well-coupled so the force acting on dust is efficiently transmitted to the gas. Above ∼1500 K, hence close to the protostar, dust grains sublimate and the medium is optically-thin so the protostar radiation propagates freely. The radiation is progressively absorbed beyond this region. Interstellar dust opacities globally increase with a decreasing wavelength, thus the UV photons are more quickly absorbed than the others. The gas-dust mixture heats up and emits radiation in the infrared (IR), corresponding to a temperature of a few hundreds Kelvins. For a star to become massive, the inflow must resist the pressure from this re-processed radiation. The ratio of the radiative acceleration to the gravitational acceleration is given by the dimensionless number called the Eddington factor

$$\Gamma = \frac{\kappa L_\star/4\pi r^2 c}{GM_\star/r^2} \simeq 8\times10^{-5}\left(\frac{\kappa}{1\,{\rm cm^2\,g^{-1}}}\right)\left(\frac{M_\star}{M_\odot}\right)^{2.5}, \tag{1.1}$$

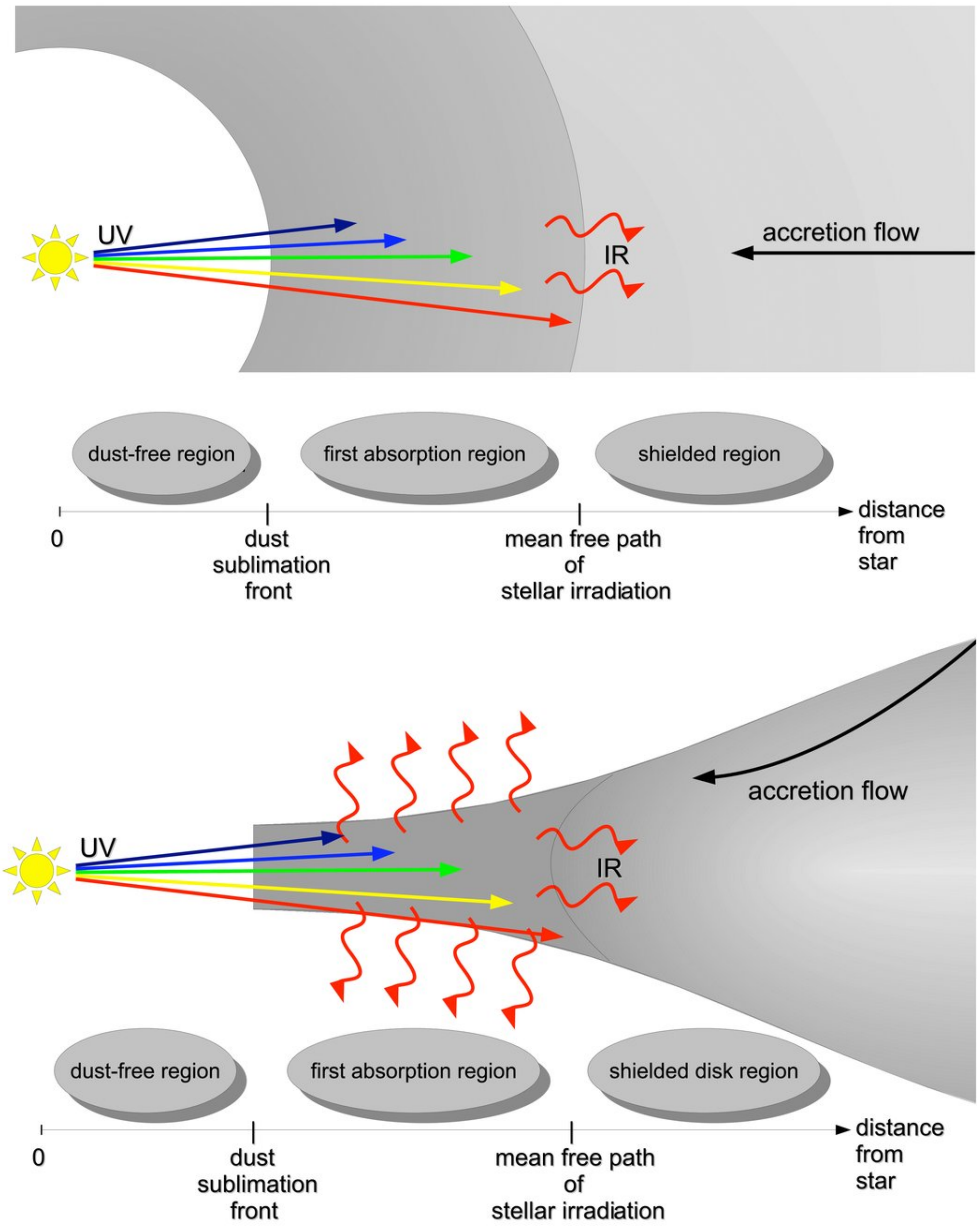

Figure 1.5: Top: schematic view of a spherically-symmetric accretion flow onto a massive protostar. Bottom: schematic view of the accretion via a disk onto a protostar. Dust re-emission escapes preferentially via the poles, where the medium is transparent. Credits: Kuiper et al. (2010b).

where we have used a simplified mass-luminosity relation: $L_\star \propto M_\star^{3.5}$ (valid between 2 and 55 $M_\odot$). The dust opacity κ varies by several orders of magnitude with the photon frequency so there is no typical value. We can however take $\kappa \simeq 5\,\mathrm{cm^2 g^{-1}}$ (Krumholz, 2017) as a lower limit adapted to protostellar disks in the Milky Way. Thus, the mass above which $\Gamma > 1$ is equal to $M \simeq 23\,M_\odot$. Reasoning on the dynamical versus radiative pressure leads to a similar result and requires to compute the dust sublimation radius. The uncertainty we had on the opacity is replaced by the uncertainties on the various prescriptions used to compute this radius (density profile, temperature profile), which can end up as a factor $\sim$1.5 on the stellar mass (Larson & Starrfield, 1971). Above this mass, radiative acceleration is sufficient to reverse the flow. Numerical simulations performed by Kuiper et al. (2010b) under the hypothesis of spherical

symmetry have confirmed the existence of this limit.

This calculation shows a main difference between low- and high-mass star formation. Any model must explain how to overcome this radiation pressure barrier, since the existence of stars above this limit is clear (*e.g.*, Crowther et al. 2010). A substancial part of the answer came from the 2D frequency-dependent radiation-hydrodynamical simulations of Yorke & Sonnhalter (2002) (confirmed later by Kuiper et al. 2010b, see bottom panel of Fig. 1.5). Their work has shown the emergence of the accretion via a disk. Thanks to their careful treatment of radiation, they were able to capture the strong anisotropy of the radiation field. They showed that in a protostar-disk system radiation tends to leave through the poles (the so-called, *flashlight effect*), which lowers the radiation pressure onto the accretion flow and hence lets the star gaining more mass. They obtained a 42.9 $M_\odot$ star from the collapse of a $\sim$120 $M_\odot$ pre-stellar core. Therefore, disk accretion, as in low-mass star formation, is a viable and sufficient accretion mode for massive stars. As I will show now, several models have passed this radiation barrier test and attempted to formulate a complete theory for massive star formation.

1.5 Current models of massive star formation

At small scales, disk accretion has been shown to be effective (Yorke & Sonnhalter, 2002) to overcome the radiation pressure barrier. The global models have attempted to explain the origin of the mass of massive stars, whether it has been pre-assembled (and how) or brought by environmental interactions. Two classes of models exist, between which the main difference is whether massive stars form in isolation or not. I will first focus on the latter class, where the process that leads to a massive star includes many dynamical interactions between a protostar and its environment.

Accretion-induced collisions are among the mechanisms able to circumvent this radiation pressure barrier problem (Bonnell et al. 1998). Since it occurs above $\sim$20 $M_\odot$, Bonnell et al. (1998) have proposed that intermediate-mass stars ($\sim$10 $M_\odot$) form through the classical star formation scenario, accreting gas from their surrounding, until they come close enough to eachother to finally merge and lead to a higher-mass object. This model predicts that massive stars would form at the center of stellar clusters. The isolated massive stars we observe would have been ejected from their birth site by gravitational interactions, like the runaway stars we have mentioned above. It would not, however, explain how massive stars with low proper motions would have formed.

In a larger frame, the competitive accretion model has emerged (Bonnell & Davies, 1998), based on the observation of mass-segregation in the Trapezium cluster in Orion, *i.e.* the more massive stars being located in the center. This has been further studied in numerical simulations, without radiative transfer (Bonnell & Davies 1998, Bonnell et al. 2001, Bonnell et al. 2004). They have simulated the dynamics of a stellar cluster forming from a turbulent molecular cloud and compared the final mass of stars to the masses of their clumps (from which stars form), their envelopes and their subsequent accretion events. They find no correlation between a star mass and its clump mass and a good correlation between a star mass and its envelope mass (for low-mass stars but not for high-mass stars). The envelope is defined as the spherical mass reservoir where at least 99% of the gas ends up in the star, *i.e.* which is not shared by other stars. Furthermore, they find a clear correlation between a star final mass and the mass subsequently accreted apart from its parent clump. Their results show that the mass of a massive star is governed by its ability to accrete the common gas and is independent of the mass of the clump from which it formed, while its envelope mass is not sufficient. They also find a linear relation between the mass of a massive star and the number of companions, which is consistent with multiple systems being more frequent for massive stars than for low-mass stars. However, these studies suffer the absence of radiative transfer and magnetic fields. In

particular, pure hydrodynamical simulations would favor fragmentation by ignoring stabilizing effects from magnetic fields (Commerçon et al. 2011a, Myers et al. 2013) and/or turbulence.

At molecular cloud scales, the Global Hierarchical Collapse model (GHC,Vázquez-Semadeni et al. 2016, Vázquez-Semadeni et al. 2019) naturally includes massive star formation as a part of a hierarchical fragmentation model, in which small-scale collapses occur within large-scale collapses. In this frame, filaments consist in flows of infalling gas ("ridges") coming from the larger scales and directed towards the central zones, called "hubs", where massive stars form. As in the competitive accretion model, it relies on a "clump-fed" accretion (Smith et al., 2009) in contrast to "core-fed" accretion of isolated models (McKee & Tan, 2003) (see below). This model is supported by the ubiquiticity of filaments, some of them containing large-scale infall motions (Schneider et al. 2010, Csengeri et al. 2011). Observations with the Atacama Large Millimeter Array (ALMA) of individually collapsing prestellar clumps and high mass infall rates onto massive cores (*e.g*, Neupane et al. 2020) are consistent with this picture, in contrast with isolated cores in the core-fed accretion models. In this frame, the accretion rate is supposed to increase with time in the area of the molecular cloud under global collapse.As a by-product, it also favors interactions and therefore collisions (Bonnell et al., 2003).

The inertial-inflow model (Padoan et al., 2019) aims at linking low- and high-mass star formation to large-scale turbulence driven by supernovæ explosions. This supersonic turbulence leads to density peaks which can collapse gravitationally (so-called *turbulent fragmentation*). The power-law end of the IMF is a natural consequence of the turbulence being scale-free, whose exponent is fixed by the temperature, the mean density and the velocity dispersion (Padoan et al., 1997). In this model, a low- to intermediate-mass star can form from a pre-stellar core before it accretes enough material from large-scale converging inertial flows to become a massive star. Consistently, the timescale to form stars in this scenario scales with the mass: the time it takes to gather 95% of the final stellar mass M_f is $0.51\mathrm{Myr} \times (M_\mathrm{f}/1\,\mathrm{M}_\odot)^{0.54}$, which gives $\sim$2 Myr for a $10\,\mathrm{M}_\odot$ star. This is the most recent model of its class.

The turbulent core accretion model (McKee & Tan, 2003) is in the second class of models. It is a somehow scaled-up version of the low-mass star formation model. It aims at explaining the mass of massive stars by inheritance from their parent core mass. In this model, the core undergoes Jeans fragmentation at higher masses (than in the low-mass star formation theory) because turbulence and magnetic fields help stabilizing it. Turbulence has a second role: it generates large gas velocities which can therefore circumvent the radiation pressure barrier, where the accretion rate goes as $\sim c_\mathrm{s}^3/\mathrm{G}$ in the isothermal case (Shu, 1977), as c_s is the isothermal sound speed and would be larger when accounting for non-thermal motions (McKee & Tan, 2002). Reaching the star final mass takes one to several free-fall times, typically $\sim$100 kyr. This model suffers a lack of consistency with observations. Indeed, it predicts the existence of starless massive pre-stellar cores, these massive clumps with no stellar activity, on the verge to collapse. However, to this date there only exist few candidates (*e.g.*, Nony et al. 2018). Hence, whether it occurs or not, this pathway should not be the most frequent to form massive stars. In spite of this apparent tension, this model is often used in massive star formation simulations as it permits to probe the small-scale dynamics while not having to deal with the global dynamics of the molecular cloud.

The need for observational constraints is striking in the case of the turbulent core accretion model since it relies on the existence of a particular structure, the massive pre-stellar core. Recent technological advances in the millimiter and infrared regime, together with polarization measurements to deduce the magnetic field properties, have not ruled-out any of the models above yet. Nonetheless, they have made the multi-physical aspect of massive star formation clear. Although theoretically-challenging, this richness also provides complementary informations on the birth and evolutionary path of massive protostars, as I will show.

1.6 The legacy of *Spitzer* and *Herschel*, the advent of ALMA

High-mass stars are embedded in very dense clouds at more than 1 kpc (except Orion, right panel of Fig. 1.9). Their observation requires far-IR (*Spitzer* and *Herschel* space observatories), (sub)millimeter imaging (SubMillimeter Array, SMA, and ALMA) at high angular resolution, and spectroscopy to identify gas motion (infall, outflows) and masers. Here I present the observational constraints regarding the conditions in which high-mass stars form.

A possible tool to derive an empirical evolutionary sequence has been provided by protostellar radiation. Ionizing radiation from young massive stars can form HII regions that expand and eventually destroy the parent cloud. The size of this region has been considered as a clock to measure its evolution (see Churchwell 2002 for a review), from hyper-compact HII region (HCHII, see also Keto 2007), to ultra-compact HII regions (UCHII), compact HII regions and finally standard HII regions (see Fig. 1.6). These sources are strong emitters of free-free radiation (also called *Bremsstrahlung*), *i.e.* when free electrons are scattered by protons without being captured. They mainly radiate at centimeter wavelengths for their typical thermal spectrum in HII regions ($T_e \sim 10^4$ K), as they are being deflected (Wynn-Williams & Becklin, 1974). In addition, the changes in density (traced in, *e.g.*, CO then ^{13}CS or N_2H_+ for denser gas), temperature, molecular abundances and masers (*e.g*, methanol and OH) in the massive protostar vicinity provide an evolutionary path as well. This gives a temporal axis to understand massive star formation and a more precise view of particular epochs, often linked to particular spatial scales, is required, together with large statistics.

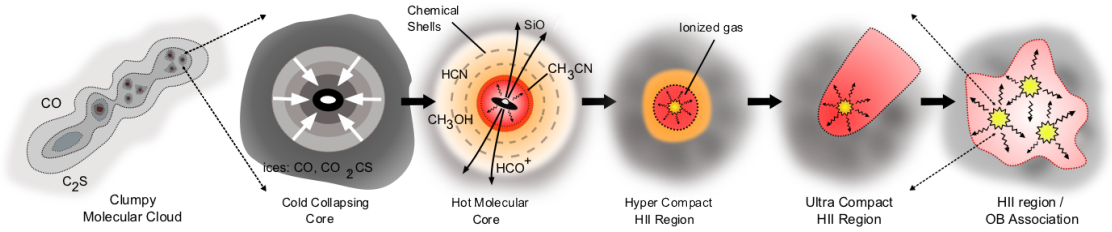

Figure 1.6: Schematic view of a massive star evolutionary sequence and its chemical tracers, mainly based of the development of its HII region. Credits: Cormac Purcell.

Since the host cloud should be a strong absorber due to its high density, *Spitzer* has been looking for such compact absorbing sources, called Infrared Dark Clouds (IRDC). Peretto & Fuller (2010) have studied a large sample of ∼11000 IRDCs with *Spitzer*, whose majority appears to be gravitationally bound and in filamentary structures that may be oriented towards hubs, in agreement with Myers (2009) and with global collapse scenarios (see Sect. 1.5). They have sizes of ≃0.5 pc and mass ≃150 $M_\odot$ and should contain massive pre-stellar cores or protostars. The core-scale observations are precious to derive initial conditions for massive star formation and distinguish between the theoretical models, as mentioned above.

Fourty-two massive ($> 40\,M_\odot$) dense cores have been mapped with the IRAM 30m telescope in Cygnus X, one of the closest and most active star-forming complexes (Motte et al., 2007). High-luminosity protostars, on the one hand, and outflows around infrared-quiet objects, on the other hand, have been detected in this sample. They cannot be accounted for as massive pre-stellar cores, which are characteristics of the turbulent core accretion model, because of this protostellar activity. In fact, the five most massive cores have been confirmed to host protostars surrounded by an envelope that can be as massive as 60 $M_\odot$ (Bontemps et al., 2010). The lifetime associated with these objects is of the order of a few free-fall times, $\sim 10^5$ yr

(Wyrowski et al., 2016). The velocity dispersion is $\sim 1 - 2\,\mathrm{km\,s^{-1}}$ (*e.g.*, Bontemps et al. 2010) and is consistent with a high level of turbulence, but not high enough to prevent the collapse. It does not permit to distinguish between a global collapse model, where the velocity dispersion decreases when the spatial scale or the surface density decrease (Ballesteros-Paredes et al., 2011) and a core stabilized against collapse by magnetic fields in addition to turbulence (McKee & Tan, 2003).

In spite of this, the quest for high-mass prestellar cores has led to a few candidates. CygXN53-MM2, in Cygnus X (Bontemps et al., 2010) and G11P6-SMA1 in IRDC G11.11-0.12 (Wang et al., 2014) are among the few massive pre-stellar core candidates traced by submillimeter dust continuum with the IRAM and SMA, respectively (see also Nony et al. 2018, with ALMA). The total number of candidates is much lower than expected by a classical IMF, which weakens the turbulent core accretion scenario as the main path to form massive stars. As these objects should be in quasi-static equilibrium, they should form and live on longer time scales than the protostars, which are evolving on free-fall time scales. This would imply a higher number of massive pre-stellar cores detections than massive protostars, which is in contradiction with observations. A complementary way to discriminate between models comes from the study of the accretion - and ejection - processes.

Accretion onto massive protostars is believed to occur in a similar manner as for their low-mass analogs, but with a much higher accretion rate. It can be inferred either from the infall, at the clump scale, or indirectly from the outflow rate. In the latter case, it relies on the proportionality between the mass loss rate of the jet and the accretion rate, on the one hand, and between the outflow velocity (on which there is no general agreement, see Beuther et al. 2002 and Nony et al. 2020) and infall velocity, on the other hand. Beuther et al. (2002) have derived the accretion rate from 26 sources with IRAM and obtained $\sim 10^{-4}$ $\mathrm{M_\odot\,yr^{-1}}$, in agreement with several high-mass star formation models. They inferred a protostar mass of $\sim 10\,\mathrm{M_\odot}$ for 19217+1651 from the outflow momentum rate, assuming its magnetic origin (Tan & McKee, 2002). Let us note though that, in addition of the several assumptions mentioned above, the measurements carry also their own uncertainties related to their angular resolution and sensitivity. Hence, one should be careful when interpreting these values. At larger scales, the typical infall rates measured are between $\sim 10^{-4}$ $\mathrm{M_\odot\,yr^{-1}}$ and $\sim 10^{-2}$ $\mathrm{M_\odot\,yr^{-1}}$ (Fuller et al. 2005, Qiu et al. 2011, Wyrowski et al. 2016, Motte et al. 2018). To sum up, accretion rates evaluated at the protostar's vicinity are not available yet, and values inferred from infall/outflow measurements should only be seen as first order-of-magnitude estimates.

There is also a clear correlation between the source radio luminosity up to $10^5\,\mathrm{L_\odot}$, the core mass and the outflow momentum rate (Anglada et al. 1992, Cabrit & Bertout 1992, Beuther et al. 2002, see the review by Anglada et al. 2018). As shown in the left panel of Fig. 1.7, this correlation continues to high luminosities, *i.e.* high-mass protostars. Collimated jets, a common feature of low-mass star formation (right panel of Fig. 1.7) are also observed around massive young-stellar objects. As there is no clear correlation between the lines luminosity in the observed winds and the stellar photospheric luminosity (Cabrit et al., 1990), the outflow mechanism likely originates from the disk and not from the star itself. It also shows that the accretion process may be the same over a broad range of stellar masses, *i.e.* disk accretion. As I will discuss later (see Sect. 1.9.4), outflows seem to have an onion-shell structure (Cabrit & Bertout, 1990), with large velocities close to the outflow axis and a decreasing velocity as gas is located further away from the axis. The cavity walls formed by the outflows have been revealed, *e.g.* with SMA in the GGD27 complex which hosts a $\sim 4\,\mathrm{M_\odot}$ protostar powering a thermal radio jet (Fernández-López et al. 2011a, Girart et al. 2017). Evidence of precession is associated to this source's molecular outflows (Fernández-López et al., 2013), similarly to those around low-mass protostars (*e.g.*, de Valon et al. 2020). Finally, the outflow main axis direction

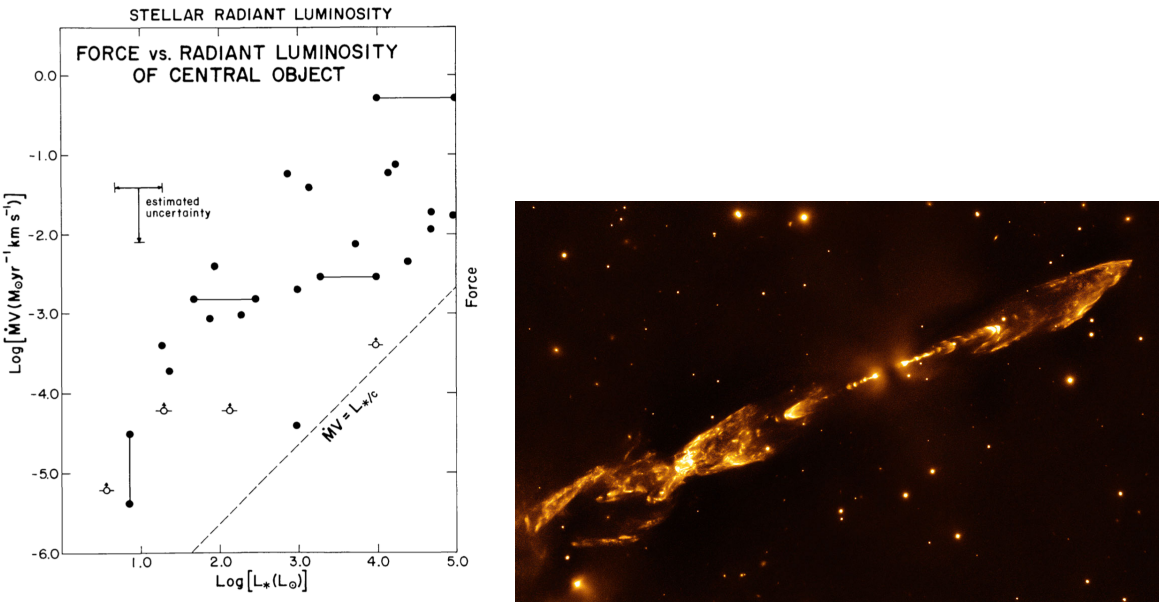

Figure 1.7: Left panel: observational values of momentum transfer rate (force) needed to accelerate the outflow against the total stellar luminosity of the central object, for a large range of stellar luminosities corresponding to low- and high-mass protostars. Credits: Lada (1985). Right panel: infrared observation of a jet ($\sim$0.6 pc in total) around the low-mass young-stellar object HH212, obtained with the Infrared Spectrometer And Array Camera (ISAAC). Credits: ESO, Mc Caughrean.

does not seem correlated to the magnetic field orientation (Zhang et al., 2016), so that the disk orientation may not be governed by magnetic braking but by other dynamical interactions, as in multiple systems. Because magnetic braking would reduce the disk size, constraints on disk geometry can help us identifying the exact role of magnetic fields in massive star formation.

Only recent measurements put (sparse but) strong constraints on the accretion disks, thanks to unprecedented angular resolution. HH 80-81 hosts a thin Keplerian disk, with a radius $\lesssim$150 AU in dust emission but $\sim$1000 AU in SO_2, temperature of $120-160$ K and a density $\gtrsim 7\times10^{-15}$ g cm^{-3} ($n\gtrsim 2\times10^{9}$ cm^{-3}, Fernández-López et al. 2011b, Girart et al. 2017).The enclosed mass within the disk radius, which accounts both for the star and the disk, is $4-18\,M_\odot$. Before this, a rare observation came from a disk of mass $1-8\,M_\odot$ and radius 330 AU in the Cepheus-A region (Patel et al., 2005). In this quest for contraints on disk geometrical and physical properties, high-angular resolution of ALMA is precious, providing continuum emission, gas tracers and polarization altogether. More recent observations of HH 80-81 reveal that the disk is perpendicular to the radio jet, has a radius $\sim$300 AU and is optically-thick below $\lesssim$170 AU (Girart et al., 2018), completing the previous measurements. An even more compact disk of radius 20 AU has been observed around a $\sim20\,M_\odot$ massive star at the end of its main accretion phase (Kraus et al., 2010). Meanwhile the disk in HH 80-81 could be prone to fragmentation (Fernández-López et al., 2011b), the massive hot core region G351.77-0.54 observed with ALMA at more than 40 AU resolution reveals twelve sub-structures within a few thousand AU with a broad range of core separations (Beuther et al., 2019), consistent with thermal Jeans fragmentation of a dense core, and possibly with the Global Hierarchical Model (Vázquez-Semadeni et al., 2016). At those scales, the temperature reaches values above 1000 K. There is no general trend about the disk stability, whose fragmentation may lead to a multiple stellar system, but the advent of ALMA will increase the statistics. In the high-mass star-forming region IRAS 23033+5951, four mm-sources are identified with the Northern Extended Millimeter

Array (NOEMA) and the IRAM telescope. Two fragments exhibit outflows and Keplerian rotation, similar to those around low-mass stars. Out of these two rotating structures, one is stable and the other is prone to fragmentation in the inner 2000 AU (Bosco et al., 2019). Disk fragmentation may either lead to the formation of companion stars or to the accretion of clumps onto the central object. In the latter case, a radiative shock can form at its surface and the energy being radiated away. The process behind this *accretion luminosity* is not fully understood, in particular the conditions under which the radiation would escape rather than being advected together with the gas. It seems, however, a recurrent mechanism in low-mass star formation, and relies on disk-mediated accretion. Hence, it advocates the same accretion method for the formation of high-mass stars as well (Caratti o Garatti et al., 2017). Altogether, despite the lack of systematical constraints, the presence of disks around young massive protostars ($L < 10^5 L_\odot$) is now well-established (see the reviews by Beltrán & de Wit 2016, Beltrán 2020). Their properties may set the initial conditions for the formation of multiple stellar systems, and they strongly depend on threading magnetic fields.

Magnetic fields could play a crucial role in preventing early-fragmentation, as it has been shown in numerical simulations (Peters et al. 2011 on core scales, Commerçon et al. 2011a on sub-100 AU scales and Myers et al. 2013 after the protostar's birth). Constraints on magnetic fields structures and strength are recent, due to new polarimetric instruments. In a sample of 21 high-mass star-forming clumps, sub-parsec magnetic fields appear to be structured (Zhang et al., 2014). The hour-glass shape due to field lines being pulled by the collapsing gas is present (Beltrán et al., 2019), as in low-mass protostellar systems (*e.g.* Maury et al. 2018). The parameter $\mu = \frac{M/\phi}{(M/\phi)_{\rm crit}}$ is the mass-to-flux to critical mass-to-flux ratio, where ϕ is the magnetic flux. It indicates whether magnetic fields can ($\mu < 1$) or cannot ($\mu > 1$) prevent collapse on their own. Several studies agree on supercritical values of $\mu = 1 - 4$ (Falgarone et al., 2008) or even $\mu \sim 1 - 2$ (Girart et al. 2009, Li et al. 2015, Pillai et al. 2015), suggesting an important role of magnetic fields. Quantitatively, the field strength has the order of $0.1 - 1$ mG in a sample of IRDCs (Pillai et al., 2016), and in a UCHII region (Tang et al., 2009), based on the Chandrasekhar-Fermi method[1] (Chandrasekhar & Fermi, 1953). Comparisons with magneto-hydrodynamical simulations have shown that fragmentation is consistent with turbulence dominating over the magnetic energy (Palau et al. 2013, Fontani et al. 2016). Nonetheless, magnetic energy has been found to be comparable to (Falgarone et al. 2008, Girart et al. 2013) or to dominate over the turbulent energy (sub-alfvénic turbulence, Pillai et al. 2015) in several sources. Girart et al. (2013) have found equipartition between angular momentum, magnetic energy and turbulent energy in a fast rotating core, with $\mu = 6$, indicating three mechanisms capable of slowing down the collapse. While we have emphasized the development of HII regions above, the question of the interaction between an expanding HII region and the magnetic field geometry is not settled. The UCHII region G5.89-0.39 around the $\sim 3 \times 10^5$ L$_\odot$ protostar (Emerson et al., 1973) has shown that the HII region expansion could disturb the molecular outflow and the magnetic field structure (Tang et al., 2009). In the case of G45.47+0.05, ALMA and VLA observations report on a photoionized outflow surrounding a jet, around a $\sim 30 - 50$ M$_\odot$ protostar with on-going accretion (Zhang et al., 2019).

These observations reveal high accretion rates around massive protostars, challenge the turbulent core accretion model by the lack of massive pre-stellar core and seem to favor the global hierarchical model. Disks and outflows are ubiquitous but constraints on disk properties remain sparse, while outflows properties appear in the continuity of low-mass protostars outflows, which points towards a common mechanism. Finally, they agree on the apparent importance of magnetic fields and turbulence, and their necessity in numerical simulations.

[1]The Chandrasekhar-Fermi method relates the plane-of-the-sky field strength with the line-of-sight velocity dispersion, using the phase velocity of transverse Alfvén waves.

1.7 Recent numerical advances

The previous calculation (Sect. 1.4) of the radiation pressure barrier shows that, first, (frequency-dependent) radiation is likely to play a major role and should be coupled to the hydrodynamics (Yorke & Sonnhalter 2002, Kuiper et al. 2010b), as it strongly influences the gas dynamics. Furthermore, it shows the weakness of the unidimensional view and the need for multi-dimensional calculations that can hardly be done otherwise than with numerical simulations. The implementation of new - or refined - physics, in particular regarding the radiation transport, has worked hand in hand with advances in this field.

In the particular case of radiation transport, it is generally too expensive to follow every photons or packets of photons (Monte-Carlo codes), even from a single source, and treat their absorption/emission/scattering events, on each time step of a simulation and coupled to the hydrodynamics. A popular approach consists in the moment methods, which describe radiation as a fluid with solid-angle integrated quantities, called moments, such as a radiative energy, flux and pressure (see Chapter 2). The 0th-order method is the Flux-Limited Diffusion (FLD) method, which evolves the radiative energy with a diffusion approximation (Levermore & Pomraning, 1981). It is particularly suited for optically-thick media and therefore adapted to dust continuum emission throughout a simulation domain. The FLD method cannot conserve the photons direction though, because it diffuses them locally based on the gradient of the radiative energy. Furthermore, every radiative transfer method can be either frequency-averaged (often called "gray") or frequency-dependent, in which case photons groups are put into frequency bins. In the gray approach, used throughout this thesis, the opacities which couple radiation to the gas-and-dust mixture are mean opacities, weighted by the blackbody function (Planck's law), hence by the gas temperature. The (gray or frequency-dependent) FLD method considers photons as being emitted locally, even if they were actually emitted by the star.As a consequence, photons emitted by the star (in UV-like bands) are actually treated as if they were emitted by the surroundings (IR-like frequencies for a protostellar disk), as the mean opacity is taken at the local blackbody temperature. Meanwhile, it has been shown that the frequency-dependence of radiation and its anisotropy play a major role (Yorke & Sonnhalter, 2002). This explains why most numerical developments in the past ten years have been focused on the optically-thin part of the problem: the treatment of the stellar radiation. Various approaches have been undertaken: ray-tracing (Kuiper et al., 2010c, Kim et al. 2017), long-characteristics (Rosen et al., 2017), Monte-Carlo radiative transfer (Haworth & Harries 2012, Harries et al., 2017, thanks to highly-parallel computing), and the M1 method (Levermore 1984, González et al. 2007, Aubert & Teyssier 2008, Rosdahl et al. 2013, Kannan et al. 2019, Fuksman et al. 2020, a part of this thesis project) which is the 1st-order method and evolves the radiative flux as well as the energy.

Most of these developments have been made in the perspective of massive star formation. The radiation pressure barrier has been broken with multidimensional simulations under the simple FLD approximation to reach stellar masses above $40\,M_\odot$ (Yorke & Sonnhalter 2002 with frequency-dependent radiation, Krumholz et al. 2009 with grey radiation). Hybrid methods, separating the stellar radiation from the diffuse emission from dust, were necessary to compute accurately the direct radiative force, which is underestimated in the frame of FLD by a factor $\sim 10 - 100$ (Kuiper et al. 2010c, Owen et al. 2014). At first sight, they have not brought a significant difference regarding the final stellar mass (Klassen et al. 2016, Rosen et al. 2016, Kuiper et al. 2010a). The highest mass obtained was $137.2\,M_\odot$ from a $480\,M_\odot$ core at the end of the accretion phase (Kuiper et al., 2010a) . On the opposite, hybrid approaches are important to capture the launching of radiative outflows and the subsequent radiative cavities (left panel of Fig. 1.8). These have been found to be unstable to radiative Rayleigh-Taylor instabilities by Krumholz et al. (2009) and Rosen et al. (2016) (with the ORION code), which appeared as a new

mode for accreting material onto the star-disk system. Meanwhile, the simulations from Kuiper et al. (2010a) and Klassen et al. (2016), with the PLUTO code, have shown stable cavities. It has been argued by Kuiper et al. (2012) that the treatment of radiation in the FLD model could yield unstable cavities. Even though the FLD was used in Krumholz et al. (2009), Rosen et al. (2016) obtained a similar result with a hybrid approach. In addition to the special treatment of stellar radiation in the latter work, both have used adaptive-mesh refinement (AMR) strategy to resolve the cavities edges, while the simulations of Kuiper et al. (2012) were undertaken with a spherical grid and a radial logarithmic scale implying a lower resolution at the border of the cavities. This lack of resolution would be the explanation for not capturing the instabilty, as the shortest modes have been claimed to be the most unstable by Jacquet & Krumholz (2011). While the accretion via RT instabilities is not clear yet, disk-mediated accretion occurs in most simulations (*e.g.* Klassen et al. 2016), appears sufficient to form massive stars, and is consistent with observational constraints (Sect. 1.6).

Magnetic fields have been neglected in the previous works, but star-forming regions are known to possess a (possibly strong) magnetic field (*e.g.* Girart et al. 2009). Several studies have accounted for magneto-hydrodynamics (MHD) equations for a perfectly conducting fluid (ideal MHD). Magnetic field offers an extra-support to the gas against gravity (see Sect. 1.9.3), and can prevent the early-fragmentation of massive dense cores (*e.g.*, Commerçon et al. 2011a). In that view, highly-magnetized massive pre-stellar cores would lead to single or binary high-mass stars while less magnetized massive pre-stellar cores would form higher-multiplicity systems of low-mass objects. The ideal MHD simulations by Banerjee & Pudritz (2007) have shown that magnetic braking (transfer of angular momentum outwards by the magnetic field lines) slows down the disk rotation and enhances the accretion rate, although this picture may change when including non-ideal MHD effects. At later times, it may launch a magnetic pressure-driven outflow which would allow the radiation to escape instead of halting accretion, as in the *flashlight effect* (Banerjee & Pudritz 2007, Peters et al. 2011, and Kuiper et al. 2015 with a subgrid model for the outflow). Another mechanism for magnetic acceleration is the magnetocentrifugal process. Gas is accelerated on the field lines that are twisted by the disk rotation and hence transports angular momentum outwards (derived in Sect. 1.9.4). MHD outflows have been reported before in low-mass star formation calculations, as the implementation of MHD modules was a priority compared to advanced radiative transfer methods (*e.g.*, Machida et al. 2008). The disk-scale gas is accelerated into an outflow at a few tens of km/s while the gas close to the star is ejected at high-velocities $\gtrsim$100 km s^{-1} into a well-collimated jet (right panel of Fig. 1.8 shows a schematic view and right panel of Fig.1.7 the high-velocity jet observed around HH212), which could be partially (35%) de-collimated by line-driven radiative forces (Vaidya et al., 2011). The inclusion of magnetic fields within the ideal MHD frame - mainly in low-mass star formation -, has led to the so-called *magnetic catastrophe*, affecting the disk: disks formed in pure hydrodynamical cases have a radius of a few hundred AU (*e.g.*, Commerçon et al. 2008); in the ideal MHD frame, a pseudo-disk of similar extent forms but is dominated by the magnetic pressure, not by thermal pressure (*e.g.* Hennebelle & Ciardi 2009), and rotation is slowed down by magnetic braking. This comes from the magnetic flux being concentrated as the gas collapses (flux-freezing condition). Hence, rotationally-supported disk formation, as found in hydrodynamical calculations and observations, is suppressed in ideal MHD simulations. Misalignment between the magnetic field and the rotation axis may contribute to resolve this issue by weakening the magnetic braking, but there is no consensus despite various studies (*e.g.*, Hennebelle & Ciardi 2009, Li et al. 2013). In massive core collapse calculations, it has been shown by Seifried et al. (2012a) that turbulent motions remove the large-scale coherent rotation motions and lead to the formation of a Keplerian disk, in agreement with similar attempts in the low-mass regime (*e.g.*, Joos et al. 2013). Another possibility may come from non-ideal MHD effects, which offer a mechanism to redistribute the magnetic

flux. Ambipolar diffusion (decoupling between neutrals and ions), together with initial turbulence, promote the formation of thermal disks (Masson et al. 2016, Hennebelle et al. 2016, Lam et al. 2019). To date, there is no dedicaded simulation of massive star formation with both non-ideal MHD and hybrid radiative transfer. Hence, the nature of outflow around massive protostars has not been revealed yet.

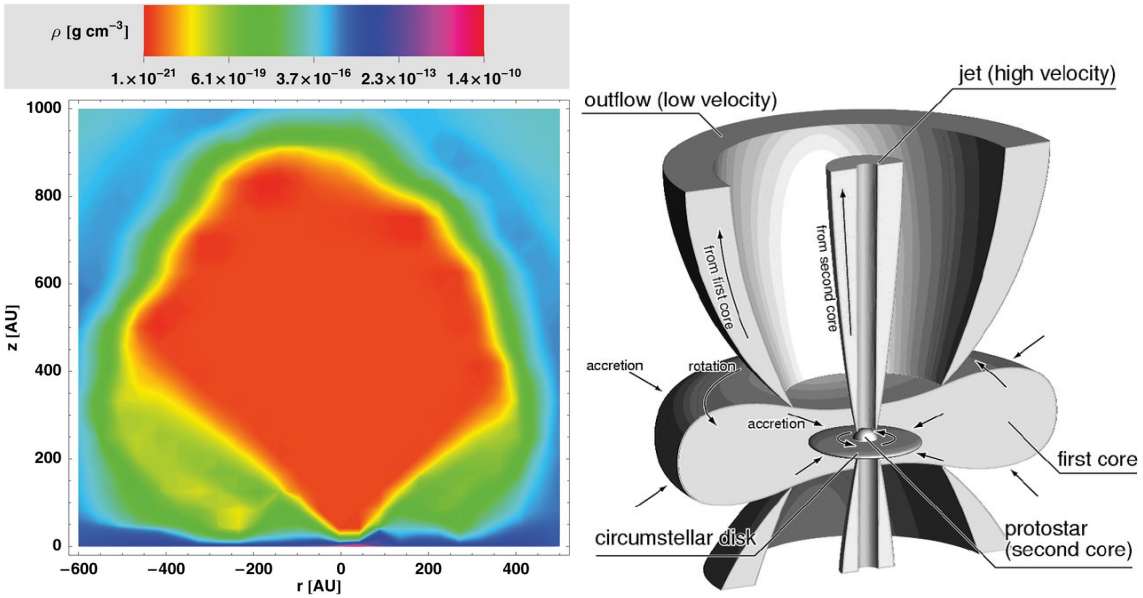

Figure 1.8: Left: radiative cavity formed in the 3D radiation-hydrodynamical simulation of the collapse of a 120 $M_\odot$ pre-stellar core (Kuiper et al., 2011). Right panel: schematic view of the magnetic outflow stucture in the low-mass star formation MHD calculation of Machida et al. (2008).

As mentioned above, radiation from a massive star ($\gtrsim 20\,M_\odot$) ionizes the gas and increases significantly its temperature, leading to an expanding bubble of ionized gas. Keto (2007) have proposed that, as the ionization increases, this starts to dominate the dynamics of the accretion. This analytical work compares well with the observations of W51e2 (Keto & Klaassen, 2008). It has been confirmed in radiation-ideal MHD simulations (with ionizing radiation but without radiative forces) from Peters et al. (2011) and radiation-hydrodynamics simulations (without magnetic fields) from Kuiper & Hosokawa (2018). Both works agree on the HII region halting accretion by suppressing the accretion disk (with the help of radiation force in the latter work). More than that, Peters et al. (2011) show it disrupts the magnetic field topology and therefore the magnetic outflow. Photoionization appears as a major contributor to the dynamics around massive protostars above a certain mass of $\gtrsim 20\,M_\odot$.

We can summarize these numerical results as follows. Radiative transfer, and more specifically, stellar irradiation, is fundamental in the formation of massive stars to accurately compute their radiative force. Multidimensional calculations are necessary to overcome the radiative pressure barrier. Accretion can continue via a disk or via Rayleigh-Taylor instabilities in the polar radiative bubbles, although the latter remains a topic of debate. When including magnetic fields and non-ideal MHD effect or turbulence, disks form and are smaller than in the (radiation-)hydrodynamical case. Magnetic fields and radiation can both contribute to stabilizing the disk (thus affecting the stellar multiplicity question and the accretion episodicity) and the lauching of outflows. The underlying mechanism for magnetic outflows is not consensual and has not been challenged yet by the treatment of the radiative force. In the mean time, ionization may disrupt the magnetic field topology (hence deactivating magnetic outflows) and

photo-evaporate the accretion disk later-on. This would set the end of the accretion phase by the massive protostar. Most of the results above have been obtained separately, neglecting or underestimating one of the other processes: radiative force, magnetic field, turbulence, ionization.

1.8 This work

As presented above, massive star formation requires multi-dimensional, multi-physics numerical simulations where radiative transfer, magnetic fields and turbulence are at play. The work I have been completing during my thesis is presented in this manuscript and focuses on the main accretion phase of massive protostars. This process is highly non-linear, with radiative feedback from the star, magnetic fields and environmental turbulence. Most recent implementations have focused on the treatment of stellar irradiation, to go beyond the diffusion approximation usually implemented for radiation-hydrodynamics. My main task has been the numerical developments and testing of such a method in the RAMSES code by coupling two radiative transfer modules. I have been studying the collapse of massive pre-stellar cores for comparison with the previous diffusion approximation and with the literature, and tackled the problem of radiative Rayleigh-Taylor instabilities as an accretion mechanism. In parallel, I have undertaken a comparison study about the disk fragmentation in numerical simulations with the spherical-grid PLUTO code, in collaboration with the Massive Star Formation group of the University of Tübingen. Finally, running the first-ever simulations including a special treatment for irradiation and non-ideal magneto-hydrodynamics, I have questioned the mechanism at the origin of outflows around massive protostars. This study also accounts for initial turbulence, as it can disturb the magnetic field topology, the disk fragmentation and therefore the accretion by the central object.

This work is organized as follows:

- In Chapter 2, I introduce the basics of radiative transfer. I present the useful radiative quantities and angular moments of the intensity, which are used to describe the radiation field as a fluid. After deriving the 0-th (Flux-Limited Diffusion) and 1st-order (M1) moments methods, I present a possible way to treat the stellar radiation with the M1 and the re-emitted radiation with the Flux-Limited Diffusion, in a so-called *hybrid* method. Finally, I introduce the equations of radiation-hydrodynamics.

- In Chapter 3, I describe the main characteristics of the adaptive-mesh refinement code RAMSES. The implementations of the Flux-Limited Diffusion and the M1 methods are presented. Then, I describe the hybrid implementation, which is at the very heart of this thesis. Finally, its accuracy is demonstrated in pure radiative transfer tests of a disk irradiated by a central source.

- Chapter 4 presents the first application of the hybrid radiative transfer method in a radiation-hydrodynamical context: the collapse of a massive pre-stellar core. I focus on the comparison between the hybrid method and the Flux-Limited Diffusion method, as it was used so far in star-formation calculations, and similar numerical experiments. Taking advantage of this new method, I investigate the presence of radiative Rayleigh-Taylor instabilities. Eventually, I portray a comparison study between the RAMSES and PLUTO codes at modeling the fragmentation in accretion disks.

- In Chapter 5, I present the first simulations of massive star formation with a hybrid radiative transfer method and non-ideal MHD for the formation of realistic disks, including an

initial turbulent velocity field. I investigate the mechanism at the origin of the outflows around massive protostars (in numerical simulations, compared with observations), the disk properties and system multiplicity, as a function of the turbulence level.

1.9 Essentials

In this section I derive a few (magneto-)hydrodynamical concepts useful to deeply understand several aspects of this thesis context. I first review the fundamentals (by increasing order of complexity) of clouds and cores stability to understand the origin of the first and second collapses, emphasizing on the physical quantities to which this equilibrium is particularly sensitive. At the end, the reader will find a presentation of the underlying mechanism of radiative and magnetic outflows.

1.9.1 Stability of a cloud: order of magnitude consideration

Let us assume a homogenous, self-gravitating cloud of mass M_c, radius R, volume V, temperature T and pressure p (left panel of Fig. 1.9). Here, we neglect external pressure forces and consider an ideal equation of state. The cloud collapses if the gravitational force exceeds the pressure force which tends to inflate it: $F_g > F_p$ (volume-averaged here). One can write the volumic pressure force and gravitational force as

$$\begin{aligned} F_p &\equiv \nabla p \sim \frac{p}{r}, \\ F_g &\equiv \rho \nabla \phi \sim G\rho^2 r, \end{aligned} \tag{1.2}$$

since $\Delta\phi = 4\pi G\rho$, where ϕ is the gravitational potential.

The force balance is then written as

$$\frac{F_p}{F_g} \sim \frac{p}{G\rho^2 r^2}. \tag{1.3}$$

The largest radius that ensures the cloud stability is then

$$r_c \sim \sqrt{\frac{p}{G\rho^2}} = \frac{c_s}{\sqrt{G\rho}}, \tag{1.4}$$

where c_s is the isothermal sound speed given by $c_s^2 = \frac{p}{\rho} = \frac{k_B T}{\mu m_H}$, where k_B is Boltzmann's constant, μ is the mean molecular weight and m_H is the hydrogen mass. This order-of-magnitude consideration shows that collapse occurs preferentially in cold, dense clouds, which are opaque to optical radiation, as shown in the right panel of Fig 1.9.

Any structure larger than the spatial scale r_c is unstable to gravitational collapse. It can be seen as a competition between two timescales: the sound-speed crossing time and the free-fall time, respectively

$$\begin{aligned} \tau_{sound} &= \frac{r_c}{c_s} \\ \tau_{ff} &\simeq \frac{1}{\sqrt{G\rho}}. \end{aligned} \tag{1.5}$$

If the free-fall time is shorter than the sound speed crossing time, the cloud does not have the time to adapt to density perturbations.

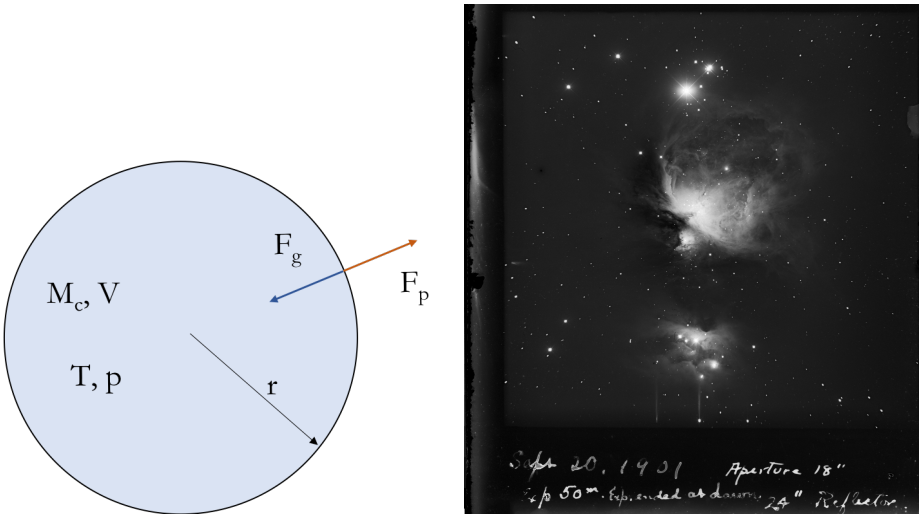

Figure 1.9: Left: spherical cloud scheme. Right: 1901 photograph of the Orion nebula (after light-to-dark inversion), the nearest active massive star-forming region (d∼0.45 kpc. Credit: George Ritchey, Yerkes Observatory - Digitization Project: W. Cerny, R. Kron, Y. Liang, J. Lin, M. Martinez, E. Medina, B. Moss, B. Ogonor, M. Ransom, J. Sanchez (Univ. of Chicago).

1.9.2 Pertubative analysis

We can perform a perturbative analysis of a self-gravitating fluid to study its stability with respect to gravitational collapse. Let us consider a parcel of gas with uniform temperature T and density ρ_0 at rest ($v = 0$). We perturb the system in the x-direction. The perturbed states, at first order, are written as $\rho = \rho_0 + \rho_1$, $p = p_0 + p_1$, etc. The conservation of mass, momentum and Poisson equations are therefore given by (second-order terms are dropped)

$$\begin{aligned} \frac{\partial \rho_1}{\partial t} + \rho_0 \frac{\partial v_x}{\partial x} &= 0 \\ \frac{\partial v_x}{\partial t} + \frac{1}{\rho_0}\frac{\partial p_1}{\partial x} + \frac{\partial \phi_1}{\partial x} &= 0 \\ \frac{\partial^2 \phi_1}{\partial x^2} &= 4\pi G \rho_1, \end{aligned} \tag{1.6}$$

to which we add the isothermal equation of state $p_1 = c_s^2 \rho_1$ (a valid assumption for an optically-thin gas). Now, we will look for solutions of the form $\rho_1 = Ce^{i(kx-\omega t)}$, for each variable, where ω is the angular frequency and $k = 2\pi/\lambda$ is the wave number of the perturbation. When injected in the above equations we obtain the following system

$$\begin{aligned} -i\omega\rho_1 + \rho_0 i k v_x &= 0 \\ -i\omega v_x + \frac{1}{\rho_0} i k c_s^2 \rho_1 + ik\phi_1 &= 0 \\ k^2 \phi_1 &= 4\pi G \rho_1, \end{aligned} \tag{1.7}$$

which leads to the dispersion relation

$$\omega^2 = c_s^2 k^2 - 4\pi G \rho_0. \tag{1.8}$$

Perturbations with $\omega^2 > 0$ will lead to an oscillatory behaviour of the system. On the other hand, $\omega^2 < 0$ leads to an exponential growth of the perturbation, *i.e.* an instability. By setting

$\omega = 0$ we obtain the critical wavelength

$$\lambda_{\rm J} = \frac{\sqrt{\pi} c_{\rm s}}{\sqrt{{\rm G}\rho_0}}, \tag{1.9}$$

so-called the Jeans length (Jeans, 1902). We recover, to a factor close to unity, the previous result: a cloud larger than its Jeans length is unstable to density perturbations.

Following this, we can easily show why the second collapse occurs because of the H_2 dissociation (left panel of Fig. 1.2). Let us take a polytropic gas so that $P \propto \rho^\gamma$, where γ is the polytropic coefficient. The Jeans mass, defined as $M_{\rm J} = \frac{4}{3}\pi\lambda_{\rm J}^3\rho$, depends on γ as

$$M_{\rm J} \propto \rho^{(3\gamma-4)/2}. \tag{1.10}$$

Therefore, for a polytropic gas whose index is below the critical value $\gamma_{\rm crit} = 4/3$, the Jeans mass decreases as the density increases, which is an unstable behavior. This occurs with the H_2 dissociation and leads to the second collapse phase.

1.9.3 Virial theorem applied to a collapsing cloud

The Virial theorem is based on macroscopic quantities, averaged over the whole system, and describes the cloud's equilibrium. We will use it to include more physics than just gravity and pressure. In the following we will distinguish between the microscopic (thermal) and macroscopic contributions to the kinetic energy and consider a magnetized cloud at equilibrium. In this case, the Virial theorem reads (see Appendix A)

$$\frac{1}{2}\ddot{I} = 3(\gamma-1)U + M + 2\Gamma + \Omega_{\rm g} + \oiint_S (\mathbf{r}\cdot\mathbf{B})\,\mathbf{B}{\rm d}\mathbf{S} - \oiint_S P_{\rm tot}\mathbf{r}\,{\rm d}\mathbf{S}, \tag{1.11}$$

where I is the momentum of inertia of the system, U is the internal energy (and accounts for microscopic motions), M is the magnetic energy, Γ is the (macroscopic) kinetic energy, $\Omega_{\rm g}$ is the gravitational energy, $\mathbf{B}$ is the magnetic field, and $P_{\rm tot}$ is the total pressure. The internal energy is given by

$$U = \frac{1}{\gamma-1}\frac{M_{\rm c} k_{\rm B}\bar{T}}{\mu {\rm m_H}}, \tag{1.12}$$

where γ is the gas adiabatic index, $M_{\rm c}$ is the cloud's mass, $\bar{T}$ is its mass-averaged temperature, $k_{\rm B}$ is Boltzmann's constant, μ is the mean molecular weight and $\rm m_H$ is the atomic hydrogen mass. The magnetic energy M is

$$M = \iiint_V \frac{B^2}{2}{\rm d}\tau. \tag{1.13}$$

For a spherical cloud the gravitational energy is

$$\Omega_{\rm g} = -\alpha\frac{{\rm G}M_{\rm c}^2}{R}, \tag{1.14}$$

where R is the cloud's radius and α depends on the density distribution. We can take the order-of-magnitude of the sum of the magnetic energy, the fifth term on the right-hand side of 1.11 and the magnetic contribution to the total pressure as

$$M + \oiint_S (\mathbf{r}\cdot\mathbf{B})\,\mathbf{B}{\rm d}\mathbf{S} - \oiint_S \frac{B^2}{2}\mathbf{r}\,{\rm d}\mathbf{S} = \beta B^2 R^3, \tag{1.15}$$

where the magnetic field complexity is encapsulated in β. For a uniform density distribution and magnetic field, $\alpha = 3/5$ and $\beta = 4\pi/3$. Orders-of-magnitude quantities such as $\bar{T}$ and B^2 are introduced because the idea here is to qualitatively determine the factors that may affect the cloud stability. Finally, the pressure term is

$$\iint_S P\mathbf{r}\,\mathrm{d}\mathbf{S} = 4\pi R^3 P_{\mathrm{ext}}, \tag{1.16}$$

considering that the external pressure is uniform.

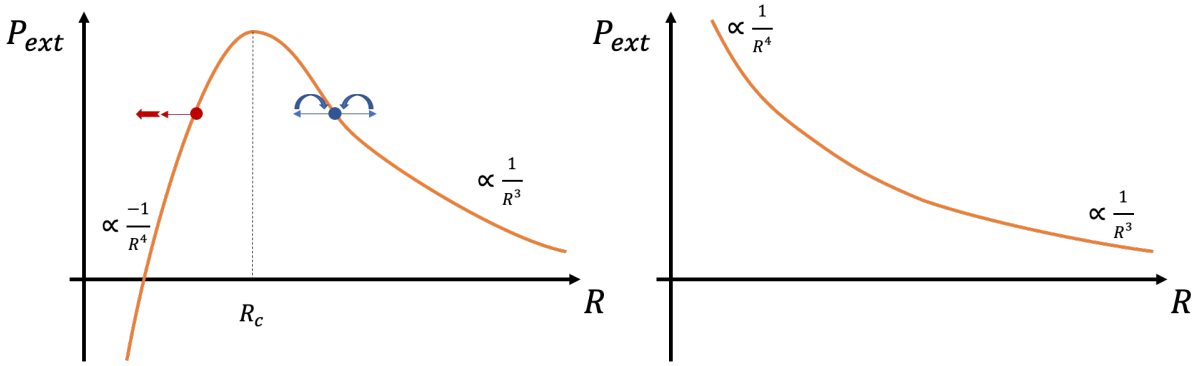

Figure 1.10: Radial profile of the external pressure at equilibrium. Left panel: absence of magnetic field. Right panel: strong magnetic field.

Let us first consider the stationary, hydrodynamical case ($B = 0$) with no kinetic energy. The common expression of the Virial theorem is recovered as

$$2\Gamma + \Omega_{\mathrm{g}} = 0. \tag{1.17}$$

The term *virial* stands for the second term in 1.17 and comes from the latin *vis* (energy, force). This theorem allows one to determine the global behaviour of the gas (its velocity and/or density) as a function of its averaged gravitational properties.

At equilibrium, from Eq. 1.11 the external pressure is given by

$$P_{\mathrm{ext}} = \frac{3M_{\mathrm{c}}k_{\mathrm{B}}\bar{T}}{4\pi\mu\mathrm{m_H}R^3} - \frac{\alpha \mathrm{G}M_{\mathrm{c}}^2}{4\pi R^4}. \tag{1.18}$$

Figure 1.10 shows the radial profile of the external pressure for the cloud to be at equilibrium with the outer medium. For high enough external pressure no equilibrium is possible. For low enough external pressure there are two types of equilibrium. If $R > R_{\mathrm{c}}$ it is stable: if the radius is decreased by compression, the external pressure is now smaller than the pressure required to satisfy the equilibrium: the radius thus increases. However, it is unstable for $R < R_{\mathrm{c}}$. If the radius is decreased, the external pressure overcomes the equilibrium pressure and the cloud collapses. The radius R_{c} is determined by $\frac{\partial P_{\mathrm{ext}}}{\partial R} = 0$ and for a uniform density distribution it is equal to

$$R_{\mathrm{c}} = \frac{4\mathrm{G}M_{\mathrm{c}}\mu\mathrm{m_H}}{15k_{\mathrm{B}}\bar{T}}, \tag{1.19}$$

Using the isothermal sound speed $c_{\mathrm{s}}^2 = \frac{k_{\mathrm{B}}\bar{T}}{\mu\mathrm{m_H}}$ we obtain the corresponding Jeans length which sets the smallest radius of stability of this cloud :

$$\lambda_{\mathrm{J}} = \sqrt{\frac{45}{16\pi}}\frac{c_{\mathrm{s}}}{\sqrt{\mathrm{G}\rho}}, \tag{1.20}$$

hence we have, once again, recovered the previous result with a coefficient close to unity. Let us now relax the assumption on the absence of magnetic fields. From Kelvin's theorem, the magnetic flux $\iint_S \mathbf{B}\,\mathrm{d}\mathbf{S} = \phi_{\mathrm{mag}} \propto BR^2$ is conserved in ideal magnetohydrodynamics. Thus, the magnetic term can be simplified as

$$\beta B^2 R^3 = \beta' \frac{\phi^2}{R}, \tag{1.21}$$

where β' depends on the magnetic field distribution. The analog of 1.18 in hydro becomes

$$4\pi R^3 P_{\mathrm{ext}} = \frac{3 M_{\mathrm{c}} k_{\mathrm{B}} \bar{T}}{\mu \mathrm{m_H}} - \frac{\alpha' \mathrm{G} M_{\mathrm{c}}^2}{R}, \tag{1.22}$$

with

$$\alpha' = \left(1 - \frac{\beta'}{\alpha \mathrm{G}} \left(\frac{\phi}{M}\right)^2\right), \tag{1.23}$$

Two cases can be distinguished depending on the value of α', corresponding to weak and strong magnetic fields. If $\alpha' > 0$, the hydro case is recovered but the magnetic field has *diluted* gravity. For $\alpha' < 0$, the picture changes completely: $\frac{\partial P_{\mathrm{ext}}}{\partial R} > 0$ so the cloud is stable, no matter its radius. Therefore, the mass-to-flux ratio M/ϕ is often used as a reference quantity to qualify the magnetic field strength of a cloud. It is normalized by a critical mass-to-flux ratio below which the cloud is stabilized by magnetic fields (Mouschovias & Spitzer, 1976).

This study, although simplified with the introduction of averaged quantities and uniform profiles, is consistent with the previous perturbation analysis. Finally, it illustrates two effects:

- thermal motions (and, in a similar way, turbulent motions) contribute to stabilizing the cloud,
- magnetic fields provide an additional support against gravity.

Therefore, turbulence and magnetic fields allow the cloud to reach higher masses before collapsing, which may contribute to form higher mass stars than with early fragmentation. The turbulent core accretion model (McKee & Tan, 2003) calls for these stabilizing mechanisms.

1.9.4 Radiative or magnetic outflows?

The presence of molecular outflows around young-stellar objects is well established. In this section we interrogate three possible mechanisms for driving such events: momentum transfer from stellar photons, magneto-centrifugally ejection from an accretion disk and magnetic tower flows. We aim at understanding the physics behind each mechanism to assess their presence (or not) in our numerical simulations (Chapter 5), and to understand the observational motivation to invoke them.

Radiative outflows

As shown in Sect. 1.4, radiative pressure around a massive stellar object can halt the accretion flow, in spherically-symmetric calculations. In a multi-dimensional framework including disk-mediated accretion, it can drive radiative outflows in the polar directions (left panel of Fig. 1.8). Photons possess a momentum $p = h\nu/\mathrm{c}$ where h is the Planck constant, ν is the photon frequency and c is the speed of light. For one photon, momentum transfer is larger as the radiation energy increases, *i.e.* as the stellar surface temperature increases and therefore as the

stellar mass increases (Fig. 1.1). In a simple view, the number of photons increases with the luminosity L and the total momentum transfer with it. Hence, it could be expected that massive (enough) protostars drive radiative outflows. The momentum transfer rate from photons to gas is given by $\dot{p}_r = L/c$ if all the momentum were to be transferred, and can be compared to the observed gas momentum rate $\dot{p}_g = \dot{M}v$ (for a constant velocity v), where $\dot{M}$ is the outflow rate. Radiative outflows are indeed formed in numerical simulations (see left panel of Fig. 1.8) that do not account for magnetic fields. However, observations tend to show that this transfer of momentum is not sufficient, by one to two orders of magnitude, to explain the outflow momentum rate (see left panel of Fig. 1.7), although it may be present.

Magneto-centrifugal mechanism

The second mechanism relies on the presence of a structured magnetic field. It requires an minimum amount of calculations to extract its most interesting properties for our purpose. Under simple assumptions (steady-state, axisymmetry), we derive various invariant functions along magnetic field lines which underline the peculiar nature of magneto-centrifugal outflows and its ability to remove angular momentum from the disk (for more details, I refer the reader to Ogilvie 2016).

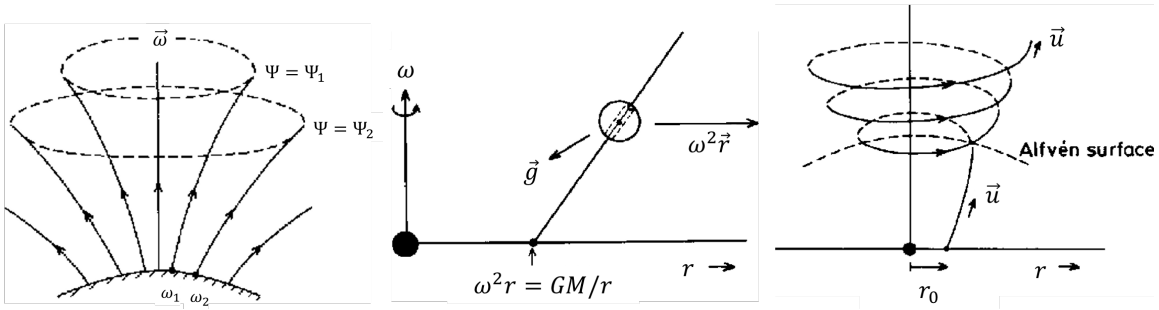

Figure 1.11: Left panel: magnetic surfaces and field lines labelled by Ψ. Middle panel: analogy between the magneto-centrifugal mechanism and a bead on a wire. Right panel: magnetic field topology below and beyond the Alfvén surface. Credits: Spruit (1996).

Let us consider a rotating, axisymmetric ($\partial_\phi = 0$) disk of cylindrical coordinates (r, ϕ, z) threaded by a magnetic field $\mathbf{B}$. The solenoidal condition (absence of monopole) reads

$$\frac{1}{r}\frac{\partial r B_r}{\partial r} + \frac{\partial B_z}{\partial z} = 0. \tag{1.24}$$

One can define the magnetic flux function $\Psi(r, z)$, so that

$$\mathbf{B}_r = -\frac{1}{r}\frac{\partial \Psi}{\partial z}, \ \mathbf{B}_z = \frac{1}{r}\frac{\partial \Psi}{\partial r}. \tag{1.25}$$

Indeed, the magnetic flux contained inside a circle of constant r and z is $\int_0^r 2\pi B_z(r', z) r' dr' = 2\pi\Psi(r, z)$, plus an arbitrary constant (chosen to be zero here). From Eq. 1.25, it follows that $\mathbf{B}.\nabla\Psi = 0$, which means that Ψ is constant along magnetic field lines. By cylindrical symmetry, it also indicates the surfaces of revolution of the magnetic field, known as *magnetic surfaces* (left panel of Fig. 1.11). A field line with one point located on this surface has the entire field line on it. We will derive other scalar fields whose gradient is parallel to that of Ψ, which means

that they only depend on Ψ and are invariant along field lines. $\mathbf{B}$ can be decomposed into its poloidal and toroidal components $\mathbf{B}_\mathrm{p} = \mathbf{B}_\mathrm{r} + \mathbf{B}_\mathrm{z}$ and $\mathbf{B}_\phi$, and written in the form

$$\mathbf{B} = \mathbf{B}_p + B_\phi \mathbf{e}_\phi = \left(-\frac{1}{r}\mathbf{e}_\phi \times \nabla\Psi \right) + B_\phi \mathbf{e}_\phi = \nabla\Psi \times \nabla\phi + B_\phi \mathbf{e}_\phi. \tag{1.26}$$

It is worth noting that $\nabla.\mathbf{B} = \nabla.\mathbf{B}_p = 0$ (axisymmetry). Similarly, we will decompose the gas velocity $\mathbf{u}$ as $\mathbf{u} = \mathbf{u}_\mathrm{p} + \mathbf{u}_\phi$. Under the assumption of a perfect-conducting fluid (ideal MHD) and looking for a steady-state solution for $\mathbf{B}$, the induction equation reads

$$\nabla \times (\mathbf{u} \times \mathbf{B}) = 0. \tag{1.27}$$

Hence, $\mathbf{u} \times \mathbf{B}$ can be defined as the gradient of a scalar field. The axisymmetry imposes this scalar not to vary with respect to ϕ, so the toroidal component $(\mathbf{u} \times \mathbf{B})_\phi = 0$. As $\mathbf{u} = \mathbf{u}_\mathrm{p} + \mathbf{u}_\phi$ and $\mathbf{B} = \mathbf{B}_\mathrm{p} + \mathbf{B}_\phi$, one obtains the toroidal component:

$$(\mathbf{u} \times \mathbf{B})_\phi = \mathbf{u}_\mathrm{p} \times \mathbf{B}_\mathrm{p} = 0. \tag{1.28}$$

Therefore, $\mathbf{u}_\mathrm{p}$ and $\mathbf{B}_\mathrm{p}$ must be parallel. Let us write

$$\rho \mathbf{u}_\mathrm{p} = k \mathbf{B}_\mathrm{p}, \tag{1.29}$$

where k is called the *mass loading*, *i.e.* the ratio between the mass flux and the magnetic flux (see, *e.g.*, Pelletier & Pudritz 1992 and Pudritz et al. 2006). An important feature of the invariants along field lines is that they carry information on the line foot point in the disk. In the case of k, it also states that each magnetic field line has its own mass flux. In steady state, the mass conservation equation reads

$$0 = \nabla(\rho \mathbf{u}) = \nabla(\rho \mathbf{u}_p) = \nabla(k \mathbf{B}_p) = \mathbf{B}_p.\nabla k \tag{1.30}$$

where we have used the axisymmetry and the solenoidal condition. Equation 1.30 implies that $k = k(\Psi)$, *i.e.* the mass loading k is constant on each magnetic surface. Using $\mathbf{u}_\mathrm{p} \times \mathbf{B}_\mathrm{p} = 0$, $\mathbf{B}_\mathrm{p} = -\frac{1}{r}\mathbf{e}_\phi \times \nabla\Psi$ from Eq. 1.26, and Eq. 1.29 we can write

$$\mathbf{u} \times \mathbf{B} = \mathbf{e}_\phi \times \left(u_\phi \mathbf{B}_p - B_\phi \mathbf{u}_p \right) = \left(\frac{u_\phi}{r} - \frac{B_\phi k}{\rho r} \right) \nabla\Psi. \tag{1.31}$$

We take the curl of this equation (which results in the steady-state induction equation), using $\nabla \times (\nabla\Psi) = 0$ and obtain

$$0 = \nabla \left(u_\phi \mathbf{B}_p - B_\phi \mathbf{u}_p \right) \times \nabla\Psi, \tag{1.32}$$

hence $\nabla \left(u_\phi \mathbf{B}_p - B_\phi \mathbf{u}_p \right)$ is parallel to $\nabla\Psi$. We have obtained another surface function ω defined as $\omega \equiv u_\phi/r - kB_\phi/(r\rho)$, called the *angular velocity* of the magnetic surface. As a consequence, the total velocity field can be written as

$$\mathbf{u} = \frac{k\mathbf{B}}{\rho} + r\omega \mathbf{e}_\phi. \tag{1.33}$$

We already knew that the poloidal velocity is parallel to the poloidal field (Eq. 1.28). Equation 1.33 states that the total velocity is parallel to the total magnetic field in a frame of reference rotating at the angular velocity ω. The fluid behaviour is commonly described with the picture of a *bead on a rotating wire* to express that the fluid is constrained to move along the field lines (middle panel of Fig. 1.11).

Let us now focus on the angular momentum. Under the steady-state and axisymmetry approximations, we write the toroidal component of the equation of motion as

$$\rho\left(\mathbf{u}_p.\nabla u_\phi + \frac{u_r u_\phi}{r}\right) = \left(\mathbf{B}_p.\nabla B_\phi + \frac{B_r B_\phi}{r}\right), \tag{1.34}$$

where the similarity between the lef-hand side and right-hand side is clear. This leads to

$$\frac{1}{r}\rho\mathbf{u}_p.\nabla(ru_\phi) - \frac{1}{r}\mathbf{B}_p.\nabla(rB_\phi) = 0, \tag{1.35}$$

which is equivalent to

$$\frac{1}{r}\mathbf{B}_p.\nabla\left[kru_\phi - rB_\phi\right] = 0, \tag{1.36}$$

using 1.30 and 1.29. Equation 1.36 shows the existence of another surface function $l = l(\psi) \equiv r\left(u_\phi - \frac{B_\phi}{k}\right)$, which is the *specific angular momentum* carried by the gas and including magnetic torque ($l = ru_\phi$ is recovered for the non-magnetic case). To go further into our analysis, we define the poloidal Alfvén number $A \equiv u_p/v_{\mathrm{A,p}}$, where $v_{\mathrm{A,p}}$ is the poloidal Alfvén velocity. Then, $A^2 = \rho u_p^2/B_p = k^2/\rho$. Now, eliminating B_ϕ in the expressions of l and ω we obtain the toroidal velocity

$$u_\phi = \left(\frac{1}{1-A^2}\right) r\omega + \left(\frac{A^2}{A^2-1}\right)\frac{l}{r}. \tag{1.37}$$

Let us consider the two asymptotic cases $A \ll 1$ and $A \gg 1$. For $A \ll 1$, $u_\phi \approx r\,\omega$, meaning that the fluid is corotating with the magnetic surfaces. For $A \gg 1$, $u_\phi \approx l/r$, *i.e.* the fluid conserves its specific angular momentum. The points (resp. surfaces) where $A = 1$ are called *Alfvén points* (resp. Alfvén surfaces, see right panel of Fig. 1.11). A singularity at the Alfvén points for the toroidal velocity (Eq. 1.37) is prevented by requiring $l(A=1) = r_{\mathrm{A}}^2\omega$ where r_{A} is the cylindrical radius at which the Alfvén point is located.

Let us describe the physical picture. The outflow material is initially at radius r_0, at the magnetic field foot point in the disk, where $B_\phi = 0$ is assumed. It rotates at the disk (typically Keplerian) angular frequency $\omega_{\mathrm{K},0}$. In this region, the field lines are corotating with the disk. The material will follow the field line and gently accelerate through an Alfvén surface. Beyond this surface, the field is not strong enough to enforce corotation (Spruit, 1996). The flow angular momentum at the Alfvén point is $l_{\mathrm{A}} = r_{\mathrm{A}}^2\omega$. Straightforwardly, it can be linked to the specific angular momentum l_0 where the field line is anchored on the disk at the radius r_0 as $l_{\mathrm{A}} = (r_{\mathrm{A}}/r_0)^2 l_0$, with $l_0 = \omega_{\mathrm{K},0} r_0^2$. A particle located in the outflow carries $(r_{\mathrm{A}}/r_0)^2$ more angular momentum than a disk particle at r_0. A typical lever arm is $r_{\mathrm{A}}/r_0 \sim 3$ (*e.g.*, Pudritz & Ray, 2019), hence a factor $\sim$10 on the angular momentum. This shows how efficient are magneto-centrifugal outflows at extracting angular momentum. The loss of angular momentum by this process is called *magnetic braking*. If all the angular momentum were to be ejected via this mechanism, the mass accretion rate and mass outflow rate would simply be linked via $\dot{M}_{\mathrm{a}} \sim (r_{\mathrm{A}}/r_0)^2\dot{M}_{\mathrm{o}}$ (consistent with numerical simulations, see *e.g.* Kölligan & Kuiper 2018). Conservation of energy (Bernoulli's theorem) along a magnetic streamline, neglecting thermal pressure and toroidal velocity, allows one to obtain the outflow terminal speed (*e.g.* Pelletier & Pudritz 1992):

$$u_\infty \simeq \sqrt{2}\omega_{\mathrm{K},0} r_{\mathrm{A}} = (r_{\mathrm{A}}/r_0) u_{\mathrm{esc},0}. \tag{1.38}$$

The terminal speed is larger than the local escape speed, $u_{\mathrm{esc},0}$, by the lever arm factor. Moreover, it scales with the Keplerian speed: the smaller is the foot point radius, the larger the terminal velocity. It explains the onion-like structure of the outflow presented in the right panel of Fig. 1.8. Finally, since the gravitational energy is encapsuled in the Keplerian speed, this mechanism can span a broad range of stellar masses, in agreement with observations (*e.g.*, Cabrit

& Bertout 1992). As a natural consequence, capturing the largest velocity component of the outflow (the so-called "jet" with velocities $\sim$100 km/s, see right panel of Fig. 1.7) can become a matter of resolution in numerical simulations. Before the Alfvén surface, the description in terms of centrifugal forces is correct and the Lorentz force does not work. Indeed, the Lorentz force is naturally perpendicular to each field line, hence the gas can freely move on them (depending on the other forces, such as gravity, thermal pressure gradient) like a bead on a wire. In the original picture, the field lines have to be inclined by more than 30 deg with respect to the vertical axis for this mechanism to work (Blandford & Payne, 1982).

A complementary, more dynamical point of view, which becomes valid beyond the Alfvén surface, can be adopted. The Lorentz force can be decomposed into a *magnetic pressure* $\nabla B^2/2$ and *magnetic tension* $\mathbf{B}.\nabla\mathbf{B}$ forces. A rotating flow dominating the magnetic field can create a toroidal component strong enough to drive a poloidal magnetic-pressure-driven wind. Then, the wound-up magnetic lines exert the magnetic tension force on the flow (*hoop stress*). It is oriented toward the rotation axis and tends to collimate the flow. When corotation is not a correct approximation anymore (typically beyond the Alfvén surface), this approach based on the Lorentz force is more adapted to magneto-centrifugal outflows.

The magneto-centrifugal process is commonly invoked for several reasons. It can explain the observed outflows and jets, and contributes to redistribute angular momentum. In fact, without angular momentum redistribution after cloud collapse, stars would rotate at their break-up speed. Furthermore, it facilitates accretion at the same time, does not require a strong magnetic field, and applies to all rotating astrophysical systems, from brown dwarfs to black holes.

Magnetic tower flow

The same approach based on the Lorentz force is characteristic of *magnetic tower flows* (Lynden-Bell, 1996), in which the gas is propulsed by the magnetic pressure gradient. These are likely to occur during the early-phases of the collapse, because of the accumulation of toroidal magnetic field at the center of the core because of rotation (Pudritz & Ray, 2019). In agreement with the previous derivations, this a valid point of view when the gas velocity exceeds the Alfvén speed, so that the field is wound-up. Hence, this type of outflows is taking place in systems where the field is weak enough, on the contrary to magneto-centrifugal outflows. Moreover, magnetic towers do not have such an onion-like velocity structure inherited from the radial velocity distribution in the disk. The speed at which the tower builds-up is comparable to the rotation velocity at the centrifugal radius, at the outer-edge of the forming disk. They lead to much slower ($\sim 1-10$ km/s, Lynden-Bell 2003) and wider outflows, as observed around massive young-stellar objects (Hirota, 2018) and in numerical simulations with ideal MHD (Banerjee & Pudritz, 2007).

The three mechanisms we have presented here can actually cohabit in launching outflows around young stellar objects. In Chapter 5, we will intend to disentangle between these, and to determine the dominant process for outflows around massive protostars.

CHAPTER 2
Radiative Transfer

Contents

RADIATIVE TRANSFER plays a major role in the formation of massive stars and its inclusion in numerical codes is recent. In the interstellar medium, where stars form, kinetic, magnetic, cosmic-ray and radiative energies are close to equipartition ($\sim 10^{-12}\,\mathrm{erg\,cm^{-3}}$). At smaller scales, as shown in Chapter. 1, radiation impacts first the cooling during the collapse phase, then the gas dynamics during the main accretion phase. However, a full treatment of radiation is computationally expensive, as every parcel of gas emits photons thermally, at various frequencies and in various directions, in addition to line absorption/emission and scattering events. Barotropic equations of state have been used to mimic the change from optically-thin to -thick regime during the collapse phase, so that the gas could heat adiabatically above a given density. However, at later times, as the central object's luminosity increases and impacts the whole gas temperature and dynamics at various opacities, radiation transport has to be treated on its own. This has been largely permitted by the development of supercomputers and methods for affordable radiative transfer. First in spherically-symmetric configurations (see *e.g.*, Vaytet et al. 2013), radiative transfer has been included in multi-dimensional codes to model non-isotropic behaviors such as shadows or the *flashlight effect* to overcome the radiative barrier in massive star formation (Yorke & Sonnhalter, 2002).

In this chapter, I will present the basic definitions and equations for radiative transfer. I will introduce the moment methods I have used in this thesis. These are fluid descriptions of radiation and permit the coupling to the hydrodynamics to be tractable while still leading to a good accuracy depending on the problem. Finally, the coupling between two such methods, which is the very heart of this work's numerical aspect, will be exposed, motivated by the problem of massive star formation.

2.1 Fundamental quantities and equation of transfer

2.1.1 Definitions

Specific Intensity

The radiation field is entirely described by the *specific intensity* $I = I(\mathbf{x}, t; \mathbf{n}, \nu)$ (if polarization is neglected), which depends on its position, time, direction and frequency, for a total of seven variables. It is expressed in $\mathrm{erg\,cm^{-2}s^{-1}Hz^{-1}sr^{-1}}$ in the cgs system. The microscopic description of the photons that compose radiation is encapsuled in macroscopic quantities (see Mihalas & Mihalas 1984 for a complete reference on radiation hydrodynamics). It is defined such that the energy carried by radiation crossing a surface dS, in a solid angle $d\Omega$, during a time interval dt and between frequencies ν and $\nu + \mathrm{d}\nu$ is

$$d\varepsilon \equiv I(\mathbf{x}, t; \mathbf{n}, \nu) dS \cos\alpha \, d\Omega \, d\nu \, dt, \tag{2.1}$$

where α is the angle between the direction $\mathbf{n}$ and the vector perpendicular to the surface dS.

The number of dimensions in the radiative transfer equations is the main obstacle in solving it. Hence, we can get rid of the direction variable of the specific intensity and work with angular-averaged quantities, to reduce the number of variables at a reasonable modelling cost and make the radiative transfer problem affordable. The ith-order moment of a quantity $f(x)$ is the average of x^i, weighted by the function f, as

$$\int x^i f(x) dx. \tag{2.2}$$

The 0th-, 1st- and 2nd-order angular moments of the specific intensity are the *radiative energy*, *radiative flux* and *radiative pressure*.

Radiative Energy

The monochromatic radiation energy density, or spectral radiative energy, at a given frequency ν is the intensity integrated over all solid angles $d\Omega$

$$E_\nu = E(\mathbf{x}, t; \nu) \equiv \frac{1}{\mathrm{c}} \oint I(\mathbf{x}, t; \mathbf{n}, \nu) d\Omega, \tag{2.3}$$

and is expressed in $\mathrm{erg\,cm^{-3}\,Hz^{-1}}$. It corresponds to the photon density multiplied by the energy of each individual photon, $h\nu$, per frequency unit. The total radiative energy is this spectral energy integrated over all frequencies

$$E = E(\mathbf{x}, t) = \int_0^\infty E_\nu \, d\nu \tag{2.4}$$

and has dimensions $\mathrm{erg\,cm^{-3}}$.

Radiative Flux

The monochromatic radiation flux $\mathbf{F}(\mathbf{x}, t; \mathbf{n}, \nu)$ (in $\mathrm{erg\,cm^{-2}\,s^{-1}\,Hz^{-1}}$) is defined such that $\mathbf{F}.d\mathbf{S}$ is the net rate of spectral radiative energy across the surface $d\mathbf{S}$, or equivalently

$$\mathbf{F}_\nu = \mathbf{F}(\mathbf{x}, t; \nu) \equiv \oint I(\mathbf{x}, t; \mathbf{n}, \nu) \, \mathbf{n} \, d\Omega. \tag{2.5}$$

The total radiation flux is then

$$\mathbf{F} = \mathbf{F}(\mathbf{x}, t) = \int_0^\infty F_\nu \, d\nu. \tag{2.6}$$

As mentioned in Sect. 1.9.4, a photon of energy $h\nu$ carries a momentum vector $h\nu/c\mathbf{n}$. The monochromatic transport of momentum vector is therefore linked to the spectral flux as $\mathrm{c}^{-2}\mathbf{F}_\nu$.

Because the moment model is a fluid description of radiation, a wave speed related to perturbations in this fluid can be defined as $\|\mathbf{F}\| / E$ and this must be smaller than the speed of light.

Radiative Pressure

In this hierarchy of moments, the tensor order increases with the moment order. Hence, the radiative energy is a scalar, the radiative flux is a vector and the radiative pressure is a 2nd-order tensor. The component (i, j) of the radiative pressure tensor is the net rate of the momentum transport i-th component across a surface perpendicular to the j-th coordinate axis, and it has dimensions dyne $\mathrm{cm}^{-2}\,\mathrm{Hz}^{-1}$. It is defined as the second-order angular moment of the specific intensity, *i.e*

$$\mathbb{P}_\nu = \mathbb{P}(\mathbf{x}, t; \nu) = \frac{1}{\mathrm{c}} \oint I(\mathbf{x}, t; \mathbf{n}, \nu) \, \mathbf{n} \otimes \mathbf{n} \, d\Omega, \tag{2.7}$$

and the total radiative pressure as

$$\mathbb{P} = \mathbb{P}(\mathbf{x}, t) \equiv \int_0^\infty \mathbb{P}_\nu \, d\nu. \tag{2.8}$$

One can compute the trace of the matrix $\mathbf{n} \otimes \mathbf{n}$, obtain $\mathrm{tr}(\mathbf{n} \otimes \mathbf{n}) = \|\mathbf{n}\|^2 = 1$ and insert it in Eq. 2.7. Hence

$$\mathrm{tr}(\mathbb{P}_\nu) = E_\nu. \tag{2.9}$$

If the radiation is isotropic (typically in an opaque material), $\mathbb{P}_\nu$ is a diagonal matrix and $\mathbb{P}_\nu = E_\nu/3\mathbb{I}$ (so-called the Eddington limit).

Thermal Radiation

In the optically-thick regime, a very important limit is the local thermodynamical equilibrium (LTE), *i.e.* when the radiation field is in equilibrium with material (typically, a stellar interior). In this case, the radiation field is a function of only one variable, the temperature, and the (isotropic) specific intensity is given by the Planck function

$$I(\mathbf{x}, t; \mathbf{n}, \nu) = B_\nu(T) \equiv \frac{2\mathrm{h}\nu^3}{\mathrm{c}^2} \frac{1}{e^{\left(\frac{\mathrm{h}\nu}{\mathrm{k_B}T}\right)} - 1}, \tag{2.10}$$

where h is Planck's constant, c is the speed of light, $\mathrm{k_B}$ is the Boltzmann constant. This function derives from Bose-Einstein quantum statistics and is called blackbody radiation.

Consequently, the spectral radiative energy of thermal radiation is

$$E_\nu(T) = \frac{4\pi}{\mathrm{c}} B_\nu, \tag{2.11}$$

and the total radiative energy is then

$$E(T) = \int_0^\infty \frac{4\pi}{\mathrm{c}} B_\nu \mathrm{d}\nu = \mathrm{a_R} T^4, \tag{2.12}$$

(so-called Stefan's law), where $a_R \equiv 8\pi^5 {k_B}^4/15c^3h^3$ is the radiation constant. From this, a radiative temperature can be defined as $T_r \equiv (E/a_R)^{1/4}$. From Eq. 2.12, the frequency-integrated Planck function is

$$B(T) = (a_R c/4\pi)T^4. \tag{2.13}$$

We will now calculate the radiative flux in the particular case of a blackbody.

A common way to compute explicitly the angular moments above is to use angular coordinates θ and ϕ instead of the somehow implicit direction $\mathbf{n}$. We can define them with respect to the z-direction, so that

$$n_x = sin\,\theta\,cos\,\phi, \quad n_y = sin\,\theta\,sin\,\phi, \quad n_z = cos\,\theta. \tag{2.14}$$

It is useful to define $\mu = cos\theta = n_z$, because then the elementary solid angle becomes $d\Omega = sin\,\theta\,d\theta\,d\phi = -d\mu\,d\phi$. From there, we can compute the radiative flux coming out from a radiating surface (in the $x-y$ plane for convenience) as

$$F_z = \int I\,n_z\,d\mu\,d\phi = \int_0^1 \mu d\mu \int_0^{2\pi} I\,d\phi. \tag{2.15}$$

Since the thermal emission is isotropic, the radiative flux coming out from a blackbody (not counting the incoming flux) is simply $F = \pi B(T) = \sigma_{SB}T^4$. It yields a possible definition for the Stefan-Boltzmann constant σ_{SB}, *i.e.* $\sigma_{SB} \equiv \frac{1}{4}a_R c$. Likewise, the thermal radiative pressure is

$$P(T) = \frac{1}{3}\frac{4\pi}{c}B = \frac{1}{3}a_R T^4. \tag{2.16}$$

2.1.2 The radiative transfer equation

The fundamental equation for radiative transfer is the equation of conservation of the specific intensity attached to a radiation beam passing through a slab of material along $\mathbf{dl}$ and across dS. The energy difference between the emerging radiation at $(\mathbf{x}+\mathbf{dl}, t+dt)$ and the incident radiation at $(\mathbf{x}, t)$ depends on how much energy is being emitted and absorbed, *i.e.*

$$\begin{aligned}[I(\mathbf{x}+\mathbf{dl}, t+dt; \mathbf{n}, \nu) - I(\mathbf{x}, t; \mathbf{n}, \nu)]\,dS\,dl\,d\Omega\,d\nu = \\ \eta(\mathbf{x}, t; \mathbf{n}, \nu)dS\,dl\,d\Omega\,d\nu - \chi(\mathbf{x}, t; \mathbf{n}, \nu)I(\mathbf{x}, t; \mathbf{n}, \nu)dS\,dl\,d\Omega\,d\nu,\end{aligned} \tag{2.17}$$

where χ is the *extinction coefficient* (cm^{-1}) and η is the *emission coefficient* ($erg\,cm^{-3}\,s^{-1}\,Hz^{-1}\,sr^{-1}$), evaluated here in the laboratory frame. The extinction coefficient (or *total absorption coefficient*) describes the part of the radiation energy which is removed from the radiation beam and is linked to the material's opacity (cross-section to interact with photons). It encapsulates both thermal absorption and scattering (see Sect. 2.1.3). The emission coefficient is defined in a similar manner as the specific intensity (see Eq. 2.1) but corresponds to the emission of radiation by the material.

The path length dl and time interval are related via $dt = dl/c$. We can use a Taylor expansion to express

$$I(\mathbf{x}+\mathbf{dl}, t+dt; \mathbf{n}, \nu) = I(\mathbf{x}, t; \mathbf{n}, \nu) + \left[\frac{1}{c}\frac{\partial I}{\partial t} + \frac{\partial I}{\partial l}\right] dl. \tag{2.18}$$

If we substitute it into 2.17 we obtain the *equation of transfer* (expressed in Cartesian coordinates here)

$$\left[\frac{1}{c}\frac{\partial}{\partial t} + \mathbf{n}.\boldsymbol{\nabla}\right] I(\mathbf{x}, t; \mathbf{n}, \nu) = \eta(\mathbf{x}, t; \mathbf{n}, \nu) - \chi(\mathbf{x}, t; \mathbf{n}, \nu)I(\mathbf{x}, t; \mathbf{n}, \nu). \tag{2.19}$$

This is the fundamental equation to be solved for radiation transport from a macroscopic point of view.

It does not capture phenomena such as polarization, interference, or dispersion. Changes in polarization and phase can be caused by scattering by dust particles, and are described by the equations of evolution of the *Stokes vector*. It is usually treated when focus is made on polarization, as in several radiative transfer codes (see *e.g* Pinte et al. 2006). Interference effects cause an oscillation of the opacity when the radiation wavelength is close to the dust grain size. This would require to capture the dust size distribution, which is beyond the scope of this work, and is likely to be a second-order effect compared to the current uncertainties on the dust opacities we use. Dispersion can be taken into account by considering the conservation of the quantity I/n^2 instead of I, n being the refractive index (see *e.g.* Oster 1963, Pomraning 1968 for the modified radiative transfer equation). As a consequence , the radiation beam follows a curved path, the interaction with matter (absorption and emission, see below) is modified and the beam can be focused or defocused (Castor, 2004). However, it is relevant if the radiation frequency approaches the plasma frequency $\omega_{\rm pe} = \sqrt{4\pi e^2 n_{\rm e}/m_{\rm e}}$ where e, $n_{\rm e}$ and $m_{\rm e}$ are the electron charge, density and mass, respectively. For a typical electron density $n_{\rm e}{\sim}1\,{\rm cm}^{-3}$ in the interstellar medium, this gives $\omega_{\rm pe}{\sim}10^5$ Hz (radio domain), which is a much smaller frequency than that of the thermal radiation we consider (which is in the infrared to UV domains).

2.1.3 Absorption, emission, scattering

Let us go further in our description of radiation transport. The extinction accounts for the radiation losses, hence a *mean free path* of photons is defined as $\lambda_{{\rm p},\nu} \equiv 1/\chi_\nu$. Let us note that the absorption, emission and scattering cross sections of various materials are isotropic in the fluid rest frame. At each frequency corresponds a cross section of interaction ($\rm cm^2$) which can vary significantly with the frequency. Once multiplied by the particle density, this gives the absorption and scattering coefficients (and therefore the extinction coefficient) above. In the laboratory frame, these would be affected by Doppler shift and aberration effects, due to the fluid motion.

We have defined χ and η as absorption and emission coefficients, respectively. It would be useful, however, to distinguish between thermal absorption/emission and scattering. As an example of thermal absorption, an atom is excited by an incoming photon and de-excited by the collision with another particle which inherit from the photon energy in the form of kinetic energy. Then, the material internal energy is increased by the photon radiative energy it has absorbed. Similarly, thermal emission converts thermal energy of a hot gas into radiative energy.

On the opposite, when a photon is scattered by a charged particle (Compton scattering, called Thompson scattering in the case of a low-energy photon), an atom or a molecule (Rayleigh scattering if elastic, *i.e.* no exchange of energy, Raman scattering otherwise), it is deviated from its original direction with a possible small change of frequency, hence the gas thermal energy is (close to) unchanged. Indeed, there can be a tiny change of frequency which means that some energy has been gained by the atom/particule. For simplicity, we will consider it to be zero.

Therefore, we split the extinction coefficient into the sum of an absorption coefficient κ and scattering coefficient σ, *i.e.*

$$\chi(\mathbf{x}, t; \mathbf{n}, \nu) = \kappa(\mathbf{x}, t; \mathbf{n}, \nu) + \sigma(\mathbf{x}, t; \mathbf{n}, \nu). \tag{2.20}$$

Likewise, we decompose the emission coefficient as

$$\eta(\mathbf{x}, t; \mathbf{n}, \nu) = \eta^{\rm t}(\mathbf{x}, t; \mathbf{n}, \nu) + \eta^{\rm s}(\mathbf{x}, t; \mathbf{n}, \nu), \tag{2.21}$$

where η^{t} is the thermal contribution and η^{s} the scattering one. At the LTE, these contributions take the form

$$\begin{aligned} \eta_\nu^{\mathrm{t}} &= \kappa_\nu B_\nu(T), \\ \eta_\nu^{\mathrm{s}} &= \sigma_\nu \oint p_\nu(\Omega' \to \Omega) I(\Omega') d\Omega', \end{aligned} \tag{2.22}$$

where $p_\nu(\Omega' \to \Omega)$ is the function of angular redistribution of scattered photons, and must verify the normalization condition $\oint p_\nu(\Omega' \to \Omega) d\Omega' = 1$. It is reasonable to assume that this function only depends on the angle between both directions, so that $p_\nu(\Omega' \to \Omega) = p_\nu(\Omega'.\Omega)$, thus $p_\nu(\Omega'.\Omega) = 1/4\pi$ for isotropic scattering.

This leads to the more detailed equation of transfer (LTE is assumed)

$$\left[\frac{1}{\mathrm{c}}\frac{\partial}{\partial t} + \mathbf{n}.\boldsymbol{\nabla}\right] I_\nu(\mathbf{x}, t; \mathbf{n}) = \kappa_\nu(B_\nu(T) - I_\nu(\mathbf{x}, t; \mathbf{n})) - \sigma_\nu I_\nu(\mathbf{x}, t; \mathbf{n}) + \sigma_\nu \int_{4\pi} p_\nu(\mathbf{n}.\mathbf{n}') I_\nu(\mathbf{x}, t; \mathbf{n}') d\mathbf{n}'. \tag{2.23}$$

There exist two asymptotic regimes, depending on the likelihood for photons to interact with the gas. This is quantified as the optical depth τ which is related to the mean free path via $\tau = l/\lambda_{\mathrm{p},\nu}$, where l is the typical length of the system. A naive interpretation is that τ is the average number of interactions a photon would have when crossing this system. More strictly, between two positions $\mathbf{x}$ and $\mathbf{x}'$ it is defined as

$$\tau_\nu(\mathbf{x}, \mathbf{x}') \equiv \int_0^l \chi(\mathbf{x} + s\mathbf{n}; \mathbf{n}, \nu) ds, \tag{2.24}$$

where ds is an elementary length. By definition, a medium with $\tau \gg 1$, is *optically-thick*. In this case, photons are trapped and diffuse by random-walk motions. Gas and radiation are tightly coupled together and the specific intensity tends towards the Planck function. This is the *diffusion limit*. On the other hand, if $\tau \ll 1$, the medium is *optically-thin* and photons can freely escape as their interactions with the gas are rare, this is the *transport limit*.

2.2 Moment models

The equation of transfer (Eq. 2.19) depends on seven variables. We are interested in a dynamical coupling between radiation and hydrodynamics, which implies solving this equation at each timestep of the simulation, together with the magneto-hydrodynamical equations, which would be very computationally expensive.

A way to reduced the dimensionality of the problem is to take angular moments of this equation. When doing so, one ends up with a hierarchy of equations of conservation on each moment of the specific intensity: the radiative energy, radiative flux and radiative pressure, presented in the previous section. Taking the 0-th and 1-st moments of the equation of transfer, one obtains the following system

$$\begin{cases} \dfrac{\partial E_\nu}{\partial t} + \boldsymbol{\nabla}.\mathbf{F}_\nu = \displaystyle\oint \left(\kappa_\nu(B_\nu(T) - I_\nu(\mathbf{n})) - \sigma_\nu I_\nu(\mathbf{n}) + \sigma_\nu \int_{4\pi} p_\nu(\mathbf{n}.\mathbf{n}') I_\nu(\mathbf{n}') d\mathbf{n}' \right) d\Omega, \\ \dfrac{1}{\mathrm{c}}\dfrac{\partial \mathbf{F}_\nu}{\partial t} + \mathrm{c}\boldsymbol{\nabla}.\mathbb{P}_\nu = \displaystyle\oint \left(\kappa_\nu(B_\nu(T) - I_\nu(\mathbf{n})) - \sigma_\nu I_\nu(\mathbf{n}) + \sigma_\nu \int_{4\pi} p_\nu(\mathbf{n}.\mathbf{n}') I_\nu(\mathbf{n}') d\mathbf{n}' \right) \mathbf{n} d\Omega. \end{cases} \tag{2.25}$$

We have dropped the notation on the dependence on position and time for conciseness. Let us simplify the right-hand side terms of the first equation, starting with the emission terms, *i.e.*

$$\begin{cases} \kappa_\nu \oint \quad B_\nu(T) \quad d\Omega = \kappa_\nu \, 4\pi \, B_\nu, \\ \sigma_\nu \oint \int_{4\pi} p_\nu(\mathbf{n}.\mathbf{n}') I_\nu(\mathbf{n}') d\mathbf{n}' d\Omega = \sigma_\nu \, \mathrm{c} \, E_\nu, \end{cases} \tag{2.26}$$

because B is isotropic and p_ν is normalized. The absorption terms simply yield

$$-\oint (\kappa_\nu + \sigma_\nu) I_\nu(\mathbf{n}) d\Omega = -(\kappa_\nu + \sigma_\nu) \, \mathrm{c} \, E_\nu. \tag{2.27}$$

Similarly, the right-hand side terms of the second equation can be simplified as

$$\begin{cases} \oint \quad \kappa_\nu \quad B_\nu(T) \quad \mathbf{n} \, d\Omega = 0, \\ \oint \quad -(\kappa_\nu + \sigma_\nu) \, I_\nu(\mathbf{n}) \quad \mathbf{n} \, d\Omega = -(\kappa_\nu + \sigma_\nu) \mathbf{F}_\nu, \\ \oint \sigma_\nu \int_{4\pi} p_\nu(\mathbf{n}.\mathbf{n}') \, I_\nu(\mathbf{n}') d\mathbf{n}' \mathbf{n} \, d\Omega = \quad \sigma_\nu \; g_\nu \; \mathbf{F}_\nu, \end{cases} \tag{2.28}$$

where we have used once again the isotropy of B_ν, and introduced g_ν, the first angular moment of the scattering angular distribution p_ν. Isotropic scattering would lead $g_\nu = 0$. Putting it altogether, we obtain the following system

$$\begin{cases} \dfrac{\partial E_\nu}{\partial t} + \boldsymbol{\nabla}.\mathbf{F}_\nu = \kappa_\nu \, (4\pi \, B_\nu - \mathrm{c} E_\nu), \\ \dfrac{1}{\mathrm{c}^2} \dfrac{\partial \mathbf{F}_\nu}{\partial t} + \boldsymbol{\nabla}.\mathbb{P}_\nu = -\dfrac{1}{\mathrm{c}} (\kappa_\nu + \sigma_\nu (1 - g_\nu)) \mathbf{F}_\nu. \end{cases} \tag{2.29}$$

From the first equation: the rate of change of the volumic radiative energy equals the rate of energy emission by the matter minus the rate of absorption and the net flow of radiative energy through a volume element's boundary. One remarks that the energy equation does not account for scattering. Indeed, scattering does not redistribute the radiative energy, only the radiative flux. A system's radiative equilibrium can be found by setting $\partial_t E_\nu \equiv 0$. Since it absorbs exactly as much as it emits, the right-hand side terms vanishes, hence $\boldsymbol{\nabla}.\mathbf{F}_\nu \equiv 0$: the flux is constant with the distance (for cartesian coordinates). The second equation states that the rate of change of volumic radiation momentum equals the net rate of momentum transfer from the matter into radiation, minus the total rate of absorption of radiation momentum by the matter and the rate of momentum transport through a volume element's boundary. For the sake of simplicity, we will write the term $(\kappa_\nu + \sigma_\nu(1 - g_\nu))$ as χ_ν when accounting for scattering without entering its details.

This system contains two equations but three moments, hence a closure relation equation is needed. Here we present the two moment methods we have used and coupled together for particular problems: the flux-limited diffusion and the M1 methods. The moment methods differ by the chosen closure relation. Furthermore, we will derive the *gray* formulation of these equations, *i.e.* their frequency-averaged version.

2.2.1 Gray radiative transfer

Equations 2.29 should be solved for every possible photon frequency, which is impossible in practice. A way to deliver a tractable method is to average these equations over the whole

frequency domain (so-called gray approach). The price to pay is the impossibility to capture processes that depend on a very precise frequency, *e.g.* line transfer. Under the gray approximation, the right-hand sides of 2.29 become

$$\begin{cases} \int_0^\infty \kappa_\nu \left(4\pi B_\nu - \mathrm{c}E_\nu\right) d\nu = \kappa_\mathrm{P} \mathrm{c} a_\mathrm{R} T^4 - \mathrm{c}\kappa_\mathrm{E} E, \\ \\ \int_0^\infty -\frac{1}{\mathrm{c}} \chi_\nu \mathbf{F}_\nu d\nu = -\frac{1}{\mathrm{c}} \chi_\mathrm{F} \mathbf{F}, \end{cases} \tag{2.30}$$

where we have introduced the following averaged opacities and extinction coefficients

$$\begin{cases} \kappa_\mathrm{P} \equiv \dfrac{\int_0^\infty \kappa_\nu B(\nu) d\nu}{\int_0^\infty B(\nu) d\nu}, \\ \\ \kappa_\mathrm{E} \equiv \dfrac{\int_0^\infty \kappa_\nu E_\nu d\nu}{\int_0^\infty E_\nu d\nu}, \\ \\ \chi_\mathrm{F} \equiv \dfrac{\int_0^\infty \chi_\nu \mathbf{F}_\nu d\nu}{\int_0^\infty \mathbf{F}_\nu d\nu}, \end{cases} \tag{2.31}$$

where κ_P is called the Planck mean opacity. Under the approximation of LTE, we have $E_\nu = B(\nu)$ hence $\kappa_\mathrm{E} = \kappa_\mathrm{P}$. The left-hand sides of 2.29 simply involve the frequency-averaged moments (Eqs. 2.4,2.6 and 2.8).

On the opposite, Monte-Carlo approaches follow photon packets with their spectral distribution and keep the frequency as a variable, but are much more expensive. Multigroup approaches (see *e.g.* González et al. 2015) tend to find a way in between the two extremes. For a given set of n frequency groups, the system 2.29 is divided into n systems, each one operating an average over its frequency domain.

Gray and multigroup (also called *frequency-dependent*) approaches apply to all moment methods. We will present subsequently the two moments methods we have used throughout this work, by increasing order of complexity.

2.2.2 Flux-limited diffusion

The flux-limited diffusion method (hereafter FLD) is a widely used method as the first implementation of radiative transfer in hydrodynamical codes, *e.g.* ORION (Krumholz et al., 2007), PLUTO (Kuiper et al., 2010c) or RAMSES (Teyssier, 2002). This approximation originally holds in the *diffusion limit*, where the medium is optically-thick. We can drop the first term of the radiative flux conservation equation, *i.e.* the flux time derivative, because it is negligible compared to the right-hand side term. Indeed, $(l/\lambda_\mathrm{p})^2$ is the average number of interactions of a photon in random walk to cross a distance l, so the associated *diffusion timescale* to cross such a distance is $\tau_\mathrm{d} \equiv (l/\lambda_\mathrm{p})^2(\lambda_\mathrm{p}/\mathrm{c}) \sim l^2/(\lambda_\mathrm{p}\mathrm{c})$, hence $\partial_t \mathbf{F}_\nu/\mathrm{c}^2 \sim \mathbf{F}_\nu/(\mathrm{c}^2\tau_\mathrm{d}) \sim \mathbf{F}_\nu\lambda_\mathrm{p}/(l^2\mathrm{c})$. Thus, the ratio between the flux time derivative and the right-hand side term is $\sim (\mathbf{F}_\nu\lambda_\mathrm{p}/l^2\mathrm{c})/(\chi_\nu\mathbf{F}_\nu/\mathrm{c}) \sim \lambda_\mathrm{p}/(l^2\chi_\nu) \sim (\lambda_\mathrm{p}/l)^2 \ll 1$ in the optically-thick regime. Hence, the conservation of the radiative flux simply reads

$$\boldsymbol{\nabla}.\mathbb{P}_\nu = -\frac{1}{\mathrm{c}}\chi_\nu \mathbf{F}_\nu. \tag{2.32}$$

In the optically-thick regime, the radiative pressure is isotropic and related to the radiative energy as $\mathbb{P}_\nu = E_\nu/3\,\mathbb{I}$ (see Sect.2.1.1), so the flux becomes

$$\mathbf{F}_\nu = -\frac{\mathrm{c}}{3\chi_\nu}\boldsymbol{\nabla}.E_\nu. \tag{2.33}$$

Under the gray approximation and at the LTE, the total radiative flux is

$$\begin{aligned}\mathbf{F} &= \int_0^\infty \mathbf{F}_\nu d\nu, \\ &= -\int_0^\infty \frac{\mathrm{c}}{3\chi_\nu}\boldsymbol{\nabla}.B_\nu(T)d\nu, \\ &= -\frac{\mathrm{c}}{3\kappa_\mathrm{R}}\int_0^\infty \boldsymbol{\nabla}.B_\nu(T)d\nu,\end{aligned} \tag{2.34}$$

where κ_R is the Rosseland mean opacity and is defined as

$$\kappa_\mathrm{R} \equiv \frac{\int_0^\infty \frac{\partial B_\nu(T)}{\partial T}d\nu}{\int_0^\infty \frac{1}{\chi_\nu}\frac{\partial B_\nu(T)}{\partial T}d\nu}. \tag{2.35}$$

It is an harmonic mean, thus its gives a higher weight to low-opacity bands. An adjustement is necessary to make sure that radiation does not propagate faster than the speed of light, *i.e.* $\mathbf{F} \leqslant \mathrm{c}E$, or $f \equiv \|\mathbf{F}\|/cE \leqslant 1$, where f is called the reduced flux. A flux-limiter, λ, has been introduced by Levermore & Pomraning (1981) in that view, so the flux is now defined as $\mathbf{F}_\nu = -\mathrm{c}\lambda\boldsymbol{\nabla}E_\nu/\chi_\nu$. It is an analytical function of $R = \|\boldsymbol{\nabla}E\|/\kappa_\mathrm{R}E$, whose value is a proxy for the various regimes of optical thickness. The flux-limited is built to yield the correct asymptotic values for the flux: $\lambda \to 1/3$ in the optically-thick limit, hence $\mathbf{F} = -\mathrm{c}/(3\kappa_\mathrm{R})\,\boldsymbol{\nabla}E$, and $\lambda \to 1/R$ in the optically-thin limit, corresponding to $\mathbf{F} = \mathrm{c}E$. The system to be solved then reduces to the radiative energy equation

$$\frac{\partial E}{\partial t} - \boldsymbol{\nabla}.\left(\frac{\mathrm{c}\lambda}{\kappa_\mathrm{R}}\boldsymbol{\nabla}E\right) = \kappa_\mathrm{P}\,\mathrm{c}(\mathrm{a_R}T^4 - E), \tag{2.36}$$

hence the radiative energy is evolved via a non-constant coefficient diffusion equation. The radiative flux follows the radiative energy gradient.

The monochromatic, volumic radiative acceleration, simply derives from the rate of change of the momentum vector $\mathrm{c}^{-2}\mathbf{F}_\nu$. It has the general form

$$\mathbf{a}_{\mathrm{rad},\nu} = \frac{\chi_\nu}{\rho\mathrm{c}}\mathbf{F}_\nu, \tag{2.37}$$

where ρ is the gas mass density. The physical meaning behind this definition is that, all the absorbed or scattered photons transfer momentum to the gas. Therefore, in the gray FLD method, the total radiative acceleration is

$$\mathbf{a}_\mathrm{rad} = \frac{\lambda}{\rho}\boldsymbol{\nabla}E. \tag{2.38}$$

Hence, in the limits of low optical depth it gives $\|\mathbf{a}_\mathrm{rad,thin}\| = \kappa_\mathrm{R}E/\rho$, and $\|\mathbf{a}_\mathrm{rad,thick}\| = \frac{1}{3\rho}\boldsymbol{\nabla}E$ at high optical depth.

Due to its simplicity and its accuracy in the optically-thick regime, it has been used in the first radiation-hydrodynamical simulations of massive star formation (*e.g.*, Yorke & Sonnhalter 2002, Krumholz et al. 2009, Commerçon et al. 2011a). However, a drawback of the FLD is its inability to capture the self-shielding behind opaque structures (*e.g.* a disk, a dense cloud), as can be seen in the result of the shadow test (see Fig. 2.1).

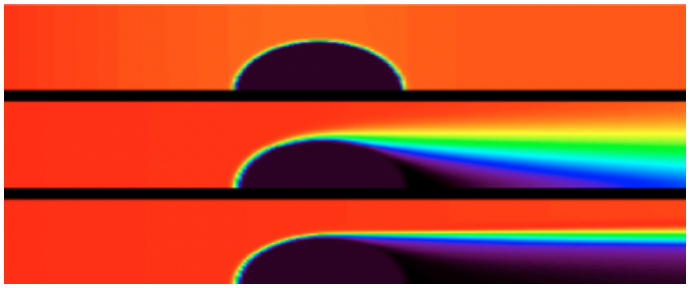

Figure 2.1: Radiative temperature (see Eq. 2.12) when an opaque structure is illuminated from the left side (shadow test), obtained with the diffusion method (top) and the M1 method with two different numerical solvers (middle and bottom). From González et al. (2007).

2.2.3 M1 model

The M1 model goes one step further, keeping both the equations of conservation of the radiative energy and of the radiative flux. No assumption is made on the regime of optical thickness. Once again, a closure relation is needed, and here it links the radiative pressure tensor to the radiative energy

$$\mathbb{P}_\nu = \mathbb{D} E_\nu, \tag{2.39}$$

where $\mathbb{D}$ is the Eddington tensor and should depend on variables such as E, $\mathbf{F}$, or any other variable of the problem. In the M1 Eddington closure, used in HERACLES (González et al., 2007), ATON (Aubert & Teyssier, 2008) and RAMSES-RT (Rosdahl et al., 2013), the Eddington tensor only depends on local variables, hence it does not require global communications. On the opposite, the Variable Eddington Tensor (VET) is an example of closure relation which uses non-local quantities (Davis et al., 2012). It consider all the vectors coming from the radiation sources in the simulated volume to the volume element under consideration, but is therefore more expensive and not adapted to MPI parallel computing. Under the assumption that the radiation flux direction is an axis of symmetry of the specific intensity I, $\mathbb{D}$ can take the form (Levermore, 1984)

$$\mathbb{D} = \frac{1-\chi}{2}\mathbb{I} + \frac{3\chi-1}{2}\mathbf{n}\otimes\mathbf{n}, \tag{2.40}$$

where χ is the Eddington factor (not to be confused with the extinction coefficient, χ_ν) and $\mathbf{n} = \mathbf{F}/\|\mathbf{F}\|$ is a unit vector directed along the flux direction. The diffusion regime is recovered under the Eddington approximation : $\mathbb{D} = (1/3)\mathbb{I}$, from $\chi = 1/3$ (lower-limit). On the other hand, $\mathbb{D} = \mathbf{n}\otimes\mathbf{n}$ corresponds to a fully directional radiation, *i.e.* in the optically-thin regime, for $\chi = 1$ (upper-limit). Various functions have been proposed for χ (see Levermore 1984) but not all are physically-motivated nor simple to implement. Under the M1 model, the Eddington factor is given by

$$\chi = \frac{3+4f^2}{5+2\sqrt{4-3f^2}}, \tag{2.41}$$

which has been derived from arguments of radiation entropy minimization (Dubroca & Feugeas, 1999) and Lorentz transformation to an isotropic photon distribution (Levermore, 1984). Since the reduced flux f is always between 0 and 1 (see Sect. 2.2.2), χ is indeed always between $1/3$ and 1. The asymptotic regime where radiation is purely directional is recovered with $f = 1$ and the diffusion regime with $f = 0$. Due to its construction, the M1 model ensures energy positivity and $f \leqslant 1$.

In its gray version (the one that we have used throughout this thesis), the M1 model is

composed of the system

$$\begin{cases} \dfrac{\partial E}{\partial t} + \quad \boldsymbol{\nabla} \cdot \mathbf{F} = \kappa_{\mathrm{P}}\, \mathrm{c}(\mathrm{a_R} T^4 - E), \\ \dfrac{\partial \mathbf{F}}{\partial t} + \mathrm{c}^2 \boldsymbol{\nabla} \cdot \mathbb{P} = -\chi_{\mathrm{F}}\, \mathrm{c}\, \mathbf{F}, \end{cases} \tag{2.42}$$

The associated total radiative acceleration is

$$\mathbf{a}_{\mathrm{rad}} = \frac{\chi_{\mathrm{F}}}{\rho \mathrm{c}} \mathbf{F}. \tag{2.43}$$

One can notice that the mean extinction coefficient here is different from κ_{R}, used in the FLD radiative acceleration and introduced in a diffusion approximation for radiation. Since κ_{R} is a harmonic mean (arising from the assumption of the radiative flux stationarity), it gives more weight to low-opacity spectral bands, while χ_{F} is an arithmetic mean and favors high opacities. Hence, for similar opacities, one could expect a greater radiative acceleration with the M1 model than with the FLD model.

As for the FLD model, the M1 model also presents the advantage of consisting in a system of hyperbolic equations, making easy its implementation in hydrodynamical codes. As it involves an additional vectorial equation to the FLD it is more expensive though, especially in 3D. One main advantage of the M1 compared to the FLD model is its ability to retain, to some extent, the directionality of the photon beam, as can be seen in Fig. 2.1. It is important to note, however, that the closure relation assumes isotropy perpendicularly to the radiative flux, consistent with the treatment of a singular radiation beam. Hence, it is not adapted to the treatment of radiation beams crossing each other. The resulting flux from two crossing rays would result in the vectorial sum of the two fluxes.

Internal energy evolution

We still need to close the matter-radiation coupling system with an additional equation on the temperature. This role is assumed by the conservation of the total energy, *i.e.* the sum of radiative energy and the internal energy. The internal energy e of an ideal gas is related to its thermal pressure via $P = (\gamma - 1)e = \rho \mathrm{k_B} T / \mu \mathrm{m_H}$, where μ is the mean molecular weight and $\mathrm{m_H}$ is the hydrogen mass. We will use the internal energy $e = C_{\mathrm{v}} T$, where C_{v} is the heat capacity at constant volume. Hence, the equation of conservation of the total energy is

$$\frac{\partial E}{\partial t} + \frac{\partial e}{\partial t} = 0, \tag{2.44}$$

thus the evolution of the internal energy is governed (assuming gray radiative transfer) by

$$\frac{\partial e}{\partial t} = \frac{\partial C_{\mathrm{v}} T}{\partial t} = \kappa_{\mathrm{P}}\, \mathrm{c}(E - \mathrm{a_R} T^4). \tag{2.45}$$

The gas temperature is evolved using this equation together with the radiative quantities.

2.2.4 Hybrid radiative transfer

As can be seen in Sects. 2.2.2 and 2.2.3, the FLD and M1 methods present complementarities. The FLD method is well-suited in optically-thick media, and includes one equation. The M1 method is more advanced and adapted for describing unidirectional radiation beams, but its closure relation is more complex.

Motivated by the question of massive star formation, we have undertaken the coupling of the two methods, both already implemented in RAMSES (Commerçon et al. 2011b and Rosdahl

et al. 2013). Indeed, their definition of the radiative acceleration differs, which is of main interest for us (as mentioned in Sect. 1.7). Our aim is to follow the protostellar radiation propagation and absorption with the M1 method. Meanwhile, the heating of the surrounding gas-and-dust mixture and its reemitted radiation is handled with the FLD method. In that view, we have chosen a gray formalism for both modules, but multigroup approaches are available (Rosdahl et al. 2013, González et al. 2015 for the FLD).

The equations governing the M1 module of the hybrid approach are therefore

$$\begin{cases} \dfrac{\partial E}{\partial t} + \quad \boldsymbol{\nabla}\cdot\mathbf{F} = -\kappa_{\rm P}\mathrm{c}E + \dot{E}^{\star}_{\rm r}, \\ \dfrac{\partial \mathbf{F}}{\partial t} + \mathrm{c}^2\boldsymbol{\nabla}\cdot\mathbb{P} = -\chi_{\rm F}\,\mathrm{c}\,\mathbf{F}, \end{cases} \tag{2.46}$$

where $\dot{E}^{\star}_{\rm r}$ is the radiative energy injection rate by stellar sources. The gas thermal emission term in Eq. 2.42 has also disappeared, since the M1 module only deals with stellar radiation here. In this work, we have focused on a single source for simplicity and because of the problems arising with multiple sources within the M1 method, as mentioned in Sect. 2.2.3. We recall that this model is gray, so the opacity and extinction coefficients are frequency-averaged coefficients. More than that, we have first considered isotropic scattering so $\chi_{\rm F} = \kappa_{\rm F} + \sigma_{\rm F}$, where $\kappa_{\rm F}$ and $\sigma_{\rm F}$ would be the flux-averaged absorption and scattering opacities, respectively. The assumption that the spectral shapes of E and $\mathbf{F}$ are similar is made, so that $\sigma_{\rm F}$ and $\kappa_{\rm F}$ are approximated by the Planck mean scattering and absorption opacities, respectively, *i.e.* $\sigma_{\rm F} \simeq \sigma_{\rm P}$ and $\kappa_{\rm F} \simeq \kappa_{\rm P}$. Doing so, all the averages are weighted by the Planck function, hence they only depend on the temperature. The mean opacity and extinction coefficients are evaluated at the stellar temperature. We consider the spectral distribution of stellar radiation to be that of a blackbody. After showing that scattering does not contribute significantly in our pure radiative transfer tests (Sect. 3.5), we have neglected it in collapse calculations, with $\chi_{\rm F} = \kappa_{\rm P}$. Since the averaged opacity only depends on the temperature, we note $\kappa_{\rm P,\star} = \kappa_{\rm P}(T_\star)$ the Planck mean opacity computed at the stellar effective temperature $T_\star$.

Finally, the set of equations we obtain is

$$\begin{cases} \dfrac{\partial E_{\rm M1}}{\partial t} + \quad \boldsymbol{\nabla}\cdot\mathbf{F}_{\rm M1} = -\kappa_{\rm P,\star}\,\mathrm{c}E_{\rm M1} + \dot{E}^{\star}_{\rm M1}, \\ \dfrac{\partial \mathbf{F}_{\rm M1}}{\partial t} + \mathrm{c}^2\boldsymbol{\nabla}\cdot\mathbb{P}_{\rm M1} = -\kappa_{\rm P,\star}\,\mathrm{c}\mathbf{F}_{\rm M1}, \\ \dfrac{\partial E_{\rm fld}}{\partial t} - \boldsymbol{\nabla}\cdot\left(\dfrac{\mathrm{c}\lambda}{\kappa_{\rm R,fld}}\boldsymbol{\nabla}E_{\rm fld}\right) = \kappa_{\rm P,fld}\,\mathrm{c}\left(\mathrm{a_R}T^4 - E_{\rm fld}\right), \\ \qquad\qquad \dfrac{\partial C_{\rm v}T}{\partial t} = \kappa_{\rm P,\star}\,\mathrm{c}E_{\rm M1} + \kappa_{\rm P,fld}\,\mathrm{c}\left(E_{\rm fld} - \mathrm{a_R}T^4\right). \end{cases} \tag{2.47}$$

This last equation ensures the coupling between radiation and the gas temperature. We have defined a radiative acceleration, *i.e.* momentum transfer from photons to gas particles, but these equations do not account for gas dynamics yet. This requires a coupling between radiative transfer and hydrodynamical equations.

2.3 Radiation Hydrodynamics equations

One needs to couple the equations of hydrodynamics (the conservation of mass, momentum and energy) to the previous system to describe the effect of radiative pressure onto the gas dynamics, as well as energy transfers important for capturing isothermal/adiabatic behaviours, without relying on approximations such as a barotropic equation of state. I will show hereafter why it is important for this work.

2.3.1 Why Radiation Hydrodynamics in star formation?

The relative importance between an ideal gas internal energy and radiative energy, at radiative equilibrium, can be evaluated by the ratio R,

$$R = \frac{e}{E} = \frac{\rho k_B T}{\mu m_H a_R T^4} \simeq 4.7 \times 10^{21} \frac{\rho}{1\,\mathrm{g\,cm^{-3}}} \left(\frac{T}{1\mathrm{K}}\right)^3. \tag{2.48}$$

It quantifies also the ratio between the thermal and radiative pressures, since $p = (\gamma - 1)e$ for an ideal gas and $P = (1/3)E$ for radiation in the diffusion regime. At energy equipartition, thermal pressure dominates over radiative pressure for $\gamma > 4/3$. Equation 2.48 shows that radiation becomes increasingly important as temperature increases and/or density decreases. An accretion disk around a massive protostar has typical densities $\sim 10^{-15} - 10^{-11}\,\mathrm{g\,cm^{-3}}$ ($nsim \times 10^{9-13}\,\mathrm{cm^{-3}}$) and temperatures $\sim 100 - 1000$ K, thus the radiative energy contribution can become comparable to the thermal energy contribution in the total energy budget, in the diffusion regime.

The dimensionless Boltzmann number (see Mihalas & Mihalas 1984) aims at quantifying the relative importance between the thermal and radiative fluxes. It is defined as

$$\mathrm{Bo} \equiv \frac{\rho c_p T v}{\sigma_{SB} T^4} \sim \frac{v}{c} R, \tag{2.49}$$

where v is the fluid velocity and c_p is the specific heat at constant pressure, and we also used $\sigma_{SB} = (1/4) c\, a_R$. Taking $v \sim c_s$, we generally have $v \ll c$ in most hydrodynamical applications. This illustrates that even when the radiative energy is comparable to the thermal energy ($R \sim 1$), photons travel much faster than the sound speed and have larger mean free paths than particles, so energy transfer can be more efficient via radiation than via thermal conduction. Furthermore, we can use the Boltzmann number in the transport regime ($l > \lambda_p$) while the previous comparison would not be of any help because gas and radiation are decoupled so that the internal energy and radiative energy evolve independently. Comparing the fluxes instead of the energies shows that radiation-hydrodynamics is relevant for a wider number of applications than what Eq. 2.48 suggests. Let us take the example of molecular clouds, in which $l \sim 1$ pc, $\rho \sim 10^{-21}\,\mathrm{g\,cm^{-3}}$, $T \sim 10$ K, and $l/\lambda_p \equiv l\,\kappa\,\rho \sim 10^3$ for $\kappa = 5\,\mathrm{cm^2\,g^{-1}}$, so most of the radiation propagates in the transport regime. As one could expect from Eq. 2.48, $R \propto \rho$ so conduction becomes inefficient in the limit of a very low-density medium. In this case, the ratio R is $\sim 10^{-3}$, so even for $v \lesssim c$ the energy transport would be mainly radiative. This is actually worse because $v \ll c$ (with $v \sim c_s \sim 10^4\,\mathrm{cm\,s^{-1}}$), so $\mathrm{Bo} \ll 10^{-3}$, *i.e.* the energy transport by radiation is even more dominant over the conduction.

Radiation-hydrodynamics is therefore relevant for many astrophysical systems, such as accretions disks around massive protostars or molecular clouds.

2.3.2 Equations in the non-relativistic regime

As shown above, in the context of star formation radiative transfer equations should be coupled to the hydrodynamical ones. A question arises regarding the frame to evaluate the various physical quantities. Indeed, the fluid advection impacts the photon energy density it emits or interacts with, and its velocity affects radiation frequency via Doppler shift and aberration effects. On the other hand, in the fluid comoving frame, the absorption and extinction coefficients presented above are isotropic but it is no longer the case in the laboratory frame. For these reasons, the comoving frame has been chosen in the RAMSES implementations we have used. As a result, additional terms appear, that we have chosen to put on the right-hand side of the system 2.47 to highlight the hyperbolic nature of these equations (when the right-hand side is set

to zero). Lorentz transformations are performed to obtain radiative transfer equations in this frame (more details in Mihalas & Mihalas 1984).

After dropping terms of order smaller than $O(v/c)$, the system of equations governing non-viscous, radiating fluid under gravity is

$$\begin{cases} \partial_t \rho + & \boldsymbol{\nabla}.[\rho \mathbf{u}] & = 0, \\ \partial_t \rho \mathbf{u} + & \boldsymbol{\nabla}.[\rho \mathbf{u} \otimes \mathbf{u} + P\mathbb{I}] & = -\rho \boldsymbol{\nabla}\phi - \lambda \boldsymbol{\nabla} E_{\rm fld} + \kappa_{\rm P,\star} \mathbf{F}_{\rm M1}/{\rm c}, \\ \partial_t E + & \boldsymbol{\nabla}.[\mathbf{u}(E+P)] & = -\rho \mathbf{u} \cdot \boldsymbol{\nabla}\phi - \lambda \boldsymbol{\nabla} E_{\rm fld} \cdot \mathbf{u} - \kappa_{\rm P,fld} {\rm c}({\rm a_R} T^4 - E_{\rm fld}) + \kappa_{\rm P,\star} {\rm c} E_{\rm M1}, \\ \partial_t E_{\rm fld} + & \boldsymbol{\nabla}.[\mathbf{u} E_{\rm fld}] & = -\mathbb{P}_{\rm fld} : \boldsymbol{\nabla}\mathbf{u} + \boldsymbol{\nabla} \cdot \left(\dfrac{{\rm c}\lambda}{\kappa_{\rm R,fld}} \boldsymbol{\nabla} E_{\rm fld} \right) + \kappa_{\rm P,fld}\, {\rm c} \left({\rm a_R} T^4 - E_{\rm fld} \right), \\ \partial_t E_{\rm M1} + & \boldsymbol{\nabla} \cdot \mathbf{F}_{\rm M1} & = -\kappa_{\rm P,\star}\, {\rm c} E_{\rm M1} + \dot{E}^{\star}_{\rm M1}, \\ \partial_t \mathbf{F}_{\rm M1} + & {\rm c}^2 \boldsymbol{\nabla} \cdot \mathbb{P}_{\rm M1} & = -\kappa_{\rm P,\star}\, {\rm c} \mathbf{F}_{\rm M1}, \end{cases} \tag{2.50}$$

where $-\lambda \boldsymbol{\nabla} E_{\rm fld}$ is the radiative force.

One will notice that all the additional terms involve FLD moments but not M1 moments. To understand this, we must specify that the diffusion regime described by the FLD actually accounts for two specific behaviours: *static diffusion* and *dynamic diffusion*. In the former case, the photon diffusion timescale $\tau_{\rm d} \equiv l^2/\lambda_{\rm P}{\rm c}$ is shorter than the timescale of the flow $\tau_{\rm f} \equiv l/v$. In the latter, $\tau_{\rm f} < \tau_{\rm d}$ so the radiation energy is advected with the fluid: this is accounted for by the inclusion of the advection term $\boldsymbol{\nabla}.[\mathbf{u}E_{\rm fld}]$. The term $\mathbb{P}_{\rm fld} : \boldsymbol{\nabla}\mathbf{u}$ describes the work done by radiative pressure. In other words, in the dynamic diffusion regime new radiation transport terms appear, even for a non-relativistic flow (oppositely to what one might first think). However, in the *free-streaming* (optically-thin) limit assumed by the M1 model, the timescale for radiation to cross a distance l is only a function of the radiation speed $\tau_{\rm r} = l/{\rm c}$. Hence, for non-relativistic flows, like ours, no extra-term appears.

These are the equations we aim to solve at each timestep in the RAMSES adaptive-mesh refinement code. I will present it in the subsequent chapter, together with the implementation of the coupling between the FLD module and RAMSES-RT and its validation tests.

CHAPTER 3

RAMSES and the Hybrid Radiative Transfer method

Contents

THE IMPLEMENTATION OF THE HYBRID RADIATIVE TRANSFER METHOD in the RAMSES code is at the very heart of this thesis work and is the topic of this chapter. I first present the main characteristics of this code and how it solves the equations of hydrodynamics. The implementations of the Flux-Limited Diffusion module (FLD, Sect. 2.2.2) and the M1 method (see Sect. 2.2.3) within RAMSES are described. Then I present their coupling, which constitutes the so-called *hybrid method*. I will display its results in pure radiative transfer tests, using the pure FLD method for comparison and Monte-Carlo codes as reference. Its accuracy at computing the dusty gas temperature in various regimes of optical-thickness (definition in Sect. 2.1.3) will be demonstrated. Finally, the question of its performance and improvements, will be discussed.

3.1 The RAMSES code

RAMSES (Teyssier, 2002) is a cosmological adaptive-mesh refinement (AMR) parallel code. It can simulate N-body interactions via gravity of collisionless particles such as dark matter or stellar clusters, but possesses also a hydrodynamical solver for the gas, which is of main interest for us. It is written in Fortran 90 and the message passing interface (MPI) is adopted for parallel computing (with a domain decomposition based on the Peano-Hilbert curve). As opposed to Smooth Particle Hydrodynamical (SPH) codes (*e.g.*, PHANTOM, Bate et al. 1995), which follow the Lagrangean evolution of fluid particles, RAMSES is a grid-based code which uses a Eulerian scheme, and the mesh is fixed. RAMSES possesses a second-order Godunov method (see below), well-suited for capturing shocks or discontinuities. It uses a finite-volume approach, *i.e.* the variables are averaged over the cell volume, as opposed to finite difference methods (*e.g.* in the ZEUS code, Stone & Norman 1992), where variables are evaluated at a given set of points. Its N-body and hydrodynamical solvers, and AMR structure, make it a very versatile code to tackle a number of astrophysical problems. In our case, as I will show, the implementation of radiative transfer via moment methods takes full advantage of the way the hydrodynamical equations are solved in RAMSES.

3.1.1 The AMR structure

A wide range of phenomena has been studied with RAMSES, from the reionization by the first population of stars on cosmological scales, to galaxy formation and evolution, and star formation. The AMR method is precious in modelling these problems, as they involve a large dynamical range ($> 10^4$). Its original description in Berger & Oliger (1984) consists in nested grids composed of rectangular patches with different aspect ratios (depending on the flow geometry, on the memory...), and is called *patch-based*. RAMSES follows a different logic, with a *tree-based* AMR structure (Khokhlov, 1998), *i.e.* refinement occurs recursively from "parent cells" into "children cells", on a cell-by-cell basis.

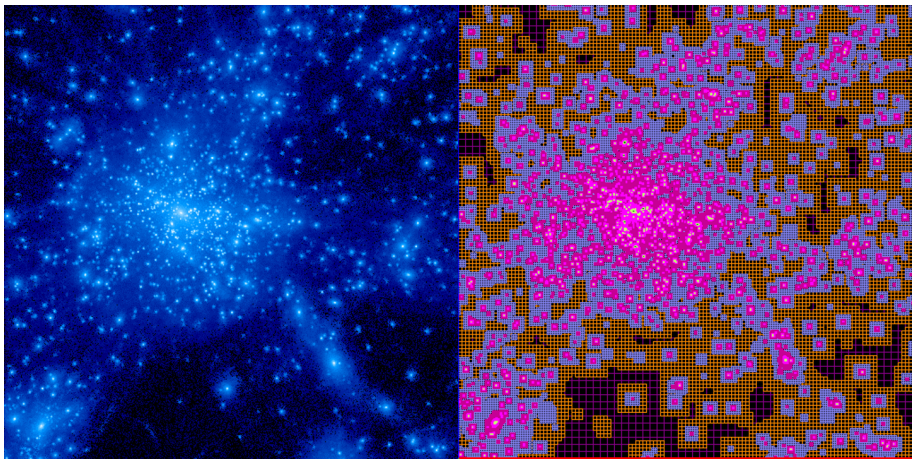

Figure 3.1: Illustration of the density field (left) and the grid (right) in a cosmological simulation. Credits: Romain Teyssier's lectures.

The basic element of RAMSES is an oct, a cube (in 3D) composed of 2^{dim} cells, where dim is the dimension. If the refinement level is labelled l, each oct is linked to its $l-1$ level parent cell and to its 2^{dim} children octs at level $l+1$ (left panel of Fig. 3.2). It also points to its $2 \times$ dim neighbooring parent cells, the oct faces. A cell with no children is called a *leaf* cell. The octs are sorted in a double linked list, each of them pointing to aforementioned cells and octs. This

forms a tree structure which facilitates the access to neighbouring cells, to compute gradients for example. The so-called *coarse* grid is defined as the lowest-resolution uniform Cartesian grid. It is composed of $2^{l_{\rm min}}$ elements in each direction, where $l_{\rm min}$ is the minimum level of refinement. As the simulation runs, the grid is refined on a cell-by-cell basis, depending on the user pre-defined criteria (density gradients, Jeans mass, geometrical constraints...), or de-refined. Two adjacent cells cannot vary by more than one level of refinement. The refinement is smoothed based on a free parameter, $n_{\rm expand}$. It sets the number of times a cubic smoothing operator is applied to mark the surrounding cells to be refined. An adaptive time-stepping strategy has been implemented, where each level is evolved on its own time step and all time steps must be synchronized (right panel of Fig. 3.2). Indeed, the time step constraint is generally more restrictive for smaller cells (see *e.g.*, Eq. 3.9). As shown in the right panel of Fig. 3.2, the cells of higher level are evolved first. If a single time step is chosen, low-resolution cells will be evolved on a much smaller time step than required, which is CPU time-consuming and can be avoided by using an adaptive time-stepping.

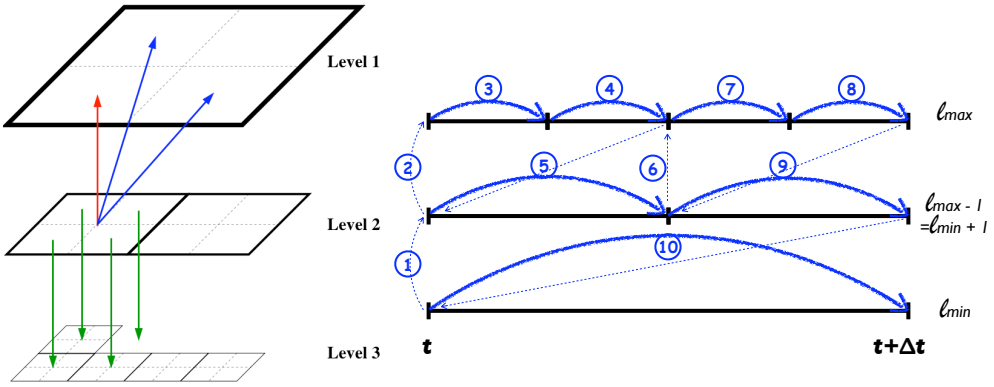

Figure 3.2: Left: AMR structure of RAMSES. Right: Scheme of the adaptive time-stepping on a three-level AMR structure. Credit: Romain Teyssier's lectures (left), Joakim Rosdahl's thesis (right).

3.1.2 Solving the Euler equations on a Cartesian grid

In the kinetic theory of gases, the Boltzmann equation describes the evolution of a particle distribution function in the phase-space. Euler equations (mass, momentum and energy conservation, at fluid scales), are moments of this equation in the limit of high collision rates, and read (for an inviscid flow)

$$\begin{cases} \partial_t \rho & + & \boldsymbol{\nabla}.[\rho \mathbf{u}] & = 0, \\ \partial_t \rho \mathbf{u} & + & \boldsymbol{\nabla}.[\rho \mathbf{u} \otimes \mathbf{u} + P \mathbb{I}] & = 0, \\ \partial_t E & + & \boldsymbol{\nabla}.[\mathbf{u}(E+P)] & = 0, \end{cases} \tag{3.1}$$

where ρ is the gas density, $\mathbf{u}$ is the velocity, P is the thermal pressure (well defined under the LTE hypothesis) and $E = \rho\varepsilon + \rho u^2/2$ is the total energy density, where ε is the specific internal energy. For this example we have not considered source terms (right-hand side) such as heating, nor external forces such as gravitational or radiative forces, in our case.

This system, as any hyperbolic system[1] of conservations laws can be written in the vector,

[1] A system in which a perturbed initial state does not affect all the spatial points instantenously but in a wave manner, with a finite propagation speed.

conservative form

$$\frac{\partial \mathbb{U}}{\partial t} + \nabla.\mathbb{F}(\mathbb{U}) = 0, \tag{3.2}$$

where $\mathbb{U} = [\rho, \rho\mathbf{u}, E]^{\mathrm{T}}$ and $\mathbb{F}$ is the flux vector and is a function of $\mathbb{U}$: $\mathbb{F}(\mathbb{U}) = [\rho\mathbf{u}, \rho\mathbf{u} \otimes \mathbf{u} + P\mathbb{I}, \mathbf{u}(E+P)]^{\mathrm{T}}$. The Jacobian of the flux function is defined as $\mathbb{J}(\mathbb{U}) = \partial\mathbb{F}(\mathbb{U})/\partial\mathbb{U}$. Equation 3.2 is a hyperbolic system of conservation laws, which goes together with the Jacobian being a diagonalizable matrix. The Jacobian's eigenvalues correspond to the characteristic wave speeds of the system.

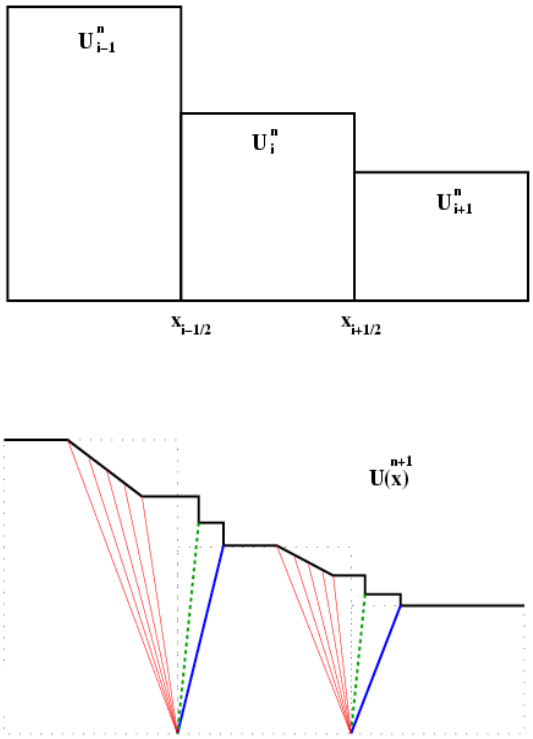

Figure 3.3: Top panel: Illustration of the initial conditions of the Riemann problem. The states $\mathbb{U}_i$ consist in constant piecewise states over the grid cells. Bottom panel: Solution of the Riemann problem for the Euler equations, involving a rarefaction wave (red), an entropy wave (contact discontinuity, green) and a shock (blue). Credits: Romain Teyssier's lectures.

Following the finite-volume method, one can write the discretized variable $\mathbb{U}_i^n$ (in 1D here) as

$$\mathbb{U}_i^n = \frac{1}{\Delta x} \int_{x_{i-1/2}}^{x_{i+1/2}} \mathbb{U}(x, t_n) dx, \tag{3.3}$$

using the temporal index n for t and $n+1$ for $t + \Delta t$, and i as the spatial index in the direction under consideration. We can integrate Eq. 3.2 over a time step $\Delta t = t_2 - t_1$ and length $\Delta x = x_2 - x_1$ (the volume in 3D)

$$\int_{x_1}^{x_2} \int_{t_1}^{t_2} \left(\partial_t \mathbb{U} + \nabla.\mathbb{F}(\mathbb{U})\right) dt dx = 0, \tag{3.4}$$

which leads to

$$\int_{x_1}^{x_2} (\mathbb{U}(t_2) - \mathbb{U}(t_1))\, dx + \int_{t_1}^{t_2} (\mathbb{F}(x_2) - \mathbb{F}(x_1))\, dt = 0. \tag{3.5}$$

In the first-order Godunov method the variables are evaluated forward in time and this system can be discretized in the explicit form

$$\frac{\mathbb{U}_i^{n+1} - \mathbb{U}_i^n}{\Delta t} + \frac{\mathbb{F}_{i+1/2}^{n+1/2} - \mathbb{F}_{i-1/2}^{n+1/2}}{\Delta x} = 0, \tag{3.6}$$

where $\mathbb{U}_i^n$ follows from 3.3 and $\mathbb{F}_{i\pm1/2}^{n+1/2}$ are the time-averaged intercell fluxes. This way, we obtain a conservative method, *i.e.* the strict conservation of the variables $\mathbb{U}$ is ensured. Moreover, discontinuities are well resolved because we compute flux differences and not derivatives, unlike finite-difference schemes. The time-averaged intercell fluxes are evaluated at the interface and are defined as (here for the interface $i + 1/2$)

$$\mathbb{F}_{i+1/2}^{n+1/2} = \frac{1}{\Delta t} \int_{t^n}^{t^{n+1}} \mathbb{F}(x_{i+1/2}, t) dt = \mathbb{F}^\star(\mathbb{U}_i^n, \mathbb{U}_{i+1}^n), \tag{3.7}$$

where $\mathbb{F}^\star(\mathbb{U}_i^n, \mathbb{U}_{i+1}^n)$ is called the Godunov flux. Even if the fluxes are not correct, Eq. 3.6 ensures a strict conservation of $\mathbb{U}$. Note that the fluxes are also averaged in space in the tranverse directions for multidimensional problems. It is clear from Eqs. 3.6 and 3.7 that the updated state $\mathbb{U}_i^{n+1}$ is given by

$$\mathbb{U}_i^{n+1} = \mathbb{U}_i^n + \frac{\Delta t}{\Delta x} \left(\mathbb{F}_{i+1/2}^{n+1/2} - \mathbb{F}_{i-1/2}^{n+1/2} \right). \tag{3.8}$$

Now, one needs to evaluate the fluxes at the interfaces as a function of time to compute 3.7. Let us recall that $\mathbb{F} = \mathbb{F}(\mathbb{U})$, and the intercell flux $\mathbb{F}(x_{i+1/2}, t) = \mathbb{F}(\mathbb{U}_{i+1/2}(t), t)$. The evaluation of $\mathbb{F}(x_{i+1/2}, t)$ requires the determination at a given time t of the intermediate state $\mathbb{U}_{i+1/2}(t)$ between two constant piece-wise states (the volume-averaged variables in each cell). This is called a *Riemann problem* (Fig. 3.3). The intermediate state $\mathbb{U}_{i+1/2}(t)$ is obtained from the left and right initial states and the wave speeds. In the simple case of the hydrodynamical advection equation, it involves one wave; for the Euler equations, three waves: a rarefaction wave, an entropy wave (contact discontinuity) and a shock. As mentioned above, each wave speed corresponds to an eigenvalue of the Jacobian.

Riemann solvers can be either exact or approximate. In the former case, a complex flux function is used and leads to an exact solution, but is computationally expensive. In the latter case, one can choose the number and nature of waves to be considered. The ubiquity of the form 3.2 has led to a number of functions to approximate the intercell flux (see, *e.g.*, Harten et al. 1983). We will see two examples of such solvers implemented in RAMSES in Sect. 3.3. An approximate solver is more diffusive, but still stable. It is also less expensive than an exact Riemann solver and allows one to have a better understanding of the flux function. It is generally easy to adapt to different physical problems as well, as we will see later with a Riemann solver widely used in hydrodynamics applied to the problem of radiative transfer. One of the Riemann solvers implemented in RAMSES is exact, in the sense that the solution is obtained iteratively, but this procedure is expensive so we will use approximate Riemann solvers throughout this thesis.

The scheme truncation error can be evaluated by the difference between the *modified equation* and the original equation. The modified equation is obtained from the Taylor expansion in space and time of the discretized equation Eq. 3.6 which introduces time and spatial derivatives. The accuracy order of the method is the leading order of the error. In some particular

cases (*e.g.*, the advection equation), the error term takes the form of a diffusion term, usually referred as *numerical diffusion*. One wants to avoid this numerical diffusion to overcome the system's physical diffusion. We have presented the first-order Godunov scheme, *i.e.* based on constant initial values, which is first-order accurate in space because the initial error is of order Δx. It is possible to show that first-order Godunov schemes are very diffusive, hence RAMSES incorporates a second-order scheme in space and time with a predictor-corrector scheme (Monotone Upstream-centered Scheme for Conservation Laws, or MUSCL, van Leer 1979). In this scheme, piecewise linear approximations are used instead of piecewise constant values for the initial condition of the Riemann problem (right-hand side of Eq. 3.7). These piecewise linear approximations are predicted states, obtained from a Taylor expansion in space and time with slope estimates. Because the cell length is introduced, the Riemann solution is no longer self-similar. Monotonicity of the solution has to be preserved, otherwise the obtained solution is oscillatory (unphysical). In that view, Total Variation Diminishing (TVD, Harten et al. 1983) schemes have been introduced, where the Total Variation stands for the sum of all the absolute differences between neighbouring cells. Various types of slope limiters are used to prevent the introduction of a local extremum by the piecewise linear approximations .

***Explicit* versus *implicit* schemes and the time step contraint**

Explicit schemes correspond to discretizing the differential equation using the variable at time t^n in all terms (except in the time derivative), as opposed to *implicit* schemes which take the variable at time t^{n+1}. Implicit schemes usually involve a large matrix inversion as we shall see below.

Meanwhile, explicit schemes are simpler but come with a cost. The Courant-Friedrichs-Levy (CFL) condition (Courant & Friedrichs, 1928) limits the time step of explicit schemes and states that no signal can cross more than one cell in one time step. In hydrodynamics, the signal speeds are given by u (the entropy wave), $u - c_s$ and $u + c_s$ (the shock and the rarefaction waves), where u is the fluid velocity and c_s the sound speed. Therefore, the time step Δt is restricted (in 1D) to

$$\Delta t_{\rm CFL} \leq {\rm C} \frac{\Delta x}{\max(\mid u - c_s \mid, \mid u + c_s \mid)}, \tag{3.9}$$

where ${\rm C} < 1$ is the Courant factor. This condition guarantees the scheme stability and accuracy. On the other hand, implicit schemes are inconditionally stable.

As we shall see, radiation transport is treated with an explicit solver in RAMSES-RT, and with an implicit solver in the FLD implementation.

Before focusing on the radiation-hydrodynamical modules that I have coupled together, let us briefly present the extension of the hydrodynamical solver of RAMSES to magneto-hydrodynamics that we use in the context of star formation in Chapter 4.

3.1.3 Magneto-hydrodynamics with ambipolar diffusion

The system 3.1 has to be modified to account for the presence of magnetic fields. We will also consider the non-perfect coupling between the gas and magnetic fields via one non-ideal process, namely ambipolar diffusion. The equations obtained give, in their conservative form

$$\begin{aligned}
\frac{\partial \rho}{\partial t} + \nabla \cdot [\rho \boldsymbol{u}] &= 0, \\
\frac{\partial \rho \boldsymbol{u}}{\partial t} + \nabla \cdot [\rho \boldsymbol{u} \otimes \boldsymbol{u} - \boldsymbol{B} \otimes \boldsymbol{B} + P_{\rm T} \mathbb{I}] &= 0, \\
\frac{\partial E_{\rm T}}{\partial t} + \nabla \cdot [\boldsymbol{u} \left(E_{\rm T} + P_{\rm T}\right) - (\boldsymbol{u} \cdot \boldsymbol{B}) \boldsymbol{B} - \boldsymbol{E}_{\rm AD} \times \boldsymbol{B}] &= 0,
\end{aligned} \tag{3.10}$$

where B is the magnetic field. The total pressure is modified by the magnetic pressure

$$P_{\rm T} = P + \frac{\boldsymbol{B}.\boldsymbol{B}}{2}, \tag{3.11}$$

where the pressure P is given by the ideal gas equation of state, and the total energy is

$$E_{\rm T} = \rho\varepsilon + \rho\frac{\boldsymbol{u}.\boldsymbol{u}}{2} + \frac{\boldsymbol{B}.\boldsymbol{B}}{2}. \tag{3.12}$$

$\boldsymbol{E}_{\rm AD}$ is the ambipolar electromagnetic force (EMF) and is defined as

$$\boldsymbol{E}_{\rm AD} = \frac{\eta_{\rm AD}}{B^2}[(\nabla \times \boldsymbol{B}) \times \boldsymbol{B}] \times \boldsymbol{B}, \tag{3.13}$$

where $\eta_{\rm AD}$ is the ambipolar diffusion resistivity. The ideal MHD limit is recovered for $\eta_{\rm AD} = 0$. The Lorentz force, which does not appear explicitly in the conservative form of the momentum equation, is given by

$$\boldsymbol{F}_{\rm L} = (\nabla \times \boldsymbol{B}) \times \boldsymbol{B} = (\boldsymbol{B}.\nabla)\boldsymbol{B} - \nabla\frac{\boldsymbol{B}.\boldsymbol{B}}{2}, \tag{3.14}$$

where the first term can be described as a *magnetic tension* force while the second one is a *magnetic pressure gradient* force.

The induction equation for the temporal evolution of the magnetic field and the solenoidal condition (absence of monopoles) are given by

$$\begin{aligned} \frac{\partial \boldsymbol{B}}{\partial t} - \nabla \times [\boldsymbol{u} \times \boldsymbol{B} + \boldsymbol{E}_{\rm AD}] = 0, \\ \nabla \cdot \boldsymbol{B} = 0. \end{aligned} \tag{3.15}$$

Let us see how RAMSES explicitly solves these equations (Fromang et al. 2006, Masson et al. 2012). We start from the ideal MHD case, for which $\boldsymbol{E}_{\rm AD} = 0$, assuming a full ionization fraction so that the plasma and the magnetic field are perfectly coupled together. In this case, the field is advected with the velocity field and the magnetic field lines are often referred as *frozen* onto the plasma.

The solenoidal condition (Eq. 3.15) is ensured to machine round-off error by a Constraint Transport (CT) method (Evans & Hawley 1988, Teyssier et al. 2006). Having a non-zero divergence would lead to a spurious force parallel to the field. In this CT method, the induction equation is written into integral form as

$$\frac{\partial}{\partial t}\iint \boldsymbol{B} \cdot d\boldsymbol{S} = \iint \nabla \times (\mathbf{u} \times \mathbf{B}) \cdot d\boldsymbol{S} = \oint \boldsymbol{E} \cdot d\boldsymbol{l}, \tag{3.16}$$

where $\boldsymbol{E}$ is the ideal EMF defined as $\boldsymbol{E} = \boldsymbol{u} \times \boldsymbol{B}$. In constrast with the finite-volume approach used for hydrodynamical variables, the magnetic field components must be evaluated on the cell faces, as in a *finite-surface* method. On a standard 3D Cartesian grid, writing the cell center coordinates as (x_i, y_j, z_k) and the faces normal to the x-direction as $x_{i\pm1/2}$, the x component of the magnetic field vector $\boldsymbol{B}$ is surface-averaged as

$$B_{x,i-1/2,j,k} = \frac{1}{\Delta y \Delta z}\int_{y_{i-1/2}}^{y_{i+1/2}}\int_{z_{i-1/2}}^{z_{i+1/2}} B_x(x_{i-1/2}, y', z')dy', dz', \tag{3.17}$$

and the other components are obtained by circular permutations (see Fig.3.4). The induction equation can be written in conservative form by integration in space and time in a similar manner as 3.5, and yields, for the component $B_{x,i-1/2,j,k}$,

$$\frac{B^{n+1}_{x,i-1/2,j,k} - B^{n}_{x,i-1/2,j,k}}{\Delta t} - \frac{E^{n+1/2}_{z,i-1/2,j+1/2,k} - E^{n+1/2}_{z,i-1/2,j-1/2,k}}{\Delta y} + \frac{E^{n+1/2}_{y,i-1/2,j,k+1/2} - E^{n+1/2}_{y,i-1/2,j,k-1/2}}{\Delta z} = 0, \tag{3.18}$$

where the components of the EMF **E** are edge-averaged (Fig.3.4). Similar expressions are derived for B_y^{n+1} and B_z^{n+1}. The EMF is the analog of the flux function for Euler systems. By updating conservatively the surface-averaged magnetic fields, the total flux $\nabla \cdot \mathbf{B}$ across each cell vanishes exactly. The determination of the time-centered, edge-averaged EMF is done via two steps: a predictor step, then a corrector step, and requires to solve a 2D Riemann problem (more details in Fromang et al. 2006).

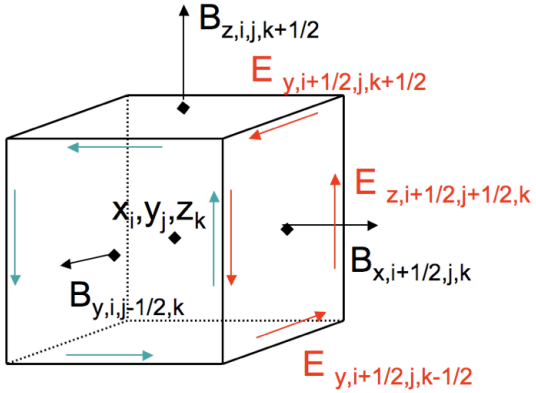

Figure 3.4: Illustration of the surface-averaged components of **B** and edge-averaged components of **E** for the Constrained Transport method. Credits: Romain Teyssier's lectures.

The extension of the Euler system to MHD (Eq. 3.10) remains hyperbolic. It can be written in the conservative form (similar to 3.2)

$$\frac{\partial \mathbb{U}}{\partial t} + \frac{\partial \mathbb{F}}{\partial x} + \frac{\partial \mathbb{G}}{\partial y} + \frac{\partial \mathbb{H}}{\partial z} = 0, \tag{3.19}$$

where

$$\mathbb{U} = \begin{pmatrix} \rho \\ \rho u_x \\ \rho u_y \\ \rho u_z \\ E_{\rm T} \end{pmatrix}, \qquad \mathbb{F} = \begin{pmatrix} \rho u_x \\ \rho u_x^2 + P_{\rm T} - B_x^2 \\ \rho u_x u_y - B_x B_y \\ \rho u_x u_z - B_x B_z \\ (E_{\rm T} + P_{\rm T}) u_x - B_x (\mathbf{B} \cdot \mathbf{u}) \end{pmatrix}, \tag{3.20}$$

and $\mathbb{G}$ and $\mathbb{H}$ are obtained by circular permutations (Fromang et al., 2006). The Jacobian matrix $\mathbb{J}(\mathbb{U}) = \partial \mathbb{F}(\mathbb{U})/\partial \mathbb{U}$ has seven eigenvalues λ_{1-7}, each of them corresponding to the speed of a physical wave:

- two fast magnetosonic waves (longitudinal, with variation in pressure and density, correlated with the magnetic field): $\lambda_{1,7} = u \pm v_{\rm f}$,
- two Alfvén waves (transverse, no variation in pressure and density): $\lambda_{2,6} = u \pm v_{\rm A}$,
- two slow magnetosonic waves (longitudinal, with variation in pressure and density, anticorrelated with the magnetic field): $\lambda_{3,5} = u \pm v_{\rm s}$,
- one entropy wave (contact discontinuity): $\lambda_4 = u$,

where $v_{\rm s}$, $v_{\rm f}$ and $v_{\rm A}$ are the slow, fast magnetosonic and Alfvén velocities, respectively. RAMSES includes several MHD Riemann solvers. The simplest (and most robust) one is the Lax-Friedrich solver, which retains the two fastest waves. The best approximate solver is the HLLD

solver (Miyoshi & Kusano, 2005), which uses five waves (all but the slow magnetosonic waves). A linear Roe solver is also implemented, it retains the seven waves but requires the linearization of the Jacobian and is therefore not adapted to strong density gradients.

In the ideal MHD limit, the resistive term $\nabla \times \mathbf{E}_{\rm AD}$ in 3.15 is neglected. The validity of this assumption relies on the value of the magnetic Reynolds number (adapted to ambipolar diffusion here), which computes the ratio of the advective to the diffusive terms (using Eq. 3.13)

$$R_{\rm m,AD} \equiv \frac{\|\nabla \times (\mathbf{u} \times \mathbf{B})\|}{\|\nabla \times \mathbf{E}_{\rm AD}\|} \sim \frac{ul}{\eta_{\rm AD}}, \tag{3.21}$$

where u and l are the plasma typical speed and length scales. When the ionization fraction is low, the resistive term is not negligible anymore.

The non-ideal MHD equations are obtained by first dividing the fluid into three phases: the ions, neutrals and electrons (Mestel & Spitzer, 1956). For each phase, the momentum conservation law is written to account for their collisions, depending on their relative density and velocity. Assuming that the fluid is quasi-neutral leads to the ambipolar diffusion. In this case, electrons and ions momentum is neglected because of their low mass and low density (low ionization fraction), respectively. The Lorentz force is felt by the ions, which transmit it to the neutrals via friction, while the neutrals diffuse through the ions.

In the ideal MHD formalism written above, we have not distinguished between the ions and the neutrals velocities because both species were coupled together. We have used the ions velocity for the induction equation and the neutrals velocity for the hydrodynamical equations. The ambipolar EMF (Eq. 3.13) comes from the drift between the ions (nearly comoving with the electrons) and the neutrals. The new induction equation is obtained by first writing the ions velocity $\mathbf{v}_{\rm i}$ as $\mathbf{v}_{\rm i} = \mathbf{v}_{\rm n} + \mathbf{v}_{\rm i} - \mathbf{v}_{\rm n}$, where $\mathbf{v}_{\rm n} = \mathbf{u}$ denotes the neutrals velocities, then assuming that the magnetic field is frozen onto the plasma of ions and electrons, *i.e.*

$$\frac{\partial \boldsymbol{B}}{\partial t} - \nabla \times [\boldsymbol{v}_n \times \boldsymbol{B} + (\boldsymbol{v}_i - \boldsymbol{v}_n) \times \boldsymbol{B}] = \frac{\partial \boldsymbol{B}}{\partial t} - \nabla \times [\mathbf{u} \times \boldsymbol{B} + \mathbf{E}_{\rm AD}] = 0. \tag{3.22}$$

Then, assuming the balance between the Lorentz force and the ions-neutrals drag force (see *e.g.*, Shu et al. 1987)

$$f_{\rm d} = (\mathbf{v}_{\rm i} - \mathbf{v}_{\rm n}) \gamma_{\rm AD}\, \rho_{\rm i}\, \rho = \mathbf{F}_{\rm L}, \tag{3.23}$$

one obtains the ambipolar EMF as

$$\mathbf{E}_{\rm AD} = (\mathbf{v}_{\rm i} - \mathbf{v}_{\rm n}) \times \mathbf{B} = \frac{1}{\gamma_{\rm AD}\, \rho_{\rm i}\, \rho} \mathbf{F}_{\rm L} \times \mathbf{B}, \tag{3.24}$$

where $\rho_{\rm i}$ is the ions density, and $\gamma_{\rm AD}$ is the drift coefficient between ions and neutrals due to ambipolar diffusion. The drift coefficient is linked to the diffusion coefficient via the Alfvén velocity, $\eta_{\rm AD} = v_{\rm A}^2 / (\gamma_{\rm AD}\, \rho_{\rm i})$. The EMF impacts the magnetic field evolution (Eq. 3.22), but it also heats the fluid as

$$\rho T \frac{ds}{dt} = \frac{\|\mathbf{F}_{\rm L}\|^2}{\gamma_{\rm AD}\, \rho_{\rm i}\, \rho}, \tag{3.25}$$

where s is the gas entropy.

It has been added to the ideal MHD EMF (Masson et al., 2012) determined by the 2D Riemann problem mentioned above (Teyssier et al. 2006, Fromang et al. 2006). The resistivities are pre-computed using a chemical network to calculate the equilibrium abundances of the molecules (neutrals) and dust grains (charged particles) in conditions of pre-stellar core collapse (Marchand et al., 2016).

The time step is severely affected by ambipolar diffusion. Indeed, such a diffusion process involves a second spatial derivative, hence the time step required for stability scales as $t_{\rm AD} \propto \Delta x^2/\eta_{\rm AD}$, which can become problematic at high resolution, but there are means to speed up the calculation (Masson et al., 2012).

The two other non-ideal MHD effects are the Ohmic dissipation (collision with electrons) and the Hall effect (non-collisional drift). These are likely to dominate at higher densities than considered throughout this work (Marchand et al., 2016) and are therefore neglected.

We will now present the radiation-hydrodynamical solvers of RAMSES, without magnetic fields. However, the extension to radiation-magneto-hydrodynamics does not present difficulties because the magnetic and radiation fields are not directly coupled.

3.2 The Flux-Limited Diffusion implementation

Here I present the main features of the FLD solver (Commerçon et al., 2011b). It has been mainly used in low- and high-mass star formation calculations (*e.g.*, Commerçon et al. 2011a, Vaytet et al. 2018). I will emphasize on the module part which will be coupled to RAMSES-RT. The FLD method is presented in Sect. 2.2.2, its coupling to hydrodynamics implies the addition of one equation to the hyperbolic system of hydrodynamics: the conservation of radiative energy. In the comoving frame, the system for the radiative fluid reads

$$\begin{cases} \partial_t \rho \ + \boldsymbol{\nabla}.[\rho \mathbf{u}] & = 0, \\ \partial_t \rho \mathbf{u} + \boldsymbol{\nabla}.[\rho \mathbf{u} \otimes \mathbf{u} + P\mathbb{I}] & = -\lambda \boldsymbol{\nabla} E_{\rm fld}, \\ \partial_t E_{\rm T} + \boldsymbol{\nabla}.[\mathbf{u}(E_{\rm T}+P)] & = -\mathbb{P}_{\rm fld} : \boldsymbol{\nabla}\mathbf{u} - \lambda \boldsymbol{\nabla} E_{\rm fld} \cdot \mathbf{u}, \\ \partial_t E_{\rm fld} + \boldsymbol{\nabla}.[\mathbf{u} E_{\rm fld}] + \mathbb{P}_{\rm fld} : \boldsymbol{\nabla}\mathbf{u} & = \boldsymbol{\nabla} \cdot \left(\dfrac{c\lambda}{\kappa_{\rm R,fld}\,\rho} \boldsymbol{\nabla} E_{\rm fld} \right) + \kappa_{\rm P,fld}\,\rho\, c \left(a_{\rm R} T^4 - E_{\rm fld} \right), \end{cases} \tag{3.26}$$

where $-\lambda \boldsymbol{\nabla} E_{\rm fld}$ is the radiative force, $-\lambda \boldsymbol{\nabla} E_{\rm fld} \cdot \mathbf{u}$ is the work done by this force and $-\mathbb{P}_{\rm fld} : \boldsymbol{\nabla}\mathbf{u}$ is the work done by radiative pressure. We choose to re-write κ as $\kappa\rho$, where κ stands now for a cross-section per unit of mass, as it is usually given under this form by opacity tables from laboratory experiments (see Fig. 3.7). The three conservative variables are the density ρ, the momentum $\rho\mathbf{u}$ and the total energy $E_{\rm T} = \rho\varepsilon + \rho\mathbf{u}^2/2 + E_{\rm fld}$ which now accounts for the radiative energy $E_{\rm fld}$ in addition to the gas kinetic energy and internal energy. This system needs two closure relations, one for the radiation and one for the gas. It is closed by the equation of state, of ideal gases in our case, and by the relation between the radiative pressure and radiative energy.

Commerçon et al. (2011b) have chosen to split the problem into two substeps. The first one is the conservative scheme that RAMSES operates with a MUSCL (explicit) method, except that the fluid has an additional radiative pressure and energy. The second one solves the radiative diffusion and gas-radiation coupling implicitly. We will briefly present the first one, and focus in more detail on the second one, which we have modified for our hybrid method.

3.2.1 The explicit step for the conservative part

The MUSCL scheme is itself decomposed into two successive steps. A first reason for this is that the computation of the flux-limiter λ requires the neighbouring cells (since it depends on a radiative energy gradient), which is not practical within this scheme. Therefore, λ is decomposed as $\lambda = 1/3 + (\lambda - 1/3)$. The first term describes an optically-thick regime where the radiative pressure is isotropic as $\mathbb{P}_{\rm fld} = 1/3 E_{\rm fld}\mathbb{I}$ (Eddington approximation), while the second term is a correction to this approximation and is written as a source term. The second

reason is that it broadens the wave fan for the Riemann problem and the radiative pressure effects are undoubtedly accounted for. More generally, the radiative pressure is written as $\mathbb{P}_{\rm fld} = \lambda E_{\rm fld}\mathbb{I}$. We refer the reader to Commerçon et al. (2011b) for the modified system of equations and its explicit integration. This way, the system of equations can be written as

$$\left\{\begin{array}{rl} \partial_t\rho \ + \boldsymbol{\nabla}[\rho\mathbf{u}] & = 0, \\ \partial_t\rho\mathbf{u} + \boldsymbol{\nabla}[\rho\mathbf{u}\otimes\mathbf{u} + (P+1/3E_{\rm fld})\mathbb{I}] & = -\rho\boldsymbol{\nabla}\phi - (\lambda-1/3)\boldsymbol{\nabla}E_{\rm fld}, \\ \partial_t E_{\rm T} + \boldsymbol{\nabla}[\mathbf{u}(E_{\rm T}+P+1/3E_{\rm fld})] & = -\rho\mathbf{u}\cdot\boldsymbol{\nabla}\phi - (\lambda-1/3)(\boldsymbol{\nabla}E_{\rm fld}\cdot\mathbf{u} + E_{\rm fld}\boldsymbol{\nabla}:\mathbf{u}), \\ \partial_t E_{\rm fld} + \boldsymbol{\nabla}[\mathbf{u}E_{\rm fld}] & = -\mathbb{P}_{\rm fld}:\boldsymbol{\nabla}\mathbf{u} + \boldsymbol{\nabla}\cdot\left(\dfrac{c\lambda}{\kappa_{\rm R,fld}\rho}\boldsymbol{\nabla}E_{\rm fld}\right) + \kappa_{\rm P,fld}\rho c\left(a_{\rm R}T^4 - E_{\rm fld}\right). \end{array}\right. \tag{3.27}$$

The left-hand side of 3.26 is a hyperbolic system $\partial_t\mathbb{U} + \boldsymbol{\nabla}.\mathbb{F}(\mathbb{U}) = 0$ with

$$\mathbb{U} = \begin{pmatrix} \rho \\ \rho\mathbf{u} \\ E_{\rm T} \\ E_{\rm fld} \end{pmatrix}, \qquad \mathbb{F} = \begin{pmatrix} \rho\mathbf{u} \\ \rho\mathbf{u}\otimes\mathbf{u} + (P+1/3E_{\rm fld})\mathbb{I} \\ \mathbf{u}(E_{\rm T}+P+1/3E_{\rm fld}) \\ \mathbf{u}E_{\rm fld} \end{pmatrix}. \tag{3.28}$$

Due to this decomposition, the maximum wave speed is $u + \sqrt{\gamma\frac{P}{\rho} + \frac{4E_{\rm fld}}{9\rho}}$ where $\gamma\frac{P}{\rho}$ is the usual sound speed, and the final term comes from the isotropic and maximal radiative pressure. Therefore, the CFL condition ensuring stability and accuracy applies to this "modified" sound speed as

$$\Delta t_{\rm CFL} \leq {\rm C}\frac{\Delta x}{u + \sqrt{\gamma\frac{P}{\rho} + \frac{4E_{\rm fld}}{9\rho}}}. \tag{3.29}$$

After solving the hyperbolic system, the solution is corrected to relax the Eddington approximation by integrating the following source terms

$$f_{\rm ne} = \begin{pmatrix} 0 \\ -(\lambda-1/3)\boldsymbol{\nabla}E_{\rm fld} \\ -(\lambda-1/3)(\boldsymbol{\nabla}E_{\rm fld}\cdot\mathbf{u} + E_{\rm fld}\boldsymbol{\nabla}:\mathbf{u}) \\ -\mathbb{P}_{\rm fld}:\boldsymbol{\nabla}\mathbf{u} \end{pmatrix}. \tag{3.30}$$

3.2.2 The implicit step for gas-radiation coupling and diffusion

The gas-radiation coupling term $\kappa_{\rm P,fld}\rho c\left(a_{\rm R}T^4 - E_{\rm fld}\right)$ and the diffusion term $\boldsymbol{\nabla}\cdot\left(\frac{c\lambda}{\kappa_{\rm R,fld}\rho}\boldsymbol{\nabla}E_{\rm fld}\right)$ are accounted for in the following implicit scheme. In fact, the associated timescales can be much shorter than the hydrodynamical one. The comparison between the diffusion and the flow advection timescales has been discussed in Sect. 2.3. The gas-radiation coupling timescale is $\tau_{\rm g-r} \equiv 1/(\kappa\rho c)$. For typical values of a collapse calculation, $\kappa\sim1\,{\rm cm^2\,g^{-1}}$ and $\rho\sim10^{-15}\,{\rm g\,cm^{-3}}$ this gives $\tau_{\rm g-r}\sim10^3$ s while the flow advection timescale is $l/v\sim10^8$ s for $l\sim1$ AU (a typical cell size) and $v\sim1\,{\rm km\,s^{-1}}$. This justifies the use of an implicit, hence unconditionally stable scheme, no matter the time step.

The system to be solved is

$$\left\{\begin{array}{rl} \partial_t E_{\rm fld} - \boldsymbol{\nabla}\cdot\left(\dfrac{c\lambda}{\kappa_{\rm R,fld}\rho}\boldsymbol{\nabla}E_{\rm fld}\right) & = +\kappa_{\rm P,fld}\,\rho\,c\left(a_{\rm R}T^4 - E_{\rm fld}\right) \\ \dfrac{\partial e}{\partial t} & = -\kappa_{\rm P,fld}\,\rho\,c\left(a_{\rm R}T^4 - E_{\rm fld}\right). \end{array}\right. \tag{3.31}$$

We write $e = C_v T$ and discretize these equations implicitly with respect to T and $E_{\rm fld}$, *i.e.*

$$\begin{cases} \dfrac{E_{\rm fld}^{n+1} - E_{\rm fld}^{n}}{\Delta t} - \boldsymbol{\nabla} \cdot \left(\dfrac{c\lambda^n}{\kappa_{\rm R,fld^n} \rho^n} \boldsymbol{\nabla} E_{\rm fld}^{n+1} \right) = +\kappa_{\rm P,fld}^n \rho^n c \left(a_R (T^{n+1})^4 - E_{\rm fld}^{n+1} \right) \\ \dfrac{C_v T^{n+1} - C_v T^n}{\Delta t} = -\kappa_{\rm P,fld}^n \rho^n c \left(a_R (T^{n+1})^4 - E_{\rm fld}^{n+1} \right). \end{cases} \tag{3.32}$$

Note that the heat capacity C_v is assumed to be constant over the time step Δt. We want to express $E_{\rm fld}^{n+1}$ and T^{n+1} as functions of all the other variables at time t. Moreover, it is clear that the spatial derivative will introduce the radiative energy from neighbouring cells.

First, this system is difficult to invert because of the nonlinear term $(T^{n+1})^4$. Commerçon et al. (2011b) have opted for a first-order expansion of this term, assuming small changes within one time step, so that

$$\begin{aligned} (T^{n+1})^4 &= (T^n + \Delta T)^4 = (T^n)^4 (1 + \Delta T / T^n)^4 \\ &\approx (T^n)^4 + 4 \frac{\Delta T}{T^n} (T^n)^4 = (T^n)^4 + 4 T^{n+1} (T^n)^3 - 4 (T^n)^4 = 4 T^{n+1} (T^n)^3 - 3 (T^n)^4. \end{aligned} \tag{3.33}$$

We can use it in Eq. 3.32 to obtain T_i^{n+1} (in the cell of index i) as a function T_i^n and $E_{{\rm fld},i}^{n+1}$ in the same cell,

$$T_i^{n+1} = \frac{C_v T_i^n + \Delta t \, \kappa_{{\rm P},i}^n \rho_i^n c \left(3 a_R (T_i^n)^4 + E_{{\rm fld},i}^{n+1} \right)}{C_v + 4 \Delta t \, \kappa_{{\rm P},i}^n \rho_i^n c \, a_R (T_i^n)^3}. \tag{3.34}$$

Discretizing the radiative energy equation in the $x-$direction, one obtains

$$\begin{aligned} E_{{\rm fld},i}^{n+1} - E_{{\rm fld},i}^n + E_{{\rm fld},i}^{n+1} (C_{i-1/2} + C_{i+1/2}) - E_{{\rm fld},i-1}^{n+1} C_{i-1/2} - E_{{\rm fld},i+1}^{n+1} C_{i+1/2} \\ = \Delta t \, \kappa_{{\rm P},i}^n \rho_i^n c \, (a_R (4 (T_i^n)^3 T_i^{n+1} - 3 (T_i^n)^4) - E_{{\rm fld},i}^{n+1}), \end{aligned} \tag{3.35}$$

where we have introduced

$$C_i \equiv \Delta t \frac{c \, \lambda_i^n}{\kappa_{{\rm R},i}^n \rho_i^n \, \Delta x_i^2}, \tag{3.36}$$

and used the constant cell size $\Delta x_i = \Delta x_{i \pm 1/2} = \Delta x_{i \pm 1}$ on a given AMR level. Replacing 3.34 in 3.35 and introducing

$$\omega_i = \kappa_{{\rm P},i}^n \rho_i^n c \, \Delta t, \tag{3.37}$$

we finally have

$$\begin{aligned} -E_{{\rm fld},i-1}^{n+1} C_{i-1/2} + E_{{\rm fld},i}^{n+1} \left[1 + (C_{i-1/2} + C_{i+1/2}) + \omega_i \left(1 - \frac{4 \omega_i a_R (T_i^n)^3}{C_v + 4 \omega_i a_R (T_i^n)^3} \right) \right] - E_{{\rm fld},i+1}^{n+1} C_{i+1/2} = \\ E_{{\rm fld},i}^n + \frac{\omega_i a_R (T_i^n)^3}{C_v + 4 \omega_i a_R (T_i^n)^3} C_v T_i^n. \end{aligned} \tag{3.38}$$

This equation is equivalent to $Ax = b$ where A is a matrix of size N (where N is the total number of cells) and x a vector containing the radiative energy values in each cell at time $n+1$. Solving this equation requires the inversion of the tridiagonal (in 1D) matrix A (since the equation on cell i involves its neighboors $i-1$ and $i+1$), which is done via a Conjugate Gradient algorithm. Convergence occurs within a maximum of $\sqrt{N}$ steps, and this can be considerably reduced by choosing particular initial conditions, so-called *matrix preconditionning*. Afterwards, gas temperature is updated via Eq. 3.34. Note that the input of the implicit scheme, *i.e.* the variables at time n, are the variables obtained after the explicit step. The FLD method is done level-by-level,

with an adaptive time-stepping strategy (Commerçon et al., 2014).

We will come back to this implicit step to build our hybrid approach. Our other focus is on the M1 method for radiation-hydrodynamics implemented in RAMSES-RT.

3.3 RAMSES-RT

The radiation-hydrodynamical implementation RAMSES-RT (Rosdahl et al., 2013) relies on the M1 closure relation, presented in Sect. 2.2.3. It has been used in the cosmological context of reionization, treating the radiation transport, absorption and emission, but also ionization of hydrogen and helium.

In their frequency-averaged form, the equations we aim to solve are the radiative energy and radiative flux conservation equations with stellar sources, *i.e.*

$$\begin{cases} \partial_t E_{\rm M1} + & \boldsymbol{\nabla}\cdot\mathbf{F}_{\rm M1} & = -\kappa_{\rm P}\,{\rm c}E_{\rm M1} + \dot{E}^{\star}_{\rm M1}, \\ \partial_t \mathbf{F}_{\rm M1} + & {\rm c}^2\boldsymbol{\nabla}\cdot\mathbb{P}_{\rm M1} & = -\kappa_{\rm P}\,{\rm c}\mathbf{F}_{\rm M1}. \end{cases} \tag{3.39}$$

The module is divided in three steps: the radiation transport step, the injection step (from the stellar sources, in our case) and the thermochemistry step (gas-radiation coupling and ionization). These are done level-by-level.

3.3.1 Radiation transport

The system of equations for radiation transport[2] is similar to 2.42 with the righ-hand side terms set to zero (no absorption, no emission), *i.e.*

$$\begin{cases} \dfrac{\partial E_{\rm M1}}{\partial t} + & \boldsymbol{\nabla}\cdot\mathbf{F}_{\rm M1} = 0, \\ \dfrac{\partial \mathbf{F}_{\rm M1}}{\partial t} + {\rm c}^2\boldsymbol{\nabla}\cdot\mathbb{P}_{\rm M1} = 0. \end{cases} \tag{3.40}$$

It can be written in the conservative form $\partial_t\mathbb{U} + \boldsymbol{\nabla}.\mathbb{F}(\mathbb{U}) = 0$ (same hyperbolic form as the hydrodynamical equations 3.2) where $\mathbb{U} = [E_{\rm M1}, \mathbf{F}_{\rm M1}]$ and $\mathbb{F}(\mathbb{U}) = [\mathbf{F}_{\rm M1}, {\rm c}^2\mathbb{P}_{\rm M1}]$ is the flux vector. Obtaining the flux requires to solve a Riemann problem. Following the work of González et al. (2007) and Aubert & Teyssier (2008), two flux functions have been implemented in RAMSES-RT. First, the Harten-Lax-van Leer (HLL, Harten et al. 1983) flux function reads

$$(\mathbb{F}_{\rm HLL})^n_{i+1/2} = \frac{\lambda^+\mathbb{F}^n_i - \lambda^-\mathbb{F}^n_{i+1} + \lambda^+\lambda^-(\mathbb{U}^n_{i+1} - \mathbb{U}^n_i)}{\lambda^+ - \lambda^-}, \tag{3.41}$$

where $\lambda^+ = \max(0, \lambda^{\rm max}_i, \lambda^{\rm max}_{i+1})$ and $\lambda^- = \min(0, \lambda^{\rm min}_i, \lambda^{\rm min}_{i+1})$ are respectively the maximum and minimum eigenvalues of the Jacobian $\partial\mathbb{F}(\mathbb{U})/\partial\mathbb{U}$. These are read from the tabulated values of González et al. (2007). As explained above, Jacobian eigenvalues correspond to the speed of physical waves. The second flux function is the Global-Lax-Friedrich (GLF) function, equal to

$$(\mathbb{F}_{\rm GLF})^n_{i+1/2} = \frac{\mathbb{F}^n_i + \mathbb{F}^n_{i+1}}{2} - \frac{\rm c}{2}(\mathbb{U}^n_{i+1} - \mathbb{U}^l_i). \tag{3.42}$$

It corresponds to the HLL function with $\lambda^- = -{\rm c}$ and $\lambda^+ = {\rm c}$, the maximum wave speed being the speed-of-light. As a consequence of using these maximal wave speeds, the radiation transport is more diffusive than with the HLL function, whose main asset is its ability to conserve

[2]Radiative quantities in RAMSES-RT are mainly expressed in number of photons, so here we convert it into a radiative energy for readability with respect to the FLD module equations. This is done via $E_{\rm M1} = N_{\rm M1}e_\gamma$ where $N_{\rm M1}$ is the number of photons and e_γ is the mean energy of the photon group considered.

the radiation direction. However, the isotropy around radiating sources (such as stars) is better modelled with the GLF function, while the HLL function favors the transport along the grid axes (Rosdahl et al., 2013). For this reason, we have chosen the GLF function in this work.

3.3.2 Radiation injection

Radiative energy is emitted by stellar sources in the case of star-formation simulations (active galactic nuclei in galaxy simulations), modelled as point-like particles or extended over a given volume. This step simply consists in solving the equation

$$\frac{\partial E_{\mathrm{M1},i}}{\partial t} = \dot{E}^{\star}_{\mathrm{M1},i}, \tag{3.43}$$

where $\dot{E}^{\star}_{\mathrm{M1},i}$ is the volumic injection rate of radiative energy in the cell of index i, which comes from subgrid models of radiating sources. In the simplest case of an isotropic source, the updated radiative energy is given as

$$E^{n+1}_{\mathrm{M1},i} = E^{n}_{\mathrm{M1},i} + \Delta t \dot{E}^{\star}_{\mathrm{M1},i}, \tag{3.44}$$

where Δt is the time step. No radiative flux is injected during this step. The flux will be updated via the photon transport step presented above.

3.3.3 Gas-radiation coupling

This is part of a thermochemistry step where absorption, emission and ionization are dealt with. Momentum transfer from photons to the gas has been added afterwards (Rosdahl & Teyssier, 2015). In our approach, radiation absorption/emission are done with the FLD solver, except for stellar radiation. Moreover, ionizing radiation plays a role at a later stage of massive star formation than our aim (Kuiper & Hosokawa, 2018), hence the treatment of ionization is beyond the scope of this work. Since ionization is neglected here, the only sources of M1 emission are the stellar sources presented previously. Hence, we will only detail here how absorption is taken care of. The system to be solved simply is

$$\begin{aligned} \frac{\partial E_{\mathrm{M1},i}}{\partial t} &= -\kappa_{\mathrm{P},i}\,\rho_i\,\mathrm{c} E_{\mathrm{M1},i}, \\ \frac{\partial \mathbf{F}_{\mathrm{M1},i}}{\partial t} &= -\kappa_{\mathrm{P},i}\,\rho_i\,\mathrm{c} \mathbf{F}_{\mathrm{M1},i}. \end{aligned} \tag{3.45}$$

This can be done by a linear expansion (like Eq. 3.44), provided the variations of the evolved quantities are not too large. For this purpose, this system is divided into sub-time steps and evolved quantities are allowed to change by less than 10% within one sub-time step. However, these can change significantly during a time step, due to transport and emission. On the one hand it affects the accuracy of this linear treatment, on the other hand it requires many substeps of computation. Therefore, an option (called *smooth_rt*) is to use the transport and injection steps to infer the radiative energy and flux variation rates

$$\begin{aligned} \dot{E}^{n}_{\mathrm{M1},i} &= \frac{E'_{\mathrm{M1},i} - E^{n}_{\mathrm{M1},i}}{\Delta t}, \\ \dot{\mathbf{F}}^{n}_{\mathrm{M1},i} &= \frac{\mathbf{F}'_{\mathrm{M1},i} - \mathbf{F}^{n}_{\mathrm{M1},i}}{\Delta t}, \end{aligned} \tag{3.46}$$

where $E'_{\mathrm{M1},i}$ and $\mathbf{F}'_{\mathrm{M1},i}$ are the buffered values of the radiative energy and flux after transport (and injection, regarding $E'_{\mathrm{M1},i}$). Then, the thermochemistry step is subcycled and updates the

radiative density and flux progressively, based on this rate and in a semi-implicit fashion

$$\begin{aligned} E_{\mathrm{M1},i}^{t+\Delta t_k} &= \frac{E_{\mathrm{M1},i}^{t} + \Delta t_k \dot{E}_{\mathrm{M1},i}^{n}}{1 + \Delta t_k \kappa_{\mathrm{P},i}\, \rho_i\, \mathrm{c}}, \\ \mathbf{F}_{\mathrm{M1},i}^{t+\Delta t_k} &= \frac{\mathbf{F}_{\mathrm{M1},i}^{t} + \Delta t_k \dot{\mathbf{F}}_{\mathrm{M1},i}^{n}}{1 + \Delta t_k \kappa_{\mathrm{P},i}\, \rho_i\, \mathrm{c}}, \end{aligned} \tag{3.47}$$

where the sub-time step of index k is characterized by Δt_k. After each of these, the gas momentum is updated with the momentum transfer due to radiation, *i.e.*

$$\Delta \mathbf{p}_{\gamma,i} = \Delta t_k \frac{\kappa_{\mathrm{P},i}\, \mathbf{F}_{\mathrm{M1},i}^{t+\Delta t_k}}{\mathrm{c}}. \tag{3.48}$$

This results in a total variation of gas momentum

$$\Delta \mathbf{p}_{\gamma,i} = \sum_k \Delta t_k \frac{\kappa_{\mathrm{P},i}\, \mathbf{F}_{\mathrm{M1},i}^{t+\Delta t_k}}{\mathrm{c}}, \tag{3.49}$$

where δt_k is the time step of the substep k so that the total time step is $\Delta t = \sum_k \Delta t_k$.

The explicit scheme for transport and injection implies a time step constrained by the CFL condition which takes the speed-of-light as the signal speed. Since this speed is significantly ($\gtrsim 1000$) larger than the typical hydrodynamical speeds, this would result in a much shorter time step, which is not feasible. Rosdahl et al. (2013) have opted for the reduced-speed-of-light approximation (RSLA), introduced in Gnedin & Abel (2001). The speed-of-light, in the explicit equations above, is reduced by a factor $100 - 1000$ and written $\tilde{\mathrm{c}}$, which results in a time step typically ten times shorter than the hydrodynamical time step.

3.4 A hybrid implementation for stellar irradiation

In the context of massive star formation, we aim at distinguishing the radiation emitted by the star from that emitted by the gas-dust mixture environment. As shown in Sect. 2.3, we choose the FLD method as a basis for radiation-hydrodynamics, on top of which the stellar radiation is treated with the M1 method implemented in RAMSES-RT. The transport of stellar radiation is done with RAMSES-RT (Eq. 3.40) and has not been modified, so I will focus on the injection, absorption and heating. A schematic view is given in Fig. 3.5. We have chosen to stick to a gray model, *i.e.* frequency-averaged radiative quantities and opacities, to save computational load. However, since both the FLD and M1 modules include a multigroup formalism, the generalization of our hybrid approach to multigroup radiative transfer is feasible.

Stellar radiation injection - RAMSES-RT

In star formation calculations, stellar sources are not just emitters but also strong gravitational attractors. They are modelled by sink particles (Bleuler & Teyssier, 2014), *i.e.* collisionless particles which interact gravitationally with the gas (and with their companions). In other contexts, sink particles can represent, for instance, a cluster of stars or supermassive black holes, but I focus here on the star formation context. Before a sink particle forms, a clump finder algorithm is employed to detect the density peaks and their associated regions, labelled as *peak patches* (see Figure 1-6 of Bleuler & Teyssier 2014). When a peak patch satisfies various criteria such as being bound or subvirial (*i.e.* collapsing), a sink particle is created at its location. Sink particles interactions are handled by the N-body solver of RAMSES. They typically occupy a few cells in radius, in which they can accrete part of the gas sitted on the cells. Various

accretion schemes are implemented in RAMSES such as the accretion above a threshold which is kept constant or varies with the local conditions. Their gravitational potential is limited by a softening length, of the order of the accretion radius. In this work, we are particularly interested in their radiative feedback.

Within the volume occupied by a sink particle, radiative energy is deposited at a rate consistent with the luminosity of the star (or the stellar cluster) it represents. We must conduct this energy generation towards the M1 radiative energy (and not the FLD radiative energy), following

$$E^{n+1}_{\mathrm{M1},i} = E^{n}_{\mathrm{M1},i} + \frac{\Delta t f_i}{V_{\mathrm{sink}}} L_\star, \tag{3.50}$$

where f_i is a distribution function and V_{sink} is the sink volume. Various distribution functions can be chosen to inject this energy, such as uniform, peaked, or spline functions. All must meet the requirement $\int_{V_{\mathrm{sink}}} f_i dV = V_{\mathrm{sink}}$. Choosing this function can be of particular importance in some cases because it sets initial conditions for the propagation of radiation, at a radius as large as the sink size (see Appendix C). Note that there is no source of M1 radiation other than the stellar sources. Consistently, the M1 transport is activated only once a sink particle is created.

Absorption and stellar radiative force - RAMSES-RT

For the absorption of radiative energy and flux, we need to compute the Planck mean opacity at the stellar temperature $T_\star$

$$\kappa_{\mathrm{P},\star} \equiv \frac{\int_0^\infty \kappa_\nu B(\nu, T_\star) d\nu}{\int_0^\infty B(\nu, T_\star) d\nu}. \tag{3.51}$$

This is a fundamental difference with the FLD method. In the gray (frequency-averaged) formalism, mean opacities do not depend on the frequency anymore but on the blackbody temperature. In the FLD method, the opacity in a cell is given by the opacity at the *local gas temperature* within that cell. On the opposite, here we attach the *stellar temperature* to the mean opacity used in the M1 module. As the mean opacity is already computed in the FLD module, we call this routine from RAMSES-RT but with the stellar temperature $T_\star$, before perfoming the absorption step. Of course, $T_\star$ is a property of the sink particle, hence it must be communicated from the sink particle module to the cooling module. It is evaluated at the beginning of the time step. Then, the equations to solve are simply Eqs. 3.45 with this Planck mean opacity, in the subcycling procedure of RAMSES-RT, while the gas momentum is incremented at each substep, *i.e.*

$$\begin{aligned} E^{t+\Delta t_k}_{\mathrm{M1},i} &= \frac{E^{t}_{\mathrm{M1},i} + \Delta t_k t \dot{E}^{n}_{\mathrm{M1},i}}{1 + \Delta t_k \kappa_{\mathrm{P},\star} \rho_i \, \mathrm{c}}, \\ \mathbf{F}^{t+\Delta t_k}_{\mathrm{M1},i} &= \frac{\mathbf{F}^{t}_{\mathrm{M1},i} + \Delta t_k \dot{\mathbf{F}}^{n}_{\mathrm{M1},i}}{1 + \Delta t_k \kappa_{\mathrm{P},\star} \rho_i \, \mathrm{c}}, \end{aligned} \tag{3.52}$$

and

$$\Delta \mathbf{p}_{\gamma,i} = \Delta t_k \frac{\kappa_{\mathrm{P},\star} \mathbf{F}^{t+\Delta t_k}_{\mathrm{M1},i}}{\mathrm{c}}, \tag{3.53}$$

where the dotted quantities are the variation rates inferred from the explicit step (see Eq. 3.46).

Heating - FLD

The exact amount of stellar radiative energy absorbed in the previous step is used to heat the gas, in the implicit part of the FLD module, which treats gas-radiation coupling. It appears as

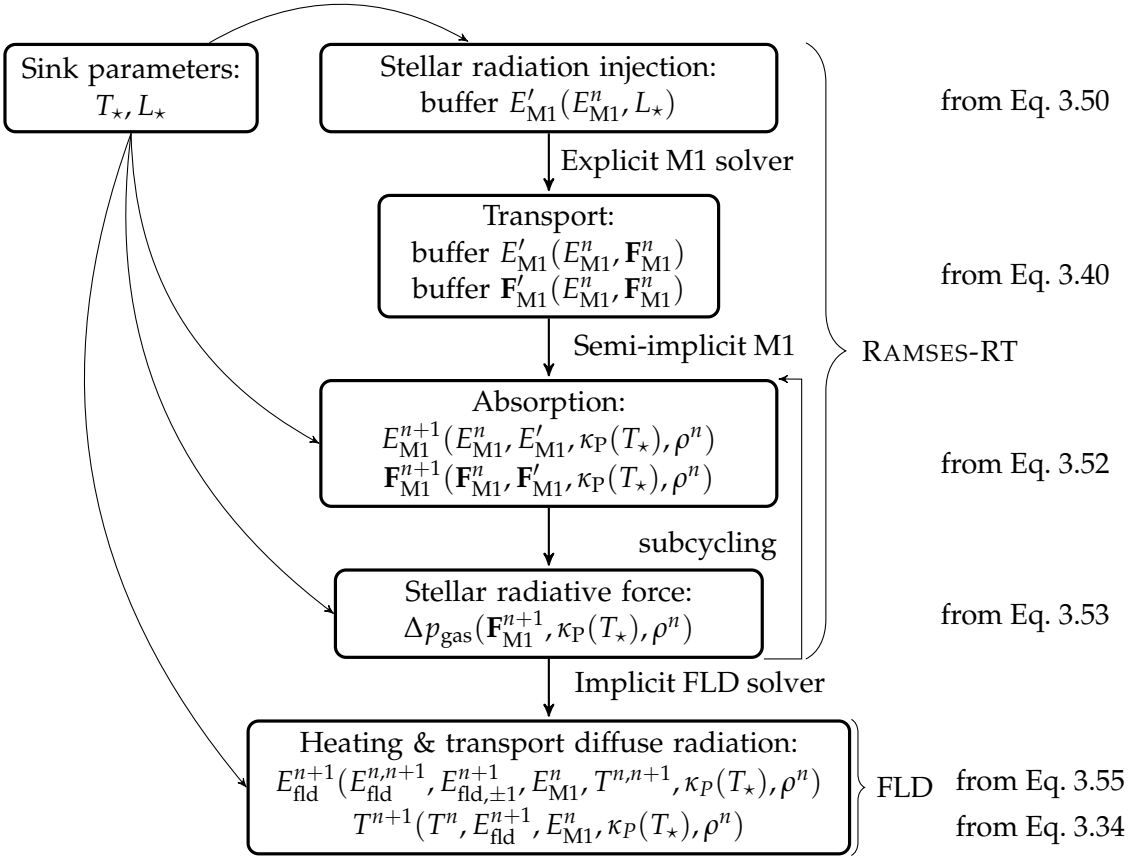

Figure 3.5: Schematic flow chart of the hybrid radiative transfer method. Exponents n denote the time step number, subscript ± 1 point to the neighboor cells. For readability we have not explicitly written the dependency with respect to the time step Δt and subtime step Δt_k.

a source term for the internal energy equation of the system

$$\begin{cases} \partial_t E_{\rm fld} - \boldsymbol{\nabla}\cdot\left(\dfrac{c\lambda}{\kappa_{\rm R,fld}\rho}\boldsymbol{\nabla}E_{\rm fld}\right) = +\kappa_{\rm P,fld}\,\rho\,c\left(a_R T^4 - E_{\rm fld}\right), \\ \dfrac{\partial e}{\partial t} = -\kappa_{\rm P,fld}\,\rho\,c\left(a_R T^4 - E_{\rm fld}\right) + \kappa_{\rm P,\star}\,\rho\,\tilde{c}E_{\rm M1}. \end{cases} \tag{3.54}$$

We perform a similar discretization as in Sect. 3.2. We end up with Eq. 3.38 modified by this energy input (in blue below), *i.e.*

$$-E^{n+1}_{{\rm fld},i-1}C_{i-1/2} + E^{n+1}_{{\rm fld},i}\left[1 + (C_{i-1/2}+C_{i+1/2}) + \omega_i\left(1 - \frac{4\omega_i a_R (T_i^n)^3}{C_v + 4\omega_i a_R (T_i^n)^3}\right)\right] - E^{n+1}_{{\rm fld},i+1}C_{i+1/2} = E^n_{{\rm fld},i} + \frac{\omega_i a_R (T_i^n)^3 C_v T_i^n + 4\omega_i a_R (T_i^n)^3 \omega_\star E^n_{{\rm M1},i}}{C_v + 4\omega_i a_R (T_i^n)^3}, \tag{3.55}$$

where $\omega_\star = \kappa_{\rm P,\star}\rho_i^n \tilde{c}\Delta t$. The temperature update 3.34 is straightforwardly modified as

$$T_i^{n+1} = \frac{C_v T_i^n + \omega_i\left(3a_R(T_i^n)^4 + E^{n+1}_{{\rm fld},i}\right) + \omega_\star E^n_{{\rm M1},i}}{C_v + 4\omega_i a_R (T_i^n)^3}. \tag{3.56}$$

When the gas cools, it transfers its energy into the radiative energy of the FLD module.

Time step constraint

By including both an explicit and an implicit solver, the hybrid method must satisfy three conditions for stability and accuracy. First, the CFL condition must be met for ensuring stability, with the reduced speed of light $\tilde{c}$. Second, as mentioned above, the implicit method has no time step constraint for stability but it relies on the linearization of the term $(T^{n+1})^4$, hence it is accurate only if the temperature variations are small. Finally, the explicit part of the FLD module is constrained by the CFL condition with a sound speed accounting for both the thermal pressure and the radiative pressure (Eq. 3.29). However, as we will see in the pure radiative transfer and radiation-hydrodynamical cases, the time step is usually limited by the CFL condition with the reduced speed of light.

3.5 Pure radiative transfer tests

In this section are presented the various tests I run to validate the hybrid method, without hydrodynamics. Separately, the FLD method and RAMSES-RT have already been widely tested (Commerçon et al. 2011b, Rosdahl et al. 2013, Commerçon et al. 2014, Rosdahl & Teyssier 2015), hence the goal here is to quantify the improvement that represents the hybrid method compared to the FLD alone in typical setups of star formation. The tests consist of a disk-like density structure made of gas and dust, irradiated by a central source (a star). Three regimes of optical thickness are considered, covering the optically-thin and thick limits. Focus is made on the converged temperature structure within the disk and the accuracy of both methods is assessed by comparing the outcoming temperature with that obtained with Monte-Carlo (MC) codes. First, I build and run the same setup with the RADMC-3D code (Dullemond et al., 2012), which is very well-suited for this type of tests. In addition to RADMC-3D, I also use data from MCFOST (Pinte et al., 2006) when available. Indeed, it uses cylindrical coordinates while the RADMC-3D grid is spherical, and will allow more accurate comparisons with RAMSES in the vertical direction. MC codes follow individual photons (or photon packets) and solve

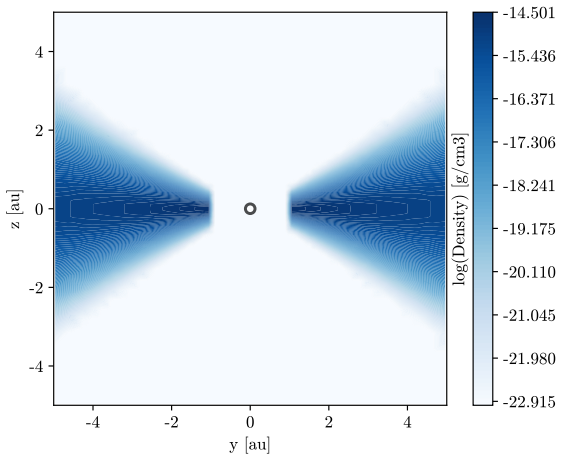

Figure 3.6: 10 AU edge-on slice of the density structure in the moderately optically-thick test with $\tau = 100$. The white dot represents the sink particle, the only radiation source for the M1 module.

exactly the radiative transfer equation, in constrast to the fluid description inherent to our moment methods. Hence, they play the role of reference solutions since no analytical function exists for such tests.

The main input parameters are presented in Table 5.1, along with the radiative method used and the maximum error, defined as the normalized difference with the temperature obtained with MC codes. Each regime of optical-thickness is characterized by the integrated optical-depth through the disk midplane, τ. The dust-to-gas ratio is taken equal to 0.01. Gas opacity is neglected, so dust is the only contributor to the dust-gas mixture opacity which is obtained by multiplying the dust opacity by the dust-to-gas ratio. We consider an ideal gas of adiabatic index $\gamma = 5/3$.

Let us briefly discuss the time step settings. The FLD runs are restricted by the time step condition for accuracy (Sect. 3.2), not by the strict time constraint which forbids signals to more than one cell within one time step (CFL condition). Hence, this time step is user-defined and could be adapted to each test to be large enough to speed-up the calculation and small enough to achieve accuracy. On the other hand, the M1 part of our hybrid approach obeys the CFL condition for the reduced speed of light, that we have chosen to be $\tilde{c} = c/1000$. In these tests, the time step required for accuracy in the FLD runs is significantly larger than that of the HY runs, which is restricted by the M1 time step.

3.5.1 Optically-thin and moderately optically-thick cases

Physical and numerical configurations

This test is taken from Pascucci et al. (2004), proposed as a benchmark for radiative transfer codes, in general applied to the physics of protoplanetary disks. This is a 2D test of a static flared disk of a given analytical profile for the gas density, depending on the cylindrical radius r and on the vertical height z. The disk extends from $r_{in} = 1$ AU to $r_{out} = 1000$ AU. The density $\rho(r, z)$ in cylindrical coordinates is given as

$$\rho(r, z) = \rho_0 f_1(r) f_2(r, z), \tag{3.57}$$

Table 3.1: Input parameters (disk mid-plane optical depth, stellar temperature), radiative transfer method and maximal temperature deviation in the mid-plane of pure radiative transfer tests.

Ref.	τ	$T_\star$ (K)	Method	$(\Delta T)_{\mathrm{max,r}}$ (%)
Pascucci et al. (2004)	0.1	5800	FLD	62
			Hybrid	2
	0.1	15000	FLD	65
			Hybrid	3
Pascucci et al. (2004)	100	5800	FLD	36
			Hybrid	25
	100	15000	FLD	57
			Hybrid	31
Pinte et al. (2009)	10^3	4000	FLD	94
			Hybrid	65

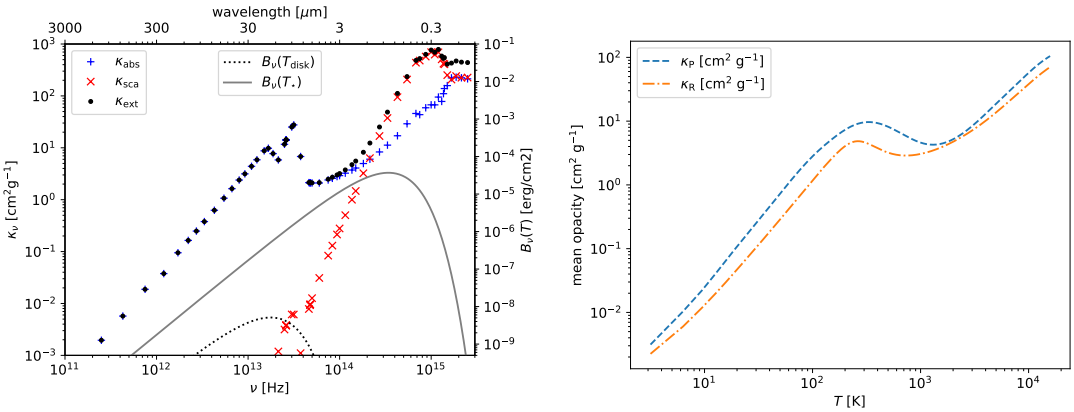

Figure 3.7: Left: Frequency-dependent opacities and blackbody spectra for $T_{\mathrm{disk}} = 300$ K and $T_\star = 5800$ K. Opacities are absorption (blue pluses), scattering (red crosses) and extinction (black dots) coefficients for the dust-and-gas mixture used in the Pasccuci test. The table contains 61 frequency bins and data are taken from Draine & Lee (1984). Apart from the broad opacity features at about 10 and 20 μm, which correspond to Si-O vibrational transitions, the opacity generally increases with the photon frequency. The opacity at stellar-like radiation frequencies is generally greater than at disk-like radiation frequencies. Right: Planck's (blue dashed curve) and Rosseland's (orange dot-dashed curve) mean opacities, as a function of temperature in the Pascucci setup.

where ρ_0 is the density normalization and is linked to the only free-parameter, the integrated optical-depth throughout the mid-plane of the disk, $\tau_\nu = \int_{\mathrm{r_{in}}}^{\mathrm{r_{out}}} \kappa_\nu \rho(r, z = 0)\, \mathrm{d}r$. The two functions f_1 and f_2 are given by

$$f_1(r) = \left(\frac{r}{r_{\mathrm{d}}}\right)^{-1}, \tag{3.58}$$

and

$$f_2(r,z) = exp\left(-\frac{\pi}{4}\left(\frac{z}{h(r)}\right)^2\right), \tag{3.59}$$

where the flaring function is

$$h(r) = z_{\rm d} \left(\frac{r}{r_{\rm d}} \right)^{1.125}. \tag{3.60}$$

In this setup, $r_{\rm d} = r_{\rm out}/2 = 500\,{\rm AU}$ and $z_{\rm d} = r_{\rm out}/8 = 125\,{\rm AU}$ are the scale-radius and the scale-height. The star is not resolved but its luminosity is based on its physical radius and surface temperature. In this test, it has a radius $R_\star = 1\,{\rm R}_\odot$ and can have two possible surface temperature: $T_{\star,1} = 5800\,{\rm K}$ and $T_{\star,2} = 15000\,{\rm K}$.

The integrated optical depth (for extinction, as in the literature) is taken to be either $\tau = 0.1$ or $\tau = 100$ at 550 nm to probe the optically-thin and moderately optically-thick regimes, respectively. Dust is made of spherical astronomical silicates of radius 0.12 micron and density of $3.6\,{\rm g\,cm^{-3}}$. Frequency-dependent dust opacities are taken from Draine & Lee (1984) as in Pascucci et al. (2004) and are displayed in the left panel of Fig. 3.7. In these setups we only take the absorption into account and do not consider scattering. The corresponding Planck and Rosseland mean opacities used in the gray M1 and FLD modules are displayed in the right panel of Fig. 3.7. We recall that we take the M1 absorption coefficient as the Planck mean opacity at the stellar temperature, $\kappa_{\rm P}\left(T_\star\right)$.

The physical conditions at the boundaries are chosen to be a fixed temperature of 14.8 K and a density floor of $10^{-23}\,{\rm g\,cm^{-3}}$. The same density floor is applied between the star and the disk edge to mimic the vacuum that RADMC-3D and MCFOST strictly apply since their respective cylindrical and spherical grids begin at $R_{\rm in}$. The 14.8 K temperature is applied throughout the computational domain as initial condition and is at equilibrium with radiation. We set the boundary condition as "outflows", so that radiation can escape.

We run the simulations with AMR levels between 5 and 14, which results in a finest resolution of $\Delta x = 0.12$ AU where Δx is the cell width. This makes possible to have several ($\approx$9) cells between the star and the disk edge and the star to have a negligible size with respect to the disk thickness ($\approx$0.01 AU against $\approx$0.04 AU for the disk height at $r_{\rm in}$). Secondly, it permits to resolve several times the mean free-path at the disk inner edge: the local optical depth is $\kappa_{\rm P}\,\rho_{\rm max}\,\Delta x \approx 0.15 < 1$, where $\rho_{\rm max}$ is the density at the disk inner edge for the case $\tau = 100$. Refinement is performed on the density gradient so that the disk inner edge is at the highest refinement level. We consider that the temperature structure is converged when the relative change between successive outputs decreases below 10^{-4} (see Ramsey & Dullemond, 2015).

Temperature structure

The RAMSES grid is Cartesian while the grids of MCFOST and RADMC-3D are cylindrical and spherical, respectively. Therefore, we interpolate temperature values on their grids to compute the relative error at the location on the RAMSES grid. Figure 3.8 plots the gas temperature in the disk mid-plane against the x-axis for the most optically-thin case, $\tau = 0.1$, once the temperature structure is converged with respect to time. The location is given by the distance to the disk inner edge, $r - r_{\rm in}$. For $T_{\star,1}$ and $T_{\star,2}$ the FLD run produces an important error throughout the disk mid-plane, up to $\approx$62% and $\approx$65%, respectively, and always underestimates the temperature. On the opposite, the hybrid method is quite accurate with a maximal error of $\approx$2% while RT codes (MCFOST and RADMC-3D) agree within 1% in this test (in accord with Pascucci et al. 2004). This important difference between FLD and hybrid methods comes from the regime of validity of each method: the FLD is not well-suited for optically-thin media. In the hybrid method, since there is not much absorption because of the low optical-depth, the M1 module is mainly at work and is adapted to optically-thin media (as tested in Rosdahl et al. 2013), which justifies its good accuracy.

For direct irradiation, the Planck mean opacity in the FLD implementation is computed at the local temperature even though the radiation has been emitted by the star. A direct conse-

quence is that the stellar radiation is absorbed by the disk with an opacity coefficient computed at the disk temperature, which is much lower than the stellar temperature. As the opacity increases with the temperature (see the right panel of Fig. 3.7), the absorption opacity with the FLD is lower and hence the temperature is lower than that given by RT codes and by the hybrid approach. The situation worsens from $T_{\star,1}$ to $T_{\star,2}$ at the disk edge and the error increases from ≈30% to ≈60%. It also illustrates the need for a better approach for treating massive stars irradiation.

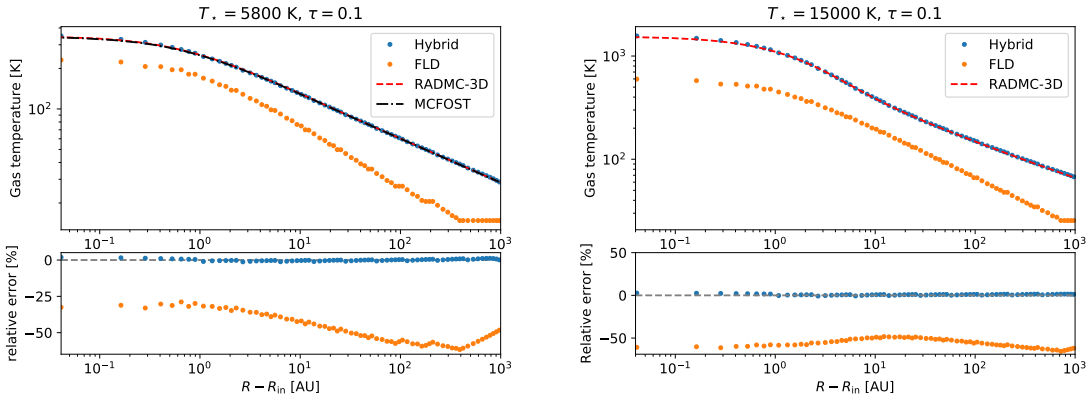

Figure 3.8: Radial gas temperature profiles in the mid-plane of the disk following the test of Pascucci et al. (2004) for $\tau = 0.1$. We compare the gas temperature computed using MCFOST (black dotted-line) and RADMC-3D (red dashed-line), the hybrid method (M1+FLD, blue dots) and the FLD method alone (orange dots) in RAMSES. Left: central star temperature $T_{\star,1} = 5800$K; right: $T_{\star,2} = 15000$K.

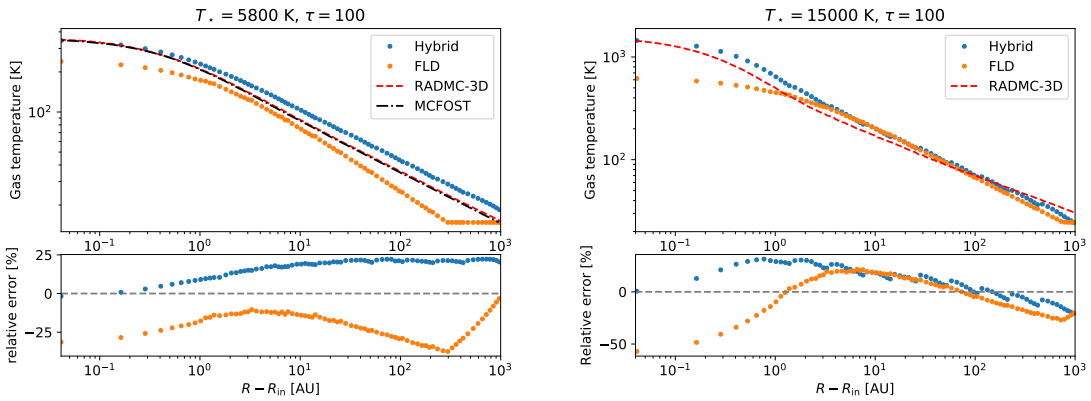

Figure 3.9: Same as Fig. 3.8, but for $\tau = 100$.

The left panel of Fig. 3.9 shows the radial temperature profile in the disk mid-plane for the moderately optically-thick case, $\tau = 100$, and for $T_{\star,1}$. The error made by the hybrid method is higher than for the $\tau = 0.1$ case and reaches a maximal value of ≈25% whereas the FLD method alone makes a maximal error of ≈36%. Also, the error made by the hybrid method is quite uniform with respect to the error made by the FLD method alone. For $T_{\star,1}$ and $T_{\star,2}$ (left and right panels of Figs. 3.8 and 3.9, respectively), the FLD method underestimates the temperature

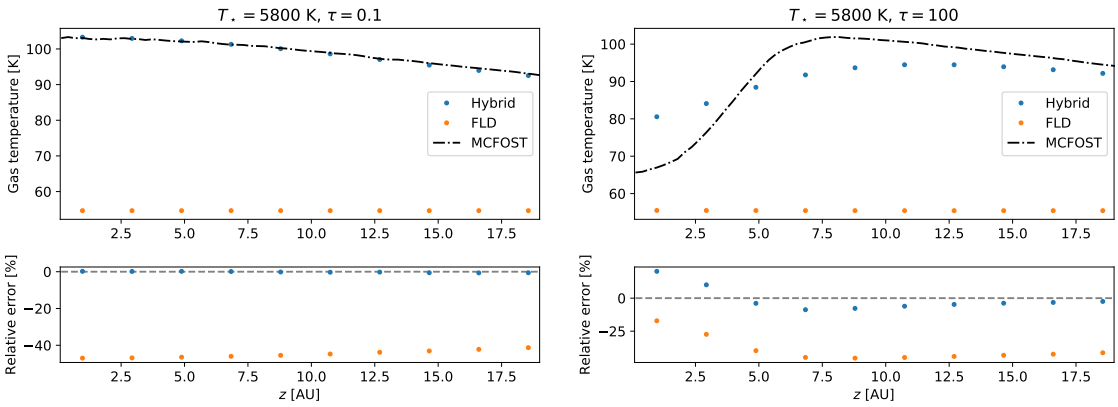

Figure 3.10: Vertical gas temperature profiles at a cylindrical radius of 20 AU, following the test of Pascucci et al. (2004). We compare the gas temperature computed using MCFOST, the hybrid method (M1+FLD) and FLD alone in RAMSES for $T_{\star,1}$, $\tau = 0.1$ (left) and $\tau = 100$ (right).

between the star and the disk edge because the medium is optically thin and because of the Planck opacity considered, as explained above. For $T_{\star,2}$, both methods converge toward a similar temperature at large radii. Absorption is stronger here than in the most optically-thin case, and stronger than for $T_{\star,1}$ (see Fig. 3.7), so the M1 photons are quickly absorbed and the FLD module of our hybrid method is at work. Therefore a significant error is expected from the gray opacity employed in the FLD module of the hybrid method. Indeed, the temperature varies significantly throughout the disk (between ≈20 and 350 K for $T_{\star,1}$ and between ≈20 and 1000 K for $T_{\star,2}$). As a consequence, a disk cell is crossed by photons of very different frequencies and the gray approach induces errors. Conversely, the frequency-dependence of RADMC-3D method permits one to distinguish the photons that are quickly absorbed (the most energetic ones) from those at lower energy that penetrate the disk more deeply and contribute to the disk heating at larger radii.

To examine the behavior of both methods with respect to the nonisotropy of the setup, we plotted the vertical temperature profile at a cylindrical radius of 20 AU (Fig. 3.10). This visualization is important for this type of tests, because an optically-thick disk produces self-shielding in the mid-plane and we expect the hybrid method to capture it better than the FLD method (González et al., 2007). Here we take the temperature given by MCFOST rather than RADMC-3D because its grid is cylindrical (and not spherical) and thus errors of interpolation are avoided. The left panel of Fig. 3.10 shows the temperature profile for the most optically-thin case, $\tau = 0.1$. No self-shielding is expected and the temperature should decrease slowly as the vertical height increases. Such a behavior is obtained with MCFOST as well as with the hybrid method. The temperature obtained with the FLD method is uniform with z, which is likely due to the isotropic nature of the FLD method. The relative error is comparable to the one in the radial profile: up to ≈47% with the FLD method and less than 1% with the hybrid approach.

On the right panel of Fig. 3.10, $\tau = 100$, MCFOST gives a lower temperature in the mid-plane than for $\tau = 0.1$, as expected. Conversely, the FLD method does not capture at all the nonisotropic nature of the radiation onto the irradiated disk: the temperature is fairly uniform. The hybrid method reproduces partly this feature, even though the error can be as large as ≈20%.

We conclude that the FLD method is not capable of reproducing the temperature profile in the optically-thin and moderately optically-thick regime. The hybrid method is very accurate in the optically-thin regime (less than ≈2%). In the moderately optically-thick regime, the hybrid method gives a non-negligible error (up to ≈31% for a 15000 K star) in the transition

between optically-thin and -thick media which shows its limitations but this is a major improvement with respect to the ≈57% error made with the FLD method. In addition, the hybrid approach captures partially (≈20% error) the self-shielding in the disk mid-plane while the FLD approximation does not.

Radiative acceleration

We look at the radiative acceleration maps obtained with the FLD and the hybrid methods for the moderately optically-thick case ($\tau = 100$). Figure 3.11 shows the radiative acceleration perpendicularly to the disk plane as obtained after temperature convergence with the FLD method (left) and the hybrid method (right). The left panel shows two peculiarities of the FLD solver. First, we recall that the FLD radiative acceleration has two asymptotic values depending on the optical regime: in the optically-thin limit it is proportional to the radiative energy and in the optically-thick limit it is equal to the radiative energy gradient divided by the density. Farther from the star, the disk structure is visible (the dark blue zones) because of the density dependence in the radiative acceleration. Second, the aspect of the FLD acceleration closer to the star is mainly due to grid effects.

The right panel of Fig. 3.11 shows the sum of the FLD and M1 radiative accelerations in the hybrid case. The combination of the optically-thin and -thick methods permits to capture the nonisotropy of the radiative acceleration. The hybrid radiative acceleration is ∼100 greater than the FLD acceleration. This result holds in the four tests: $\tau = 0.1$, $\tau = 100$ and $T_{\star,1}$, $T_{\star,2}$. It is in agreement with the study of Owen et al. (2014). This is mainly due to the temperature at which the M1 opacity is taken. Stellar photons are at a frequency that is ∼10 times greater than that of photons emitted by the surrounding gas, which implies an opacity ∼100 greater (see Fig. 3.7). As shown previously, the radiation transport in the optically-thin limit is accurately treated with our hybrid approach and leads to a strong improvement for the radiative acceleration due to the direct irradiation, which is one of the main contributors expected in the dynamics of massive star formation.

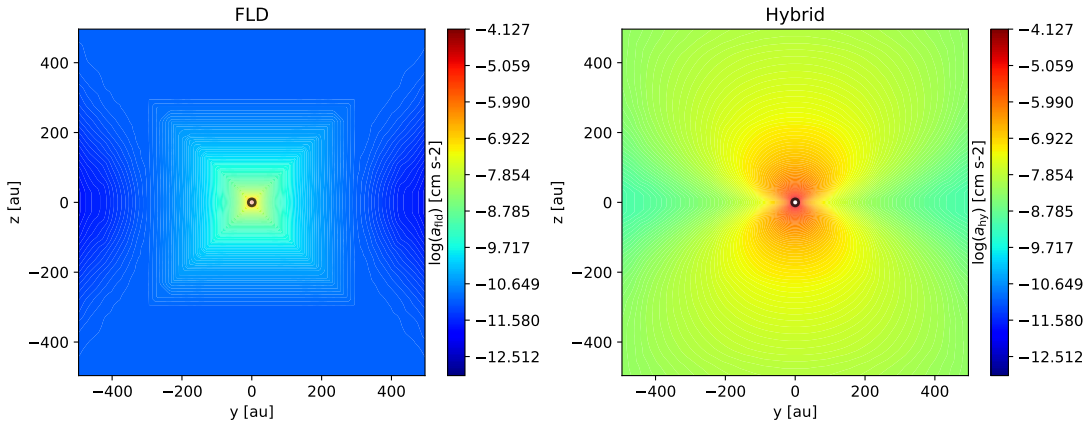

Figure 3.11: 1000 AU disk edge-on slices of the radiative acceleration, following the test of Pascucci et al. (2004) obtained with RAMSES after stationarity is reached. Left: FLD run; right: hybrid run. Star and disk parameters: $\tau = 100$ and $T_{\star,1}$. The hybrid radiative acceleration is about 100 times greater than the FLD one.

3.5.2 Very optically-thick case

The second test is a similar but more challenging setup with a higher integrated optical depth and a sharper density profile than Pascucci et al. (2004) at the disk edge, as presented in Pinte et al. (2009). The disk extends from a cylindrical radius $r_{in} = 0.1$ AU to $r_{out} = 400$ AU and the integrated optical depth (for extinction) is $\tau_{810nm} = 10^3$. The flared disk density profile $\rho(r,z)$ is analytically given by

$$\rho(r,z) = \rho_0 \left(\frac{r}{r_d}\right)^{-2.625} \exp\left(-\frac{1}{2}\left(\frac{z}{h(r)}\right)^2\right), \tag{3.61}$$

where the flaring function $h(r)$ is as before, $r_d = r_{out}/4 = 100$ AU and $z_d = r_{out}/40 = 10$ AU. The star has a radius $R_\star = 2\,R_\odot$ and the stellar surface temperature is $T_\star = 4000\,K$.

We use the opacity table from Weingartner & Draine (2001) which gives the absorption opacity of dust grains with respect to the wavelength. These opacities were calculated for spherical astronomical silicates (see Draine & Lee 1984) of size 1 micron and density 3.6 g cm^{-3}.

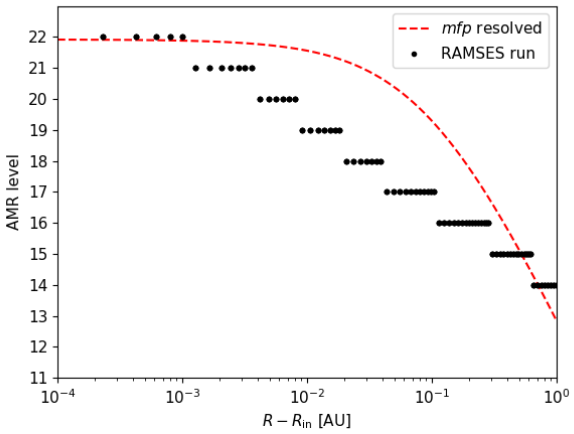

Figure 3.12: AMR level needed to resolve the mean free path (mfp) of photons (red dashed-line) and effective AMR level (black dots) in the disk midplane following the test of Pinte et al. (2009). This test is very challenging for an AMR code.

The sharp increase in density at the disk inner edge makes this test particularly challenging because the local variation of optical depth must be resolved while the discretized equations involve locally constant absorption opacities. At the same time, it is crucial to resolve the local mean free path to prevent an excess of photon absorption, which leads to overestimating the temperature. Resolving both is even more challenging for AMR-grid codes than for cylindrical-grid codes with no material inside R_{in} and a logarithmic scale. In RAMSES we choose to refine the grid based on a density gradient criterion so that the disk edge is at the finest resolution and the transition from optically-thin to -thick is as resolved as possible. There is a drawback: having the greatest resolution at the disk inner edge is very computationally expensive because, first, it affects many more cells than if the refinement is operated on the central cell (as usually done because the sink particle is located there). In addition, two adjacent cells cannot differ by more than one level of refinement and generally the number of cells at the same AMR level is much higher than two. Therefore, it also means a higher resolution at larger radii. For that reason, Ramsey & Dullemond (2015) choose not to use AMR but instead, a logarithmically-scaled grid particularly adapted to this setup. Figure 3.12 shows the AMR level needed to

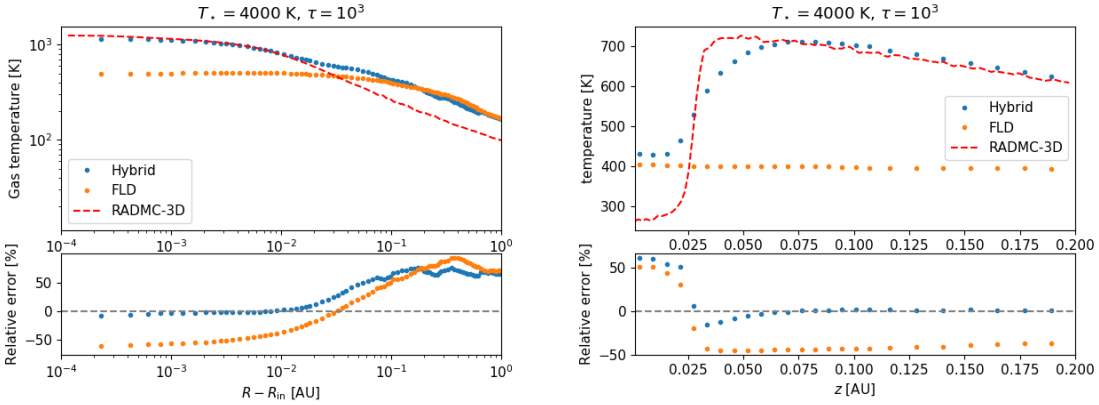

Figure 3.13: Left: Radial gas temperature profile in the mid-plane of the disk following the test of Pinte et al. (2009). Right: Vertical gas temperature profile at a cylindrical radius of 0.2 AU in the disk. We compare the gas temperature computed using RADMC-3D, the hybrid method (M1+FLD) and the FLD method alone in RAMSES. The integrated optical depth in the disk mid-plane is $\tau_{810\text{nm}} = 10^3$ and the stellar temperature is $T_\star = 4000$ K.

resolve the local mean free path as a function of the radius in the disk midplane along with the AMR level set with RAMSES. Hence, we perform our calculations with $l_{\text{max}} = 22$, which gives a finest cell width of 1.9×10^{-4} AU, so that the mean free path at the disk inner edge is resolved. The computational cost does not make possible to extend the zone over which the mean free path is resolved, nor to compare the temperature over the entire disk radius with RADMC-3D.

The left panel of Fig. 3.13 plots the radial temperature profile in the disk mid-plane obtained with RAMSES with the FLD and hybrid methods versus RADMC-3D. The FLD method underestimates the temperature at the disk inner edge, as in the test of Pascucci et al. (2004). The temperature slope given by the hybrid method is in a better agreement with RADMC-3D than the one given by the FLD method. For the hybrid method, the temperature at the inner edge of the disk is accurately computed (up to ≈7% error) but is overestimated at larger radii where it becomes fairly constant at ≈65% error. It can be seen that the error made by the hybrid approach is not negligible as the mean free path becomes unresolved (Fig. 3.12). The temperature profile obtained with our hybrid method is very similar to what has been obtained in comparable studies (see Fig. 8 of Ramsey & Dullemond 2015).

The right panel of Fig. 3.13 shows the vertical temperature profile. The temperature profile shape given by the hybrid method is similar to RADMC-3D but with self-shielding partially captured (up to ≈61% error), unlike in the FLD method. The hybrid method then recovers the correct temperature (≈2% error) at a larger disk height.

This setup highlights the need to resolve the mean free path of photons to obtain the correct temperature at the disk edge and it shows that the hybrid approach is more accurate than the FLD approximation to compute the temperature structure of an optically-thick disk. Moreover, this setup is challenging for our hybrid method because most of the direct irradiation is absorbed in the inner parts of the disk so the rest of the disk temperature structure is mainly obtained with the FLD method. As shown in Ramsey & Dullemond (2015), a frequency-dependent irradiation scheme is not more accurate in this test. However, a multigroup FLD method (González et al., 2015) would improve this, as mentioned by Ramsey & Dullemond (2015).

3.5.3 Temperature structure with isotropic scattering

Although it is not planned to include scattering in the collapse calculations, we have also explored the accuracy of our hybrid scheme when including isotropic scattering. Hence, we examine how the gray opacities are modified when including isotropic scattering in the FLD and M1 equations. It can be shown that taking the scattering into account does not modify the zero-th order moment of the RT equation (the conservation of the radiative energy), because the source term involves the radiative energy and its redistribution is the same with and without scattering. However, the first moment of the RT equation is modified as the coupling between the gas and the radiative flux is enhanced by the scattering. Therefore, the opacity in this equation is the extinction (absorption+scattering) opacity instead of the absorption opacity, *i.e.*

$$\frac{1}{c^2}\frac{\partial \mathbf{F}_\nu}{\partial t} + \boldsymbol{\nabla}.\mathbb{P}_\nu = -\frac{1}{c}(\kappa_\nu+\sigma_\nu)\mathbf{F}_\nu. \tag{3.62}$$

As a consequence, the Rosseland mean opacity used in the FLD method follows the general Eq. 2.35 before we neglected scattering, *i.e.*

$$\kappa_{\mathrm{R,fld}} \equiv \frac{\int_0^\infty \frac{\partial B_\nu(T)}{\partial T} d\nu}{\int_0^\infty \frac{1}{\kappa_\nu+\sigma_\nu}\frac{\partial B_\nu(T)}{\partial T} d\nu}. \tag{3.63}$$

Similarly, the gray version of the flux evolution equation (Eq. 2.42) in the M1 module introduces the Planck mean opacity as defined in Eq. 2.31 but with the extinction opacities, *i.e*

$$\begin{cases} \dfrac{\partial \mathbf{F}_{\mathrm{M1}}}{\partial t} + c^2\boldsymbol{\nabla}\cdot\mathbb{P}_{\mathrm{M1}} &= -\chi_{\mathrm{P},\star}\, c\mathbf{F}_{\mathrm{M1}}, \\ \chi_{\mathrm{P},\star} &\equiv \dfrac{\int_0^\infty \chi_\nu B(T_\star,\nu)d\nu}{\int_0^\infty \chi_\nu d\nu}, \end{cases} \tag{3.64}$$

where $\chi_\nu = \kappa_\nu+\sigma_\nu$. To summarize, the inclusion of isotropic scattering has no explicit impact on the radiative energy repartition but it increases the absorption and redistribution of the radiative flux. To test the behavior of the hybrid approach with isotropic scattering we run the most optically-thick case of the setup from Pascucci et al. (2004), with $\tau = 100$.

The left panel of Fig. 3.14 shows that the temperature in the mid-plane of the disk is well reproduced by the hybrid approach, as compared to the result obtained with MCFOST. The maximal error is ≈20% with the hybrid against ≈40% with the FLD method alone. The right panel of Fig. 3.14 emphasizes that most of the shielding effect in the disk mid-plane is captured by the hybrid approach, unlike for the FLD method. We compare both panels of Fig. 3.14 with the left panel of Fig. 3.9 and right panel of Fig. 3.10, respectively, as they show the result of the same setup without scattering. We observe that the temperature structure is not much influenced by the treatment of scattering. First, as shown in the left panel of Fig. 3.7, scattering only dominates at high-frequencies and therefore mainly at the first interaction of stellar photons with the medium, which corresponds to the disk inner edge. After this interaction, photons are reemitted at the local temperature, where the absorption opacity dominates. This explains why the temperature at the disk inner edge is 400 K with isotropic scattering against ∼350 K without scattering. Second, since opacities are frequency-averaged in our hybrid approach, taking isotropic scattering into account does not impact much the Planck and Rosseland mean opacities, except at high temperatures. Since the temperature structure is not strongly modified, and in order to build on previous results from the literature, we do not consider scattering in the collapse calculations in Chapter 4.

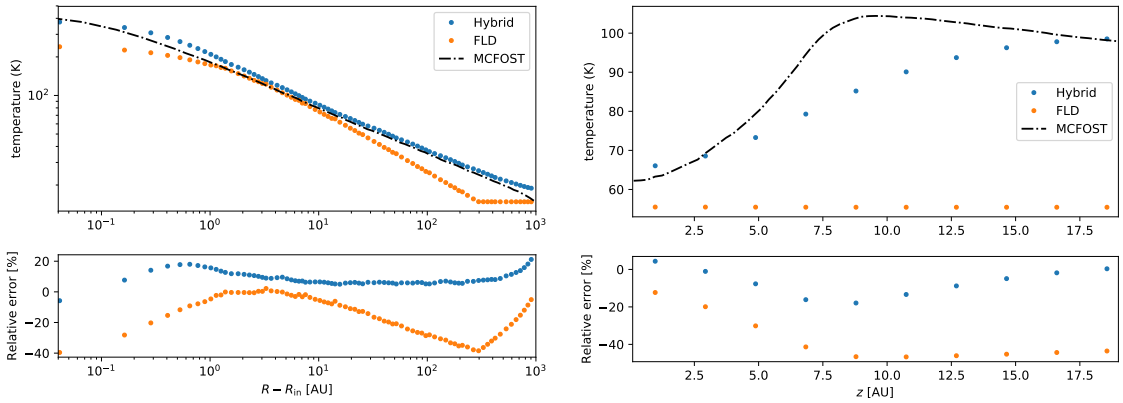

Figure 3.14: Gas temperature profiles, following the test of Pascucci et al. (2004). We compare the gas temperature computed using MCFOST, the hybrid method (M1+FLD) and the FLD method alone in RAMSES, with isotropic scattering. $T_\star = 5800$ K and the integrated optical depth in the disk mid-plane is $\tau = 100$. Left: radial profile in the disk mid-plane. Right: vertical profile at a disk radius of 20 AU.

3.5.4 Performance test

In this section, we compare the performance of the FLD and the hybrid methods. As mentioned earlier, the FLD implementation without hydrodynamics is implicit and therefore is not restricted by the CFL condition in our pure radiative transfer tests, in constrast to the M1 part of our hybrid method. Therefore, we do not compare the computational time in those tests. Still, we can probe the scaling properties of each method. We run the test from Pascucci et al. (2004), with $\tau = 100$ and $T_\star = 5800$ K. For this test, we choose a grid with two levels of refinement: 8 and 9, which leads to $\sim 2 \times 10^7$ cells. Figure 3.15 shows the strong scaling results from 2 to 32 cores. The number of cells and the very centered nature of the setup are not adapted to a large number of cores. RAMSES divides the domain into cubes, whereas an angular division would be more profitable for scaling properties but is not adapted to our Cartesian grid.

We can see that the scaling properties of the FLD and the hybrid methods are very similar and close to the theoretical line. The departure from the theoretical line (speedup of $\simeq$11 instead of 16 for 32 cores) is likely due to the high number of global communications which occur in the FLD conjugate gradient algorithm.

3.5.5 Perspectives

The hybrid method can be easily adapted to a multi-frequency treatment, regarding the FLD and/or the M1 method. This has not been done during the present thesis by lack of time, but we present here its feasability. On the FLD side, a multigroup approach would be at work once the heated gas re-emits its thermal energy. Hence, it does not affect the M1-FLD interface and therefore does not require extra work.

On the M1 side, the heating from stellar photons in the FLD solver, written as $\omega_\star E^n_{\mathrm{M1},i}$ (Eqs. 3.34 and 3.38), shall be replaced by a sum of over the M1 groups, *i.e.*

$$\sum_g \omega_\star E^n_{\mathrm{M1},i,g} = \rho_i^n \, \tilde{c} \, \Delta t \sum_g \kappa_{\mathrm{P},\star,g} E^n_{\mathrm{M1},i,g}, \tag{3.65}$$

where g in the M1 group index. A question arises on the opacity per M1 group $\kappa_{\mathrm{P},\star,g}$. For a

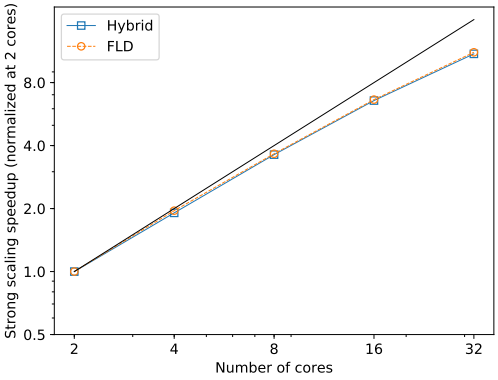

Figure 3.15: Strong scaling result for 2 to 32 cores in the test of Pascucci et al. (2004), with $\tau = 100$, $T_\star = 5800$ K. The ideal theoretical speedup is represented by the black line. We compare the strong scaling between the hybrid method (M1+FLD, blue squares) and the FLD method alone (orange circles). We normalize the speedup by that obtained with two cores.

single stellar source, the opacity could be defined on frequency intervals $[\nu_{1,g}, \nu_{2,g}]$ as

$$\kappa_{\mathrm{P},\star,g} \equiv \frac{\int_{\nu_{1,g}}^{\nu_{2,g}} \kappa_\nu B(T_\star, \nu) d\nu}{\int_{\nu_{1,g}}^{\nu_{2,g}} \kappa_\nu d\nu}. \tag{3.66}$$

On the other hand, to distinguish between several sources, one could take the same definition as before for the mean opacity and choose a different temperature $T_{\star,g}$ per group (this question was not relevant for one stellar source), *i.e.*

$$\kappa_{\mathrm{P},\star,g} \equiv \frac{\int_0^\infty \kappa_\nu B(T_{\star,g}, \nu) d\nu}{\int_0^\infty \kappa_\nu d\nu}, \tag{3.67}$$

where g would label each (group of) stellar source(s). This would eventually depend on the problem to consider.

We address here two possible motivations for choosing a multigroup M1 method. First, if one studies a single massive star feedback, it can be interesting to switch from gray opacities to several frequency bins. A motivation for this would be a gain in accuracy on the first interaction between stellar radiation and gas. In particular, as mentioned in Sect. 3.5.3 for typical protoplanetary disk opacities, scattering dominates the total (absorption and scattering) dust opacities at high frequencies. A multigroup approach can, therefore, compute a radiative acceleration which may differ between low-frequency bands and high-frequency bands. It can also allow a fraction of low-frequency photons to penetrate further into the environment (the disk midplane for instance), while almost all the photons would be absorbed immediately within a gray method. This may influence the thermal support and impact fragmentation. Second, as discussed in Sect. 3.3, radiation beams do not properly cross with the M1 method, but rather sum up (due to flux conservation). Hence, a multigroup approach seems like a promising alternative when treating with several stellar sources, as could be the case in the formation of multiple stellar systems.

CHAPTER 4

Massive Star Formation with RadiationHydrodynamics

Contents

MASSIVE STAR FORMATION FROM THE COLLAPSE OF A MASSIVE PRE-STELLAR CORE is the topic of the present and the following chapters, using the RAMSES code with the newly implemented hybrid radiative transfer method. We build a study of increasing complexity, divided in two main topics covered by the two chapters. In this mainly numerically-motivated chapter, we first focus on the influence of using such a new radiation transport method with respect to the previously used flux-limited diffusion approximation. This step aims at validating our method in a radiation-hydrodynamical context, but also complements previous studies with similar physics and setups (*e.g.*, Rosen et al. 2016). Then, we present the preliminary results of a side-project on the comparison of two high-performance codes when it comes to modelling disk fragmentation in high-mass star formation. In the following and physically-motivated chapter, we open the study of massive star formation to the presence of magnetic fields and initial turbulence.

The collapse calculations we present in these chapters share a simular global evolution (Fig. 4.1). We start from a rotating massive pre-stellar core whose density profile typically

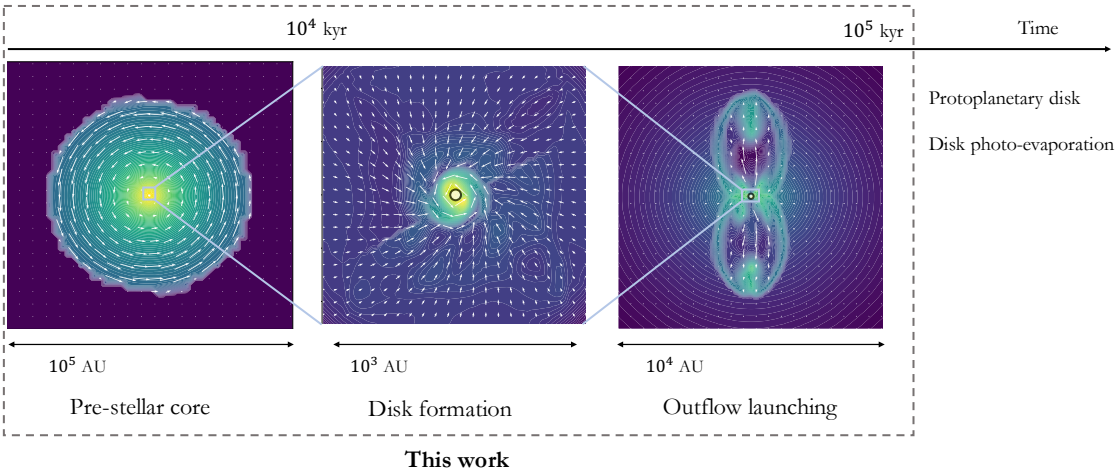

Figure 4.1: Overview of the common evolution and features of the collapse calculations presented in this chapter. The snapshots correspond to density slices in the run M0 (Chapter 5).

follows a power-law. This core is bound and gravitationally unstable, and collapses within a few kyr. Because of angular momentum conservation, a disk forms in the inner regions and a sink particle is created as a subgrid model for the formation of a protostar. In addition to accreting material, sink particles radiate and exert a feedback on their surroundings. We follow the main accretion phase of the central object to understand the early-stages of massive star formation. The late stages, which lead to planet formation or disk photo-evaporation by the stellar ionizing radiation (Kuiper & Hosokawa, 2018) are not studied. As discussed in Sec. 1.6, the existence of massive pre-stellar cores is not settled, although a few candidates exist (Nony et al., 2018). In order to build-up on numerical results from the literature, and avoid the computational cost of larger-scale simulations, we adopt this stage for our initial conditions as well.

The simulations we present here vary by their initial conditions (density profile, amount of rotational support, turbulent velocity field), or the physics modelled. This chapter covers radiation-hydrodynamical simulations, while the following includes the presence of magnetic fields in a radiation-magnetohydrodynamical framework (Chapter 5).

4.1 Collapse of a massive pre-stellar core with hybrid RT and hydrodynamics

The aim of this application is, mainly, to assess the impact of the hybrid radiative transfer method in a simulation of massive star formation. To do so, we start from initial conditions similar to a recent study from Rosen et al. (2016), who also use an AMR code with a Cartesian grid. The included physics is willingly limited to radiation-hydrodynamics (no magnetic fields) to focus on the comparison with previous works with similar numerical setups (Rosen et al. 2016, Klassen et al. 2016), as well as the results obtained with the FLD method. References to observational results (outflow and accretion disk properties, mean accretion rate) will be kept concise as it will be explored in more details in Chapter 5. Emphasis is made on two aspects. First, the outflows are expected to be more powerful with the hybrid method than with the FLD method (Fig. 3.11). Second, we use this numerical experiment to investigate the presence of radiative Rayleigh-Taylor instabilities. The accretion by these structures has been actively discussed in the community (*e.g.*, Krumholz et al., 2009, Kuiper et al. 2012) and an AMR code is well-suited to tackle this problem, as we will show later.

4.1.1 Included physics

Our simulations are run with the RAMSES code (Teyssier, 2002) which includes a hydrodynamics solver, sink particle algorithm (Bleuler & Teyssier, 2014), and radiative transfer with either the Flux-Limited Diffusion module alone (which we call the FLD run) or coupled to RAMSES-RT (the HY run) within our hybrid approach. The opacities were originally used in the low-mass star formation calculations of Vaytet et al. (2013) which include frequency-dependent dust opacities (Semenov et al. 2003, Draine 2003). We modify the gray opacities to account for dust sublimation for $T > 1500$ K, as its importance for the shielding properties of massive disks has been highlighted in Kuiper et al. (2010b). We model it in the same way as Kuiper et al. (2010a) (Eqs 21 and 22 therein) with a dust-to-gas ratio that decreases with temperature, and a sublimation temperature that increases with the density. The profile of the dust-to-gas mass ratio is given by

$$\frac{M_{\rm dust}}{M_{\rm gas}}(\rho, T) = \left(\frac{M_{\rm dust}}{M_{\rm gas}}\right)_0 \left(0.5 - \frac{1}{\pi}\arctan\left(\frac{T - T_{\rm evap}(\rho)}{100}\right)\right) \tag{4.1}$$

where $\left(\frac{M_{\rm dust}}{M_{\rm gas}}\right)_0$ is the initial dust-to-gas mass ratio, and the evaporation temperature is given by

$$T_{\rm evap}(\rho) = g\left(\frac{\rho}{1\,{\rm g\,cm^{-3}}}\right)^{\beta} \tag{4.2}$$

with $g = 2000\,$K, $\beta = 0.0195$ (Isella & Natta, 2005). At high temperature, when all dust grains are evaporated, the gas opacity is dominant and is taken equal to $0.01\,{\rm cm^2\,g^{-1}}$ for comparison purposes with previous studies, such as Krumholz et al. 2009, Kuiper et al. 2014, Rosen et al. 2016, Klassen et al. 2016. Note that this treatment is not time-dependent, thus if the temperature decreases, the dust fraction increases again instantaneously instead of accounting for inertia in the process of dust creation/destruction.

4.1.2 Setup

We start from initial conditions similar to Rosen et al. (2016): a $150\,{\rm M_\odot}$ spherical cloud of radius 0.1 pc in a box of size 0.4 pc to limit boundary effects. The density profile is spherically-symmetric and $\rho(r) \propto r^{-1.5}$. The free-fall time is then

$$\tau_{ff} = \sqrt{\frac{3\pi}{32{\rm G}\bar{\rho}}} \simeq 42.5\,{\rm kyr}, \tag{4.3}$$

where G is the gravitational constant and $\bar{\rho}$ is the mean density computed for a uniform sphere of mass $150\,{\rm M_\odot}$. The density at the border of the cloud is 100 times the (uniform) density of the ambient medium. The cloud is in solid-body rotation around the x-axis with rotational to gravitational energy of ≈4%, typical of observed cores (Goodman et al., 1993). The initial dust-to-gas mass ratio is $\left(\frac{M_{\rm dust}}{M_{\rm gas}}\right)_0 = 0.01$.

The hydrodynamical solver chosen is the Lax-Friedrich solver, whose main asset here is its stability, at the price of a higher numerical diffusion than other solvers such as HLL (similar to that applied to radiative transfer in Sec. 3.3). The coarse resolution is level 7 (equivalent to a 128^3 regular grid) and the finest resolution is 4096^3 (*i.e.*, level 12, five levels of refinement), which gives a physical maximum resolution of 20 AU. In order to limit artificial fragmentation (Truelove et al., 1997), we impose to have at least 12 cells per Jeans length. Sink particles can only form in cells refined to the highest level. Sink creation sites are identified with the clump finder algorithm of Bleuler & Teyssier (2014). The clump finder algorithm marks cells whose density is above a given threshold ($3.85 \times 10^{-14}\,{\rm g\,cm^{-3}}$ in these calculations, which corresponds

to $n = 10^{10}$ cm^{-3}). The marked cells are attached to their closest density peak, which form a "peak patch". We check connectivity between the patches, then the significance of a peak patch is given by the ratio between the peak density and the maximum saddle density lying at a boundary of the peak patch. If the peak-to-saddle ratio is lower than a given value (2 here) the patch is attached to the neighbor patch of highest saddle density. The remaining peak patches are labeled as clumps. Each clump must then meet two conditions to lead to a sink creation: it has to be bound and subvirial. The region around a sink particle is also refined to the highest level. Sink particles gain mass by accreting material located within their accretion radius. The accretion scheme is based on a density threshold (Federrath et al., 2010). Consider a cell located within the accretion radius: its accreted mass by the sink is $\Delta m = \max(0.1(\rho - \rho_{\rm sink}) \times \Delta x^3, 0)$ (Bleuler & Teyssier, 2014), where Δx is the maximum resolution, $\rho_{\rm sink}$ is the Jeans density within the sink cell, and the choice of 0.1 is empirically-motivated. We merge sinks when their accretion radii overlap, while the accretion radius is set to $4\Delta x \approx 80$ AU. A softening length equal to the accretion radius is used to prevent the gravitational potential to diverge if the distance to the sink becomes small. The sinks actually model physics on much smaller scales than what can be captured in the simulation: each sink *represents* a star with a given radius and luminosity, from which we can derive an effective temperature. The radius and luminosity of the star mimicked by the sink are computed from the pre-main sequence evolution models of Kuiper & Yorke (2013) and depend on their time-averaged accretion rate and their mass.

4.1.3 Results - overview

We run one simulation with FLD only (denoted as FLD) and one with FLD+M1 (denoted as HY) until $t \simeq 30\,{\rm kyr} \simeq 0.71\tau_{\rm ff}$. As the initial density profile is peaked, a sink particle is expected to form in a few kyr. Both runs lead to the formation of several sink particles, one of which is much more massive than the other sink particles and that we refer to as the main sink or star. A disk and radiative outflows form around the main sink. The criteria for determining the disk and outflows are explained below. We identify a disk on a cell-basis after converting Cartesian coordinates into cylindrical coordinates centered on the main sink and aligned with the angular momentum vector (computed on a sphere of radius 100 AU), according to the several criteria of Joos et al. (2012):

- The disk is a rotationally-supported structure (*i.e.*, not thermally supported): $\rho v_\phi^2/2 > f_{\rm thres} P$, where v_ϕ is the azimuthal velocity and P is the thermal pressure. The value of $f_{\rm thres} = 2$ is chosen, as in Joos et al. (2012). Our use of $f_{\rm thres} > 1$ (instead of 1) leads to a more restrictive condition on the identification of cells belonging to the disk;
- In order to avoid large low-density spiral arms, a gas number density threshold is set: $n > 10^9\,{\rm cm}^{-3} = 3.85 \times 10^{-15}\,{\rm g\,cm}^{-3}$;
- The gas is not on the verge of collapsing too rapidly along the radial direction: $v_\phi > f_{\rm thres} v_r$, where v_r is the radial velocity;
- The vertical structure is in hydrostatic equilibrium: $v_\phi > f_{\rm thres} v_z$, where v_z is the vertical velocity.

We define outflows as gas flowing away from the central star at a velocity greater than the escape velocity, which corresponds to $v_r > v_{\rm esc} = \sqrt{2{\rm GM}_\star/r}$, where r is the distance to the sink and $\rm M_\star$ is the sink mass.

The time evolution of the main sink, disk and outflow masses, along with the accretion rate, are displayed in Fig. 4.2. First, the sink masses are almost equal in both runs before $t \simeq 14$ kyr

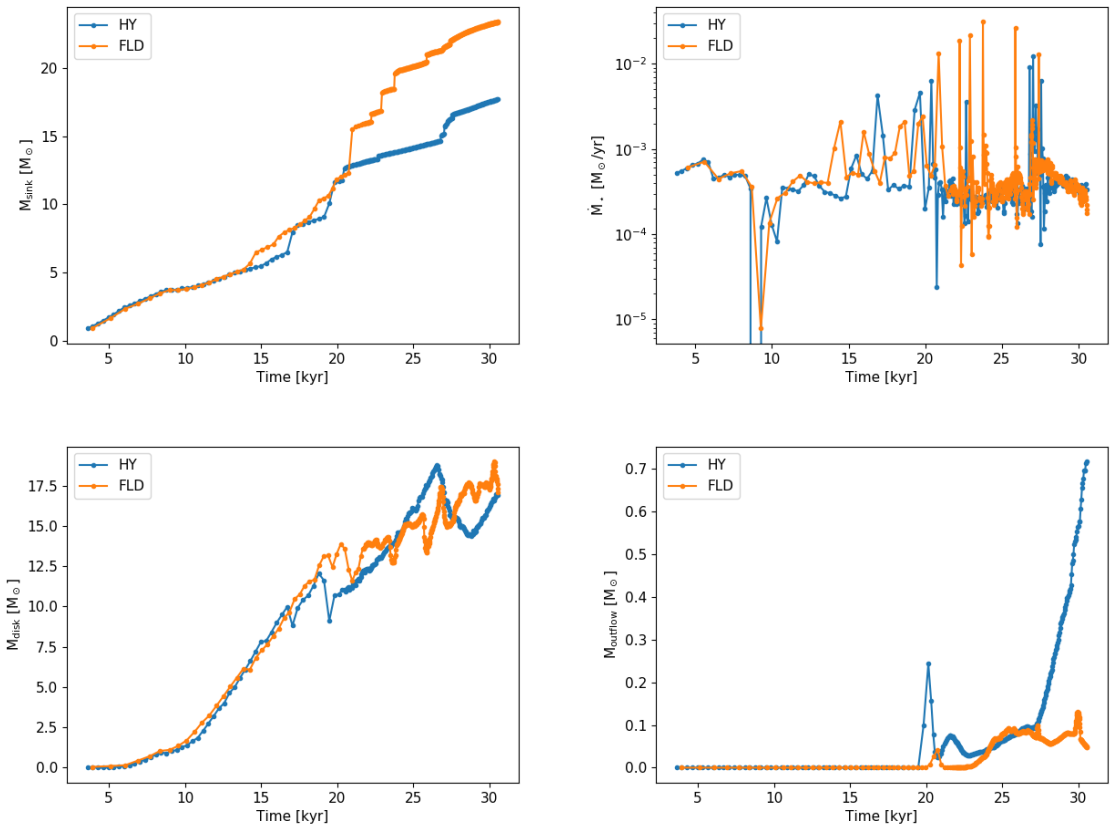

Figure 4.2: Time evolution of the main sink mass (top-left panel), accretion rate (top-right), disk mass (bottom-left), and outflow mass (bottom-right), for runs HY (blue) and FLD (orange).

and $M_\star = 5\,M_\odot$. Even though their evolution differs between 14 kyr and 20 kyr, their values remain similar and the divergence appears only at $t \simeq 20$ kyr, when $M_\star = 12\,M_\odot$ (in the HY run). At that point, the radiative cavities appear in the HY run (see the bottom-right panel of Fig. 4.2). They appear in the FLD run after the massive star has reached $16\,M_\odot$. From this time on, the sink mass increases more slowly in the HY run, this can be seen on the accretion rate (top-right panel of Fig. 4.2). The final stellar mass is $M_\star = 23.3\,M_\odot$ in the FLD run and $17.6\,M_\odot$ in the HY run.

As it is shown on the top-right panel of Fig. 4.2, the stars experience bursts of accretion separated by $\sim$100 yrs to a few kyr. These bursts are due to a low-mass companion (sink particle) being accreted by the most massive star. In each run, the main sink experiences accretion rates of $M_\odot \sim 10^{-4} - 10^{-2}\,M_\odot.yr^{-1}$, which is consistent with previous numerical studies (Klassen et al., 2016) and observations (review by Motte et al. 2018 and references therein). In total, eight companions are formed and accreted in each run. These accretion events contribute to a total of $6.7\,M_\odot$ in the FLD run and $3.9\,M_\odot$ in the HY run, hence about 28% and 22% of the final primary star mass, respectively. All sinks appeared after the primary mass was greater than $10\,M_\odot$ and were accreted in less than 3 kyr (except one, formed at large radius and which does not fall directly onto the primary sink). In each run, the most massive secondary is $\sim 2\,M_\odot$ and gathers most of its mass when orbiting close to the primary, in the disk densest regions. Our merging criterion can lead to overestimating the mass of the primary star and underestimate the system multiplicity, compared to Rosen et al. (2016) who allow merging only if the smaller sink particle is less massive than $0.05\,M_\odot$ and obtain a high multiplicity (29 companions more massive than $0.01\,M_\odot$). Assessing the impact of the merging criterion (as well as sink formation) would require a dedicaded study, which is beyond the scope of the current work but connected to the study presented hereafter (Sect. 4.2).

4.1.4 Disk properties

As shown in the bottom-left panel of Fig. 4.2, the disks obtained are massive ($\approx 17\,M_\odot$ at the end of the simulation) and similar in mass in both runs. The disk mass we obtain is also consistent with the previous numerical work of Klassen et al. (2016).

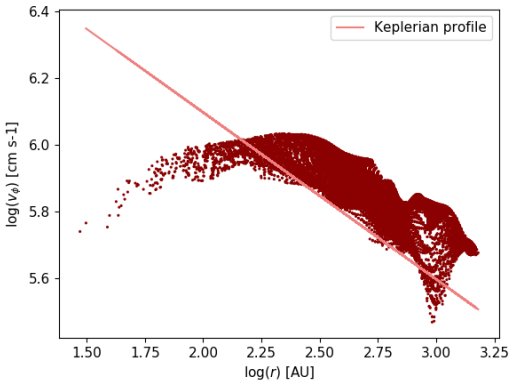

Figure 4.3: Radial rotational velocity profile in the disk cells for the HY run at $t = 30$ kyr and Keplerian profile computed with the main stellar mass. The sink softening length extends up to 80 AU ($\log(r) \approx 1.9$). The slope of the velocity profile is consistent with Keplerian rotation.

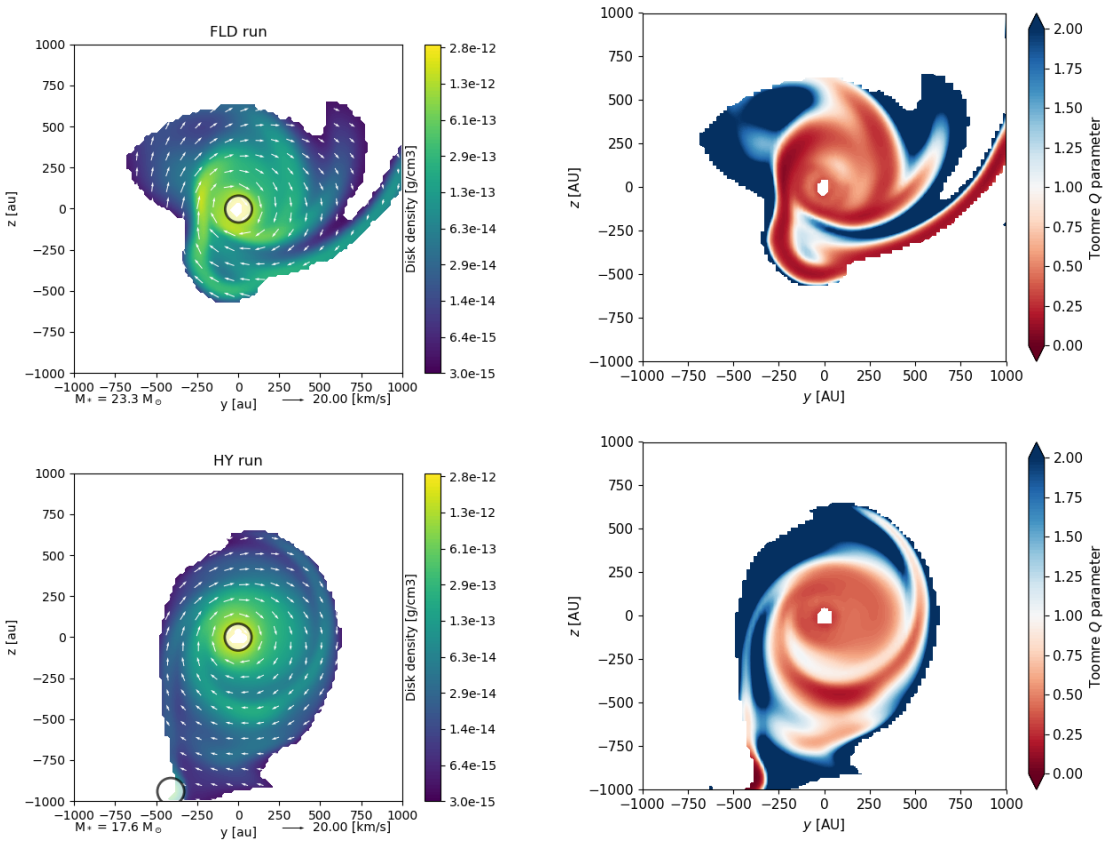

Figure 4.4: Density slices of the disk selection (left panels) and Toomre Q parameter (right panels) in a $(2000\,\mathrm{AU})^2$ region centered on the location of the most massive sink particle (left panels), in the FLD run (top) and the HY run (bottom), at $t = 30$ kyr. The corresponding particle density is $8 \times 10^8\,\mathrm{cm}^{-3} < n < 7 \times 10^{12}\,\mathrm{cm}^{-3}$.

We investigate the disk stability by computing the Toomre parameter Q defined by

$$Q = \frac{c_\mathrm{s}\kappa}{\pi G \Sigma} \tag{4.4}$$

where c_s is the sound speed, κ is the epicyclic frequency and is equal to the rotation frequency for a Keplerian disk and Σ is the surface density. We recall that the Toomre parameter computes the ratio of the thermal support and differential rotation support over gravitational fragmentation and that the disk is locally unstable if $Q < 1$. The gas in our simulation is initially in solid-body rotation but the disks formed exhibit rotation curves consistent with Keplerian rotation, as shown in Fig. 4.3, except very close to the sink because of the softening length. As a result, the epicyclic frequency κ is equal to Ω, the Keplerian angular frequency.

To compute Q, we have taken the surface density integrated over the x-axis (perpendicular to the disk). Moreover, the selection given by the criteria presented above gives a disk with a vertical structure. Therefore, we evaluate the Toomre Q parameter in the disk selection, then we average Q over the disk height. For completeness, we have also computed Q with c_s and κ evaluated in the disk midplane and have obtained very similar results.

We also take the radiation into account as an extra-support against fragmentation because the radiative pressure contributes to the sound speed (Mihalas & Mihalas 1984, eq. 101.22 therein)

$$c_\mathrm{s}^2 = \Gamma_1 \frac{P + P_\mathrm{r}}{\rho} \tag{4.5}$$

where P is the gas pressure, P_r is the radiative pressure; $\Gamma_1 = 5/3$ for a non-radiating fluid ($P_r = 0$, pure hydrodynamical case), and $\Gamma_1 \simeq 1.43$ if $P_g = P_r$). Therefore, we argue that even for a disk in a strong radiation field and gas-radiation coupling ($P_r \sim P_g$), Q only increases by a factor of $\simeq 1.3$ as compared to the pure hydrodynamical case. Figure 4.4 displays the local Toomre Q value taking the radiative support into account but the values of Q without the radiative support lead to the same conclusions.

As shown in Fig. 4.4, the disks obtained in both runs are Toomre unstable close to the massive star and in the spiral arms. This is consistent with the regular creation of sink particles in those spiral arms. Eight low-mass short-lived companions are generated in both runs. Even though the appearance of sink particles is quite resolution-dependent, we limit it with our refinement criterion based on the Jeans length.

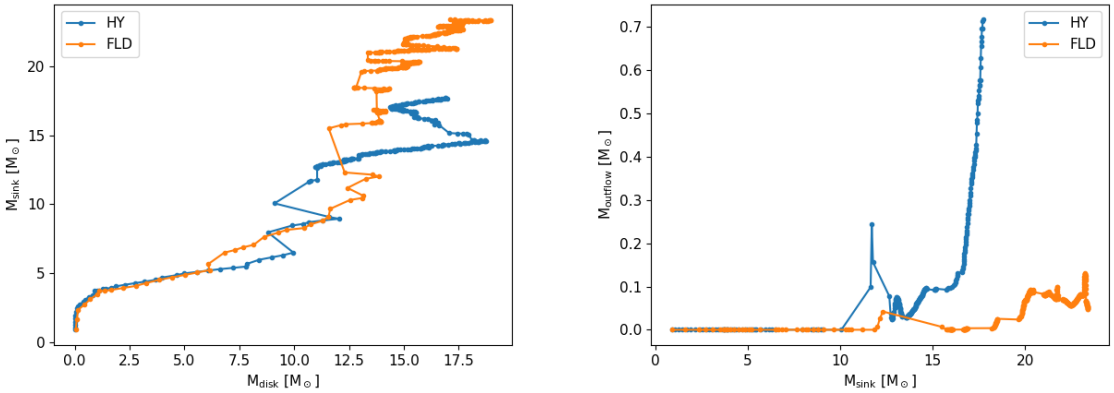

Figure 4.5: Primary star mass versus disk mass (left) and outflow mass versus star mass (right), for both FLD and HY runs.

The left panel of Fig. 4.5 shows the main star mass against the disk mass. Both generally increase with time but the disk also undergoes losses of mass as it feeds the main sink particle. Indeed, the main accretion mode in our simulation is disk accretion, although the accretion bursts are due to the accretion of sink particles recently created in the Toomre unstable spiral arms of the disk. The accretion in our simulation is more stable than what is obtained in the work of Klassen et al. (2016), where the global disk instability leads to an increase of $\simeq 10\,M_\odot$ in a few kyr in their $100\,M_\odot$ run. The disks obtained within this work have a radius $R \simeq 500 - 1000$ AU, typical of massive star formation simulations including radiation-hydrodynamics and neglecting magnetic fields. Starting from different initial conditions ($M = 120\,M_\odot$, $\rho \propto r^{-2}$), Kuiper et al. 2010a and Kuiper et al. 2011, in 2D and 3D, respectively, obtained larger disks (structures in Keplerian rotation) with $R \gtrsim 1000$ AU. Observational constraints on the disk mass remain sparse (Motte et al., 2018), but a few examples of massive and large disks exist, such as AFGL4176, a $\sim 25\,M_\odot$ star observed with ALMA which exhibits a disk of radius $\approx 1000 - 2000$ AU and mass $\approx 12\,M_\odot$ in Keplerian-like rotation (Johnston et al., 2015). Finally, this disk has recently been found to be Toomre-unstable and to possess spiral arms (Johnston et al., 2020), which is consistent with our results.

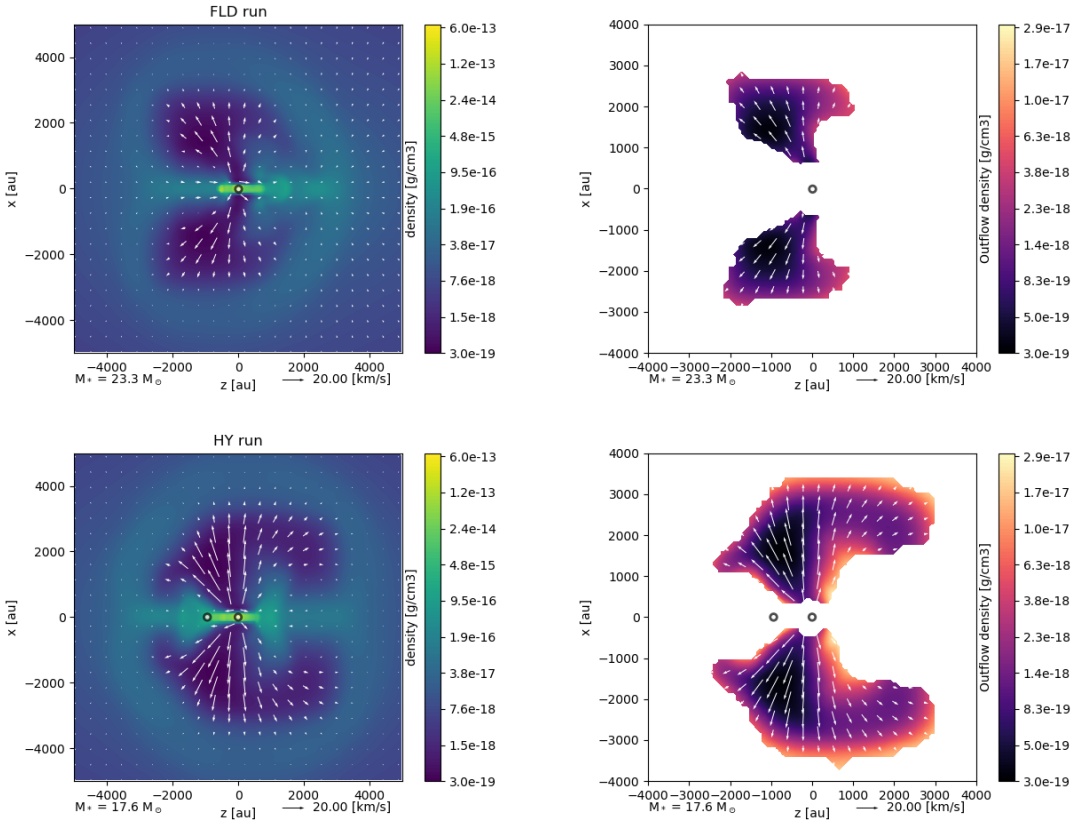

Figure 4.6: Left panels: density slices perpendicular to the disk in a $(10000\,\mathrm{AU})^2$ region. Right panels: density in outflow selections in a $(8000\,\mathrm{AU})^2$ region. Top panels: FLD run; bottom panels: HY run. $t = 30$ kyr. Figures are centered on the location of the most massive sink particle and velocity vectors are overplotted. The corresponding particle densities are $7 \times 10^4\,\mathrm{cm}^{-3} < n < 2 \times 10^{12}\,\mathrm{cm}^{-3}$ (left panels) and $7 \times 10^4\,\mathrm{cm}^{-3} < n < 7 \times 10^6\,\mathrm{cm}^{-3}$ (right panels).

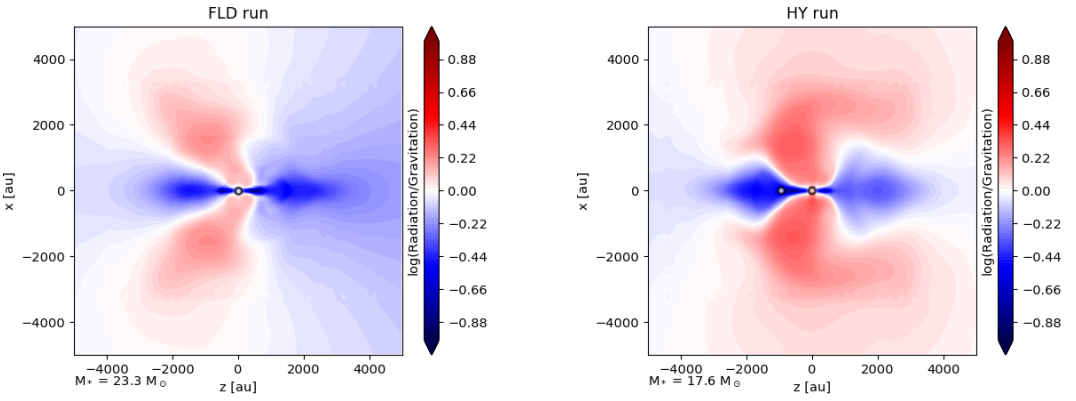

Figure 4.7: Radiative force to gravitational force normalized ratio in the FLD run (left panel) and HY run (right panel) in a $(10000\,\mathrm{AU})^2$ region perpendicular to the disk. $t = 30$ kyr. Figures are centered on the location of the most massive sink particle. Regions of outflows (see Fig. 4.6) are dominated by the radiative force.

4.1.5 Radiative cavities - outflows

As mentioned in Sec. 4.1.3, we define outflows as gas flowing away from the central star at a velocity greater than the escape velocity. In the FLD run, radiative cavities appear at $t \simeq 22$ kyr (bottom-right panel of Fig. 4.2). They develop earlier and at lower stellar mass ($M_\star = 12\,\mathrm{M}_\odot$, $t \simeq 20$ kyr) in the HY run than in the FLD run ($M_\star = 16\,\mathrm{M}_\odot$, right panel of Fig. 4.5). In both runs, the cavities grow symmetrically with respect to the disk plane until they reach an extent of $\simeq 2000$ AU in the FLD run and $\simeq 3000$ AU in the HY run at $t \simeq 30$ kyr (see Fig. 4.6). The right panels of Fig. 4.6 display a slice of the density within the outflow selection of cells. Cavities are made of low-density material, with $\rho \simeq 10^{-19}\,\mathrm{g\,cm^{-3}}$ ($n \simeq 10^4\,\mathrm{cm^{-3}}$). The gas velocity is also higher in the HY run, $\approx$25 km s^{-1}, against $\approx$15 km s^{-1} in the FLD run. As displayed in Fig. 4.7, gas is pushed away by the radiative force, which locally exceeds gravity. It illustrates the flashlight effect: the radiative force dominates in the poles while the gravity, and hence the accretion, dominates in the disk plane. The consequence of the stronger radiative force is that the outflows in the HY run are able to transport higher density gas than in the FLD run (see right panels of Fig. 4.6) as it spans a wider angle, particularly in the vicinity of the star (see Fig. 4.7). Indeed, the outflows displayed in Fig. 4.6 have masses $M_{\mathrm{o,HY}} \simeq 0.6\,\mathrm{M}_\odot > M_{\mathrm{o,FLD}} \simeq 0.06\,\mathrm{M}_\odot$, as displayed on the bottom-right panel of Fig. 4.2. During almost all the simulations the outflows in the HY run are more massive than in the FLD run. In addition, the temporal evolution at $t \simeq 30$kyr seems to show that this mass is still going to increase in the HY run but not in the FLD run. We finally note that the peak in the outflow mass at $t \simeq 20$kyr is due to the launching of the outflows in a high-density medium close to the star, which therefore gives a higher outflow mass: the low-density cavity has not formed yet.

4.1.6 Accretion via Rayleigh-Taylor instabilities?

No Rayleigh-Taylor instabilities appear in the aforementioned runs (FLD and HY). They have been shown to contribute significantly to the star-disk system evolution and to the final mass of the star in several studies (Krumholz et al., 2009, Rosen et al., 2016, Rosen et al., 2019). Discussions about the presence of these instabilities in massive star formation simulations lean on arguments of numerical resolution, since the smaller-scale modes are the most unstable (Jacquet & Krumholz, 2011). Here we try to tackle this problem by cranking up the resolution to see if we get any.

We conduct a run whose spatial resolution permits one to resolve the seeds of radiative Rayleigh-Taylor instabilities. We call this run HY-RTi, based on the HY run restarted at the time when radiative cavities appear. We rely on the AMR framework to resolve the radiative cavities interfaces with a refinement strategy based on the gradient of the stellar radiation

$$\frac{\nabla E_{\mathrm{M1}} \Delta x}{E_{\mathrm{M1}}} < 10\%, \tag{4.6}$$

where E_{M1} is the M1 module radiative energy and Δx the cell width. This means that if the radiative energy of the M1 module changes by more than 10% between two adjacent cells, these cells are flagged for refinement. We add a second and a third conditions to flag a cell: $E_{\mathrm{M1}} > E_{\mathrm{thres}} = 3 \times 10^{-12}\,\mathrm{erg\,cm^{-3}}$, and $\|x\| > 1500$ AU (over and under the sink-disk plane). The last condition is applied once the cavities are developed beyond this height. The second and third criteria are necessary to not over-refining other regions than the interfaces of the cavities, which would explode the cost of the simulation.

The left panel of Fig. 4.8 shows the radiative cavities in the HY-RTi run with AMR level contours overplotted and the right panel of Fig. 4.8 displays the M1 radiative energy with respect to the radius. The zone within the contours "11" is at the AMR level 12, which is the highest level. Contours show that the radiative energy drop around $R = 5000$ AU is resolved

to the AMR level 12, which is the highest level. As a result, the finest resolution is put on the cavity interfaces. Despite this refinement strategy, no radiative Rayleigh-Taylor instability has

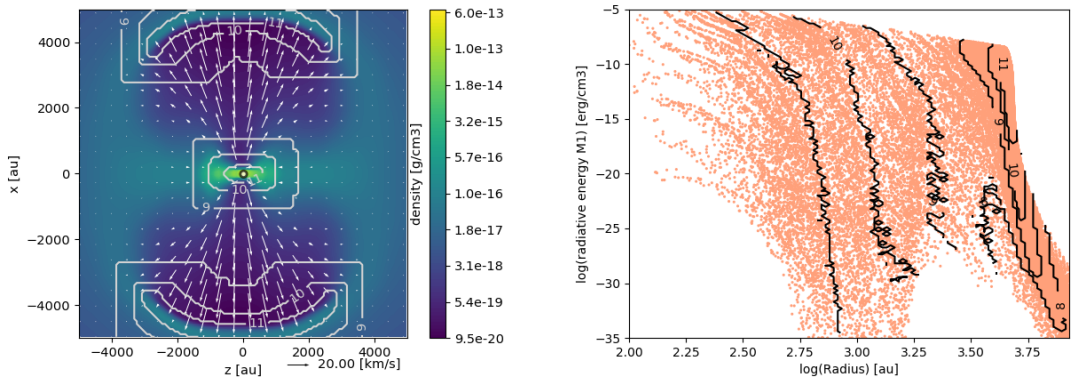

Figure 4.8: HY-RTi run at $t{\sim}0.7\tau_{\rm ff}$. Left panel: density slice perpendicular to the disk in a $(10000\,\mathrm{AU})^2$ region. Right panel: scatter plot of the M1 radiative energy against the radius. Contours show the AMR level. The cavity edges are zones of primary absorption for the stellar radiation and are resolved to the highest level (12).

developed in any of our simulations. We explain below why this result is not numerical but physical.

We compare the typical advection time of the flow $\tau_{\rm adv}$ and the growth time of the instability $\tau_{\rm instab}$; the condition for the instability to develop is $\tau_{\rm adv} > 3\tau_{\rm instab}$ (Foglizzo et al., 2006). First, the flow in the bubble has supersonic speeds and forms a shock of thickness $H{\simeq}300$ AU (measured on the density profile) when it encounters the accretion flow. In the shock frame (whose velocity is $2\,\mathrm{km\,s^{-1}}$), we measure a gas velocity of $10\,\mathrm{km\,s^{-1}}$. Hence, the advection timescale of the gas in the shock is $\tau_{\rm adv} \simeq 0.1$ kyr.

We now compute the growth rate of the Rayleigh-Taylor instability for the shortest perturbations we can capture (of spatial scale $\lambda = \Delta x_{\rm min} = 20$ AU, which is the fastest growing mode) using the equation (80) from Jacquet & Krumholz (2011). We obtain a growth rate of $\omega \simeq 4.5\,\mathrm{kyr^{-1}}$, hence a growth timescale of $\tau_{\rm instab} \simeq 0.2$ kyr. This is longer than the advection timescale $\tau_{\rm adv}$, so the gas is advected before the instability develops. Furthermore, the calculation in Jacquet & Krumholz (2011) is based on the adiabatic approximation which is valid when the cavity edge temperature is taken to be equal to the dust sublimation temperature (~ 1100 K). Numerically, we get a temperature of a few ~ 100 K at the cavity edge, thus the adiabatic approximation breaks down in our simulation. Physically, the cavity edge is mainly heated by stellar radiation, which is geometrically diluted in the optically-thin cavity. Therefore, it can be shown that the cavity edge should have a temperature of a few 100 K at a distance of ~ 3000 AU from a $\sim 10^5\,\mathrm{L_\odot}$ source. Moreover, the cavity interior is optically-thin and thus is not adiabatic, as mentioned in Jacquet & Krumholz (2011). If compressed, the gas radiates away its energy instead of heating as an optically-thick gas (adiabatic) would.

For these reasons, we go one step further and relax the adiabatic approximation in the cavity interior. Hence, the entropy within the cavity cannot account for radiation. We compute the total entropy (gas plus radiation) as a function of the coupling between gas and radiation via the local optical depth τ. We recall here how the entropy of a photon gas is obtained, starting from the thermal radiative pressure derived in Eq. 2.16: $P_{\rm r} = \frac{1}{3}a_{\rm R}T^4$. The first law of thermodynamics states (in terms of extensive variables)

$$T dS_{\rm rad} = d\varepsilon + P_{\rm r} dV = d(E_{\rm r} V) + P_{\rm r} dV, \tag{4.7}$$

where ε is the internal energy, and $E_\mathrm{r} = \mathrm{a_R} T^4$. Once integrated, the entropy of radiation is

$$S_\mathrm{rad} = \frac{4}{3}\mathrm{a_R} T^3 V = 4\frac{P_\mathrm{r} V}{T}. \tag{4.8}$$

Hence, the total specific entropy we derive is

$$s_\mathrm{tot} = \frac{k_\mathrm{B}}{m(\gamma-1)} \ln\left(P_\mathrm{g}\,\rho^{-\gamma}\right) + \min(\tau, 1)\frac{4P_\mathrm{r}}{\rho T}, \tag{4.9}$$

where k_B is Boltzmann's constant, m is the molecular hydrogen mass, P_g is the gas pressure, and P_r is the radiation pressure. The first term corresponds to the standard gas entropy.

The maximum growth rate is given by the Brunt-Väisäla (or buoyancy) frequency, which is the oscillation frequency of a fluid particle in a stratified medium

$$\omega = \sqrt{\frac{\gamma-1}{\gamma} g_\mathrm{eff} \nabla S}, \tag{4.10}$$

where S is the total entropy s_tot normalized by k_B/m and g_eff is the effective gravity $g_\mathrm{eff} = g - \kappa F/\mathrm{c}$, with $\kappa F/\mathrm{c}$ the radiative acceleration. We compute ω in our simulation at the bubble edge and get $\omega \lesssim 10\,\mathrm{kyr}^{-1}$, which gives $\tau_\mathrm{instab} \gtrsim 0.1\,\mathrm{kyr} \simeq \tau_\mathrm{adv}$. Therefore, no Rayleigh-Taylor instability should develop in our simulation.

4.1.7 Physical outcomes

We have applied the hybrid radiative transfer and the FLD methods to a radiation-hydrodynamical problem: the collapse of a massive prestellar core. Both runs lead to the formation of a massive star ($M > 8\,\mathrm{M}_\odot$). The multi-dimensionality of our simulations leads to accretion via the flashlight effect: accretion occurs through a disk while radiation escapes via the poles (Yorke & Sonnhalter, 2002). Low-mass sink particles are created in the Toomre unstable spiral arms of the disk, they move together with the fluid and are rapidly accreted onto the central massive star. At the end of the simulation ($t \simeq 30\mathrm{kyr} \simeq 0.71\tau_\mathrm{ff}$), the star mass is $23.3\,\mathrm{M}_\odot$ in the FLD run and $17.6\,\mathrm{M}_\odot$ in the HY run, showing no signs of decrease in the accretion. When the star reaches $12\,\mathrm{M}_\odot$ (HY run) or $16\,\mathrm{M}_\odot$ (FLD run), radiative polar cavities develop because of the stellar radiative pressure. The difference in stellar masses can be explained by the direct radiative pressure onto the disk and the wide-angle cavity, which lowers the total accretion rate. Radiative outflows in the HY run are $\sim$50% more extended than in the FLD run. The cavities are found to be stable, even when refining their edge to the finest resolution. We have computed the growth time scale of radiative Rayleigh-Taylor instabilities, which is longer than the time scale at which gas is advected through the cavity edges. To summarize, disk accretion is found to be sufficient at feeding the star, while no radiative Rayleigh-Taylor instability develops.

Our method also contains a few assumptions and limitations we shall discuss. As shown in Sec. 3.5, the hybrid method is accurate within $\approx 25 - 65\%$ in the optically-thick limit. In the prestellar core collapse problem, the accretion disk around the protostellar source is very optically-thick ($\gtrsim 10^3$) and the photon mean free path is barely resolved in AMR codes with current computational facilities. The disk midplane temperature is therefore affected by this error: it is generally overestimated (no matter the method), which increases the Jeans length and therefore stability. Physically, the disk midplane is colder and could be prone to fragmentation. Meanwhile, the temperature in the optically-thin cavities is computed more accurately with the hybrid method.

In the following subsection, we assess the performance of the hybrid method in this radiation-hydrodynamical application by comparing the computational time. Indeed, as explained in Sect. 3.5.4, such a comparison was not meaningful in the pure radiative transfer tests where the time step could be controlled, especially for the implicit FLD method.

4.1.8 Performance

Here, we look at the total CPU time in the previous collapse calculations. The HY run took ≈ 5100 CPU hours, against ≈ 3900 for the FLD run, which consists in an additional time of about $\approx 30\%$. The time step in the HY run is first constrained by the M1 CFL condition when the primary sink forms, which is responsible for this difference of computational time: more steps were needed to reach the same physical time. As mentioned in Sec. 3.2, the FLD modifies the hydrodynamical CFL time step : the sound speed accounts for both thermal and radiative pressures. It decreases as the radiative pressure (hence energy) increases, while the M1 time step is fixed. As the central sink gains mass, its temperature and luminosity generally rise and so does the radiative energy. Therefore, the FLD time step decreases in both runs, but is still greater than the M1 time step in the HY run, at first. Then when the outflows are launched, both runs are limited by the FLD time step, because both the radiative energy has become significant and the density is very low in the outflow (hence the modified sound speed increases). From this time on, the time step is comparable in both runs. However, the number of iterations in the conjugate gradient is $\sim 10\%$ smaller in the HY run than in the FLD run, and so is the elapsed time per time step.

After this first application of the hybrid radiative transfer method in a radiation-hydrodynamical context, we present preliminary results on disk fragmentation, as modelled by two radiation-hydrodynamical codes, namely PLUTO and RAMSES.

4.2 Modelling disk fragmentation in numerical codes

4.2.1 Context

The multiplicity is higher for massive stars than for their low-mass counterpart (see, *e.g.*, Duchêne & Kraus 2013 and brief discussion in Sect. 1.2). Moreover, the scenario of disk-mediated accretion is currently supported by both observations (see *e.g.*, Girart et al. 2017) and numerical experiments, including ours (Sect. 4.1.4). Disk fragmentation is one of the mechanisms that can lead to a multiple stellar system. Observational constraints on disks around massive protostars are becoming increasingly numerous, and ALMA is now providing the first clues of disk fragmentation (Ilee et al., 2018). Hence, the questions of multiplicity and disk fragmentation are to be tackled in numerical simulations.

Meanwhile, the use of sink particles to mimic the formation of stars at smaller scales than what can be numerically resolved, may affect both the disk presence (*e.g.*, Rosen et al., 2016) and its fragmentation. Hence, this topic is of main importance for the numerical studies of massive star formation and in line with the observational capabilities (Ahmadi et al., 2019). It has been recently studied in a work that focused on the disk properties and evolution in a radiation-hydrodynamical context, without using sink particles except for the central object (Mercado-Oliva & Kuiper, *subm.*, hereafter OK20). In this section, we present the preliminary results regarding a side-project to this thesis, in collaboration with A. Mercado-Oliva and R. Kuiper from the University of Tübingen. We focus on a comparison between the RAMSES code (Teyssier, 2002) and the PLUTO code (Mignone et al., 2007) at modelling disk fragmentation in the context of high-mass star formation.

Let us first present the numerical tools used in OK20, and how we can provide a complementary point of view. PLUTO integrates the equation of hydrodynamics with a frequency-dependent ray-tracing technique for the stellar irradiation (Kuiper et al., 2010c), while the diffuse emission is treated with the FLD method. The spatial grid is spherical, centered on the (massive) protostar, and allows for a logarithmic spacing along the radial direction. This leads to a particularly high spatial resolution in the disk inner regions, as compared to Cartesian AMR codes with the same total number of cells, and facilitates the implementation of ray-tracing techniques for the treatment of irradiation. The price to pay is the assumption on the problem's geometry, *i.e* a single star fixed at the center, which is not adapted to multiple stellar systems. Moreover, the resolution decreases with the radius and some components of interest cannot be fully resolved, typically the outflow cavity edges and the outer parts of the disk. One aim of their study is to show that the Jeans length (defined in Sect. 1.9) is not properly resolved in most numerical works done with AMR codes, which could lead to spurious fragmentation and excessive formation of sink particles (Fig. 4.9). More quantitatively, it shows that a finest resolution of 5 AU is required to avoid the aforementioned problem, in this particular setup. The disk pressure scale-height must also be resolved, but this condition appears to be much less restrictive, except very close to the star (< 30 AU). Since the RAMSES grid is Cartesian and we have used sink particles throughout this thesis (we can also choose not to, see below), we compare the results obtained with both approaches in order to increase this study's robustness. In addition, the AMR framework allows us to have a finer resolution than OK20 in the outer regions of the disk, if the refinement conditions are met. Throughout this thesis, we set the refinement criterion so that the Jeans length has to be refined by at least 12 cells, while being limited by the finest resolution of 5 AU in the current study.

We will first run a simulation with only one sink particle, to mimic the numerical method of OK20 and compare the disk properties (Sect. 4.2.3), then we extend our study to the presence of secondary sink particles. Let us note that OK20 do not use sink particles, hence in their analysis

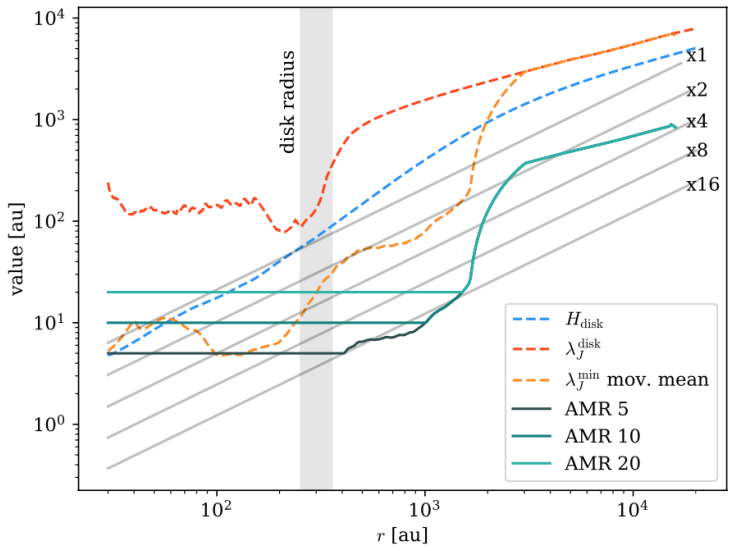

Figure 4.9: From OK20: Comparison of disk midplane grid cell sizes in their fixed grid (gray lines) and the resolution with an AMR grid (green lines). At large scale, the AMR cell sizes are taken as $\lambda_{\rm J}^{\rm min}/8$, following Rosen et al. (2016); at small scale, it is the higher resolution available ($5-10-20$ AU for AMR 5, 10, 20, respectively). The different relevant scales of the system are shown in dashed lines: the pressure scale-height $H_{\rm disk}$ (blue), the azimuthal median Jeans length (red) and the minimal azimuthal Jeans length (orange), averaged for the time period [6,8] kyr, and the corresponding disk radius is shown in the gray box. The number following the label for the AMR curves indicates the minimum cell size in au. The lines label their various runs, from the lowest (x1) to highest resolution (x16) run.

they distinguish the *fragments* (*i.e.* hydrodynamical objects) that could lead to gravitational collapse, and the background disk, via post-processing tools. Fragments are gas structures and are detected by their temperature exceeding that of the background disk. This choice is intended to detect structures additionally heated by compressional motions, while a density criterion would preferably lead to spiral arms and short-lived structures formed by gas collision. A clear distinction is made between the gaseous disk and sink particles in our RAMSES run, which are different objects. Hence, fragments and sink particles (which are able to radiate as protostars, for example) are intrinsically different. After comparing the background disk properties, we we will study the temporal evolution of the most massive sink properties, which is equivalent to their central star. Finally, OK20 follow the fragments with a post-processing tracker, in order to study their properties (and number) as a function of time. With the objective to follow our fragments properties with the same tools as OK20, we will present our method to convert our AMR Cartesian grid-based variables on PLUTO's spherical grid to use this tracker in Sect.4.2.6. When not using sink particle nor post-processing tool to detect fragments, we will refer to overdensities as *clumps*.

4.2.2 Initial conditions

We use similar initial conditions as OK20 (Meyer et al., 2018). We start from a massive pre-stellar core of mass $M_{\rm c} = 200 M_\odot$ and radius $R_{\rm c} = 20\,625$ AU$\sim$0.1 pc, whose density profile follows

$$\rho(r) = \rho_0 \left(\frac{r}{r_0}\right)^{-3/2}, \tag{4.11}$$

where $\rho_0 = 2.89 \times 10^{-14}\mathrm{g\,cm^{-3}}$ at $r_0 = 30$ AU, which sets the domain inner boundary in OK20. This results in a mean density $\bar{\rho} = 3.25 \times 10^{-18}\mathrm{g\,cm^{-3}}$ and an approximate free-fall time

$$\tau_{ff} = \sqrt{\frac{3\pi}{32\mathrm{G}\bar{\rho}}} \simeq 37.6\mathrm{kyr}. \tag{4.12}$$

OK20 have chosen the theoretically-motivated (*i.e.* not representative of typical cores rotation profiles) setup from Meyer et al. (2018) which favors fragmentation, because of the initial differential rotation imposed by the angular frequency:

$$\Omega(R) = \Omega_0 \left(\frac{R}{10\mathrm{AU}}\right)^{-3/4}, \tag{4.13}$$

where R is the cylindrical radius, and $\Omega_0 = 9.84 \times 10^{-11}\mathrm{s^{-1}}$, which results in a rotational-to-gravitational energy ratio of 5% (see Appendix B). It has been used by Meyer et al. (2017) to study the accretion bursts of massive protostars as a result of the accretion of disk clumps. As in OK20, we use outflow boundary conditions and a minimal temperature of 10 K. In the following section, we present the results obtained with the formation of secondary sink particles turned off and a HLL-type Riemann solver (HLLD for RAMSES, Miyoshi & Kusano 2005, HLLC in OK20). In Sec. 4.2.5, we run the same simulation with sink particles and the Lax-Friedrich solver for its robustness and because it allows for bigger time steps. We will refer to the first run as run 1SINK and the second one as run SINKS, for readability.

4.2.3 Disk properties

Let us present an evolution overview of the simulation. We enforce a single sink particle creation at the beginning of the run, to mimic the conditions in OK20. While the central density increases, cylindrical symmetry is broken within ≈4 kyr, when a dense clump forms in the sink vicinity and moves outward, while two dense ($\rho > 10^{-12}\,\mathrm{g\,cm^{-3}}$, corresponding to $n > 3 \times 10^{11}\,\mathrm{cm^{-3}}$) rotating disks grow around the sink and the clump, respectively. The two disks are linked by a gas filament and form a symmetric structure until then. Such structures have been observed in OK20 as well, linking fragments together. The development of spiral arms occurs around each disk, while the gas filament acts as a nonaxisymmetric perturbation. As the background disk of density $\rho > 10^{-14}\,\mathrm{g\,cm^{-3}}$ ($n > 3 \times 10^{9}\,\mathrm{cm^{-3}}$) grows, the sink and the clump move away from each other. The growth of spiral arms and their interaction with the sink-clump gas filament leads to secondary clump formations, which quickly enhance the system complexity. One of these secondary clumps develops its own disk-like structure. It is neither well defined nor long lived, because of the tidal effects and numerous collisions with clumps and spiral arms. After approaching the sink at a distance of ∼150 AU to the sink, the aforementioned secondary clump gets tidally disrupted. The remaining gas collides with the sink-clump gas filament. This collision projects gas outside of the disk plane, which falls back onto the sink, leading to the vertical density structure visible on the bottom-right panel of Fig. 4.10. The sink benefits from these events by accreting a massive ∼5 $\mathrm{M_\odot}$ clump in less than 100 yr. We choose to stop the simulation at that time because the time step diminishes prohibitively for numerical reasons linked to the HLLD solver. At the end of the run, t∼17.3 kyr, the system is still highly dynamical, with a ≈17.4 $\mathrm{M_\odot}$ protostar surrounded by the long-lived clump (top-right panel of Fig. 4.10). In comparison with OK20, we obtain a system that is not centered at all on the most massive object until it reaches ∼5 $\mathrm{M_\odot}$, corresponding to $t > 12$ kyr. Before ∼12 kyr, the stellar luminosities in both runs differ by several orders of magnitude (right

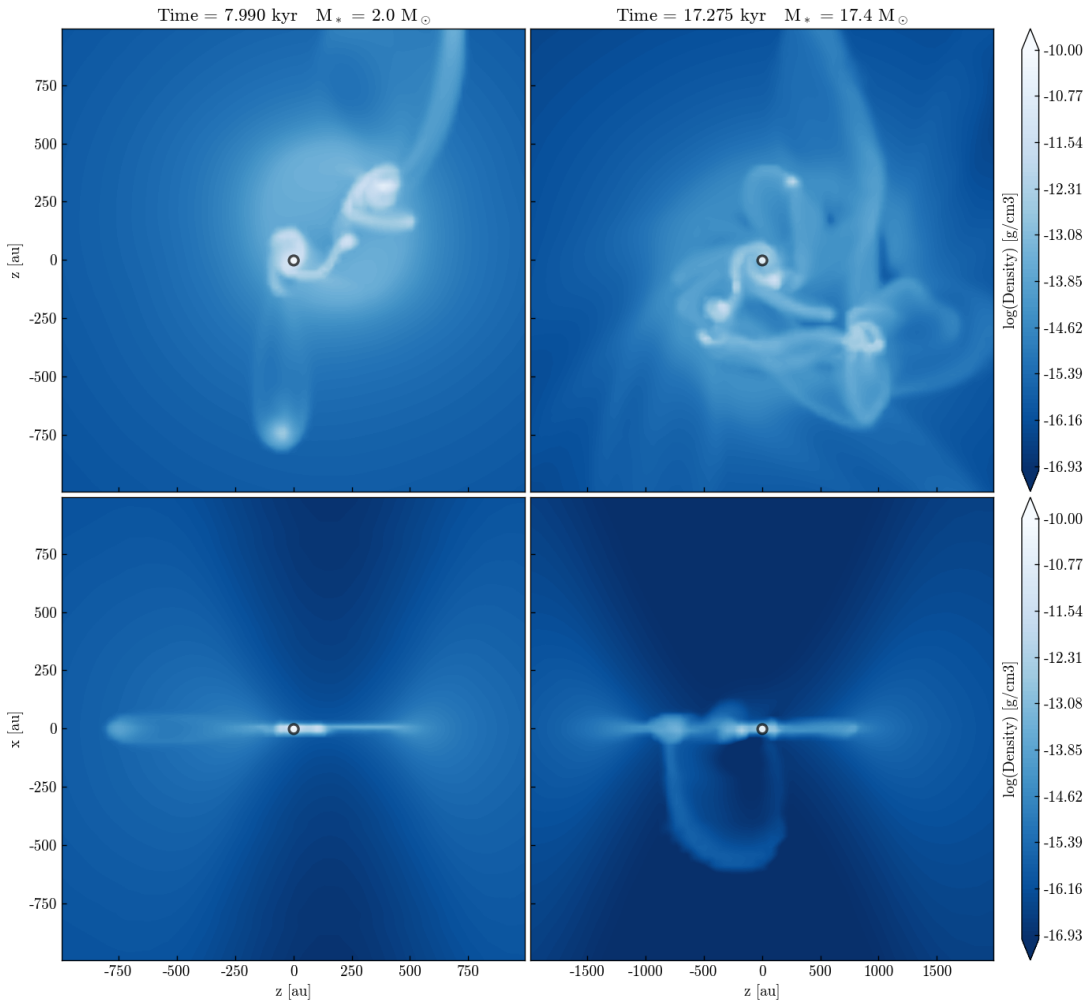

Figure 4.10: Density slices of size 2000 AU (left column) and 4000 AU (right column) at times ≈8 kyr (left column) and ≈17.5 kyr (right column) in the disk plane (top) and perpendicularly to the disk (bottom), in the RAMSES run 1SINK. The slices are centered on the sink particle.

panel of Fig. 4.13), as discussed below. For these reasons, we compare the global disk properties in this run and in OK20 after $t = 12$ kyr.

Let us first focus on the radial profiles of the density, temperature and Keplerianity in the disk plane to quantify the differences between both codes. All profiles and snapshots are centered on the sink particle. As in OK20, we take the azimuthal median value, in order to filter-out the fragments/spiral patterns and to obtain the background disk properties. However, our disk is characterized by the presence of the second massive clump and the many clump-clump, clump-spiral arm and clump-filament collisions, hence the median does not remove all azimuthal variability. Regarding the density and Keplerianity, as in OK20, we average the quantity over a period of 4 kyr between 12 kyr and 16 kyr, then between 16 kyr and the end of our run, in order to smooth out the variations due to orbital motions. We plot these quantities starting from the innermost radius with respect to the sink, *i.e.* our finest resolution, 5 AU. The

inner boundary of PLUTO's grid is at a radius 30 AU, as indicated by the vertical line, and is located beyond our sink accretion radius (20 AU).

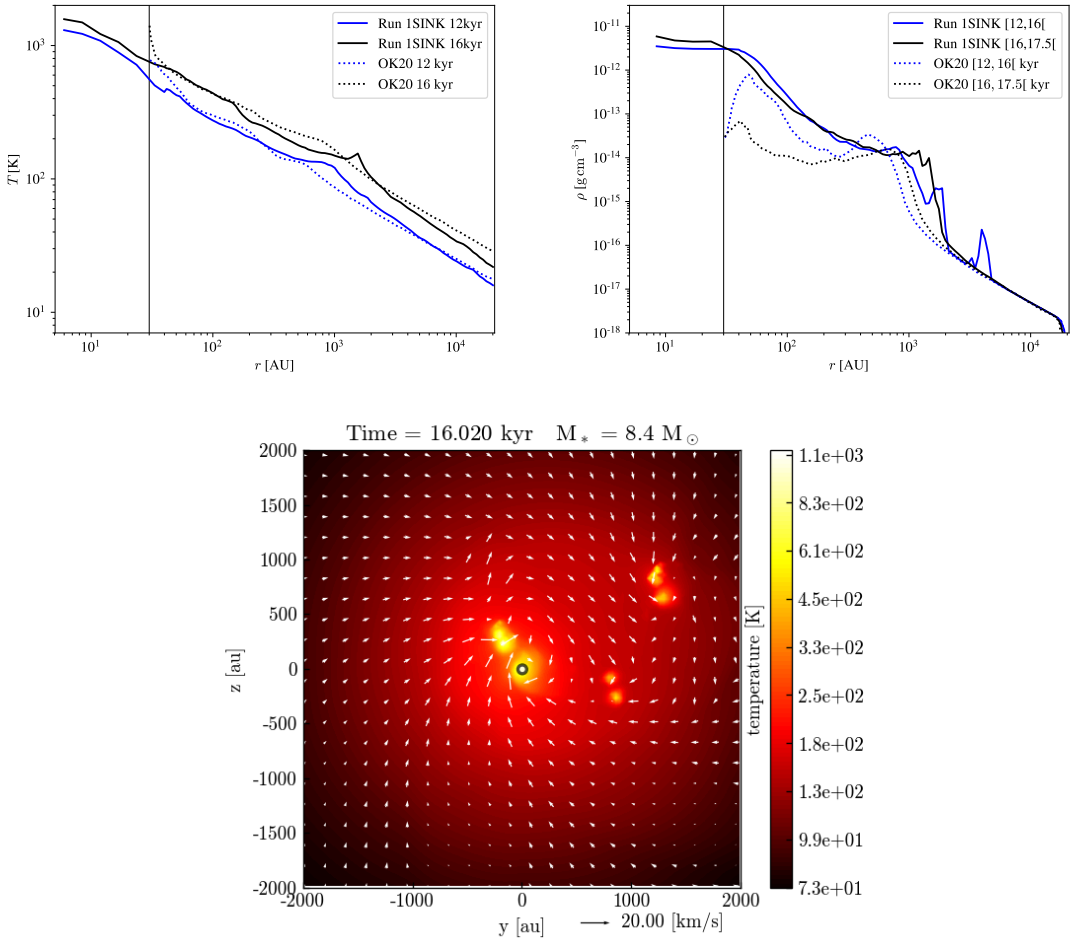

Figure 4.11: Radial temperature (top left) and density (top right) profiles in the disk midplane. The density profiles are time-averaged over $[12, 16[$ kyr and $[16, 17.5[$ kyr. Bottom panel: temperature slice of size 4000 AU in the disk plane at $t \approx 16$ kyr. Velocity vectors are overplotted. Run 1SINK.

Before comparing the temperature profiles, let us recall that OK20 include the accretion luminosity in their work. The total luminosity L is $L \equiv L_{\rm int} + L_{\rm acc}$, where the internal luminosity $L_{\rm int}$ is given by Pre-Main Sequence tracks, while the accretion luminosity varies as $L_{\rm acc} \propto \dot{M}$ where $\dot{M}$ is the instantaneous accretion rate. For a typical accretion rate of $10^{-3}\,{\rm M}_\odot\,{\rm yr}^{-1}$ and a stellar mass $< 10\,{\rm M}_\odot$, the total luminosity is roughly equal to the accretion luminosity $\sim 10 L_\odot$ (Hosokawa et al., 2010), whereas the internal luminosity is less than $\sim 0.1 L_\odot$. As shown on the right panel of Fig. 4.13, it dominates at early ($t < 12$ kyr) times. We choose to compare the temperature profiles after $t \sim 12$ kyr so that the two stellar luminosities are comparable.

The temperature profile (top-left panel of Fig. 4.11) is lower than that obtained with PLUTO with $T \sim 550$ K at $t = 12$ kyr at the disk inner edge, against $T \sim 750$ K. As their simulation domain is, by construction, optically-thin below 30 AU, their temperature at ~ 30 AU is higher than in our case, where most of the stellar radiation has been absorbed on the way. Let us compare the temperature profiles throughout the disk and beyond. On the method side, most radiation

within the disk is modelled by a gray FLD method in both runs, which lead to a similar temperature structure, provided the disk densities are in reasonable agreement. Hence, we interprete the differences we may obtain in terms of different disk structures and thermodynamics.

Two distinct radiative regimes are clearly visible on the temperature profiles: an optically-thick disk and an optically-thin medium at larger radii. Hence, we compare the power-law exponents $T \propto R^{-\alpha_{1,2}}$ where α_1 denotes the exponent in the disk and α_2 beyond the disk. Implicitly, here we call disk the optically-thick structure that extends up to $\sim 10^3$ AU. Within the disk, we obtain a good agreement with $\alpha_1 \sim 0.42$, while OK20 have $\alpha_1 \sim 0.47$. Following the radiative transfer benchmark tests presented in Sect.3.5, an optically-thick disk irradiated by a central object has a typical temperature profile between $\alpha_1 = 1/3$ (frequency-dependent radiative transfer) and $\alpha_1 = 0.5$ if the opacity is kept constant (independently of the frequency and the temperature, Pascucci et al. 2004, Pinte et al., 2009). Hence, both studies obtain a slope which is between these two limits. The deviation to the value $1/3$ may come from the frequency-averaged FLD approximation used in both works, and from the higher density in the disk outer parts, compared to these benchmark tests. The temperature profile exhibits a small bump at disk edge which is more pronounced in our work than in OK20 and is linked to the long-term presence of the secondary clump. Indeed, an azimuthal mean gives four additional temperature bumps corresponding to each clump visible on Fig. 4.11. The median cannot remove all azimuthal variability, especially here with the AMR grid having more cells in the regions of interest. Because of this temperature bump, the power-law exponent beyond the disk appears to be steeper ($\alpha_1 \sim 0.7$) than in OK20 ($\alpha_1 \sim 0.6$ at 16 kyr, $\alpha_1 \sim 0.54$ at 12 kyr).

The right panel of Fig 4.11 shows the density radial profile. First, the density peak at $\sim$4000 AU is due to two opposed spiral arms fading away. Both simulations agree on the density at the disk outer edge $\rho \sim 10^{-14}\,\mathrm{g\,cm^{-3}}$ ($n \sim 10^9\,\mathrm{cm^{-3}}$), but their differences generally increase as the radius decreases. This is likely a consequence of the inner disk boundary condition. In OK20, the time-averaged density at the disk inner edge remains constant with time at $\rho \approx 3 \times 10^{-14}\,\mathrm{g\,cm^{-3}}$, indicating that the grid inner boundary condition could be responsible for this. In our run, the density decreases quasi-monotonously with the radius, and display a plateau below $\sim$30 AU, at a density $\rho > 10^{-12}\,\mathrm{g\,cm^{-3}}$ ($n > 10^{11}\,\mathrm{cm^{-3}}$). We investigate whether our accretion scheme acts as an inner boundary condition for the disk density profile, as this question has been raised recently (Hennebelle et al., 2020). We recall that, at each time step, our sink accretes part (10%) of the gas whose density exceeds the local Jeans density. The Jeans density in the central cells is of the order of $10^{-10}\,\mathrm{g\,cm^{-3}}$ ($n \sim 10^{13}\,\mathrm{cm^{-3}}$), hence no gas is accreted until this density is reached. As shown on the left panel of Fig. 4.13, several kyrs pass by before the density is high enough for gas to be accreted, while gas is being accumulated in the sink volume. Hence, the higher density we obtain compared to OK20 appears to be linked to the accretion scheme chosen. I will discuss the implications on the accretion by the central object below. Regarding the disk mass, as it is evaluated in the studies led with PLUTO and RAMSES, respectively, this density discrepancy would lead to a minor difference as long as ρ decreases less rapidly than r^{-1} (because the disk thickness is close to constant with the radius, see the bottom panels of Fig.4.10). Actually, our profile is consistent with $\rho \propto r^{-1.5}$ (for $r > 30$ AU), so the inner regions dominate the disk total mass budget. We measure a disk mass $M_\mathrm{d} \approx 8\,\mathrm{M_\odot}$ (as computed in Sec. 4.1.3) at $t = 16$ kyr. The inner 30 AU contain $\approx 1\,\mathrm{M_\odot}$ and the inner 60 AU (where we observe an order-of-magnitude density difference between both codes) contain half the disk mass. Hence, our different accretion schemes lead to a factor $\sim$2 difference regarding the disk mass predicted by our models. A disk mass of $8\,\mathrm{M_\odot}$ is consistent with AFGL 4176 (Johnston et al., 2015) and larger than $1.6\,\mathrm{M_\odot}$, as measured for G023.01-00.41 (Sanna et al., 2019). These disks exhibit Keplerian and sub-Keplerian rotation curves, respectively. We aim to compare these properties to our simulated disk.

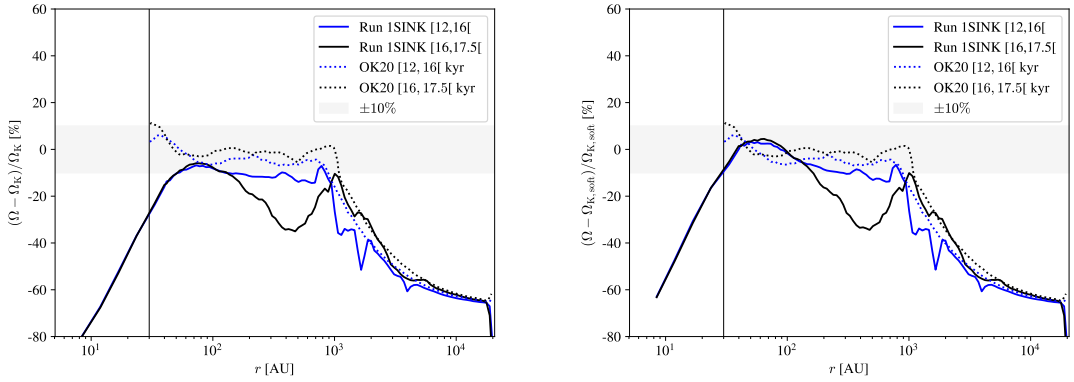

Figure 4.12: Radial Keplerianity profiles in run 1SINK and OK20. Left panel: we use the usual Keplerian angular velocity (Eq. 4.14). Right panel: we use the Keplerian angular velocity accounting for the softening length (Eq. 4.15).

We investigate the disk Keplerianity by computing the deviation between the disk angular velocity and the Keplerian angular velocity defined as

$$\Omega_K \equiv \sqrt{\frac{GM_{\rm sink+gas}(<r)}{r^3}}, \tag{4.14}$$

where $M_{\rm sink+gas}(<r)$ is the total enclosed mass within the radius r. The results of OK20 and ours are displayed in left panel of Fig. 4.12. The disk formed in OK20 agree with a Keplerian profile within ≈10%, while ours exhibit two radial intervals with sub-Keplerian velocities: within the first ∼100 AU, and between ∼200 AU and 1000 AU (only for $t \in [16, 17.5[$ kyr).

First, the epoch $[16, 17.5[$ kyr corresponds to the tidal disruption of a massive clump, followed by a gas-filament collision. The collision is nearly radial and slows down the rotating gas. This explains the sub-Keplerian angular velocity (−40%) between ∼200 AU and 1000 AU. On the opposite, the disk is nearly Keplerian on the $[12, 16[$ kyr interval. Second, we obtain sub-Keplerian values at radii $r < 100$ AU (−30% at 30 AU), and this deviation increases as the radius decreases. We investigate whether this is a consequence of the softening length used in our sink prescription. The softening length is introduced in N-body calculations to prevent the gravitational potential to diverge as the distance between two bodies approaches zero. Throughout this thesis, the softening length has been kept to its default value, which is the sink accretion radius (20 AU in these runs), and may lower the gas rotation velocity in the disk. Hence, we define a modified Keplerian angular velocity to account for this by summing up the modified sink gravitational potential and that of the gas, so that the expected angular velocity is

$$\Omega_{\rm K,soft} = \sqrt{\frac{GM_{\rm gas}(<r)}{r^3} + \frac{GM_{\rm sink}}{(r+{\rm r_{soft}})r^2}}, \tag{4.15}$$

where $\rm r_{soft} = 20$ AU. The results are displayed on the bottom panel of Fig. 4.12 and show a good ($\lesssim$ 10%) agreement between the disk angular velocity and this modified Keplerian velocity. We can conclude that the softening length is likely responsible for the sub-Keplerian values observed close to the sink.

The Keplerianity can be used to have an order-of-magnitude estimate of the disk size, setting the disk radius as the largest radius where angular velocity is consistent with Keplerianity to less than 10%. As can be seen from Fig. 4.12, both profiles exhibit the temporal shift toward large radii, as the disk size increases due to the angular momentum transported by the

infalling rotating material. They agree well on disks sizes increasing with time up to $\gtrsim 10^3$ AU at the end of the simulation. The disk growth shows no sign of saturation. This is not surprising because the simulations in OK20 have ended at $\sim$50% of the approximate free-fall time computed above, as their disk has entered a quiescent epoch, *i.e.* it does not fragment anymore. Hence, a huge amount of mass ($> 150\,M_\odot$) and angular momentum remains available in the free-falling envelope. Overall, these results are more consistent with the disk around AFGL 4176 (Johnston et al., 2015), while G023.01-00.41 likely represents an earlier phase with possible centrifugal equilibrium up to a few hundreds AU only (Sanna et al., 2019).

Let us focus on the disk dynamics. The presence of spiral arms is a permanent feature in these simulations, as in OK20. We plot density slices at times $\approx$8 kyr and $\approx$17.5 kyr in the disk plane and perpendicularly to it, in Fig. 4.10. As can be seen in the top panels, spiral arms have formed around the sink and the clump, individually. The arms extremities are the preferable birth places for new dense clumps, as can be seen on the top right panel, as in OK20 regarding the apparition of fragments. The top panels of Fig. 4.10 reveal the presence of two disk components: small ($\sim$200 AU) disks around the sink and the secondary clump, respectively, and one larger and more diffuse disk ($\sim 400 - 1000$ AU), centered on the center of mass between the two objects. As shown on the top-right panel of Fig. 4.10, the disk around the sink has resisted better to the numerous collisions than the disk around the clump. Indeed, the clump itself has suffered various dynamical events that removed mass from it, while the sink particle can only grow in mass. Consequently, the large disk center of mass has been displaced closer to the sink position.

4.2.4 Stellar properties

The protostar mass evolution is shown in the left panel of Fig. 4.13. The masses obtained at the end of each run are $\simeq 17.4\,M_\odot$ in our case against $\simeq 20\,M_\odot$ in OK20. Both accretion histories display accretion bursts of several solar masses in a short amount of time, due to clump/fragment accretion. Because of the early formation of a companion clump, the sink mass in our simulation is nearly twice smaller than in OK20 during most of the simulation. As mentioned earlier, the accretion in OK20 occurs when gas crosses the domain inner boundary, while it must reach the local Jeans density in our run. The accretion scheme and the presence of a massive companion are likely the causes for the differences in mass we observe. After $\sim$16 kyr, the sink mass goes from $8.4\,M_\odot$ to $17.4\,M_\odot$ because of several clumps entering the sink radius and increasing the local density above the Jeans density. This is reminiscent of the episodic accretion that takes place during the entire simulation but with larger masses involved. Since the luminosity increases with the sink mass, we compare the sink luminosities in the right panel of Fig. 4.13. The accretion luminosity implemented in OK20 corresponds to the luminosity peaks visible at all times. It is nearly equal to the total luminosity before $\sim$10 kyr. Throughout this thesis, we choose not to include accretion luminosity due to the lack of theoretical background on this mechanism. In this study, most of the disk is shielded against the stellar radiation. Hence, the influence of the accretion luminosity is rather limited regarding disk fragmentation and accretion.

With the possibility to include the accretion luminosity in future works, we briefly discuss what would be its amplitude, compared to that of OK20. Here, even in a similar setup, we obtain much stronger accretion events than OK20. As a clump mass is accreted, it proportionally powers the accretion luminosity, so the luminosity during these events largely dominates the internal luminosity for a short amount of time, similarly to the $\sim 10^6 L_\odot$ peak in OK20. Hence, our accretion scheme would favor rarer and higher-luminosity bursts than the numerical method of OK20. This would likely lead to a distinct heating of the outflow cavities (see *e.g.* Caratti o Garatti et al. 2017), but this is beyond the scope of this work.

In this work, we have obtained a 17.4 $M_\odot$ massive star surrounded by a massive $\sim$8 $M_\odot$ Keplerian disk and a long-lived ($>$ 13 kyr) clump originating from initial fragmentation. The divergences between this work and OK20 regarding density profile and sink mass history can be attributed to different accretion schemes and numerical grids. Our accretion scheme, based on the Jeans density in the sink cells, favors a small number of accretion events due to clump being accreted, against a smoother mass accretion in OK20. In this precise setup, we obtain with a Cartesian grid a multiple system with at least a massive sink and a long-lived hydrodynamical clump formed from initial fragmentation. In comparison, OK20 report, with a spherical grid, a massive central star with a 4 kyr old fragment at $\gtrsim$1500 AU. A spherical grid is more adapted to model the background disk, while our Cartesian AMR grid is well-suited to follow a multiple stellar system without any symmetry restriction, but may also introduce perturbations to the original axisymmetry (a spherically-symmetric density profile with rotation along a given axis).The global dynamics indicates that our simulation could have led to multiple system formation if sink particles were introduced, because clumps are more likely to be destroyed than sink particles, as we shall see below. To strengthen our study regarding the fate of this multiple system, we introduce below a similar run conducted with several sink particles.

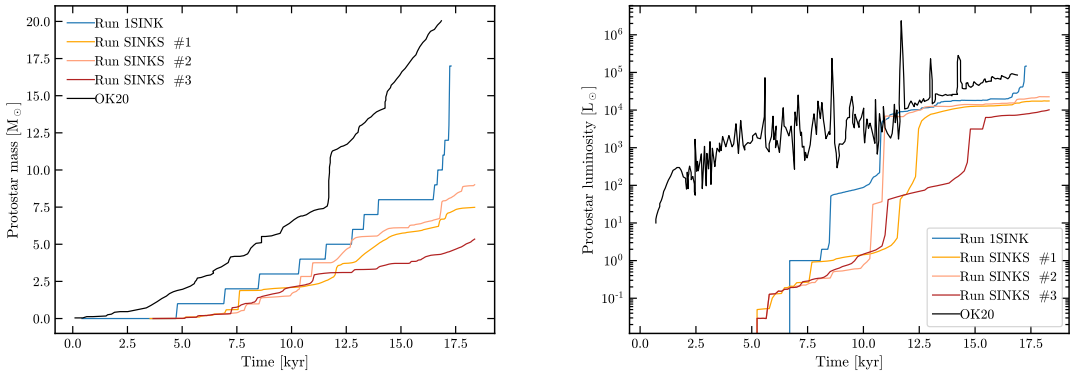

Figure 4.13: Protostar's mass (left) and luminosity (right) as a function of time. The blue line corresponds to run 1SINK, the orange-like lines correspond to each component of the long-lived triple stellar system in the RAMSES run SINKS. The black line corresponds to the central sink in OK20.

4.2.5 Run with secondary sink particles

The previous results indicate that this setup is well suited for stellar cluster formation, and assuming only one sink creation does not seem appropriate to describe it. We extend the comparison study between PLUTO and RAMSES with the use of secondary sink particles, consistent with the current use of RAMSES in the star formation context (see Sec. 4.1 and Chapter 5). We refer to this run as run SINKS. We first focus on the system multiplicity (in terms of sink particles) as a function of time.

The most striking result from this run is the formation of a long-lived triple system of intermediate-mass stars, as we shall see later. Throughout the entire simulation, a total of 13 sink particles (including the primary) have formed, which does not contradict the 60 fragments formed in OK20. Ideally, for a full agreement between both simulations, all of our sinks

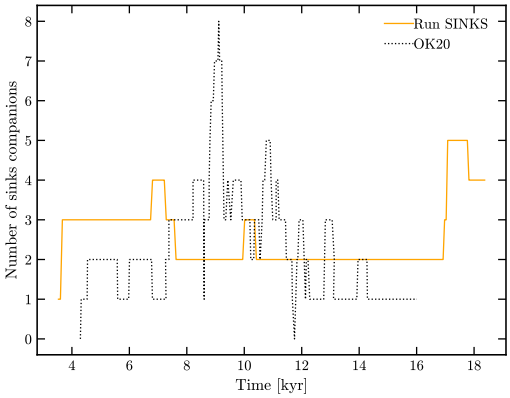

Figure 4.14: Number of fragments (black, OK20) and companion sink particles (orange, RAMSES run SINKS) with a minimum lifetime of 200yr, as a function of time.

companions should correspond to fragments having collapsed, but this occurs on sub-grid scales and cannot be captured and used as reference. Hence, having a smaller number of sinks than number of fragments in OK20 is encouraging. For comparison, the number of fragments (OK20) and secondary sink particles, *i.e.* not accounting for the primary sink, with a minimum lifetime of 200 yr (taken to be a smaller value than the typical orbital period) is plotted as a function of time in Fig. 4.14. Regarding our use of sink particles, let us briefly recall the conditions for sink creation after a density clump has been identified: it has to be bound and subvirial (Sect. 4.1.2). The average number of long-lived fragments/secondary sink particles throughout the entire simulation is $\sim 2-3$ in both runs. In more than half of our simulated time, it is constant and equal to 2 (corresponding to the triple system), whereas it varies between one and eight in OK20. In opposition to OK20, the disk in our run does not reach a quiescent state after $t > 15$ kyr. This is the most dynamical epoch of the simulation, *i.e.* the epoch with the highest number of companions, namely five. A similar epoch has been recorded in OK20 but at earlier times ($t \sim 9$ kyr), with up to eight long-lived fragments. The formation of sink particles appears to facilitate the subsequent formation of sink particles, either by perturbing the disk structure, or by forming a secondary disk which can fragment, as in run 1SINK for clump formation. Runs 1SINK and SINKS differ significantly from OK20 in that they form a long-lived multiple system, on which we focus now.

As mentioned above, we form three sink particles before ≈ 4 kyr, the primary sink and two companions which will survive until the end of the run (Fig. 4.15). While OK20 report four fragment destruction mechanisms, namely merging, shearing (tidal disruption close to the star), drain by the central star (the spiral arm on which it sits is elongated by the gravitational pull) and thermal expansion, the only destruction mechanism for a sink particle is to merge with another sink particle. This would be a possible explanation for the long lives of sink particles in our simulation, although run 1SINK shows that this setup tends to the formation of multiple stellar systems. As shown on the top panels of Fig. 4.15, a background disk forms, it is not centered on any of the three most massive sink particles in particular, and it is very similar to the one obtained in run 1SINK (Fig. 4.10). Indeed, as displayed in the left panel of Fig. 4.13, the three sink masses are comparable at all times, with sink #3 slightly less massive than the others. As in OK20, we report the formation of secondary disks around each massive sink particle of typical radius ~ 150 AU (top panels of Fig. 4.15). These small disks feed from the larger disk material. Comparing Figs. 4.15 and 4.10, the background disk is thinner when using sink particles. A possible explanation comes from the sink particles being collisionless

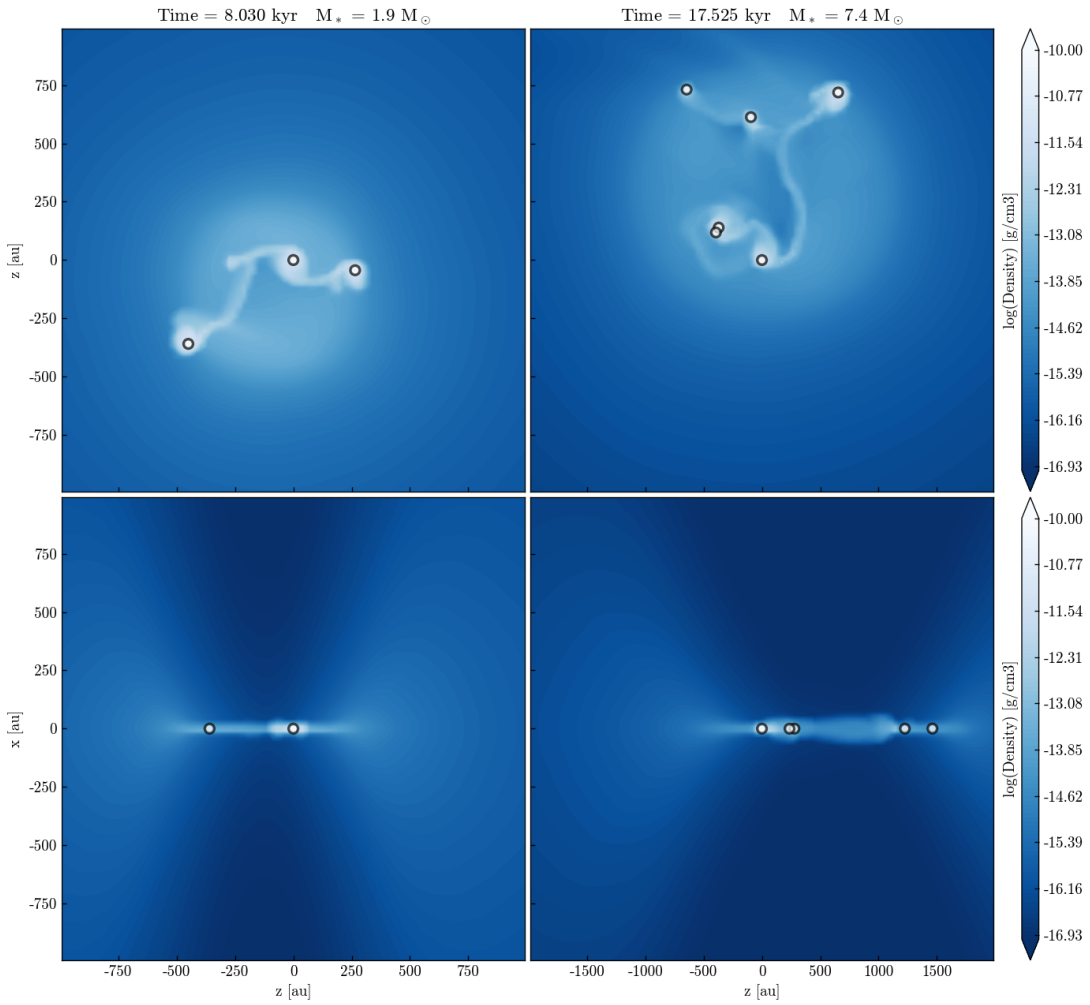

Figure 4.15: Density slices of size 2000 AU at time ≈8 kyr (left row) and 4000 AU at time ≈17.5 kyr (right row) in disk plane (top) and perpendicularly to the disk (bottom), in the RAMSES run SINKS. The slices are centered on the primary sink particle. The corresponding particle density is $2.6 \times 10^6\,\mathrm{cm}^{-3} < n < 2.6 \times 10^{13}\,\mathrm{cm}^{-3}$.

particles. They cannot collide with the gas and cause the formation of a density structure off the disk plane as in run 1SINK. Furthermore, sink particles cannot expand thermally and increase the disk pressure height. We do not compare the disk temperature profile with OK20 because here we have several stellar sources located within the disk, and we never approach axisymmetry. The final masses are respectively $7.5\,\mathrm{M}_\odot$, $9\,\mathrm{M}_\odot$ and $5.3\,\mathrm{M}_\odot$. Hence, the center of mass of the system is close to the geometric center. It is encouraging to note that the total mass of gas converted into stars, *i.e.* the total stellar mass, is $19.6\,\mathrm{M}_\odot$ at $t = 17$ kyr, against $17.4\,\mathrm{M}_\odot$ previously and $20\,\mathrm{M}_\odot$ in OK20 . We also observe that the accretion history is smoother for this run than run 1SINK (left panel of Fig. 4.13), but still shows slightly more discontinuous accretion features than OK20. This small difference can be attributed to the use of sink particles for companions in our simulation. While a hydrodynamical fragment can be disrupted close to the central mass and partly accreted, the accretion of a sink companion concerns its entire

mass. This type of differences justifies the present study: if the Jeans length is not resolved, too many sink particles could be formed and lead to a highly discontinuous accretion rate; this introduces an additional uncertainty. Nonetheless, the only massive sinks formed in this run do not merge, so this difference remains small. Moreover, by choosing a finest resolution of 5 AU, adapted to this setup (see Fig. 4.9), the fragmentation should be mainly physical and not numerical.

The right panel of Fig. 4.13 shows the total luminosity of each of the three most massive sinks in this run and that of the central star in OK20. When a star enters the Kelvin-Helmoltz contraction phase, its internal luminosity increases by roughly two orders of magnitude (Hosokawa & Omukai, 2009), as shown here for $t > 11$ kyr. The luminosity is interpolated, based on the mean accretion rate and the sink mass. The phase changes occur at different masses for different accretions rates, hence the luminosity can be interpolated between two protostellar phases, and the luminosity jump is smoothed over time. The luminosity jump is not visible for OK20 who integrate the accretion luminosity, which dominates until this phase. Such an evolution shows that there is a threshold in mass above which stellar luminosities become comparable (for similar mean accretion rates), rather than a single star luminosity dominating the total luminosity of the system. Observationally, it may significantly alter the gas distribution in the neighbourhood of a single star compared to a multiple system, as each star can power its own radiative cavities above $\sim$10 $M_\odot$ (Sect. 4.1). Numerically, the inclusion of accretion luminosity worsens the differences between runs without and with sink particles (where accretion bursts are stronger), as it additionally heats up the gas and dominates the total luminosity at early times. More generally, the inclusion (or not) of the accretion luminosity, combined with the inclusion (or not) of sink particles impacts the total stellar luminosity at a given time. The temperature within the cavities heated by this luminosity, as observed by high angular resolution instruments like ALMA, may put constraints on these questions.

The third step of our study is to compare our runs directly to PLUTO, *i.e.* with the same post-processing tools. We have hydrodynamical fragments forming in our runs without secondary sink particles and need a tool to follow their evolution. Hence, in order to follow the fragments with the tracker developed by OK20 for their spherical grid, I have developed a script to interpolate the variables of interest on the AMR grid of RAMSES and to project them on a spherical grid. This is presented hereafter.

4.2.6 Extension of the comparison study and perspectives

Following the sink particles properties within a RAMSES run is straightforward. For a full comparison between two radiation-hydrodynamical simulations without companion sink particles performed by PLUTO and RAMSES (run 1SINK), respectively, we aim to use the tracker developed by OK20. It will permit us to follow the properties of hydrodynamical fragments (mass, temperature, lifetime, number) by identifying them and following their trajectory. More generally, it will permit us to use unique diagnostic tools. In order to benefit from this tool, I have developed a simple post-processing interpolation script. Our attempt is meant to be simple and less time-consuming as possible, to be able to run it on tens of outputs so we can follow the fragments over many orbits. Moreover, the fragments are defined on spheres of radius 50 AU while our finest resolution is 5AU, hence we do not look for a precise and expensive interpolation method. We do not enter the AMR structure but only work from the arrays of Cartesian coordinates (and variables), as they are dealt with in the OSYRIS python package used throughout this thesis.

The use of python interpolation tools on such a non-regular grid is prohibitively expensive. As the AMR grid is time-dependent, attempts to reduce it to a regular, Cartesian grid constant

with time, are not satisfactory. A manual interpolation would require to scan the RAMSES grid twice, first to get the position and variables of each cell, then to identify its neighbours. Hence it would scale as ${n_{\rm RAMSES}}^2$ (the number of cells in the RAMSES grid, $\sim 10^6$ cells in this run). Therefore, we take advantage of the destination grid being regular and constant with time to do a "nearest"-type interpolation and go through the RAMSES grid only once, so that the computational time scales as $n_{\rm RAMSES}$.

PLUTO's grid has cell-centered coordinates $(r_{\rm c}, \theta_{\rm c}, \phi_{\rm c})$ of index (i_r, j_θ, k_ϕ) and size $(n_r - 1, n_\theta - 1, n_\phi - 1)$, with edge-centered values logarithmically spaced in the radial direction and linearly spaced in the azimuthal and polar directions. It is generated with the standard NUMPY tools, so we can easily reconstruct a similar one, and fill it with the variables interpolated from the RAMSES output. We take advantage of the existence of an analytical relation between the indices (i_r, i_θ, i_ϕ) and the cell-centered coordinates $(r_{\rm c}, \theta_{\rm c}, \phi_{\rm c})$. Therefore, for every cell-centered Cartesian coordinates (x, y, z) of RAMSES's grid, we can compute the index of the nearest cell in the PLUTO grid, after converting the Cartesian coordinates to spherical coordinates. In the radial direction (the similar developments in the azimuthal and polar directions are straightforward), the edge-centered coordinates in the PLUTO grid are given by

$$r(i_r) = r_{\rm min} \times \left(\frac{r_{\rm max}}{r_{\rm min}}\right)^{\frac{i_r}{n_r - 1}}, \tag{4.16}$$

where $i_r \in [0, n_r - 1]$, and $r_{\rm min}$ and $r_{\rm max}$ are the inner and outer radii. Hence, one can obtain the cell-centered radius defined as (for $i_r \in [0, n_r - 2]$)

$$r_{\rm c}(i_r) \equiv \frac{r_i(i_r + 1) + r_i(i_r)}{2} = \frac{1}{2}\left[\left(\frac{r_{\rm max}}{r_{\rm min}}\right)^{\frac{1}{n_r - 1}} - 1\right] \times r_{\rm min}\left(\frac{r_{\rm max}}{r_{\rm min}}\right)^{\frac{i_r}{n_r - 1}} = {\rm k} \times r(i_r), \tag{4.17}$$

where ${\rm k} = \frac{1}{2}\left[\left(\frac{r_{\rm max}}{r_{\rm min}}\right)^{\frac{1}{n_r - 1}} - 1\right]$ is a constant once the parameters of the PLUTO grid are set. Therefore, by equating the cell-centered radius $r_{\rm c}$ to the spherical radius of each cell from RAMSES, that we will call $r_{\rm RAMSES}$, one can obtain the approximate index

$$i'_r = (n_r - 1)\frac{\log\left(\frac{r_{\rm RAMSES}}{{\rm k}\, r_{\rm min}}\right)}{\log\left(\frac{r_{\rm max}}{r_{\rm min}}\right)}, \tag{4.18}$$

which is rounded to obtain the radial index in PLUTO's grid corresponding to this cell's radius. Similar steps are done to obtain j'_θ and k'_ϕ. Two types of exceptions can arise with this "nearest"-type interpolation. In the first case, PLUTO's local cells are larger than the RAMSES ones, so we simply average the values given by RAMSES's cells. In the second case, PLUTO's local cells are smaller than the RAMSES ones (usually the case close to the central sink, as a consequence of the logarithmical spacing), so we complete the PLUTO grid with the nearest values already in place.

The next step is to test this interpolation tool and subsequent use of OK20's tracker. We use the run SINKS, in which sink particles have been introduced where fragments may have formed, for comparison. By gaining mass, the sinks have depleted part of the surrounding gas and therefore reduced the density locally. Hence, we use a Gaussian kernel to deposit the mass of the sinks back onto the grid in the density field with

$$G_{\rm 3D,i}(\mathbf{r}; \sigma) = \frac{1}{(\sqrt{2\pi}\sigma)^3} \exp\left(-\frac{\|\mathbf{x} - \mathbf{x}_{\rm sink,i}\|^2}{2\sigma^2}\right), \tag{4.19}$$

where σ is the standard deviation and is taken to be $2\Delta x$ (which corresponds to half the sink accretion radius) and $\mathbf{x}_{\mathrm{sink,i}}$ is the position of the $i-$th sink.

Figure 4.16 shows the density and temperature slices after interpolation on the PLUTO grid and fragments identification. Most fragments correspond to sink particles in our run, but not all. On the one hand, some fragments were identified before a sink particle formed at the same location, showing the agreement between our methods (we recall that a sink should correspond to a fragment after gravitational collapse). On the other hand, a sink particle located far away from the central star and not massive enough to radiate, has not been detected by the tracker (which is based on the temperature excess compared to the background temperature). This may point at sink particles being produced too early, *i.e.* neither they have accreted enough mass to radiate nor is the gas temperature they sit on high enough to lead to second collapse. Our comparison project will help us to shed light on the conditions for sink particle introduction in the star formation context. A possibility mentioned in OK20 regards the H_2 dissociation temperature (2000 K), necessary for second collapse, as an extra-condition for sink production. Meanwhile this may be adapted to sink creation in irradiated disk fragmentation, where the star provides an additional heating source, this would require a very high resolution for the first sinks, whose only heating process is adiabatic contraction in a cold $\sim$10 K medium.

We have presented the preliminary results of a comparison study between PLUTO and RAMSES at modelling disk fragmentation. It is valuable at pointing out the biases introduced by the modelisation of a disk on a Cartesian grid and the use of sink particles, and symmetrically, the modelisation of multiple stellar systems on a spherical grid. Our outcomes differ by the formation of a single stellar system in OK20, while our work shows the formation of binary-like and triple systems, which may be a very fundamental limit when comparing studies done with spherical and Cartesian grids (see *e.g.* Krumholz et al. 2009). Apart from this, we obtain reasonable agreements on the disk dynamics phenomena (before quiescence), the conversion ratio of gas turned into stars, and the disk Keplerianity. In agreement with the resolution constraint we have chosen to begin with (and which will be further refined), the number of sinks we obtain is not excessive compared to the number of long-lived fragments in OK20. In addition, most long-lived fragments in OK20 reach the H_2 dissociation limit and could therefore be good candidates of cores on the verge to form protostars.

This is the first step of a more complete work that will include a resolution study. I have developed a simple tool in order to interpolate the variables from the RAMSES AMR grid to the spherical grid from PLUTO. This will allow us to use the fragment tracker developed by OK20 and follow the fragments properties in our future runs without sink particles. Eventually, we will include magnetic fields, as they have been shown to limit initial fragmentation (Commerçon et al., 2011a).

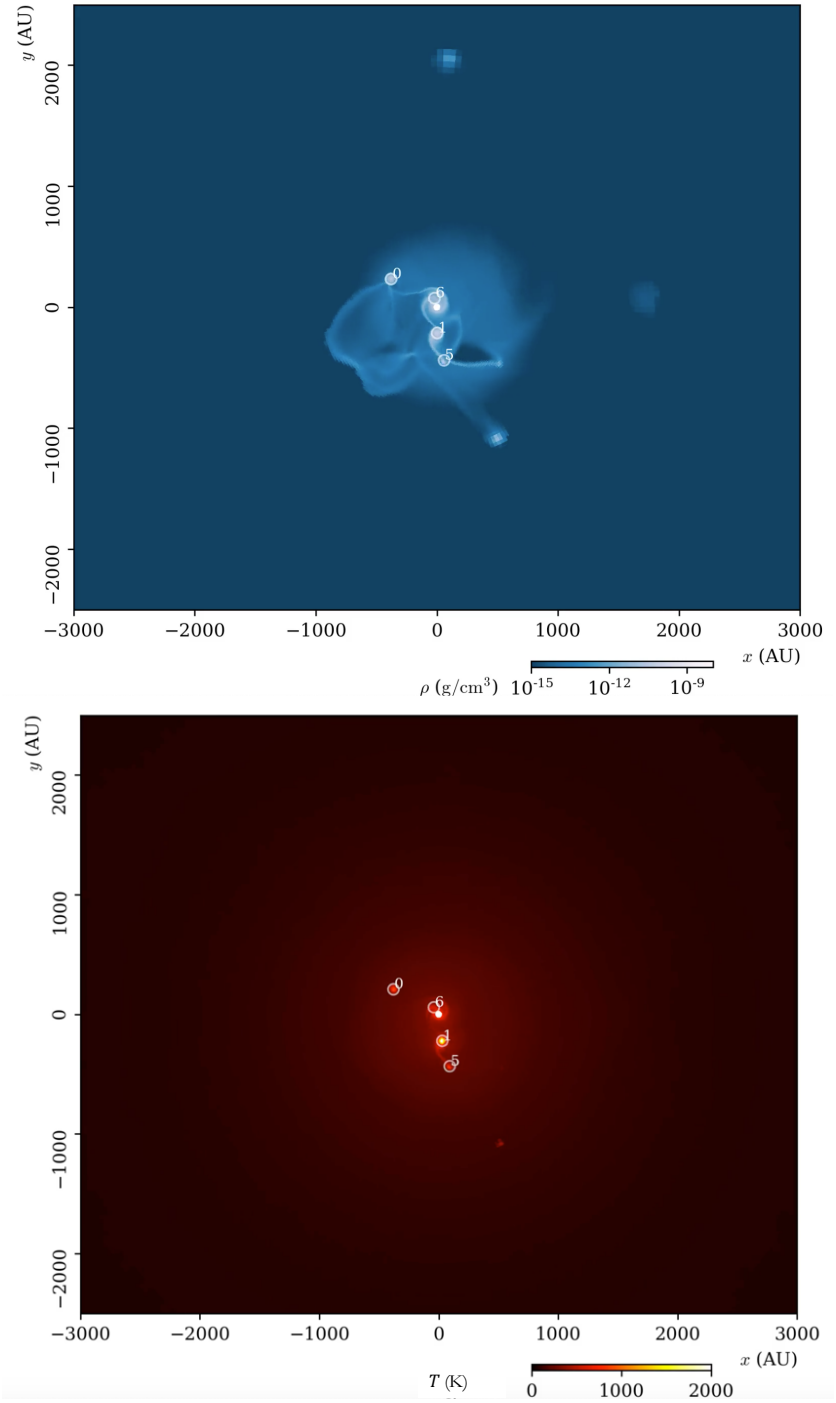

Figure 4.16: Density (top panel) and temperature (bottom panel) slices in the disk midplane from RAMSES run, after interpolation on the PLUTO grid and fragments identification with the tracker developed for OK20.

CHAPTER 5

Collapse of turbulent cores with radiation-magneto-hydrodynamics

Contents

IN THIS CHAPTER, WE ACCOUNT FOR MAGNETIC FIELDS AND TURBULENCE, two ingredients that are known to be present in massive star-forming regions (Zhang et al. 2014, Bontemps et al. 2010). In this second application of the hybrid radiative transfer method to massive star formation (see Chapter 4 for the first application), we include more realistic physics, improving its consistency with observational constraints on the environment around massive protostars. We investigate the collapse of a massive magnetized core, including initial velocity perturbations consistent with turbulence. A non-ideal magnetohydrodynamical effect, namely ambipolar diffusion, is accounted for, to prevent the artificial accumulation of magnetic field preventing disk formation (the so-called *magnetic catastrophe*, see *e.g.* Hennebelle & Fromang 2008). We use the hybrid radiative transfer method presented in Chapter 3, which prevents the radiative force to be underestimated as in the FLD method (Owen et al., 2014). Driven by

this physically-motivated numerical experiment, we intend to identify the driving mechanism for massive protostars outflows, as well as the outflow and disk properties that can be directly compared with observations.

Common features of collapse calculations are presented at the beginning of Chapter 4.

5.1 Context

Let us first understand why do we need the physical ingredients mentioned above, namely non-ideal MHD and a specific method for stellar irradiation. For a more general review of the numerical advances on massive star formation, we refer the reader to 1.7.

Disk-mediated accretion for massive protostars has emerged in multi-dimensional simulation as part of the so-called flashlight effect (Yorke & Sonnhalter 2002, Kuiper et al. 2010a), to overcome the radiation barrier problem (Larson & Starrfield, 1971). Meanwhile, progress has been made in the low-mass star formation context with the inclusion of magnetic fields in numerical simulation in the ideal magneto-hydrodynamics (MHD) frame (*e.g.* Fromang et al. 2006). Many studies have shown that in a collapsing core, the flux-freezing condition leads to the accumulation of magnetic fields in the central region, inducing a strong magnetic braking and preventing disk formation (see *e.g.* Hennebelle & Fromang 2008, and Seifried et al. 2011 in the high-mass regime). This is referred to as the magnetic catastrophe, since many disks are observed around low- and high-mass protostars (Cesaroni et al., 2005). Three ingredients have been introduced and shown separately how to bring disks back and reconcile numerical simulations and observations in that respect: misalignment between the rotation axis and the magnetic field axis, turbulence, and non-ideal MHD effects. Misalignment (Joos et al., 2012) and turbulence (Joos et al. 2013, Lam et al. 2019 for low-mass stars, Seifried et al. 2012a for high-mass) directly reduce the magnetic braking efficiency. Non-ideal (also called resistive) MHD effects, namely ambipolar diffusion (AD), Ohmic dissipation and the Hall effect provide a mechanism to limit the accumulation of magnetic fields strength and therefore the magnetic braking. AD is likely the most-studied non-ideal MHD effect, as it starts dominating at lower densities than the others, and indeed promotes disk formation in the low-mass regime (Masson et al., 2016). In several studies, non-ideal MHD appears as the main regulator of disk formation (AD in Hennebelle et al. 2016), even when subsonic turbulence is included (Wurster & Lewis, 2020).

Disks are not only important for accretion and multiplicity (see Sect. 4.2), which are among the main questions when studying massive star formation. Early theoretical works have shown they can power fast ($\gtrsim$ 100 km s^{-1}) jets by centrifugal acceleration (Blandford & Payne, 1982, Pudritz & Norman 1983, Pelletier & Pudritz 1992) or slow ($\sim 1-10$ km s^{-1}) magnetic-pressure-gradient driven tower flows (Lynden-Bell, 1996, Lynden-Bell 2003) by twisting the field lines and accumulating enough toroidal magnetic field. The former is characterized by a very collimated structure and a magnetic field whose poloidal component is dominant at the launching region (the inner disk regions), while the latter gives rise to a wide-angle outflow and is dominated by the toroidal component in the launching region (as fields lines are wound-up by the disk) and in the entire flow. For a review on the numerical advances regarding these processes we refer the reader to Pudritz et al. 2006, and for their role in star formation to Pudritz & Ray (2019).

The presence of these two types of outflows, namely magneto-centrifugal and magnetic tower flows, has been confirmed in numerical simulations. Both outflows have been obtained under the ideal MHD approximation, in the low-mass regime (Hennebelle & Fromang 2008 and Banerjee & Pudritz 2006), later-on in the high-mass regime (Hennebelle et al. 2011, Seifried et al. 2012b). Using sub-AU resolution 3D calculations of massive core collapse, Banerjee & Pudritz (2007) obtained the early bipolar outflows but do not follow the calculation after a

star has formed. Relaxing the ideal MHD approximation, the question has been tackled with the inclusion of Ohmic dissipation by Matsushita et al. (2017) and Kölligan & Kuiper (2018). Matsushita et al. (2017) used 3D nested grids with equatorial symmetry to reach very high-resolution (0.8 AU). They find that the ratio between the mass outflow rate and the mass accretion rate is nearly constant throughout the stellar mass spectrum, indicating a common launching mechanism, in line with the observational constraints (see *e.g.*, Wu et al., 2004). With a 2D spherical grid, Kölligan & Kuiper (2018) studied the launching of both types of outflows with an even higher resolution (0.09 AU) and Ohmic dissipation around a massive protostar. They found that only a spatial resolution of $\lesssim$ 0.17 AU at 1 AU could provide numerically-converged results on the magneto-centrifugal jets, while distinguishing both types of outflows was very difficult in their low-resolution run. The conclusions from these works are twofold. First, the outflow mechanisms during low- and high-mass star formation could be the same. Second, sub-AU resolution is required to obtain converged results on the magneto-centrifugal jets. Nonetheless, these MHD-oriented works have neglected an ingredient: radiative transfer.

Most numerical studies on massive star formation have focused on its radiative transfer aspect, due to the radiation pressure barrier (Larson & Starrfield, 1971), and neglected magnetic fields. They have shown the production of radiative outflows as well. First radiation-hydrodynamical implementations have relied on the Flux-Limited Diffusion (FLD) approximation (Levermore & Pomraning, 1981), which is well-suited for radiation transport in optically-thick media but is not adapted to strongly anisotropic radiation fields. Further developments have focused on the particular treatment the stellar radiation, also called irradiation. First, it propagates along rays, hence it requires a method capable of conserving its directionality. Second, the dust opacities are very sensitive to the radiation frequency, and stellar radiation is ultraviolet-like (UV) radiation while dust emission is infrared (IR). The desired numerical method should track this frequency information, from stellar radiation emission to absorption by the surrounding dust. Numerous irradiation implementations have been designed for massive star formation (Kuiper et al. 2010c,Rosen et al. 2017, Mignon-Risse et al. 2020) or for the physical structure of protoplanetary disks (Flock et al. 2013, Ramsey & Dullemond 2015, Gressel et al. 2020, Fuksman et al. 2020). Radiative cavities have been found to form after the central star has reached $\sim$10 $M_\odot$, so the corresponding luminosity can drive a radiative force capable to overcome the gravitational force (and ram pressure). Radiative outflows are characterized by velocities of $\sim 10 - 20\,\mathrm{km\,s^{-1}}$ (Rosen et al. 2016, Mignon-Risse et al. 2020). Nonetheless, the stellar radiative acceleration appears to be insufficient to explain the momentum rate of bipolar outflows observed around protostars of all masses (Lada 1985, Cabrit & Bertout 1992), by $1-2$ orders of magnitude.

In the meantime, the common inclusion of radiative transfer and MHD in numerical codes has shown that both effects contribute to limit the fragmentation. Without sink particle, Commerçon et al. (2011a) showed the prevention of early core fragmentation, while Myers et al. (2013) obtained similar results at later times. Secondary fragmentation is also inhibited, as found by Peters et al. (2011). Only few works have focused on the co-launching of radiative and magnetic outflows, since it requires a hybrid radiative transfer method (not to underestimate stellar feedback), (non-ideal) MHD (to obtain a realistic disk and self-consistent outflows) and sub-AU resolution. To circumvent this difficulty, subgrid models have been used to mimic protostellar outflows and found to dominate over the radiative ones (Rosen & Krumholz, 2020) and to enhance the flashlight effect (Kuiper et al., 2015).

Two studies have focused on the impact of stellar radiation on the launching and structure of magnetic outflows. On the one hand, including photoionizing radiation (but no radiative force) and in the ideal MHD frame, Peters et al. (2011) have shown that the development of H_{II} regions perturbs the magnetic fields topology and weakens the tower flow. Nonetheless, Peters et al. (2014) show that the CO emission associated to ionization feedback could not re-

produce observations. On the other hand, Vaidya et al. (2011) have focused on the collimation of magnetic jets in axisymmetric setups with ideal MHD and prescriptions for radiative forces. They observe that line-driven radiation force from a $30\,M_\odot$ star starts to compete with magnetic forces for disk field strengths $\lesssim 5$ G at $r = 1$ AU and moderately reduces the jet collimation but do not disrupt the magnetic field geometry. There is no, to date, self-consistent numerical experiment on the interaction between radiative feedback and magnetic outflows in the context of massive star formation.

Meanwhile, the presence of non-negligible magnetic fields in massive star-forming clouds is clear, as we mentioned in Sect. 1.6. In a nutshell, the signs of rotation within an outflow as well as the presence of a disk obtained with ALMA (Hirota et al., 2017) have brought evidence of outflows originating from a MHD disk wind for high-mass protostars, similarly to their low-mass counterparts. These results are twofold. First, there is growing evidence that massive protostellar outflows originate (at least partially) from the same mechanism as for low-mass protostars, as was already pointed out by, *e.g.*, Lada (1985). Second, and regardless of the outflow mechanism (although the two are certainly linked, depending on the mechanism) disk-mediated accretion is the favoured accretion process for massive protostars as well (see the short up-to-date review by Beltrán, 2020). As presented above, the modelisation of magnetized disks requires non-ideal MHD effects to circumvent the so-called magnetic catastrophe. We have shown in Chapter 4 that the massive star radiative force could create cavities. Would it dominate over magnetic forces at launching outflows, or would it be sufficient to disturb the field geometry, preventing the launching of MHD outflows ?

In this chapter, we present the first numerical simulations including both a hybrid radiative transfer method and non-ideal MHD (namely, ambipolar diffusion), aiming at identifying the launching mechanism of outflows around massive protostars, as well as their accretion conditions with realistic physical ingredients. To do so, we consider an initial velocity field consistent with turbulence (of various amplitudes, corresponding to several runs) in order to mimic non-idealized environmental conditions for massive protostar birth. Finally, we will investigate to what extent our results compare with current observational constraints on massive protostars outflows and on the disk-outflow-magnetic field alignment.

This study is organized as follows. The numerical methods are presented in Sect. 5.2. In Sect. 5.3 we analyze the evolution of the four runs, emphasizing on the disk-magnetic field alignment and the sink and disk properties. Section 5.4 is dedicated to the study of the outflows: their origin, their properties and their comparison with observations.

5.2 Methods

5.2.1 Radiation magneto-hydrodynamical model

We integrate the equations of radiation-magneto-hydrodynamics (MHD) in RAMSES (Teyssier 2002, Fromang et al. 2006) with ambipolar diffusion (Masson et al., 2012), the M1 method for stellar radiation and the Flux-Limited Diffusion (FLD) otherwise (Commerçon et al. 2011b, Rosdahl et al. 2013, Rosdahl & Teyssier 2015, Mignon-Risse et al. 2020). The set of equations we

aim to solve are

$$
\begin{aligned}
\frac{\partial \rho}{\partial t} + \nabla \cdot [\rho \boldsymbol{u}] &= 0, \\
\frac{\partial \rho \boldsymbol{u}}{\partial t} + \nabla \cdot [\rho \boldsymbol{u} \otimes \boldsymbol{u} + P\mathbb{I}] &= -\lambda \nabla E_{\rm fld} + \frac{\kappa_{\rm R}\rho}{\rm c}\boldsymbol{F}_{\rm M1} + \boldsymbol{F}_{\rm L} - \rho\nabla\phi, \\
\frac{\partial E_{\rm T}}{\partial t} + \nabla \cdot [\boldsymbol{u}\left(E_{\rm T} + P + \frac{B^2}{2}\right) & \\
-(\boldsymbol{u}\cdot\boldsymbol{B})\boldsymbol{B} - \boldsymbol{E}_{\rm AD}\times\boldsymbol{B}] &= -\mathbb{P}_{\rm fld}\nabla : \boldsymbol{u} - \lambda \boldsymbol{u}\nabla E_{\rm r} \\
&\quad + \nabla\cdot\left(\frac{{\rm c}\lambda}{\rho\kappa_{\rm R,fld}}\nabla E_{\rm r}\right) - \rho\boldsymbol{u}\cdot\nabla\phi, \\
\frac{\partial E_{\rm M1}}{\partial t} + \nabla\cdot\boldsymbol{F}_{\rm M1} &= -\kappa_{\rm P,\star}\,\rho{\rm c}E_{\rm M1} + \dot{E}^{\star}_{\rm M1}, \\
\frac{\partial \boldsymbol{F}_{\rm M1}}{\partial t} + {\rm c}^2\nabla\cdot\mathbb{P}_{\rm M1} &= -\kappa_{\rm P,\star}\,\rho{\rm c}\boldsymbol{F}_{\rm M1}, \\
\frac{\partial E_{\rm fld}}{\partial t} - \nabla\cdot\left(\frac{{\rm c}\lambda}{\rho\kappa_{\rm R,fld}}\nabla E_{\rm fld}\right) &= \kappa_{\rm P,fld}\,\rho{\rm c}\left({\rm a_R}T^4 - E_{\rm fld}\right), \\
\frac{\partial \boldsymbol{B}}{\partial t} - \nabla\times[\boldsymbol{u}\times\boldsymbol{B} + \boldsymbol{E}_{\rm AD}] &= 0, \\
\nabla\cdot\boldsymbol{B} &= 0, \\
\Delta\phi &= 4\pi{\rm G}\rho,
\end{aligned}
\tag{5.1}
$$

where ρ is the dust-and-gas mixture density, $\boldsymbol{u}$ is the velocity, P is the thermal pressure, λ is the FLD flux-limiter, $E_{\rm fld}$ is the FLD radiative energy, $\boldsymbol{F}_{\rm L} = (\nabla\times\boldsymbol{B})\times\boldsymbol{B}$ is the Lorentz force, ϕ is the gravitational potential, $E_{\rm T}$ is the total energy $E_{\rm T} = \rho\varepsilon + 1/2\rho u^2 + 1/2B^2 + E_{\rm fld}$ (ε is the internal energy), $E_{\rm M1}$ is the M1 radiative energy, B is the magnetic field, $\boldsymbol{E}_{\rm AD}$ is the ambipolar EMF, $\mathbb{P}_{\rm fld}$ is the FLD radiative pressure, $\kappa_{\rm P,fld}$ is the Planck mean opacity in the FLD module, $\kappa_{\rm R,fld}$ is the Rosseland mean opacity, $\rm a_R$ is the radiation constant, $\boldsymbol{F}_{\rm M1}$ is the M1 radiative flux, $\mathbb{P}_{\rm M1}$ is the M1 radiative pressure, $\kappa_{\rm P,\star}$ is the Planck mean opacity at the stellar temperature, $\dot{E}^{\star}_{\rm M1}$ is the stellar radiation injection term. The term $\kappa_{\rm P,\star}\rho{\rm c}E_{\rm M1}$ couples the M1 and the FLD methods via the equation of evolution of the internal energy

$$
C_{\rm v}\frac{\partial T}{\partial t} = \kappa_{\rm P,\star}\,\rho{\rm c}E_{\rm M1} + \kappa_{\rm P,fld}\,\rho{\rm c}\left(E_{\rm fld} - {\rm a_R}T^4\right) \tag{5.2}
$$

We use the ideal gas relation for the internal specific energy $\rho\varepsilon = C_{\rm v}T$ where $C_{\rm v}$ is the specific heat capacity at constant volume. This equation closes the system and is used to evolve the gas temperature together with the radiative quantities.

5.2.2 Physical setup

We start from a massive core of mass $M_{\rm c} = 100\,{\rm M}_\odot$ and radius $R_{\rm c} = 0.2\,{\rm pc}$. Its density profile is given by $\rho = \rho_0/(1 + (r/r_0^2))$ where $\rho_0 = 7.7\times10^{-18}\,{\rm g\,cm^{-3}}$ (equivalent to $n = 2\times10^6\,{\rm cm^{-3}}$) and $r_0 = 0.02$ pc are the density and radius of the central plateau, respectively. The initial temperature is uniform with $T = 20$ K, and so is the radiative energy of the FLD module with $E_{\rm fld} = {\rm a_R}T^4$. We assume an ideal gas equation of state with an adiabatic index $\gamma = 5/3$ and a mean molecular weight $\mu_{\rm gas} = 2.31$ as we consider H and He with a mass concentration of He equal to 0.27 as in (Vaytet et al., 2013). The outer-medium density is ten times smaller than the density at the border of the core.

The core free-fall time is then

$$
\tau_{ff} = \sqrt{\frac{3\pi}{32{\rm G}\bar{\rho}}} \simeq 143\,{\rm kyr}, \tag{5.3}
$$

where G is the gravitational constant and $\bar{\rho}$ is a mean density computed as if the density distribution was uniform in this sphere: $M_c/(4/3\pi R_c^3)$. More exactly, the free-fall time is shorter in the inner parts of the core ("inside-out" collapse, Shu 1977), and is $\sim$24 kyr at the central plateau border, which contains $\sim$15 $M_\odot$.

The core is threaded by a uniform magnetic field oriented along the $x-$axis. We set the magnetic field strength by the mass-to-flux to critical mass-to-flux ratio $\mu = (M/\Phi)_0/(M/\Phi)_{\rm crit}$ where $(M/\phi)_0 = M_c/(\pi B_0 R_c^2)$ and $(M/\phi)_{\rm crit} = 0.53/(3\pi)\sqrt{5/G}$ (Mouschovias & Spitzer, 1976). Strong ($\mu = 2$) and moderate ($\mu = 5$, $B_0 = 68\mu G$) magnetic fields are considered here. A drawback of this uniform distribution is that the mass-to-flux ratio decreases as $\mu \sim 1/R$ and is larger in the inner parts of the core, with $\mu \approx 50$ in the central plateau (for runs with $\mu = 5$) corresponding to a weakly magnetized medium. We expect, however, the central magnetic field strength to increase as $B \propto \rho^{2/3}$ as the core contracts and before ambipolar diffusion starts dominating (at $\rho \sim 10^{-15}$ g cm^{-3}, or $n \sim 10^8$ cm^{-3}), so the mass-to-flux ratio will decrease in the central regions. Thus, the magnetic field will play a dynamical role in the collapse.

An initial velocity dispersion is imposed to mimic a turbulent medium, and follows a Kolmogorov power spectrum $P(k) \propto k^{-5/3}$, similar to Commerçon et al. (2011a). One realization is considered. The turbulence is not sustained but the sound-crossing time at 20 K ($\sim$1 Myr) is significantly larger than the simulation time here, which is a fraction of the free-fall time. A low level of (solid-body) rotation, $E_{\rm rot}/E_{\rm grav} = 1\%$, is initially imposed along the $x-$axis, and dominates the specific angular momentum in subsonic runs. We consider four runs (see Table 5.1), varying the initial Mach number $\mathcal{M}$ and Alfvénic Mach number $\mathcal{M}_{\rm A}$. Regarding the Mach number, runs M05 and M05B2 have subsonic turbulence with $\mathcal{M} = 0.5$ while run M2 has a supersonic turbulence with $\mathcal{M} = 2$. The relative impact of turbulence and magnetic fields is addressed by considering subalfvenic ($\mathcal{M}_{\rm A} < 1$, M0 and M05B2) and superalfvenic turbulence ($\mathcal{M}_{\rm A} > 1$, M05 and M2).

As in Chapter 4, we model the dust sublimation by decreasing progressively the dust-to-gas ratio with the temperature (see Eqs. 4.1 and 4.2). Finally, we set the opacity in the primary sink particle volume to a value chosen so that the local optical depth is the minimal optical depth allowed numerically (10^{-4}). This floor value for the optical depth is a numerical parameter used in optically-thin cells in order to gain performance with the FLD solver (see Appendix A of Vaytet et al. 2018). One of our objective is to identify the outflow launching mechanism, but a property of our hybrid scheme for irradiation is that part of the stellar radiation can be absorbed locally before leaving the sink volume. Then, it would be treated with the FLD, which is not adapted to such strongly anisotropic radiation, and the corresponding opacity when interacting with the gas would be much smaller, hence reducing the radiative force (see Sect 3.4). By decoupling gas and radiation within the sink volume we circumvent this limitation (Appendix C).

5.2.3 Resolution and sink particles

Boundary conditions are periodic and the simulation box is 0.8 pc large, hence the gravitational effects due to the periodicity are marginal[1]. The coarse grid is 32^3, with 10 additional levels of refinement, leading to a finest resolution of 5 AU, which is adapted to the Jeans length and vertical scale height in massive protostellar disks (see Fig. 4.9). We run a similar set of simulations with a finest resolution of 10 AU. We will use the prefix LR, as "low-resolution", to refer to these runs. The same refinement strategy and sink particles parameters as in Chapter 4 are employed, and a more detailed presentation can be found in Sect. 4.1.2. Let us briefly recall that refinement is performed on the Jeans length (Truelove et al., 1997), sinks are introduced

[1] At the core border, the gravitational acceleration exerted on a gas particle scales as $a_{\rm grav} \sim M_c/R_c^2$. In comparison, the acceleration due to the nearest (0.6 pc) periodic core is $\sim M_c/(3R_c)^2 = a_{\rm grav}/9$.

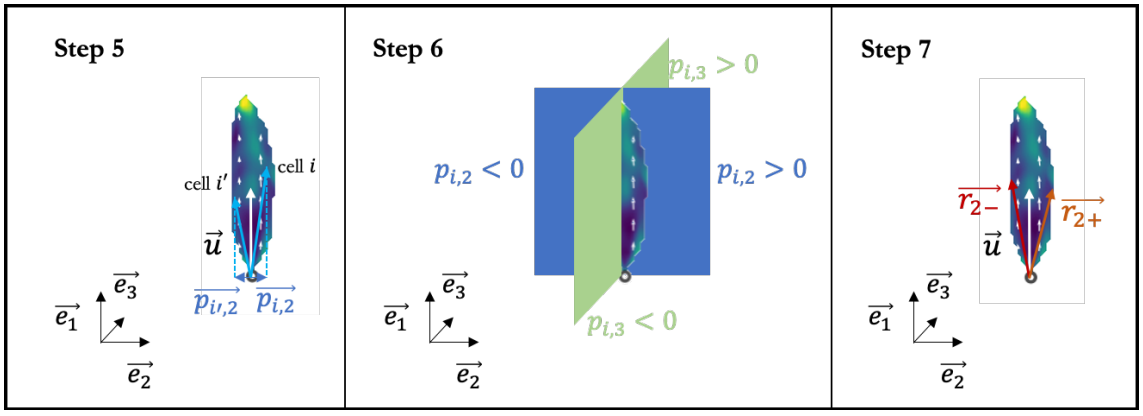

Figure 5.1: Outflow selection slice perpendicular to the disk in run M0, showing three of the eight steps to compute its opening angle. It displays the projection vector $\mathbf{p}_i$ associated to cell i (Eq. 5.6, left panel), the four subselections based on this projection (middle panel) and the geometric center vector $\mathbf{u}$ and two of the outermost positions vectors $\mathbf{r}_{2,\pm}$ used to compute the opening angle (Eq. 5.7, right panel).

at the finest resolution level after a clump has been identified as gravitationally bound and subvirial (Bleuler & Teyssier, 2014), and sinks merge when their accretion radii (4 cells in radius, 20 AU) overlap.

5.2.4 Analysis: disk and outflow identification

On the one hand, disk properties are presented in Sect. 5.3.5. To derive them, we use the same disk identification criteria as in Sect. 4.1.3, taken from Joos et al. (2012). On the other hand, Sect. 5.4 is dedicated to the study of the outflows. We are looking at potentially fast ($\gtrsim 10\,\mathrm{km\,s^{-1}}$) bipolar outflows but we do not want to extract very biased properties by only selecting their higher-velocity component. As for the disk, they are identified on the cell-by-cell basis, and we elaborate on the criterion presented in Sect. 4.1.3 (the gas radial speed must exceed the escape velocity) to account for the turbulent medium. The velocity component perpendicular to the disk $v_\perp$ must exceed a threshold of $0.8\,\mathrm{km\,s^{-1}}$. The velocity threshold condition is added to the escape speed condition because the escape speed vanishes when r goes to infinity, whereas the turbulent runs have non-zero radial velocities which would be attributed to outflows. Taking the component perpendicular to the disk strengthens this criterion, so that potential thermal-pressure-driven, radiative-pressure-driven or interchange-instability-driven flows occurring at the disk edge, parallel to the disk plane, are not counted as outflows. Thanks to this process, we can easily obtain the mean properties of the outflow. To go further and extract its geometry, we developed the method below.

We present here our method to extract the outflow opening angle, trying not to make strong assumptions on the outflow geometry (*e.g.*, conical, strictly perpendicular to the disk or to the axes, axisymmetric). Looking at bipolar outflows, we distinguish two components, each one located on one side of the disk plane, and compute their properties individually. We consider the primary sink as the origin, call $\mathbf{r}_\mathrm{i}$ the position vector of the cell of index i and create the basis $(\mathbf{e}_1, \mathbf{e}_2, \mathbf{e}_3)$ where $\mathbf{e}_1$ is colinear to the specific angular momentum vector $\mathbf{j}$ and $\mathbf{e}_2, \mathbf{e}_3$ are in the disk plane.

1. As detailed above, first select all cells with $v_r > v_\mathrm{esc}$ and $v_\perp > 0.8\,\mathrm{km\,s^{-1}}$.

2. For each cell in the outflow selection, compute the dot product between the position vec-

tor $\mathbf{r}_i$ and $\mathbf{j}$ and create two sub-selections to distinguish the two cases: $\mathbf{r}_i \cdot \mathbf{j} > 0$ ("above" the disk) and $\mathbf{r}_i \cdot \mathbf{j} < 0$ ("below") that we will refer to as "A" and "B" outflows (Fig. 5.18). Now we focus on one sub-selection between the two, *i.e.* one outflow.

3. Define the position vector of geometric center (see Fig. 5.1)

$$\mathbf{u} = \frac{\sum_i \mathbf{r}_i \, dV_i}{\sum_i dV_i}, \tag{5.4}$$

where dV_i is the volume of the cell of index i. We observe transient clumps of denser gas being ejected within the outflows so taking the barycenter instead of the geometric center would lead to more variability and difficulty in interpreting the outcomes.

4. Following the methodology of Cabrit & Bertout (1992), we get the maximal radius $R_{\rm outflow}$ and the volume-averaged velocity $v_{\rm outflow}$ of the selection to compute the outflow momentum rate

$$F_{\rm outflow} = \frac{v_{\rm outflow}^2 \sum_i \rho_i \, dV_i}{R_{\rm outflow}}. \tag{5.5}$$

This corresponds to the required force to accelerate the flow from a null velocity to the characteristic velocity $v_{\rm outflow}$ in a time scale $R_{\rm outflow}/v_{\rm outflow}$.

5. Compute the projection $\mathbf{p}_i$ (left panel of Fig. 5.1) of the cell position vector perpendicularly to the position vector of the geometrical center $\mathbf{u}$

$$\mathbf{p}_i = \mathbf{r}_i - \frac{\mathbf{r}_i \cdot \mathbf{u}}{\|\mathbf{u}\|^2}\mathbf{u}. \tag{5.6}$$

6. Create four sub-selections $\mathbf{p}_{i,2} > 0$, $\mathbf{p}_{i,2} < 0$, $\mathbf{p}_{i,3} > 0$ and $\mathbf{p}_{i,3} < 0$ (middle panel of Fig. 5.1). The subscripts 2 and 3 denote the basis vectors $\mathbf{e}_2$ and $\mathbf{e}_3$, respectively.

7. In the $\mathbf{p}_{i,2} > 0$ sub-selection, identify the cell with $\|\mathbf{p}_i\| = \max_i(\|\mathbf{p}_{i,2}\|)$; its position vector is labelled $\mathbf{r}_{2,+}$. This corresponds to the outermost cell in the positive $\mathbf{e}_2$ direction. We perform the same step for $\mathbf{p}_{i,2} < 0$ (outermost cell in the negative $\mathbf{e}_2$ direction), $\mathbf{p}_{i,3} > 0$ and $\mathbf{p}_{i,3} < 0$, and obtain $\mathbf{r}_{2,-}$, $\mathbf{r}_{3,+}$, $\mathbf{r}_{3,-}$ (right panel of Fig. 5.1).

8. We define the outflow opening angle $\theta_{\rm outflow}$ as the average of the four angles between $\mathbf{u}$ and $\mathbf{r}_{2,+}$, $\mathbf{r}_{2,-}$, $\mathbf{r}_{3,+}$ and $\mathbf{r}_{3,-}$, respectively, *i.e.*

$$\theta_{\rm outflow} = \text{mean}(\arccos\left(\frac{\mathbf{r}_{2-3,\pm} \cdot \mathbf{u}}{\|\mathbf{r}_{2-3,\pm}\| \, \|\mathbf{u}\|}\right) \times 2), \tag{5.7}$$

where the factor 2 arises because the four angles correspond to semi-opening angles.

Let us note that, by projecting the cell positions onto the disk plane $(\mathbf{e}_2, \mathbf{e}_3)$, we implicitly assume that the outflow is perpendicular to the disk. Since this is not generally valid, our resulting opening angle is decreasingly accurate as the misalignment between the outflow and $\mathbf{j}$ increases.

5.3 Temporal evolution

5.3.1 Overview

As the gravitationally-unstable cloud cores collapse, the first sink particles form at $t \approx 29$ kyr in the four simulations. Except in run M2, where we get a filament-like structure of width

Table 5.1: Initial conditions of the four runs: name, Mach number, Alfvénic Mach number, mass-to-flux to critical mass-to-flux ratio, respectively.

Model	$\mathcal{M}$	$\mathcal{M}_{\rm A}$	μ
M0	0	0	5
M05	0.5	1.4	5
M2	2	5.7	5
M05B2	0.5	0.57	2

$\sim$2000 AU due to the strong turbulent support (see below), the dense region ($\rho \gtrsim 10^{-16}\,\mathrm{g\,cm^{-3}}$, $n \gtrsim 10^{7}\,\mathrm{cm^{-3}}$) becomes rapidly concentrated in a sphere of diameter $\sim$2000 AU (second row of Fig. 5.2). Accretion disks with plasma beta $\beta = P/P_{\rm mag} > 1$ (where $P_{\rm mag} = B^2/2$ is the magnetic pressure) form in all runs and are not strictly aligned with the large-scale angular momentum (Fig. 5.5), except in run M0. In runs M0 and M05B2, in which turbulence is subalfvenic, no secondary sink forms. With superalfvenic turbulence (runs M05 and M2), a secondary (and long-lived) sink particle forms in the primary sink accretion disk. In the most turbulent run (M2), three additional sink particles form from initial fragmentation and four in the disk plane, but merge with the primary or secondary sinks. We will study in more details the question of the stellar multiplicity in Sect. 5.3.5.

The density-magnetic field strength histograms for runs (from left to right) M0, M05, M2, M05B2 at $t = 50$ kyr are shown in Fig. 5.3. At densities below $\sim 10^{-15}\,\mathrm{g\,cm^{-3}}$ ($n \sim 10^{8}\,\mathrm{cm^{-3}}$), we recover the ideal MHD limit where B increases with ρ. In runs M0 and M05B2, the high-B, low-ρ part of the histogram is populated by outflowing material originally. At high densities, the plateau-like feature is present in the four runs, and constrasts with ideal MHD calculations, as shown in the low-mass regime (Masson et al., 2016). This is due to ambipolar diffusion, which becomes effective above $\rho \gtrsim 10^{-15}\,\mathrm{g\,cm^{-3}}$. The effective diffusion coefficient varies non-linearly with the magnetic field strength $\eta_{\rm AD} \propto B^2/\rho$ which explains its strong regulating effect. The plateau is located between $\sim$0.1 G in the superalfvenic runs (M05, M2), and $\sim$0.3 G in the subalfvenic runs (M0, M05B2). The inclusion of ambipolar diffusion will prevent the magnetic field strength to increase unrealistically, which would change the disk structure and possibly the outflows (we recall that a strong magnetic field is expected in the magneto-centrifugal mechanism, see Sect. 1.9.4).

We observe that pockets of magnetized plasma ($\beta < 1$) are regularly expelled from the disk outer edge (left and middle panel of Fig. 5.6). This is visible in run M0 but hardly seen in the other, turbulent runs. We investigate in Sect. 5.3.3 whether the magnetic interchange instability, which has been found to redistribute magnetic flux after accumulation around sink particles (Krasnopolsky et al., 2012), is responsible for this. Nevertheless, the filamentary structures formed out of this process are not dense/thick enough to be observed in column density. This phenomenon is not the only asymmetry arising in the simulation.

We observe the presence of filamentary structures linking the densest regions (where the sink-disk system is) to the surroundings, that we will refer to as "streamers". These are visible as the north-west and south-east filaments in Fig. 5.2 (last panel of the second row). They have a density $\rho \gtrsim 10^{-15}\,\mathrm{g\,cm^{-3}}$ ($n \gtrsim 10^{8}\,\mathrm{cm^{-3}}$) and are dominated by thermal pressure ($\beta > 1$), on the contrary to the gas that surrounds them. They appear as a path for the accretion flow and pull the magnetic field lines, which in turn form an hour-glass shape. Since the Lorentz force has no component parallel to the field lines, the gas can move onto the lines to join the streamers without any magnetic resistance, in a similar way as the bead-on-a-wire picture for magneto-centrifugal jets. These streamers form perpendicularly to the core-scale magnetic field, in all runs. In run M0, this plane is also that of the accretion disk. Nonetheless, they connect to the disk outside of the disk plane, either from above or below, breaking the north-south symmetry.

Table 5.2: Simulations outcomes: $t_{\rm out}$ (kyr) denotes the time when sustained outflows appear, $M_\star(t_{\rm out})$ ($M_\odot$) is the primary sink mass at this time, $M_{\star,\rm end}$ is its mass at the time $t_{\rm end}$ of the run and $M_{2,\rm end}$ is the secondary sink mass at the same time.

Model	$t_{\rm out}$	$M_\star(t_{\rm out})$	$t_{\rm end}$	$M_{\star,\rm end}$	$M_{2,\rm end}$
M0	36.0	3.7	80.4	15.8	-
M05	56.4	6.6	71.5	8.8	7.7
M2	66.2	5.1	78.5	6.2	9.9
M05B2	39.1	3.8	66.2	11.0	-

In runs M05 and M05B2, the streamers are much thicker due to the additional turbulent support. This gives rise to the filament-like structure of width $\sim$2000 AU in run M2, as mentioned above. Overall, the streamers develop perpendicularly to the core-scale magnetic fields but do not seem to set the disk formation plane. The symmetry breaking they provide is precious to us, considering that 16% of the outflows reported in Wu et al. (2004) are monopolar. We study in more details the disk-magnetic fields alignment in Sect. 5.3.2 and the outflow-magnetic fields alignment in Sect. 5.4.6.

Outflows are launched in all runs. Nonetheless, they are delayed (and disturbed) in the superalfvenic runs M05 and M2, in comparison to runs M0 and M05B2, and even monopolar in run M2. We will follow three leads regarding their origin (Sect. 5.4.1): radiative acceleration, magnetic tower flow, and magneto-centrifugal mechanism. For the latter, we will introduce some of the concepts derived and presented in more details in Sect. 1.9.4.

5.3.2 Alignment between the angular momentum and the magnetic field

One objective of this work is to make progress on the question of whether disks and outflows, respectively, align with core-scale magnetic fields. Here we investigate the specific angular momentum components, and the alignment between this vector and the large-scale magnetic field (along the $x-$axis) as a function of the Mach number and the magnetic field strength.

Figure 5.4 shows the specific angular momentum $\mathbf{j}$ as a function of the spatial scale for three epochs: $t = 0, 30, 50$ kyr. We recall that each run has a tiny rotational support (1%) of solid-body rotation aligned with the $x-$axis. In our reference case, run M0, the specific angular momentum (not shown here) is initially aligned with the magnetic field axis and remains so (within less than 6 deg). Figure 5.4 shows the increase of the specific angular momentum in the central part of the domain as collapse occurs, due to angular momentum conservation. The angular momentum set by the initial turbulence is dominated by its y-component. The dominating component of $\mathbf{j}$ varies with the sphere radius over which it is computed, as a consequence of the initial (turbulent) velocity field. The initial rotation, aligned with the $x-$axis, dominates at large scales ($> 10^4$ AU) in runs M05 and M05B2 (left and right panels), but not in run M2 where it is actually smaller. This means that the turbulent gas is rotating counter-clockwise with respect to the initial rotation. In the two runs with superalfvenic turbulence, M05 and M2 (left and central panels of Fig. 5.4), the dominating components at disk scales at $t = 50$ kyr are the initial dominating components at larger scales. These are the $x-$ and $y-$ components in the subsonic run M05 and the $z-$ and $y-$ components in the supersonic run M2. This is in agreement with the study of Machida et al. (2019) in the low-mass regime, in which they vary the angle between the rotation axis and the magnetic field direction. They observe that the disk

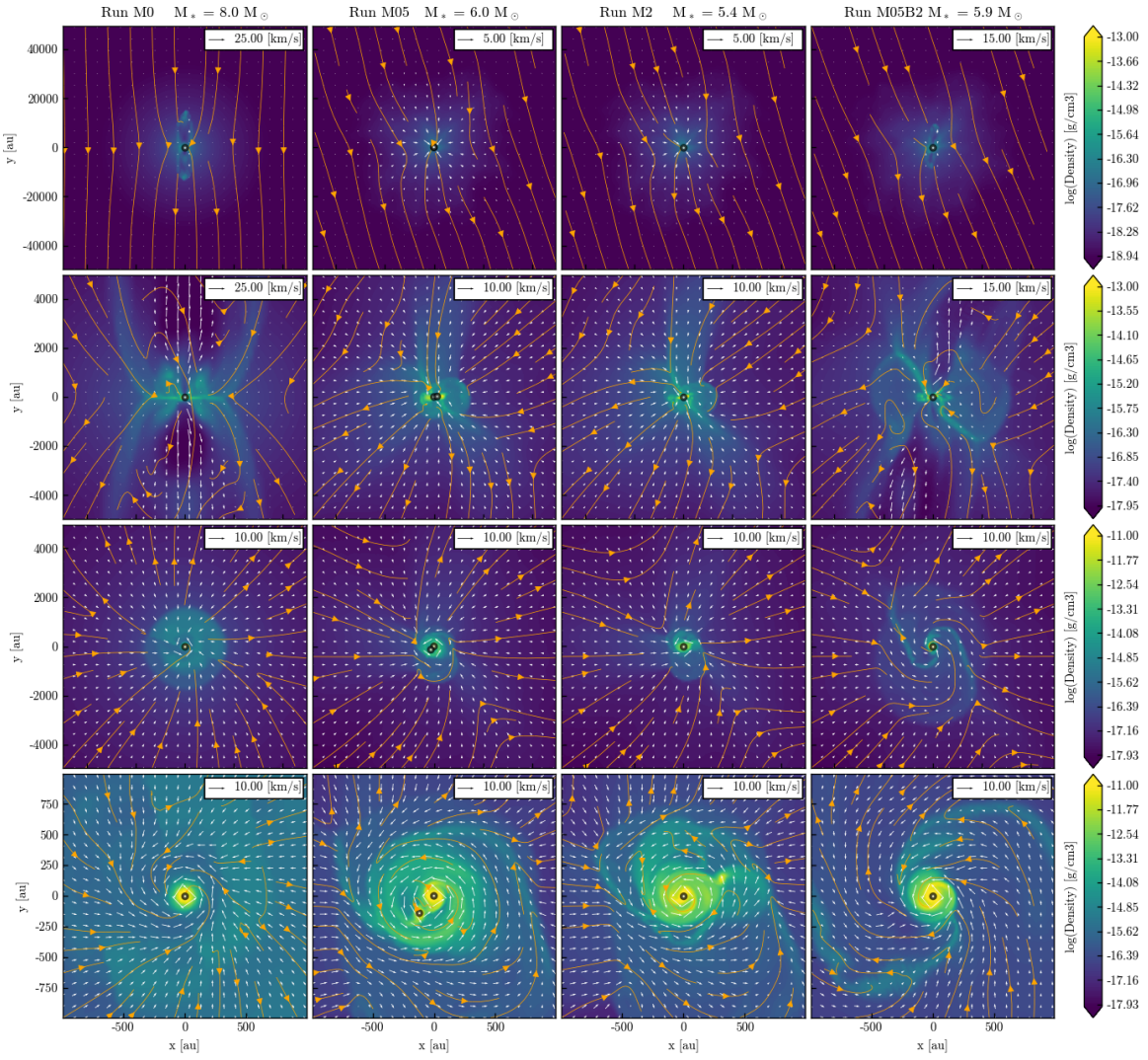

Figure 5.2: Density slices parallel (first and second row) and pendicular (third and fourth row) to the disk plane, at $t \approx 50$ kyr. Streamlines corresponding to magnetic field lines, and arrows corresponding to the velocity field, are overplotted. From left to right: run M0, M05, M2, M05B2. A mass density $\rho = 10^{-19}\,\mathrm{g\,cm^{-3}}$ corresponds to a particle density $n = 2.6 \times 10^{4}\,\mathrm{cm^{-3}}$ and $\rho = 10^{-11}\,\mathrm{g\,cm^{-3}}$ to $n = 2.6 \times 10^{12}\,\mathrm{cm^{-3}}$.

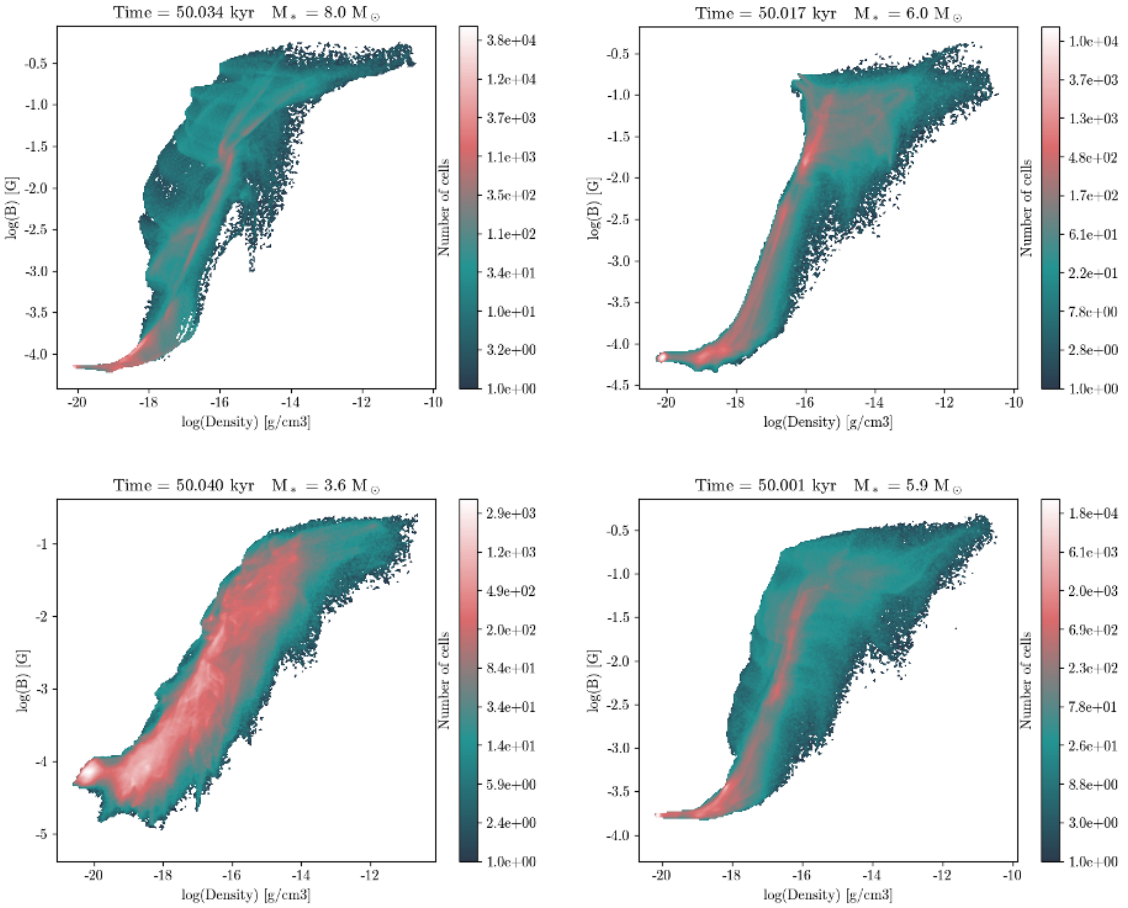

Figure 5.3: Density-magnetic field strength histograms at $t = 50$ kyr. Top: run M0 (left), M05 (right), and bottom: M2 (left), M05B2 (right).

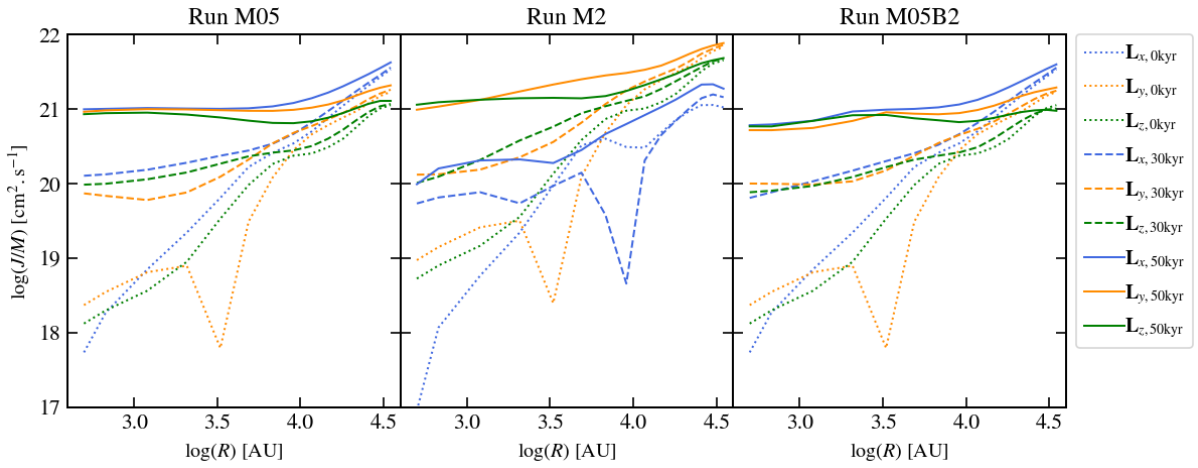

Figure 5.4: Specific angular momentum $\mathbf{j} = \mathbf{J}/M = \frac{1}{M}\int_{r<R} \mathbf{r} \times \rho \mathbf{v}\, \mathrm{d}V$ as a function of the sphere radius R for runs M05 (left), M2 (middle) and M05B2 (right). Time $t = 0$ kyr describes the initial conditions, $t = 30$ kyr is roughly the first sink formation epoch (a rotating structure is already present), and $t = 50$ kyr corresponds to a massive protostar surrounded by its accretion disk.

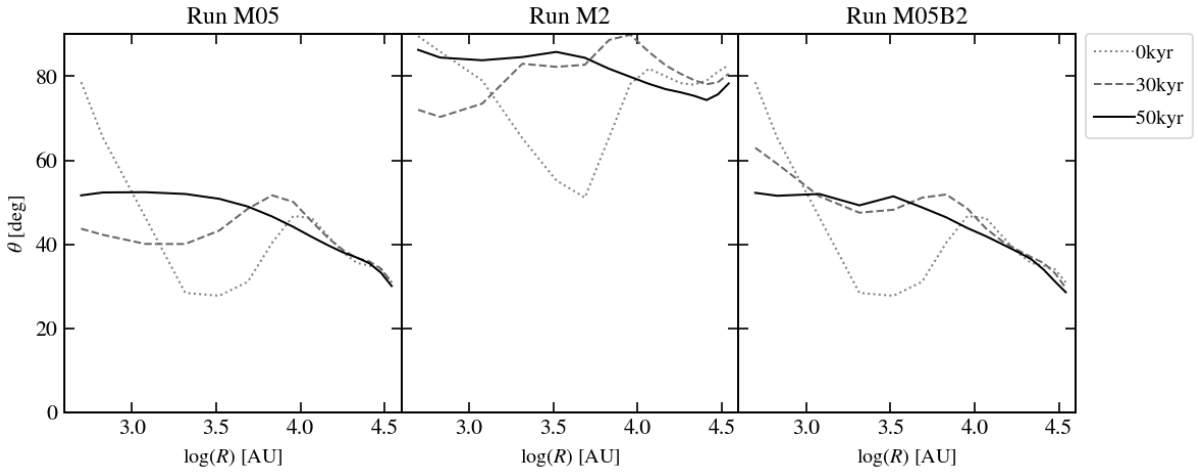

Figure 5.5: Angle between the specific angular momentum **j** and the x-axis as a function of the sphere radius R for runs M05 (left), M2 (middle) and M05B2 (right). The same timesteps as Fig. 5.4 are pictured here.

plane is mainly set by their initial rotation (*i.e.* specific angular momentum) axis, even with an initially strong magnetic field ($\mu = 1.2$).

Let us focus on the influence of magnetic fields. The left and right panels of Fig. 5.4 only differ by the magnetic field strength: $\mu = 5$ in run M05 (left) and $\mu = 2$ in run M05B2 (right). At small scales, the component $\mathbf{j}_x$ in run M05 is $\approx$2 times larger than in run M05B2. This is a consequence of the magnetic braking, *i.e.* the transport of angular momentum outwards, which is more efficient when rotation and magnetic fields are aligned in a collapsing core (Joos et al., 2012). It prevents disk formation perpendicularly to the magnetic field and favors configurations where the angular momentum is misaligned with the magnetic field.

In Fig. 5.5, we show the angle between **j** and the $x-$axis, which corresponds to the direction of the large-scale magnetic field. The orientation of the angular momentum varies significantly with the scale considered and with time. We get similar results for sub- and supersonic turbulences as Joos et al. (2013), namely a strong misalignment between **j** and **B**. The orientation on small scales converges in time as the disk forms and increases in size (see the left panel of Fig. 5.9). On larger scales, the orientation does not vary except in the most turbulent run, M2 (Fig. 5.5), which is likely due to the velocity field changing configuration from the initial turbulent one to the radial direction as all the simulated gas feels the gravitational pull. Comparing left and right plots of Fig. 5.5 shows that increasing the magnetic field strength, up to the point where the initial turbulence is subalfvenic, does not favor the alignment between **j** and **B**. This is consistent with Machida et al. (2019) who find that the only run with the disk perpendicular to the magnetic field is for a perfect alignment of the rotation axis and the magnetic field direction.

Overall, the disk normal in our simulations is misaligned ($50 - 85$ deg, Fig. 5.5) with the large-scale magnetic field, largely influenced by the initial rotation. If the disk formation were a large-scale process, we would expect the disk normal to align with the core-scale angular momentum. Actually, as shown in the middle and right panels of Fig. 5.4, $\mathbf{j}_y < \mathbf{j}_z$ (to be distinguished from $\mathbf{j}_x$, which is more affected by magnetic braking) at the disk scale while $\mathbf{j}_y > \mathbf{j}_z$ at core scales. The disk orientation here does not appear to be set by the angular momentum direction at scales larger than $\sim 10^4$ AU. This would indicate that disk formation is a "local" process, in agreement with the recent observations in the low-mass regime Gaudel et al. (2020).

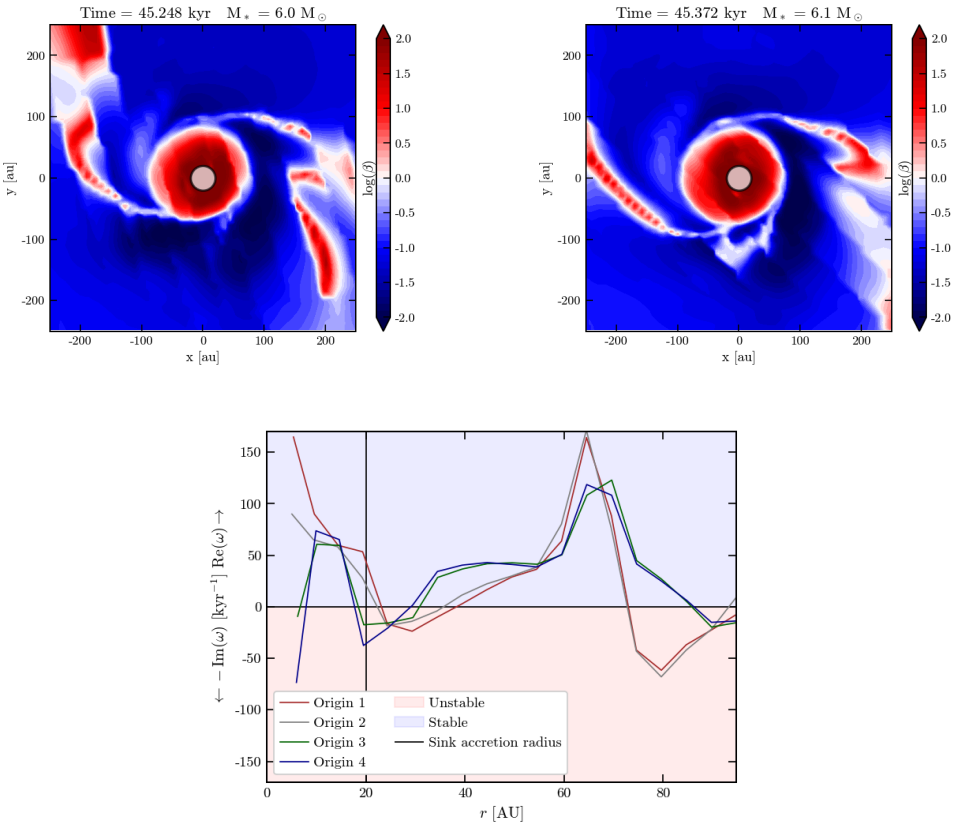

Figure 5.6: Interchange instability in run M0. Top-left and top-right panels: plasma β at $t = 45.25$ kyr (before the instability develops) and $t = 45.37$ kyr. Bottom panel: square root ω of N^2 (see Eq. 5.9): $\mathrm{Im}(\omega)$ gives the growth rate of the interchange instability. We compute it in the $y-$ direction in the disk plane, at $t = 45.25$ kyr, taking as origin the four closest points to the sink center.

5.3.3 Interchange instability

It can be observed on the left and middle panels of Fig. 5.6 that a pocket of magnetized plasma is released from the disk edge. This occurs several times in the simulations but is more difficult to distinguish in the turbulent runs. In this section we check whether the interchange instability (also called magnetic Rayleigh-Taylor instability), which is a convective instability that redistributes the magnetic flux, is responsible for this.

The instability occurs in the $y-$direction if (Lovelace & Scott 1981, Kaisig et al., 1992)

$$\frac{\left\| \dfrac{\partial((\gamma-1)P + B_x^2/2)}{\partial y} \right\|}{\left((\gamma-1)c_s^2 + v_A^2\right) \left\| \dfrac{\partial \rho}{\partial y} \right\|} > 1, \tag{5.8}$$

where x is the normal direction to the disk, $v_A = B/\sqrt{\rho}$ is the Alfvén velocity. The condition of instability is roughly given by the balance between gravity and the (total) pressure gradient. We have derived the growth rate $\omega = \mathrm{Im}(N)$ analogously to the Brunt-Väisäla frequency (which is a frequency associated to convective instabilities) from

$$N^2 = \frac{1}{1+\alpha}\left(\frac{\gamma-1}{\gamma}\frac{\partial s}{\partial y} + \alpha \frac{\partial \log(B/\rho)}{\partial y}\right) g_{\mathrm{eff}}, \tag{5.9}$$

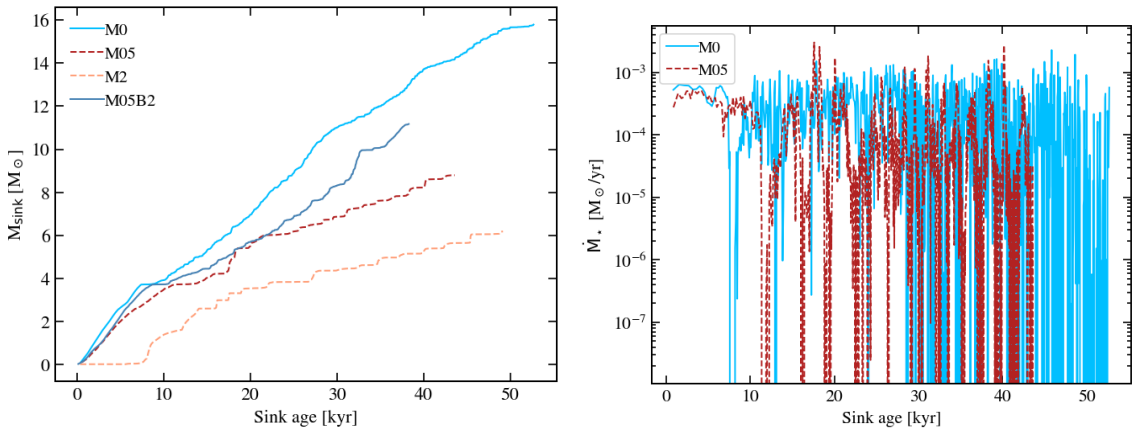

Figure 5.7: Primary sink mass (left panel) and accretion rate (right panel) as a function of the sink age for the four runs. The accretion rate is plotted for one subalfvenic (M0) and superalfvenic (M05) run for readability.

where we defined $\alpha \equiv v_A^2/c_s^2$, $s = \frac{1}{\gamma-1}\ln(P\rho^{-\gamma})$ is the normalized gas entropy (see Sect. 4.1.6), $g_{\rm eff} = g - v_\phi^2/r$ is the effective gravity at radius r (sum of the gravitational and centrifugal accelerations), y is the direction along which the instability develops.

Right panel of Fig. 5.6 shows the square root of N^2 in the y direction in the disk plane, varying the x and z coordinates of the origin among the four closest cells to the sink center. Zones where this value is pure imaginary are unstable, which correspond to the disk edge in multiple directions. The growth rate at the disk edge is $\omega \approx 70\,{\rm kyr}^{-1}$ for the origin cells of coordinates $[3, 2]$ AU (Origin 1) and $[-2, 2]$ AU (Origin 2), so the timescale for the instability to develop is $\tau_{\rm instab} \approx 14$ yr. The unstable zone is ≈ 20 AU wide, in which the gas is flowing at a radial velocity $v_r \approx 0.8\,{\rm km\,s}^{-1}$ so the advection timescale is $\tau_{\rm adv} \approx 120$ yr. Since $\tau_{\rm instab} \gtrsim \tau_{\rm adv}/3$ (Foglizzo et al., 2006), this is consistent with the interchange instability being at work. When taking the cells $[3, -3]$ (Origin 3) and $[-2, -3]$ AU (Origin 4) as the origin of the profile, it is less clear whether this part of the disk edge is stable or not. Hence, the small unstable part of the disk edge may explain why this instability is less visible than in Krasnopolsky et al. (2012) and too faint to be observable.

5.3.4 Sink mass history

Left panel of Fig. 5.7 displays the primary sink mass as a function of time. The most massive star formed is $M \simeq 16\,{\rm M}_\odot$, in run M0. Globally, two different behaviours are visible, between subalfvenic and superalfvenic runs. On the one hand, runs M0 and M05MU2, and on the other hand, runs M05 and M2 show similar sink mass histories. There is a delay of $\sim$8 kyr between runs M05 and M2 but a comparable slope (mean accretion rate). The mass accretion is much smoother in the subalfvenic cases than in the superalfvenic cases where clumps or sink companions lead to major accretion events. This is confirmed when looking at the instantaneous accretion rate, displayed in the right panel of Fig. 5.7 for runs M0 and M05. The values for runs M05B2 and M2 are not displayed here, for readability, and show similar features with runs M0 and M05, respectively. It is mainly between 10^{-4} and $10^{-3}\,{\rm M}_\odot\,{\rm yr}^{-1}$ in run M0, in agreement with observational values (Motte et al., 2018 and references therein). The accretion rate in run M05, which includes initial turbulence, is first comparable to M0. After $\sim$12 kyr it becomes erratic, having most of the time zero values. These correspond to clumps/companions being

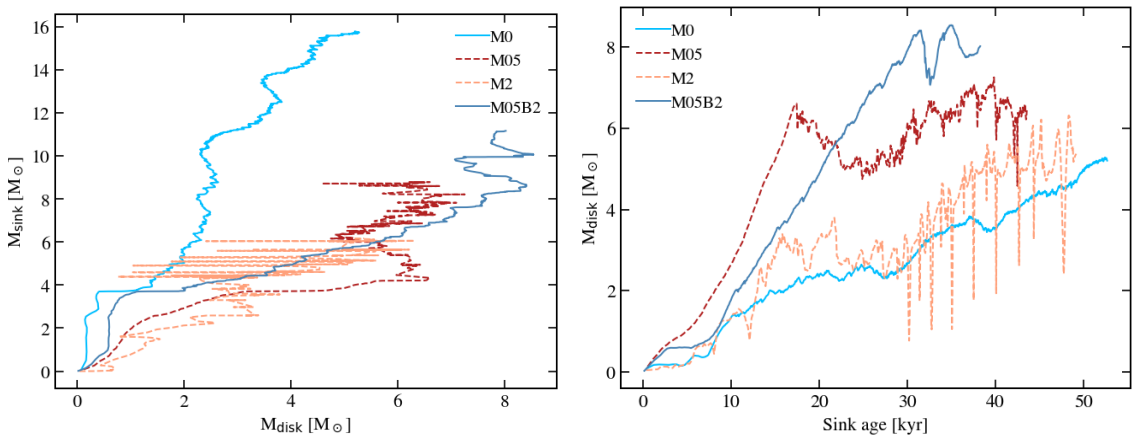

Figure 5.8: Primary sink mass against the disk mass (left panel), and disk mass as a function of time (right panel) for the four runs. The accretion rate is plotted for one subalfvenic (M0) and superalfvenic (M05) run for readability.

accreted in a single time step.

We recall that our sink accretion scheme relies on the presence of high-enough density gas within the sink volume. Hence, the total absence of accretion, at a given time, means that the sink volume has not gathered enough material to be accreted. The main accretion events in the superalfvenic runs are more dramatic than in the subalfvenic runs, with companion sink particles or orbiting massive clumps raising the primary sink mass by a fraction of a solar mass. Considering our resolution and sink merging criterion, it is not possible to capture formation of a close ($\sim$ AU separation) binary system.

Nonetheless, we report the formation of a binary system in the two superalfvenic runs (M05 and M2, see Table 5.2). In run M2, the secondary sink has been formed ≈ 17 kyr after the primary. It occurred at the extremity of a spiral arm which developed during the accretion of another sink particle. The secondary particle survives until the end of the run, *i.e.* a lifetime $\gtrsim 33$ kyr. This system also formed in the corresponding lower-resolution run (LRM2), with an age difference of $\approx$18 kyr instead of $\approx$17 kyr. Thanks to a slightly smaller resolution, run LRM2 has been carried out up to $t\sim$96 kyr and the secondary sink particle is $\approx$50 kyr old. The stellar masses are 9.2 $M_\odot$ and 8.1 $M_\odot$. The same formation mechanism led to the birth of a long-lived companion in run M05. Similarly, a binary system formed in LRM05 too but at later times, with final masses of 19.7 $M_\odot$ and 7.6 $M_\odot$ at $t \approx 100$ kyr. The secondary sink is 30 kyr old. Interestingly, after $t \sim 78$ kyr, the primary sink gains only a fraction of a solar mass within more than 20 kyr, while the companion accretes 6 $M_\odot$. Overall, we obtain long-lived (at least tens of kyr) binary systems in the superalfvenic runs, with mass ratios close to 1 (except in run LRM05 where it may tend towards it). The only formation process we observe is disk fragmentation, while the sinks formed from initial core fragmentation have merged. We recall that we have operated refinement based on the thermal Jeans length, while a similar MHD criterion is slightly less restrictive (see the discussion in Myers et al. 2013). The Jeans length can vary significantly in the disk, hence the numerical convergence regarding binary formation in run M2 advocates for a physical fragmentation, rather than numerical.

The left panel of Fig. 5.8 shows the relation between the sink and the disk masses (the proper disk mass evolution is discussed in Sect. 5.3.5). As discussed later, the disk mass determination is highly perturbed after the secondary sink formation in runs M05 and M2, which arrives at $\sim$6 $M_\odot$ in run M05 and $\sim$4 $M_\odot$ in run M2. Apart from the binary epoch, it appears that there is a correlation between several sink mass gain events and disk mass loss events in the four runs,

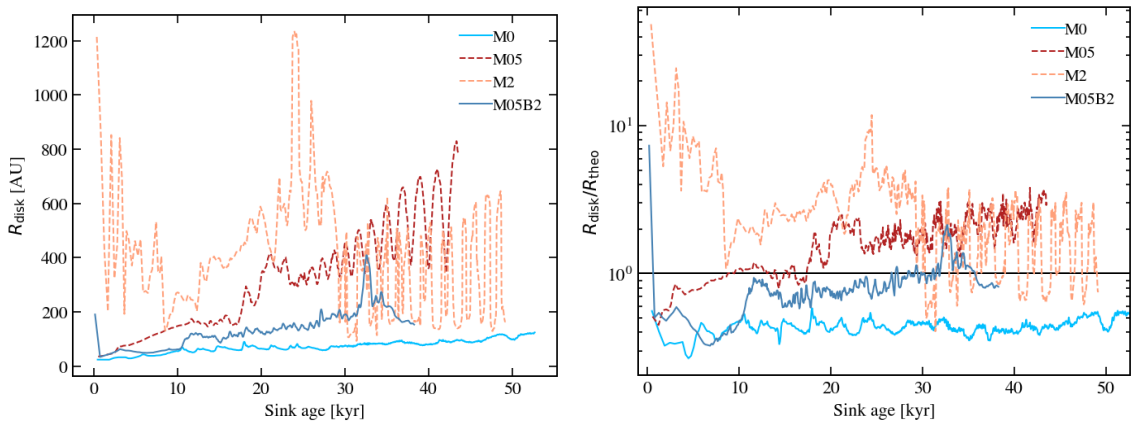

Figure 5.9: Radius (left panel) and ratio between the disk radius and the theoretical value (right panel, Eq. 5.10) as a function of time, for the four runs.

but the masses involved are much smaller in the subalfvenic runs. This is consistent with the gas falling smoothly onto the central star via the accretion disk, in subalfvenic runs, while the disk forms clumps first before they are accreted in superalfvenic runs.

5.3.5 Disk properties

Disks are formed in all four runs. They differ significantly by their properties in terms of dynamics, mass, and size. Furthermore, binary systems form in the two superalfvenic runs, affecting disk properties and their measurements.

Disk mass and multiplicity

The disk mass temporal evolution is displayed in the right panel of Fig. 5.8. It globally increases with time, with more variations in the superalfvenic runs. We obtain disk masses ranging from $\approx 1 - 8\,\mathrm{M}_\odot$ (for $t > 10$ kyr). As shown in the left panel of Fig. 5.9), the largest disk is formed in the most turbulent simulation, but is not the most massive one. In fact, the disk selection is not continuous in the M2 run. This is attributed to the presence of spiral arms sweeping-off the gas and creating zones where the density is too low for the corresponding cells to be attributed to the disk selection. Furthermore, the disks are highly dynamical and less well-defined in the superalfvenic runs than in the subalfvenic runs. Starting from an apparently stable state, the disk edge is perturbed and spiral arms develop (where secondary sink particles form) and grow outward. The disk size appears to encapsulate the secondary disk and the disk size variations are linked to this secondary disk motions. Both are embedded in a rotating structure of larger radius (≈ 500 AU for run M05 and ≈ 1000 AU for run M2) and density $\rho \gtrsim 5 \times 10^{-16}\,\mathrm{g\,cm^{-3}}$ ($n \gtrsim 10^8\,\mathrm{cm^{-3}}$), that we will refer to as the circumbinary disk. In the case of run M2, this rotating structure is even more dynamically active than in run M05. The disk size (as defined here) is strongly affected by whether the gas in a given cell satisfies our density threshold criterion and whether infall motions take place too (bottom-left panel of Fig. 5.10). As a consequence, the disk criteria are not fulfilled and this is not accounted for in the disk mass, which is thus lower than in run M05. On the opposite, the disk radius is not affected in the same way since disk-like components are still present at large radii. Binary formation in runs M05 and M2 strongly affects the disk, as we define it. The periodic pattern on the disk radius at $t > 25$ kyr for run M05 and $t > 30$ kyr for run M2 is a consequence of the secondary sink

environment being accounted for or not. Consistently, the period is equal to this secondary sink orbital period and is ≈ 1.5 kyr. It can be seen on the sink mass history (left panel of Fig. 5.7) that the primary sink is partially starved due to the presence of the secondary sink, as compared to the subalfvenic runs where no binary forms. In both runs, the secondary sink mass quickly becomes comparable to (and even slightly greater than, in run M2) the primary sink mass. Such balanced mass ratios have been obtained in the radiation-hydrodynamical simulations of Krumholz & Matzner (2009) and could be integrated for longer times, with final masses of $41.5\,\mathrm{M}_\odot$ and $29.2\,\mathrm{M}_\odot$ and separation of 1590 AU. The binary separation is $350-600$ AU in run M05 and $400-700$ AU in run M2. These are elliptic orbits and the separation is slightly increasing with time. As mentioned above, the binary systems formed from disk fragmentation rather than core fragmentation. Such systems are close to Keplerianity (top-right and bottom-left panel of Fig. 5.10) up to $\sim$1000 AU. In the absence of a strong stellar activity from one component, they could be identified as large disks (Johnston et al., 2015). The disk radius of HH80-81, estimated to be $\sim$291 AU (Girart et al., 2018), is in better agreement with the magnetically-regulated indivual disks radii we obtain than with purely hydrodynamical disks (see Chapter 4 and *e.g.*, Kuiper et al. 2011).

Analytical estimate

Finally, we compare the disk sizes with the theoretical predictions from Hennebelle et al. (2016) for magnetically-regulated disks. Those are obtained from the equality between various timescales. On the one hand, the timescale to generate toroidal field from differential rotation and the timescale for ambipolar diffusion to diffuse it vertically. On the other hand, these are the magnetic braking and the rotation timescales. The disk radius set by ambipolar diffusion is then

$$r_{\mathrm{d,AD}} \simeq 18\mathrm{AU} \times \delta^{2/9} \left(\frac{\eta_{\mathrm{AD}}}{0.1\mathrm{s}}\right)^{2/9} \left(\frac{B_z}{0.1\mathrm{G}}\right)^{-4/9} \left(\frac{M_\mathrm{d}+M_\star}{0.1\,\mathrm{M}_\odot}\right)^{1/3}, \tag{5.10}$$

where δ is the ratio between the initial density profile and the singular isothermal sphere (SIS, Shu 1977), and M_d is the disk mass. By comparing our density profile to the SIS, we take $\delta = 10$, in agreement with Hennebelle et al. (2011), and the mean magnetic field strength within the disk as a proxy for the component B_z.

First, the disk sizes agree within a factor of $\approx 2-3$ with the prediction above. The disk in run M05 is slightly larger, and the disk in run M2 is significantly larger than the value predicted by Eq. 5.10 at early times. We investigate whether the radius, as given by our disk definition (which loosely encapsulates the secondary disk and gives an approximation of the binary separation) in superalfvenic runs is more consistent with hydrodynamical disks, whose size is set by the centrifugal barrier. Equalling the rotational energy $E_\mathrm{rot} = M_\mathrm{c}(R\Omega)^2 = M_\mathrm{c}(J/M_\mathrm{c})^2/R^2$ and the gravitational energy GM_c/R we obtain the hydro disk radius

$$r_{\mathrm{d,hy}} \simeq 150\mathrm{AU} \times \left(\frac{J/M_\mathrm{c}}{5\times10^{21}\,\mathrm{cm^2\,s^{-1}}}\right)^2 \left(\frac{M_\mathrm{c}}{100\,\mathrm{M}_\odot}\right)^{-1}. \tag{5.11}$$

For run M05, $J/M_\mathrm{c} \simeq 8\times10^{21}\,\mathrm{cm^2\,s^{-1}}$, hence $r_{\mathrm{d,hy}} \simeq 400$ AU, and $J/M_\mathrm{c} \simeq 10^{22}\,\mathrm{cm^2\,s^{-1}}$ so $r_{\mathrm{d,hy}} \simeq 600$ AU for run M2. These values roughly meet the disk radius (*i.e.*, the binary separations) shown in Fig. 5.9 after the secondary sink has formed. Hence, the binary separation appears to depend on the initial turbulent velocity field. The circumbinary disk which surrounds the two sink+disk systems is about twice larger than the binary separation. Nonetheless, the individual disks around each sink are $\sim 100-200$ AU in radius, similarly to the disks in runs M0 and M05B2 and consistent with magnetic regulation. For run M2, it is visible in the left-bottom panel of

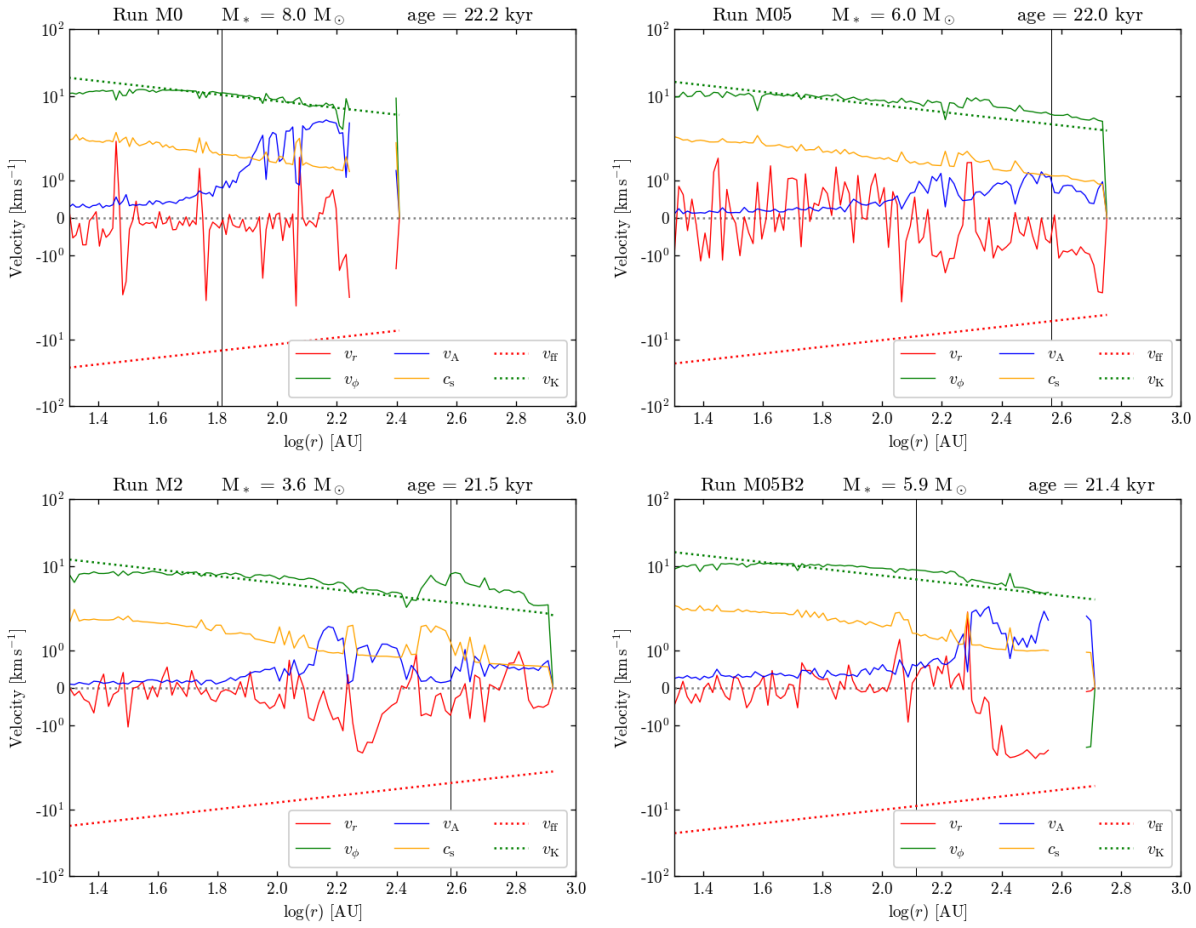

Figure 5.10: Azimuthally-averaged radial and azimuthal velocities, Alfvén speed, isothermal sound speed, free-fall velocity and Keplerian velocity as a function of the radius at $t = 50$ kyr. The vertical line indicates the disk radius plotted in Fig. 5.9. Top row: run M0 (left), M05 (right). Bottom row: run M2 (left), M05B2 (right).

Fig. 5.10 as the radius at which the Alfvén velocity equals the sound speed ($\simeq$150 AU). To conclude, the disk around each sink appears to be set by magnetic regulation, while the binary separation is linked to the centrifugal radius that can be derived from the initial turbulent field.

Characteristic velocities and magnetic field components

Figure 5.10 shows the radial profile of the azimuthally-averaged characteristic velocities in the disk selection. Overall, the azimuthal velocity is in agreement with a Keplerian profile. It is slightly super-Keplerian in turbulent runs (M05, M2, M05B2) at radii $\gtrsim$ 60 AU. In all runs, it becomes sub-Keplerian as the radius decreases. This is due to the gravitational field being dominated by the central object and diminished by the sink softening length (Bleuler & Teyssier, 2014). In this study we have set it equal to the accretion radius, *i.e.* 20 AU here. The disks are roughly Keplerian, hence the infall velocity is much smaller than the free-fall velocity and typically smaller than 1 km s^{-1}. The rotation motions, and infall motions beyond the disk, are supersonic.

As shown in the left panel of Fig. 5.6, the disks are dominated by thermal pressure rather

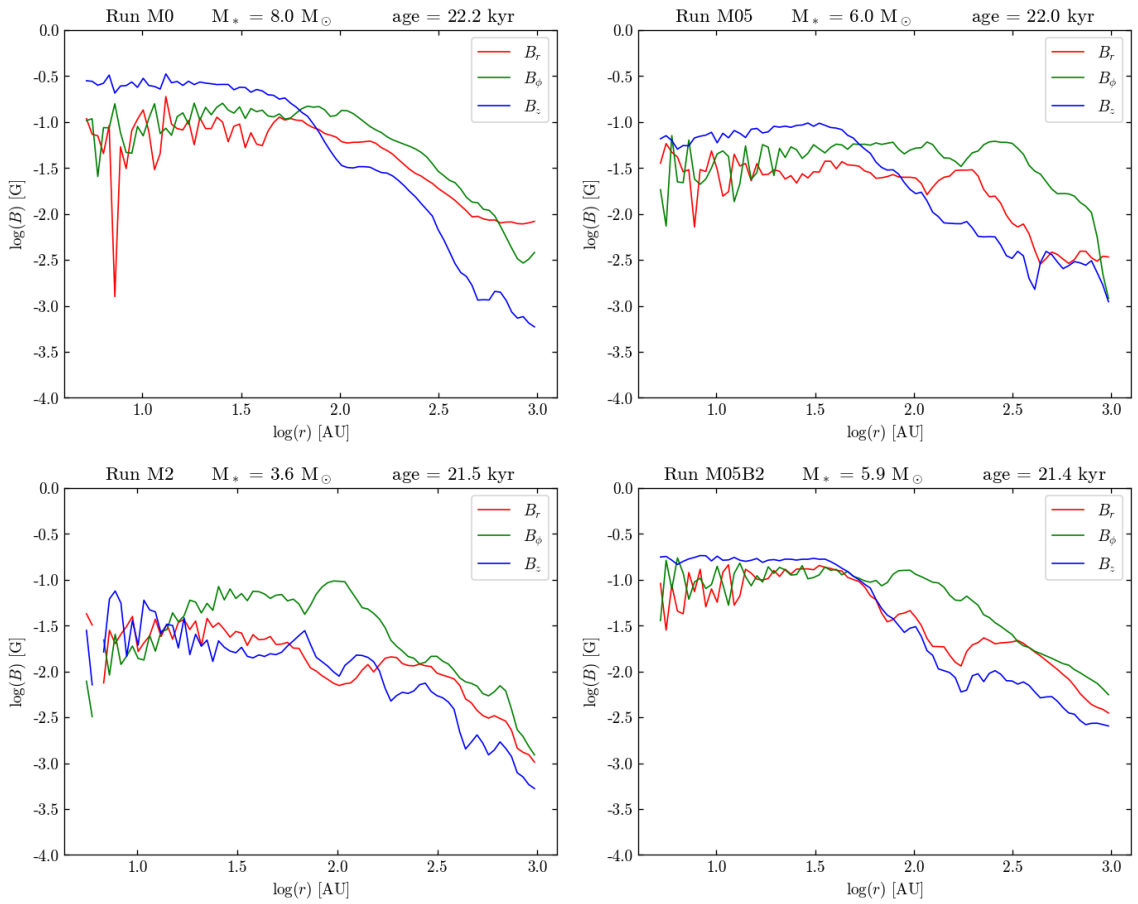

Figure 5.11: Azimuthally-averaged magnetic field components as a function of the radius at $t = 50$ kyr. Top row: run M0 (left), M05 (right). Bottom row: run M2 (left), M05B2 (right).

than by magnetic pressure, setting the disk vertical equilibrium. Radial equilibrium is set by centrifugal forces. We recall that the disk radius is defined as the radius enclosing 90% of the total mass of the disk selection cells, and we note that this radius is slightly smaller than the point where a change from thermally-dominated to magnetically-dominated region is observed. This applies well to runs M0 and M05B2, but not to runs M05 and M2. Indeed, the presence of a binary in these runs makes difficult the determination of the disk radius based on the criteria we have presented above, which is often confused with the circumbinary disk. We argue that a physically-motivated criterion for the identification of individual disks is the plasma beta with $\beta > 1$. In our simulations, it encapsulates that the disk size is regulated by ambipolar diffusion, in contrast to the ideal MHD case (Masson et al., 2016). This criterion is not sufficient though because of the existence of thermally-dominated ($\beta > 1$) filaments, as well as parts of the circumbinary disk.

Figure 5.11 displays the azimuthally-averaged magnetic fied components in cylindrical coordinates centered on the primary sink, using the angular momentum vector as the vertical direction z. Hence, the selected cells are in the disk plane but are not restricted to the disk selection in order to probe the outer regions too. Strikingly, the vertical component B_z dominates all disks for $r \lesssim 50$ AU, except run M2. This is a necessary condition for launching centrifugal jets, as we will see in Sect. 5.4. At larger radii, including within the disk radius, the toroidal component B_ϕ dominates in all runs. This is due to the magnetic field lines being twisted by the disk rotation, and is the powering source of magnetic tower flows. In contrast, Banerjee & Pudritz (2007) find that the poloidal component dominates over the toroidal component throughout the disk. Since the toroidal component is generated by super-Alfvénic differential rotation, their outcome can be explained by the ideal MHD assumption which leads to an ever-increasing magnetic field strength (up to 10^3 G in their work). Interestingly, a magnetic field topology which favors a certain type of outflows is not sufficient to drive them. In fact, run M2 exhibits a strong disk toroidal magnetic field but launches its first outflows more than 10 kyr after this snapshot ($t = 50$ kyr). Indeed, the escaping gas must first overcome the ram pressure, which is higher in the turbulent runs since there is a greater injection of kinetic energy from the start.

Eventually, the radial component B_r dominates at even larger radii. It has been produced by the magnetized, collapsing gas (and the streamers), pulling the field lines which fan out at infinity and forming an hour-glass shape (*e.g.*, Maury et al. 2018).

5.4 Outflows

5.4.1 Origin

Analytical estimation

We aim at identifying the candidates for driving bipolar outflows: radiative acceleration, magnetic tower flow, and magneto-centrifugal acceleration. While modelling the latter requires strong assumptions on the magnetic field topology, we choose to compare analytically the radiative and magnetic pressure-driven accelerations.

The radiative and magnetic-pressure-gradient accelerations are respectively defined as $a_{\rm rad} = \kappa F/\mathrm{c} = \kappa L/4\pi r^2 \mathrm{c}$ where κ is the dust-and-gas mixture opacity, F is the radiative flux coming from the star, L is the stellar luminosity, r is the distance to the star, and $a_{\rm pmag} = 1/\rho \nabla P_{\rm mag} = 1/\rho \nabla B^2/2$. In the ideal MHD regime, $B \propto \rho^{2/3}$ and $\rho \propto r^{-2}$ from our initial conditions, so $B \propto r^{-4/3}$. It follows that the acceleration due to the magnetic pressure gradient can be approximated as

$$\frac{1}{2\rho}\frac{\partial B^2}{\partial r} = \frac{-4}{3}\frac{B_0^2}{r_0 \rho_0}\left(\frac{r}{r_0}\right)^{-5/3} \tag{5.12}$$

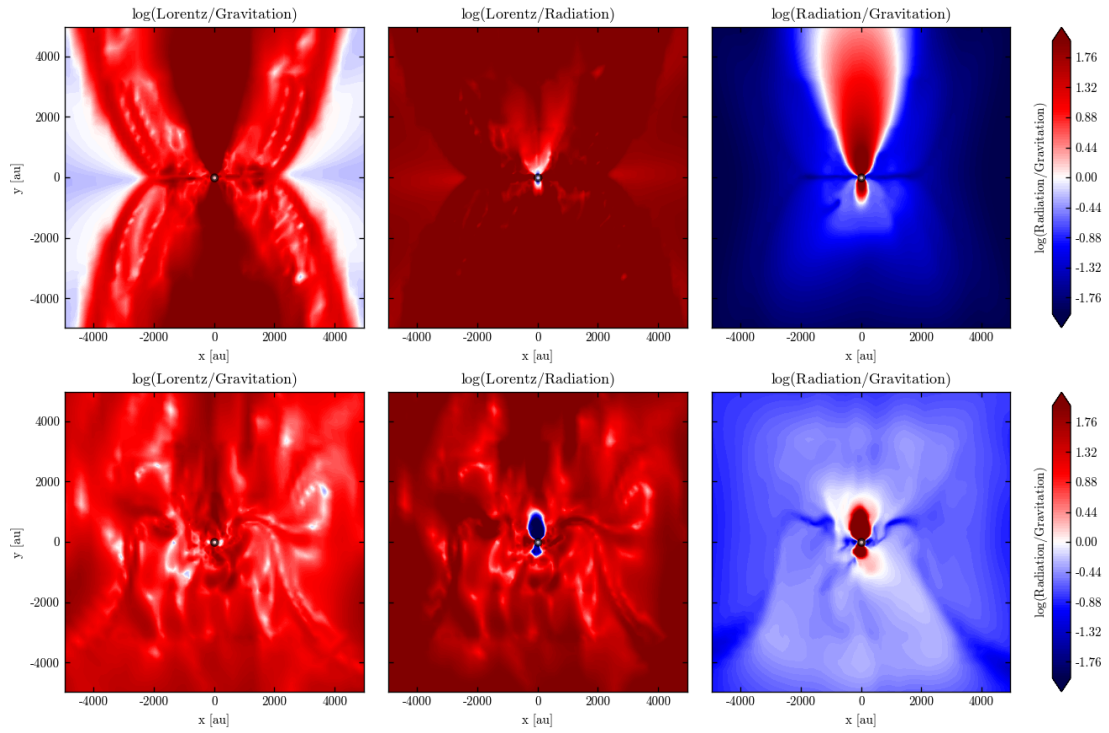

Figure 5.12: Slices of 10000 AU of three forces ratios when $M = 10\,\mathrm{M}_\odot$ ($L = 2 \times 10^4 L_\odot$) in run M0 (top) and when $M = 23.8\,\mathrm{M}_\odot$ ($L = 1.2 \times 10^5 L_\odot$) run LRM0. Left panels: Lorentz against gravitational acceleration; middle panels: Lorentz acceleration against radiative acceleration; right panels: radiative acceleration against gravitational acceleration.

Now comparing the radiative and magnetic accelerations absolute values and deducing the luminosity for the radiative acceleration to overcome the magnetic acceleration, one obtains

$$\begin{aligned} a_{\mathrm{rad}} \equiv \frac{\kappa L}{4\pi r^2 \mathrm{c}} &> \left\| \frac{1}{2\rho}\frac{\partial B^2}{\partial r} \right\| \equiv a_{\mathrm{pmag}}, \\ L &> \frac{16\pi}{3}\mathrm{c}\rho_0^{-1} r_0 B_0^2 \kappa_0^{-1} \left(\frac{r}{r_0}\right)^{1/3} \left(\frac{\kappa}{\kappa_0}\right)^{-1} \\ &\gtrsim 2 \times 10^4 L_\odot \left(\frac{r}{r_0}\right)^{1/3} \left(\frac{\kappa}{\kappa_0}\right)^{-1} \left(\frac{\rho_0}{10^{-15}\,\mathrm{g\,cm^{-3}}}\right) \left(\frac{B_0}{0.1\mathrm{G}}\right)^2, \end{aligned} \tag{5.13}$$

taking $r_0 = 50$ AU, $B_0 = 0.1$ G, $\kappa_0 = 50\,\mathrm{cm^2\,g^{-1}}$ (the gray opacity to stellar radiation), $\rho_0 = 10^{-15}\,\mathrm{g\,cm^{-3}}$ (corresponding to $\sim 10^8\,\mathrm{cm^{-3}}$) as references, after r_0 has been fixed. From this equation, we can anticipate a change of regime from magnetic-dominated to radiation-dominated outflows as the protostellar luminosity increases, but only at small to intermediate scales. Indeed, Eq. 5.13 shows that the radiative acceleration decreases more rapidly with the distance than the magnetic acceleration, so that, at large distances, magnetic tower flow is the dominant mechanism. This analysis remains valid as long as the two components do not interact with each other. Actually, the radiative force can push on the field lines and perturb the field topology (Vaidya et al., 2011), while the tower flow dense parts can shield the rest of the outflow from stellar radiation (see the dense gas in the southern outflow, right panel of Fig. 5.13). More generally, the previous formulation is no longer valid for $r > 1/(\kappa\rho_{\mathrm{outflow}})$ (optically-thick outflow), except to show that the radiative acceleration is overwhelmed by magnetic-pressure gradient.

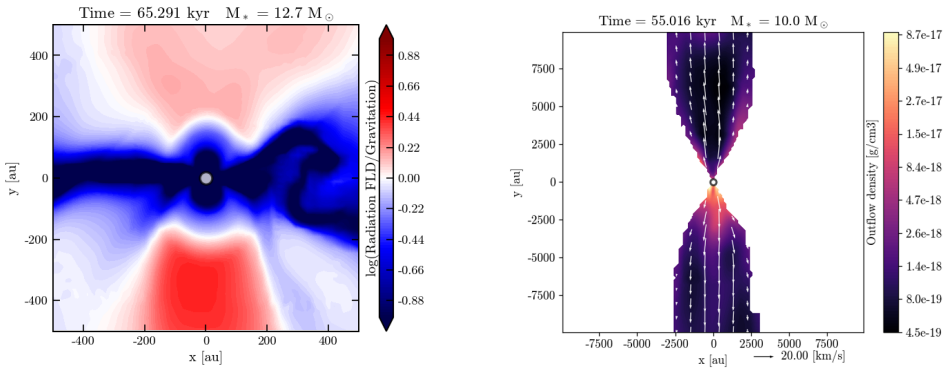

Figure 5.13: Left panel: ratio of the FLD radiative acceleration and the gravitational acceleration. Right panel: gas density in the outflow selection. Slices of 1000 AU (left) and 20000 AU (right) perpendicularly to the disk plane, run M0. The gas outflow density corresponds to particle densities between $\sim 10^5$ cm^{-3} and $\sim 10^7$ cm^{-3}.

Fiducial case: run M0

Let us identify which of the two forces dominates when the star becomes massive ($\gtrsim 8\,M_\odot$), in run M0 for simplicity. Figure 5.12 shows slices perpendicular to the disk plane of the ratios $a_{\rm Lor}/a_{\rm grav}$ (left panel), $a_{\rm Lor}/a_{\rm rad}$ (middle panel) and $a_{\rm rad}/a_{\rm grav}$ (right panel) when the central star is $10\,M_\odot$ and $L = 2\times10^4 L_\odot$ in run M0 and when $M = 23.8\,M_\odot$ and $L = 1.2\times10^5 L_\odot$ in run LRM0. Run LRM0 permits us to reach a higher stellar mass and therefore a larger luminosity. One can clearly see that both the Lorentz force and the radiative force contribute to the gas acceleration in the outflow, as they exceed the gravitational force. Interestingly, in run M0 the radiative force contribution is very asymmetric with respect to the disk plane. This is due to the density distribution not being symmetric, with denser gas in the southern direction stopping stellar radiation propagation, while the northern direction is particularly optically-thin at this time step. We briefly discuss this asymmetry below. The extent of the radiatively-dominated region is more constant with time in run LRM0. Indeed, it reflects a fundamental problem when modelling radiative transfer: if the photon mean free path is not resolved, absorption is overestimated. Hence, there is more absorption in run LRM0, which explains why, despite a larger stellar luminosity than in the run M0 snapshot, radiation does not propagate further away. As shown on the middle panel of Fig. 5.12, the Lorentz acceleration dominates the radiative acceleration everywhere but in the vicinity of the star (closer than ≈300 AU in run M0). This time, run LRM0 illustrates the stronger radiative force with a more extended zone where radiative force dominates over Lorentz force. The center panel and right panel show very similar features, revealing that the radiative force domination is limited by absorption in run LRM0, while it is mainly limited by geometrical dilution (inherent to an optically-thin channel) in run M0.

To begin with, the radiative acceleration can be decomposed as the sum of the stellar radiative acceleration, treated with the M1 module, and the FLD radiative acceleration. The latter corresponds to momentum transfer from dust-reprocessed (infrared-like) radiation, after stellar radiation (the main luminosity source in these simulations) has been absorbed. As shown in the left panel of Fig. 5.13, this force also contributes to the outflow, since it dominates over the gravitational force. Although its contribution is marginal compared to the direct stellar radiative force in the outflows here, it could play a more important role in the gas dynamics in the regions shielded from stellar radiation. Indeed, it is greater in the southern outflow, where

density is higher (right panel of Fig. 5.13). From the same figure, we observe regions of outflow density higher ($\rho > 10^{-18}\,\mathrm{g\,cm^{-3}}$, $n \gtrsim 10^{5}\,\mathrm{cm^{-3}}$) than in purely radiative outflows (see *e.g.*, Rosen et al. 2016, Mignon-Risse et al. 2020). As a consequence, stellar radiation is absorbed and cannot contribute to the gas acceleration at large ($> 10^4$ AU) distances when such a transient density region is present. The ejection of optically-thick material is a common feature in our simulation, as we discuss below.

Now, let us focus on the magnetic mechanism. As shown in Fig. 5.12, the Lorentz force dominates the gas dynamics in the outflow. It can be decomposed as the sum of a *magnetic-pressure gradient force* and a *magnetic tension force*. While the former pushes the gas along the direction of greater field variations, giving rise to a magnetic tower flow, the latter impedes the bending of the field lines. From the simulations outputs, we compute the magnetic-pressure-gradient force in the direction perpendicular to the disk and compute the ratio to the gravitational force (left panel of Fig. 5.14). We only take the toroidal component of the magnetic field, as it is the only one contributing to the gas dynamics in the poloidal direction (Spruit, 1996). This acceleration appears to dominate over gravitation in all the outflow, by about one order of magnitude. Therefore, the outflow in our simulation contains a magnetic tower flow (Lynden-Bell 1996, Lynden-Bell 2003). This mechanism originates from the field lines being wound-up as the gas collapses, accumulating toroidal magnetic field. As shown in the middle panel of Fig. 5.14, the toroidal component (blue) indeed dominates the outer zones of the outflow, while the poloidal component dominates close to the outflow axis. In that respect, we obtain a similar outflow magnetic structure as many works in the literature (see *e.g.*, Seifried et al. (2012b). From Fig. 5.14 it can be seen that the tower flow mechanism does not seem to originate from the inner disk because the disk radius in run M0 is $\approx$100 AU (Fig. 5.9), but from much larger scales. Actually, the tower flow develops on disk scales and widens later-on. As in Kato et al. (2004), we find that the outflow itself is dominated by magnetic pressure ($\beta < 1$ while the outflow edge corresponds to $\beta \approx 1$), as displayed in the right panel of Fig. 5.14. In addition to the possible thermal pressure gradient from the outer medium, collimation is enforced by the magnetic tension force when the field lines are sufficiently wound-up. While we have emphasized the poloidal component from the Lorentz acceleration in the left panel of Fig. 5.14, there is also a collimating component as well, as can be seen from the direction of the Lorentz acceleration vectors in the right panel of Fig. 5.14. The tower grows (*i.e.* the frontier between the outflow and the outer medium) as the field anchored on the disk rotates, and the tower growth is predicted to occur at the disk rotation velocity (Lynden-Bell, 1996). Indeed, looking at the evolution of the tower frontier position over 32 kyr, we find a mean growth velocity of $\approx 6\,\mathrm{km\,s^{-1}}$. In the mean time, the gas azimuthal velocity in the disk is $\approx 5\,\mathrm{km\,s^{-1}}$ at the outer radius (Fig. 5.10). This is consistent with Lynden-Bell (1996).

Since the poloidal magnetic field component dominates close to the outflow axis (middle panel of Fig. 5.14 and top-left panel of Fig. 5.11), we investigate whether the magneto-centrifugal process originally described by Blandford & Payne (1982) is at work. In this process, gas is centrifugally accelerated along field lines anchored in the disk and corotating with it. In the most commonly studied case, the disk is considered to be cold so that the thermal pressure gradient does not contribute to the gas lifting. Distinguishing centrifugal acceleration from a magnetic tower acceleration is a complicated task in such AMR calculations, as underlined by Seifried et al. (2012b). In fact, the system is far from the ideal MHD, axisymmetric, stationary case and the criterion from Blandford & Payne (1982) only applies to the disk surface. They derived strict conditions in terms of magnetic lines inclination to launch the flow centrifugally, but neglect disk thermal pressure which is obviously non-negligible in our calculation (see Fig. 5.6). Moreover, analytical results rely on several invariants along the field lines (see *e.g.* Ogilvie 2016), but it is difficult to trace the field line on which a gas particle has been centrifu-

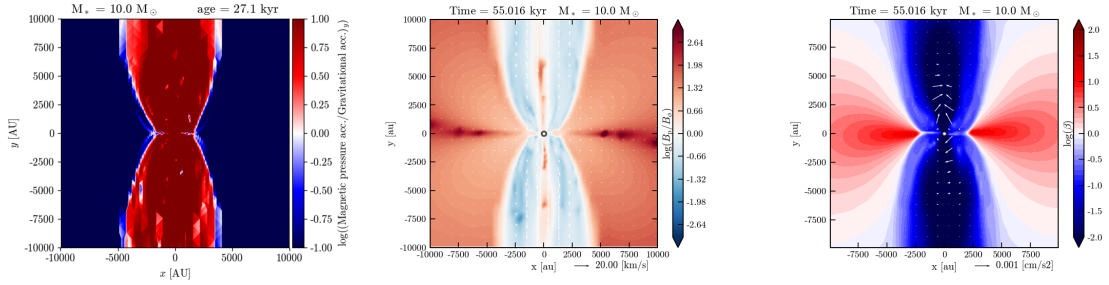

Figure 5.14: Left panel: ratio of the magnetic-pressure-gradient acceleration and the gravitational acceleration, in the vertical direction. Middle panel: ratio of the poloidal and toroidal components of the magnetic field and velocity vectors overplotted. Right panel: Plasma β and Lorentz acceleration vectors overplotted. Slices of 20000 AU perpendicularly to the disk plane, when $M = 10\,\mathrm{M}_\odot$, run M0.

gally accelerated, back to the line foot point in the disk. For that purpose, Seifried et al. (2012b) have derived a criterion to estimate whether centrifugal acceleration is taking place, based on grid-evaluated quantities. They assume that $B_\phi = 0$, so that the field lines corotate with the gas. Since B_ϕ is never strictly equal to zero in our calculation, we apply this criterion only where $B_\mathrm{p} > B_\phi$. Their idea is to determine, for a given point, the isocontour along which the effective gravity (accounting for centrifugal forces) is constant: it draws a line along which gas can freely move, regarding these forces. Then they compare, in the $(r, z)-$plane (in cylindrical coordinates), the gas trajectory along this line to the field lines inclination, by comparing the derivative $\partial z(r)/\partial r$ to B_z/B_r, where $z(r)$ is given by the isocontour equation (Eq. 16 of Seifried et al. 2012b). Eventually, at any given point, centrifugal acceleration occurs if $\partial z(r)/\partial r$ is larger than the field line inclination, *i.e.*

$$\log\left(\frac{r}{z}\frac{1}{GM}\left(\frac{v_\phi^2}{r^2}(r^2+z^2)^{3/2} - GM\right) \Big/ \left(\frac{B_z}{B_r}\right)\right) > 0, \tag{5.14}$$

where the first term corresponds to $\partial z(r)/\partial r$. We visualize this criterion in the right panel of Fig. 5.15: centrifugal acceleration occurs in red regions. Hence, the zone close to the outflow axis, where we previously found B_p to dominate, is consistent with centrifugal acceleration.

In the cold disk limit, gas is accelerated centrifugally from the disk surface to the Alfvén point, where the poloidal velocity equals the poloidal Alfvén speed. We check this by visualizing these velocities as a function of the distance to the sink. As shown in the top-left panel of Fig. 5.11, B_p dominates for disk radii $\lesssim 50$ AU, hence the centrifugal mechanism may be at work below 50 AU. Therefore, we select cells at a cylindrical radius smaller than 100 AU, so that their expected launching radius is a few tens of AU, consistently with the zone where the magnetic field is mainly poloidal within the disk. Left panel of Fig 5.15 shows these velocities in the northern (A) and southern (B) outflows of Run M0, when $M = 10\,\mathrm{M}_\odot$. First, the poloidal velocity is found to increase only when $r > 60 - 80$ AU. This is inconsistent with the cold disk approximation, and indeed, thermal pressure gradient, radiative pressure and magnetic pressure are present in this simulation and are likely responsible to lift the gas up to these heights. Second, gas acceleration appears to take place up to the Alfvén point, in agreement with the theory (*e.g.*, Spruit 1996). Beyond the Alfvén surface and close to the outflow axis, the gas velocity is larger than the Alfvén velocity so the field lines should follow the gas and twist the field lines, generating a toroidal component. However, this is not what we observe, as shown on the middle panel of Fig. 5.14. Even beyond the Alfvén surface ($\gtrsim 1000 - 2000$ AU), the poloidal component dominates, close to the outflow axis. This feature is reminiscent of many

studies including a magnetic tower flow (*e.g.* Kato et al. 2004, Banerjee & Pudritz 2007, Seifried et al. 2012b, Kölligan & Kuiper 2018. A plausible explanation for the generation of the poloidal component close to the axis (beyond the Alfvén surface) is the vertical inflation of the magnetic tower (Kato et al., 2004).

This mechanism is the best candidate for the fast outflows around young-stellar objects, hence we compare the highest velocities we obtain with the magneto-centrifugal mechanism predictions. The terminal velocity v_∞ is predicted to be (*e.g.* Pudritz et al. 2006)

$$v_\infty \simeq \frac{r_{\rm c,A}}{r_{\rm c,0}} v_{\rm esc,0}, \tag{5.15}$$

where $r_{\rm c,A}$ is the (cylindrical) Alfvén radius, $r_{\rm c,0}$ is the launching radius, so that $r_{\rm c,A}/r_{\rm c,0}$ is the lever arm and is typically $2-3$ (Pudritz & Ray, 2019), and $v_{\rm esc,0}$ is the escape velocity at the launching radius. Centrifugal outflows have an onion-like velocity distribution, with the highest speed close to the axis corresponding to the gas initially close to the central object. In our simulation, gas is launched ~ 100 AU above the disk. Hence, we take the launching radius as $r_{\rm c,0} = 100$ AU and $M = 10\,{\rm M}_\odot$. The corresponding escape velocity is $\approx 11\,{\rm km\,s^{-1}}$. This leads to $v_\infty \simeq 33\,{\rm km\,s^{-1}}$, which is of the same order as the fastest velocities we obtain at this time step, *i.e.* $v \sim 32\,{\rm km\ s^{-1}}$ on one side of the disk and $v \sim 20{\rm km\ s^{-1}}$ on the other side (Left panel of Fig. 5.15). These small velocity differences suggest that this mechanism may be either transient in our simulation (the radiative acceleration being able to accelerate the gas to $v \sim 20\,{\rm km\ s^{-1}}$) or not symmetric with respect to the disk plane (as can be seen in the right panel of Fig. 5.13). This north-south asymmetry in the ejection may arise from the asymmetry in the streamers. These channels feeding the disk are not located in the disk plane. The basis of the tower flow is larger than the disk size and can accelerate gas located above it, *i.e.* parts of the streamers, and inherit from this asymmetry. We note also that a launching from the disk instead of $\sim$100 AU above it would result it a maximal velocity more than twice larger.

Finally, as discussed in the high-resolution studies of Banerjee & Pudritz (2007) in the ideal MHD frame and Kölligan & Kuiper (2018) with non-ideal MHD, obtaining numerically converged results on this mechanism requires sub-AU resolution. However, the co-presence of a "slow" magnetic tower flow and "fast" centrifugal wind we obtain agrees with their work.

5.4.2 A channel for radiation?

The magnetic tower flows develop at a smaller stellar mass ($M \approx 4-7\,{\rm M}_\odot$) (Table 5.2) than what is found in RHD simulations regarding radiative outflows ($M > 10\,{\rm M}_\odot$, see *e.g.* Kuiper et al. 2012). Hence, they could act as a channel of radiation to propagate, as proposed by Krumholz et al. (2005) for protostellar outflows. Banerjee & Pudritz (2007) proposed the same mechanism for tower flows, but their calculation did not include radiative transfer. Despite the regular presence of optically-thick gas in the outflow, most of the outflow volume is optically-thin. To assess the effect of the radiative force, we compare the outflow extent in run M0 with a similar run with the FLD method (that we will call the M0FLD run), which underestimates the radiative force (Owen et al. 2014, Mignon-Risse et al. 2020, see also Appendix C). When the central star is $\sim 5\,{\rm M}_\odot$, the outflow is $\sim$3000 AU large in the M0FLD run against more than 4500 AU in run M0. Interestingly, the outflow front is composed of a dense region, corresponding to expelled gas shocking with the outer medium. This region does not exist in the M0FLD run. Moreover, the outflow appears more symmetric (axisymmetric and north-south) in the M0 run, indicating that the radiative force stabilizes the outflow structure.

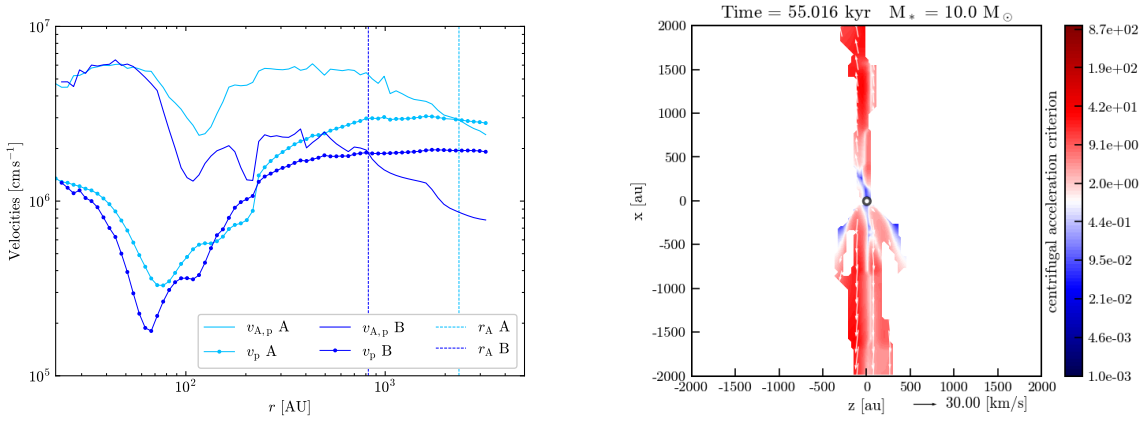

Figure 5.15: Left panel: poloidal velocity and poloidal Alfvén velocity as a function of the distance to the sink, in a cylindrical selection of cells with $r_{\rm cyl} < 100$ AU. A and B label the northern and southern outflow, respectively, and the vertical lines indicate the positions of the Alfvén points: $v_{\rm p} = v_{\rm A,p}$. Right panel: criterion for centrifugal acceleration (Eq. 5.14) from Seifried et al. (2012b) applied to a slice of 4000 AU perpendicularly to the disk plane. Run M0, $M = 10\,{\rm M}_\odot$.

Influence of a turbulent medium: runs M05, M2, M05B2

We observe outflows in all four runs. They occur at t∼30 kyr in the subalfvenic runs. Meanwhile, their launching is considerably delayed in the superalfvenic runs, by ∼20 kyr in run M05 and ∼35 kyr in run M2, compared to the subalfvenic runs (see Table 5.2).

All outflows are consistent with a magnetic tower flow, characterized by magnetic-pressure gradient overcoming gravity. This mechanism requires the accumulation of toroidal field due to rotational motions. The inclusion of a non-coherent velocity distribution in our turbulent runs should perturb the magnetic field coherence, impeding the launching of the outflow. As shown in the top-right and bottom-left panels of Fig. 5.11, ∼22 kyr after sink formation a strong toroidal magnetic field has built up, but no outflow has been launched yet in runs M05 and M2. Indeed, the density structure formed by the combined effect of infall and turbulent motions is a filament-like structure of a few thousands AU (see Fig. 5.2) almost perpendicular to the disk plane, which carries an additional ram pressure to be overcome by the outflow, no matter its origin.

Magnetic and radiative forces have different natures. On the one hand, magnetic outflows require structured magnetic fields which can be perturbed by a turbulent velocity dispersion, orbital motions in a binary system (Peters et al., 2011), and more generally the system's geometry. Because of this, magnetic outflow launching is a long-term process and can be prevented. On the other hand, the launching (close to the star) of radiative outflows does not depend on the system's geometry because it is isotropic. Its launching and propagation does depend on the environment optical depth, so one can expect transient and smaller radiative outflows in a turbulent medium, unless radiation can find its way out and accelerate gas instantaneously. Without magnetic fields, infalling filaments of gas are self-shielded against radiation and form a network of dense filaments and optically-thin channels centered on the massive star (Rosen et al., 2019).

In the present study, with magnetic fields and superalfvenic turbulence, gravity is diluted and material gently falls via thermally-supported ($\beta > 1$) streamers on a moderately-magnetized complex structure of ∼1000 AU squared (run M2). Dynamics is enhanced by the presence of a secondary star-disk system. As a consequence, we observe two failed attempts of launching

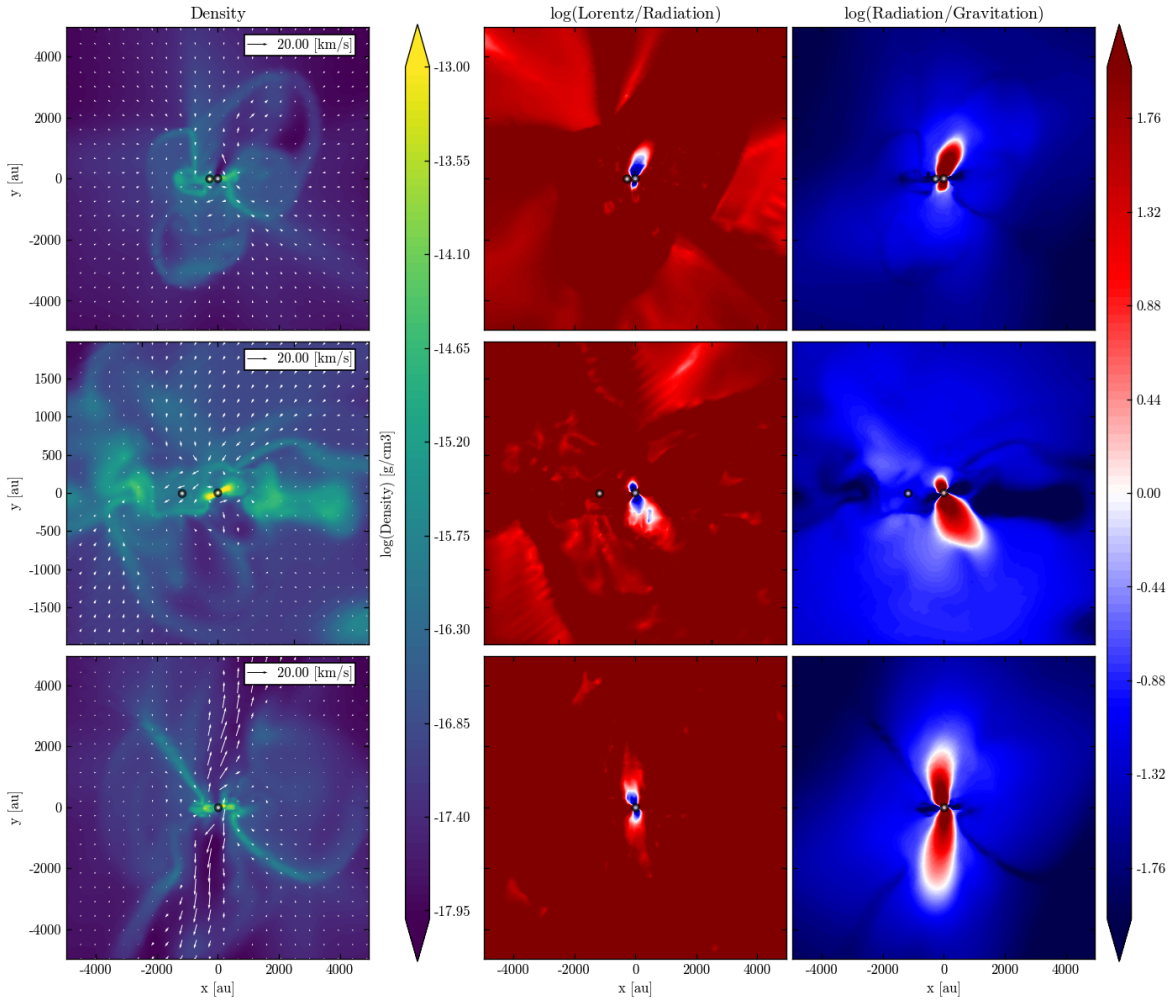

Figure 5.16: Slices with the disk seen edge-on. Left column: density slice. Middle column: ratio of the Lorentz acceleration to the radiative acceleration. Right column: ratio of the radiative acceleration to the gravitational force. From top to bottom: run M05 (10000 AU, $t = 67.0$ kyr, $M = 8.2\,\mathrm{M}_\odot$, $L = 1.4 \times 10^4\,\mathrm{L}_\odot$), run M2 (4000 AU, $t = 72.6$ kyr, $M = 5.6\,\mathrm{M}_\odot$, $L = 8 \times 10^3\,\mathrm{L}_\odot$) and run M05B2 (10000 AU, $t = 61.1$ kyr, $M = 9.6\,\mathrm{M}_\odot$, $L = 1.7 \times 10^4\,\mathrm{L}_\odot$). The gas densities in the left column correspond to particle densities between $\sim 10^5\,\mathrm{cm}^{-3}$ and $\sim 10^{10}\,\mathrm{cm}^{-3}$.

outflow, as dense gas passes through it. Eventually, the monopolar outflow launches, and survives for ~ 3 kyr before it becomes difficult to characterize it as an outflow, since it has been perturbed by the environment motions and no gas is newly ejected from the basis. A similar process occurs in run M05. While the ram pressure is lower than in run M2 and consequently, an outflow successfully developed, the formation of a secondary sink at about the same time has progressively displaced the center of mass of the system. The primary sink disk moves on a $\sim 350 - 600$ AU orbit and the outflow is broadened, from the basis, consequently. Nonetheless, it is sustained until the end of the run, oppositely to run M2. As mentioned previously, the orbit is eccentric. When the primary sink approaches the apastron, it stays longer in the same area and has more time to accelerate the gas radiatively. Finally, despite the turbulent support, the subalfvenic run M05B2 has no difficulties launching the outflows at about the same time as in the fiducial run, because the initial magnetic field is stronger. The toroidal magnetic field reaches similar values as in the less-magnetized, non-turbulent run M0 (> 0.1 G). The magnetic tower develops at about the same speed as in run M0 (see top-right panel of Fig. 5.18). The presence of a turbulent velocity field contributes to the "north-south" asymmetry, clearly visible in the right-most panel of Fig. 5.2. The bipolar outflows, which are not strictly identical in run M0, are even more distinguishable in terms of extent or orientation (bottom-right panel of Fig. 5.18).

Once the outflows are launched in runs M05 and M2, the relative contribution from radiative acceleration to the total acceleration is larger than in the fiducial case (Fig. 5.16). First, by delaying the launching, the central star has time to reach slightly higher masses (hence, luminosity). Second, the magnetic field is less organized than in the non-turbulent case, hence the component of the Lorentz force contributing to the outflow is smaller.

To conclude, the presence of a turbulent velocity field delays and perturbs the launching of outflow, when the turbulence is superalfvenic. The mechanism remains the same as in the non-turbulent case, namely a magnetic tower flow, but the radiative contribution is larger. In the most turbulent case, a monopolar outflow formed, while the outflows are bipolar in all other runs. This particular case shows the possibility of launching MHD outflows even when the orientation between the disk and the core-scale magnetic field is close to 90 deg, in agreement with (Joos et al., 2013). This contrasts with (Ciardi & Hennebelle, 2010) who did not include turbulence but only misaligned rotation. Hence, including initial rotation only may be an oversimplification regarding the processes affected by the angular momentum-magnetic field misalignment, since a realistic turbulent velocity field actually carries angular momentum along all directions.

In the next sections, we compare the outflows properties to several observational studies based on low- and high-mass protostars statistical samples.

5.4.3 Outflow velocity, mass, dynamical time, ejection rate

As mentioned in the previous section, the outflows in our simulations are launched by a magnetic tower flow, while radiative acceleration is an additional (non-negligible) contributor to the gas velocity and magneto-centrifugal acceleration may take place too (although in this study we cannot obtain numerically-converged results on that mechanism). If there is indeed a high-velocity component (due to the magneto-centrifugal process) encapsulated in a low-velocity cylinder, they cannot be easily distinguished above sub-AU resolutions (Kölligan & Kuiper, 2018).

Before comparing the outcomes of our simulations with observational values, let us precise that some of these observable quantities are often plotted against the stellar luminosity (see *e.g.* Lada 1985). The luminosity does not only stand as a tracer for the evolutionary stage. As mentioned by several authors (see *e.g.* Wu et al. 2004), it can be used as a proxy for the accretion

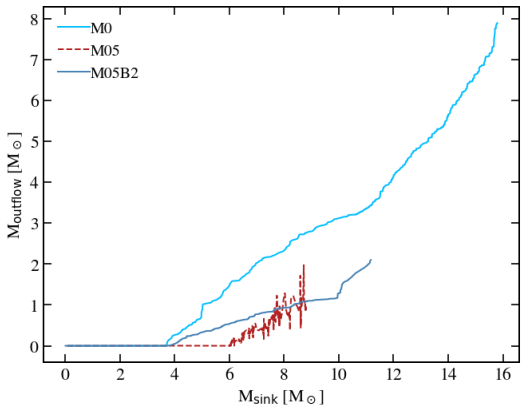

Figure 5.17: Outflow mass as a function of the sink mass.

rate if the high-mass protostars have higher accretion rates than their low-mass counterparts, which is observed to be the case (Motte et al., 2018). This is of main interest here, since MHD disk outflows are powered by the gravitational energy from accretion, with a predicted ratio of mass outflow rate to mass accretion rate $\sim$0.1 (see Pudritz & Ray 2019 and references therein). Matsushita et al. (2017) obtain a ratio $\gtrsim$0.2 which can approach unity when the core initial magnetic energy is comparable to the gravitational energy. Nevertheless, in this manuscript we will refer to a mean accretion/ejection rate by run, rather than an instantaneous rate. Similarly, we will draw conclusions regarding each run, rather than particular evolutionary stages within each of them.

First, as shown in the left panel of Fig. 5.15, the maximal outflow velocity in run M0 is $\simeq$20 km s^{-1} for one outflow lobe and $\simeq$32 km s^{-1} for the other, at the time when the central star is 10 M$_\odot$. These values do not change much during the simulation, but may depend on the initial core mass. We compare them with those obtained by Nony et al. (2020) on the most massive core ($\sim$102 M$_\odot$) of their $1-100$ M$_\odot$ sample (in the W43-MM1 protocluster), on which they obtain a median velocity of 47km s^{-1}. This core exhibits a monopolar outflow with a maximal velocity of $34 \pm$ km s^{-1} and 10000 ± 200 AU length, which agrees well with one of the two outflow lobes in run M0. Interestingly, while we have attributed the monopolar nature of the outflow in run M2 to the ram pressure of the turbulent gas, this occurence in W43-MM1 could be due to an inflow of material according to Nony et al. (2020).

We plot the outflow mass as a function of the sink mass in Fig. 5.17. The outflow mass generally increases with time and has values $1-6$ M$_\odot$ during the epoch covered. While it appears to be highly variable in run M05 (the periodicity is attributed to the orbital motions within the binary system), it only increases in subalfvenic runs, and more rapidly in the non-turbulent run M0. Considering their mass and dynamical time, we obtain a mean ejection rate of $\sim 2 \times 10^{-4}$ M$_\odot$ yr^{-1} in run M0, $\sim 7 \times 10^{-5}$ M$_\odot$ yr^{-1} in run M05 and $\sim 5 \times 10^{-5}$ M$_\odot$ yr^{-1} in run M05B2.

Let us compare the outflow masses we obtain with observations. Wu et al. (2004) built a statistical study of 391 high-velocity outflows, covering several evolutionary stages. For $L > 10^3$ L$_\odot$ objects, they obtain outflow masses of a few solar masses up to 10^2 M$_\odot$ with averaged dynamical times of 100 kyr. This is consistent with the study of Beuther et al. (2002), focused on the CO $J = 2-1$ emission towards 26 massive star-forming regions. They obtain outflow masses of typically $M_{\rm outflow} \sim 0.1 (M_{\rm c}/\,{\rm M}_\odot)^{0.8}$ M$_\odot$ (where $M_{\rm c}$ is the core mass) and dynamical time scales of the order of the core free-fall time. In the sample of 11 massive star-forming regions of (Wu et al., 2005), the outflow mass is found to be between a few solar masses too,

while the maximal mass is 60 $M_\odot$ and averaged dynamical timescales of 20 kyr. Similarly, (Zhang et al., 2005) extract a mean outflow mass of 20.6 $M_\odot$ and a median of 15.6 $M_\odot$ from a sample of 69 sources.

The upper-mass limits of $60 - 100\,M_\odot$ are significantly larger than what we obtain, as well as the values of $15.6 - 20.6\,M_\odot$ of (Zhang et al., 2005), although they might be reached at later times in our study. The outflow mass presented in Beuther et al. (2002) for a core mass similar to ours ($M_c = 100\,M_\odot$) is $\sim 4\,M_\odot$, which is consistent with our results. Since they obtain much larger outflow masses for more massive cores, these may either point at our initial conditions, which would correspond to the lower core mass range for massive star formation, or to some extent at the time scale covered by our study, which is too short for the outflows to reach such observational values. All these studies agree on typical accretion rates of a few $10^{-4} M_\odot\,\mathrm{yr}^{-1}$, similar to those obtained here (middle panel of Fig. 5.7).

On the numerical experiments side, Matsushita et al. (2017) obtain outflow masses well correlated to the protostar's mass with an almost $1 - 1$ relation between both. Hence, for the typical protostar masses we obtain here, their outflow mass is typically $2 - 15\,M_\odot$. Nonetheless, they cover a timescale of only 10 kyr, which is likely attributed to the Ohmic dissipation constraints. Hence, they consider very high accretion rates, in order to reach a mass of a few tens of solar masses. If we only consider their runs with an accretion rate of the order of a few $10^{-4}\,M_\odot\,\mathrm{yr}^{-1}$, this sets an outflow mass of $\sim 4\,M_\odot$ for a $\sim 4\,M_\odot$ central protostar, while the disk is becoming gravitationally-unstable and the outflow mass highly variable. Nonetheless, as mentioned in Table 5.2, we notice a delay of at least 8 kyr (corresponding to at least $4\,M_\odot$ accreted) between the sink formation and the outflow launching, which is not the case in Matsushita et al. (2017). Hence, while we should not directly compare their outflow mass with ours at a given time (or sink mass), this gives a correct order of magnitude estimation. Finally, we compare our results to the ideal MHD study conducted by Seifried et al. (2012b), which is one of the few works focusing on magnetic outflows in the massive star formation context. In the absence of turbulence, they obtain mass outflow rates of $10^{-4} M_\odot\,\mathrm{yr}^{-1}$, which agrees with our non-turbulent run M0.

On the one hand, the outflow ejection rate is consistent with observations. On the other hand, the outflow mass is smaller than most observed. This discrepancy can be explained by our initial conditions corresponding to the low-mass limit of massive cores, as shown above with the estimate of Beuther et al. (2002).

5.4.4 Outlow momentum rate

Top-left panel of Fig. 5.18 displays the outflow momentum transfer rate (also called outflow force) computed from Eq. 5.5, each point corresponding to an outflow (either northern, labelled "A" or southern, "B") at a given time step. For runs M0 and M05B2, we have F_{outflow} of the order of $10^{-4}\,M_\odot\,\mathrm{km\,s}^{-1}\,\mathrm{yr}^{-1}$ and a dispersion that covers roughly one order of magnitude. These are consistent with the aforementioned numerical work of Seifried et al. (2012b). Run M05 exhibits highly dispersed values from 2×10^{-5} to $10^{-2}\,M_\odot\,\mathrm{km\,s}^{-1}\,\mathrm{yr}^{-1}$. In fact, the outflow is disturbed because it is launched from the primary sink disk, which orbits around the center of mass of the binary system. The temporal evolution of gas density and velocity (in direction and norm) within the outflow does not show a clear trend. In addition, the orbital motions by the primary sink induce variations in the distance between the sink and the outermost outflow point (see the top-right panel of Fig. 5.18), affecting the outflow momentum rate calculation. Nonetheless, turbulence reduces the outflow expansion, while providing dense gas so that the outflow is nearly as massive as in run M05B2 while being $\sim$10 times smaller. In that regard, it is understandable to obtain a higher value by a factor of $\sim$10 compared to runs M0 and M05B2.

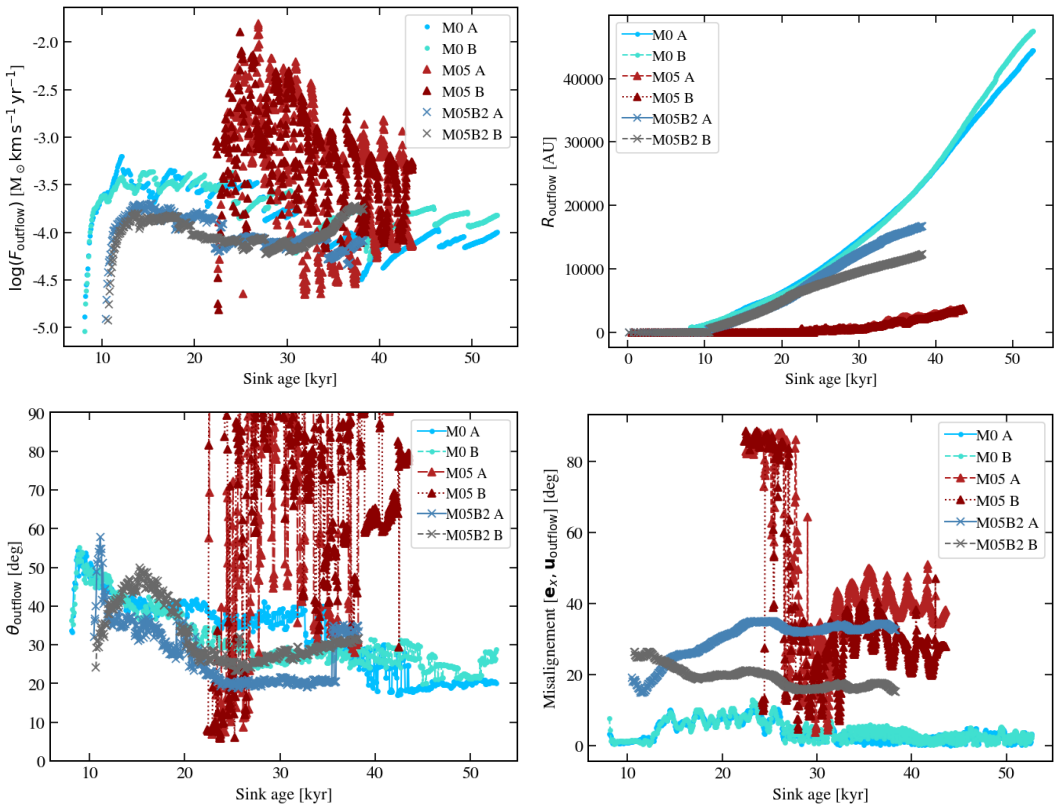

Figure 5.18: Outflows properties as a function of the most massive sink mass: momentum rate (top-left), maximal outflow radius (top-right), opening angle (bottom-left) and angle between the outflow and the large-scale magnetic field (bottom-right). Outflows generally come by pair so they are individually labelled as A and B.

Let us compare these results with the current observational constraints (observed in CO), for $L > 10^3 L_\odot$ objects. Indeed, the pioneer study of Lada (1985) has shown a general trend between the outflow force and the stellar luminosity from $1 L_\odot$ to $10^5 L_\odot$, suggesting a common outflow mechanism for low- and high-mass protostars, which is likely a magnetic mechanism. Hence, let us determine whether our outflows forces are consistent with this trend, with up-to-date outflow samples. In the statistical analysis of Wu et al. (2004) towards high-velocity outflows, the outflow force goes from 10^{-4} to $1\,\mathrm{M_\odot\,km\,s^{-1}\,yr^{-1}}$. Our core mass, $10^2\,\mathrm{M_\odot}$, is the lowest core mass of the sample and gives $F_{\mathrm{CO}} = 10^{-3}\,\mathrm{M_\odot\,km\,s^{-1}\,yr^{-1}}$. Wu et al. (2005) found values between $\sim 5 \times 10^{-4}\,\mathrm{M_\odot\,km\,s^{-1}\,yr^{-1}}$ and $2 \times 10^{-1}\,\mathrm{M_\odot\,km\,s^{-1}\,yr^{-1}}$. We note that the uncertainty is almost two orders of magnitude on these values though. Including the measurements from Beuther et al. (2002), Zhang et al. (2005) obtain outflow forces of $10^{-4} - 10^{-2}\,\mathrm{M_\odot\,km\,s^{-1}\,yr^{-1}}$. Hence, the outflow momentum rate we obtain in the subalfvenic runs is consistent with the lower values mentioned above, that is $10^{-4}\,\mathrm{M_\odot\,km\,s^{-1}\,yr^{-1}}$. Superalfvenic turbulence in run M05 may provide an explanation for higher outflow forces measurements $\sim 10^{-2}\,\mathrm{M_\odot\,km\,s^{-1}\,yr^{-1}}$, since it brings new material into the outflow, reduces the expansion (which affects the dynamical time). It also adds a ram pressure to be overcome by the outflow, so that the outflow dynamical properties are tightly linked to the conditions for its existence.

5.4.5 Opening angles

Close to the star, the outflow shape resembles a conical shape before collimation occurs ($\lesssim$ 2000 AU) and extends the outflow in an elliptic shape. In Sect. 5.2.4 we have presented our method to compute the outflow opening angle (see also Fig. 5.1). We have adopted a method adapted to the elliptic shape of the outflows we observe, which is similar to Offner et al. (2011).

The bottom-left panel of Fig. 5.18 shows $\theta_{\mathrm{outflow}}$ as a function of the sink age. We mentioned above that the outflow launched was quite similar between runs M0 and M05B2. Consequently, the values and evolution of the opening angle are, at first order, similar. During a first phase, the magnetic tower flow broadens so $\theta_{\mathrm{outflow}}$ increases, then the base of the tower stops growing much but the outflow propagates, diminishing geometrically the opening angle. During this second phase, the angle has values of 20 to 40 deg which are asymmetric from one outflow to the other, in the same run. Finally, it tends toward $20 - 25$ deg. Hence, the outflow re-collimates, which is partly due to the toroidal component of the magnetic fields (right panel of Fig. 5.14) and to the pressure from the outer medium. In run M05, the measurement of the opening angle is greatly affected by the orbital motions of the sink because the outflow has a size ($\sim$2000 AU, top-right panel of Fig. 5.18) comparable to the orbit, and an orbital velocity similar to the tower growth speed, by definition (Sect. 5.4.1). Since both velocities and spatial extents are of the same order, the outflow geometry becomes complex. Similarly, the outflow definition, which relies on a radial velocity larger than the escape velocity with respect to the primary sink, biases the selection toward the higher velocity component of the outflow. This high velocity component is often close to the outflow axis, implying a smaller opening angle. Because the outflow speed is comparable to the orbital speed (and slightly larger when a channel allows radiative acceleration to accelerate the gas inside it), the outflow is continuously re-launched from the base, which ends up in a larger opening angle than when it has time to propagate and to reduce the angle geometrically. Hence, the opening angle in run M05 is not comparable to a single observation. If any, it shows that the stellar motions in a turbulent medium, or a multiple stellar system, will strongly affect this type of geometrical measurements. Eventually, the dispersion of $\theta_{\mathrm{outflow}}$ decreases at later times as the ratio between the outflow extent and the orbit becomes much greater than one. In that case, $\theta_{\mathrm{outflow}}$ is typically between 60 deg and 80 deg, and the orbital motion seems to have played a dominant role in the outflow broadening.

Collimated outflows are observed around O- and B-type protostars (Arce et al., 2006), but several studies point toward less collimated outflows in the high-mass regime than in the low-mass regime (see *e.g.*, Beuther et al. 2002, Wu et al. 2004). Indeed, opening angles between 17 deg and 25 deg have been reported in IRAS 20126+4104 (Moscadelli et al., 2005) and IRAS 16547-4247 Rodriguez et al. (2005), but likely originate from a magneto-centrifugal jet given the velocities involved (34 to 112 km s^{-1} for IRAS 20126+4104).

As mentioned above, the outflow morphology we find differs from the conical geometry except a few kyr (a propagation up to ∼2000 AU) after the launching. Between the star and this radius, the outflows in runs M0 and M05B2 roughly fit a conical shape. This epoch corresponds to the highest values of $\theta_{\rm outflow}$ measured, with $\theta_{\rm outflow} \approx 30-60$ deg until then. For comparison, Pety et al. (2006) fit a conical shape to an outflow of ∼450 AU for a low-mass protostar, with an opening angle of 60 deg. If the outflow mechanism is indeed the same of low- and high-mass stars, and this is a magnetic tower flow, then the outflow detected by Pety et al. (2006) should re-collimate at larger radii and later times.

Wu et al. (2004) and Beuther et al. (2002) find average opening angles of ∼53 deg over the same samples of $> 10^3 L_\odot$ sources (corresponding to $5-15$ M$_\odot$ protostars in Wu et al. (2004)) mentioned above, which are higher limits though, due to angular resolution and projection effects (Beuther et al., 2002). These are typically larger than what we obtain in runs M0 and M05B2. The sample of Beuther et al. (2002) covers an outflow radial extent range of 10000 AU to 4×10^5 AU. For such radii, our simulations suggest that the opening angle should actually decrease (the outflow width remains roughly constant but the radial extent increases), while they obtain larger opening angles than ours. Thus, the discrepancy with our results cannot be attributed to the outflow radial extent and has to be explained otherwise. Therefore, it may indicate a different outflow launching process or a smaller pressure confinement by the outer medium, if these values were to be confirmed with higher angular resolution studies.

5.4.6 Alignment with the magnetic field

Low- and high-mass pre-stellar cores are threaded by magnetic fields, but their exact role is not clear yet. Since disk-mediated accretion is observed in the low-mass regime, and now in the high-mass regime as well (see *e.g.* Cesaroni et al. 2017), and disks are required to launch MHD outflows (supported by *e.g.*, Hirota et al. 2017), studying the alignment between core-scale outfows and magnetic fields should provide insights onto their exact role during (massive) star formation.

We call misalignment the angle formed by the vector of the outflow geometric center position vector with respect to the $x-$axis (corresponding to the initial magnetic field orientation). Its value is plotted in the bottom-right panel of Fig. 5.18. Let us start with the non-turbulent run M0, taking into account the disk-magnetic field orientation determined in Sect. 5.3.2, since most launching processes theoretically imply (for simplification reasons) that the outflow will be strictly perpendicular to the disk. Let us note that magnetic tower flows are expected to be launched along the poloidal directions (ending-up in a mean perpendicular angle with the disk). In fact, they correspond to the gradient of the toroidal magnetic pressure. The field toroidal component is due to disk rotation, generating a strong gradient in the poloidal direction.

In this run, the initial angular momentum is originally aligned with **B** and the disk remains perpendicular to it within ∼6 deg, as mentioned in Sect. 5.3.2. If the outflows were launched perfectly perpendicularly to the disk, or in other words, if the system were purely axisymmetric, this would lead to a misalignment of $\lesssim 6$ deg. As mentioned in Sec. 5.3.1, several factors have broken the north-south symmetry as well as the axisymmetry, and we find a misalignment of less than 10 deg which tends towards a few deg as the outflow extends.

Let us now study the opening angle in the turbulent runs. In runs M05 and M05B2, the angle between the specific angular momentum **j** (*i.e.* the disk normal) and **B** is ≈ 50 deg. On the one hand, in run M05B2, the misalignment between the outflow and the core-scale magnetic field, is between $15-25$ deg for one outflow and between $15-35$ deg for the other, instead of the ≈ 50 deg that could be expected. On the other hand, in run M05, the values of the misalignment at late times are $25-40$ deg and $35-50$ deg, respectively, instead of ≈ 50 deg. To understand this, let us describe the misalignment evolution in more details. As mentioned above regarding the opening angle, the misalignment is highly variable until $\sim$30 kyr in run M05, because of the orbital motion of the primary sink. These bipolar outflows are not symmetric and there is no clear trend toward an alignment with the large-scale magnetic field orientation. If any, the misalignment seems to gently increase with time in run M05. Despite these variations, the misalignment angle is smaller than what could be expected from the disk-magnetic fields misalignment (50 deg). It can be understood in terms of the outflows developing in the directions of least resistance. As mentioned in Sect. 5.3.1, the streamers formed perpendicularly to the core-scale magnetic fields and reached the rotating (circumbinary) disk from above and below, thus the outflows avoid the streamer direction and therefore have a misalignment angle smaller than 50 deg (a better alignment). Let us now identify the reasons for the differences observed between runs M05 and M05B2. While runs M05 and M05B2 show similar disk-magnetic fields misalignment (Fig. 5.5, set by the initial angular momentum), the outflow-magnetic fields misalignment is smaller in the latter run. In the former run, the sink rotation periodically provides channels where streamers are absent, to launch outflows quasi-perpendicularly to the disk, *i.e.* with an angle of 50 deg with respect to **B**. Finally, a few words on the short-lived (≈ 3 kyr) monopolar outflow in run M2. It develops nearly-perpendicularly to the disk (with a disk-magnetic field misalignment of $\sim$90 deg), with an outflow-magnetic field angle of $\sim$80 deg. It shows that, indeed, a disk perpendicularly oriented to the core-scale magnetic fields has trouble launching outflows but this is possible though (Joos et al., 2013).

To sum up, in the four runs, the outflow orientation appears to be mainly set by the disk orientation, which depends on the initial angular momentum (Sect. 5.5). Nonetheless, it never corresponds to a strict perpendicular angle with the disk, and is affected by the ambient dynamics, in particular by the streamers. Let us now compare these values to observational studies, in both the low- and high-mass regimes, because, as we will see, so far there is no hint for a different orientation mechanism depending on the stellar mass.

In the low-mass regime, Hull et al. (2013) observe that the angle distribution between outflows and magnetic fields on scales of $\sim$1000 AU is consistent with random distribution or preferentially perpendicular, on a sample of 16 low-mass protostars. On the core-scale, Hull et al. (2014) reached similar conclusion. With a sample of four low-mass isolated protostars, Chapman et al. (2013) came to the opposite conclusion, with a positive correlation between the outflow axis and the magnetic fields direction. Interestingly, Galametz et al. (2018) show that the best alignment between the magnetic fields and the outflow axis is observed for sources with no large ($>$ 100 AU) disk nor multiplicity. Finally, in the high-mass regime, Arce et al. (2020) reach the same conclusions as Hull et al. (2014): they find either a $50-70$ deg preferential orientation or a random orientation between the outflow and the magnetic fields.

To begin with, our results seem to favour a random inclination, as observed by Hull et al. (2013) and Hull et al. (2014), since the outflow orientation is mainly set by the disk orientation, which depends on the initial momentum carried by turbulence. Second, the sample of Chapman et al. (2013) is most likely comparable to our non-turbulent run M0, since they only observe isolated protostars, but our run M0 also includes a tiny amount of rotation along the same axis as the magnetic fields. Nonetheless, run M0 presents the formation of streamers, which, as we have seen, reorient the outflow along the magnetic field axis. Therefore, the positive correlation between the outflow axis and the magnetic fields in Chapman et al. (2013) may

be a consequence of this mechanism. Moreover, the present study is consistent with the observations of Galametz et al. (2018). In fact, we only observe large rotating structures and multiple systems for superalfvenic runs, for which the outflow-magnetic field misalignment is indeed larger than in the subalfvenic runs. Overall, our work would suggest that the preferential perpendicular orientation (> 45 deg) or random orientation would be obtained for systems with the Alfvenic Mach number $\mathcal{M}_{\rm A} > 1$, as a consequence of the disk orientation being set by the initial angular momentum. On the contrary, it would suggest that a better alignment is obtained for $\mathcal{M}_{\rm A} < 1$, because the streamers (perpendicular to **B**) re-orient the outflows towards the core-scale magnetic field axis.

Finally, let us take a look at the magnetic field strength within the outflow. As the tower flow grows, its mean magnetic field strength decreases. We measure a mean field strength of 15 mG in run M0 at the time when the outflow reaches ~ 2000 AU, 5 mG when it reaches ~ 5000 AU. Using the Chandrasekhar-Fermi method with ALMA/VLA observations, Hirota et al. (2020) obtained a value of 30 mG at $100 - 200$ AU in the outflows of the high-mass protostar Orion Source I. Computing the average in the outflow at a height between 150 AU and 250 AU, we have a field strength of $\approx$60 mG in run M0, $\approx$50 mG in run M05 (measuring it at late times), $\approx 50 - 60$ mG in run M05B2 (depending on the lobe) and $\approx$50 mG in run M2 (in the transient outflow). To first-order these are consistent with Hirota et al. (2020).

5.5 Conclusions

We have conducted four numerical simulations of massive pre-stellar core collapse including ambipolar diffusion and a hybrid radiative transfer method. This allows us to avoid, on the one hand, the magnetic field strength overestimation of the ideal MHD framework, and on the other hand, the radiative force underestimation of the Flux-Limited Diffusion method, to characterize the protostellar outflows in an unbiased way. Moreover, it leads to the formation of thermal pressure-dominated disks, rather than magnetic pressure dominated pseudo-disks. We have included an initial velocity field consistent with turbulence, and varied the Mach and Alfvenic Mach numbers to consider four runs with respectively, no turbulence, superalfvenic-subsonic turbulence, superalfvenic-supersonic turbulence and subalfvenic-subsonic turbulence. We summarize our results as follows:

1. Even in the absence of turbulence, asymmetries naturally arise via the presence of streamers (thermally-dominated filaments slightly denser than their surroundings) which connect onto the disk off the disk plane, and via the interchange instability which redistributes magnetic flux at the disk edge, breaking the axisymmetry.

2. Keplerian disks formed in all runs. They have typical sizes $100 - 200$ AU around individual stars and are consistent with magnetic regulation. In the superalfvenic runs, they are located within a larger rotating structure (circumbinary disk, see below). In this case, the rotation profile is close to Keplerian rotation within a few hundreds AU.

3. We report the formation of stable binary systems when turbulence is superalfvenic. They formed from disk fragmentation rather than initial fragmentation. Their binary separation is between 300 AU and 700 AU and may be linked to the initial angular momentum (*i.e.* amount of rotation) carried by the turbulent velocity field.

4. Outflows developed in all runs, but are (at least) delayed with superalfvenic turbulence, in comparison to subalfvenic turbulence. They are mainly bipolar, but in the superalfvenic, supersonic turbulence run we only observe a transient, monopolar outflow such as the few observed (16% in Wu et al. 2004). To a larger extent, this brings to the forefront the importance of the environmental ram pressure in the outflow physics.

5. All outflows emerge from a common mechanism: a magnetic tower flow (Lynden-Bell, 1996) while the radiative acceleration contribution is dominant close to the star. There are hints of a magneto-centrifugal acceleration but this requires dedicated studies at higher-resolution to be confirmed.

6. The radiative force does not disrupt the field topology, at least up to $\sim 10^5$ $L_\odot$ (~ 20 $M_\odot$) in run LRM0. The high-resolution runs are still running, so we will further report on this question.

7. In comparison with CO observations, we find an overall agreement on the outflow mass rate and momentum rates with the core low-mass range of the samples. This comes with two interpretations. A possibility is that our initial conditions, namely a massive core of $100 M_c$, are representative of the low-mass range of high-mass stars precursors. Another possibility is a different launching mechanism from that observed here, *e.g.* entrainment of molecular gas by a wide-angle outflow (see Arce et al. 2006) or by a high-velocity jet.

8. We do not find agreement with observational constraints about opening angles in sub-alfvenic turbulence runs. We produce outflows that are wider than the observed collimated jets, but more collimated than the wide-angle outflows observed. In run M05, the stellar motions in its binary system cause the outflows to widen. A further lead would be to determine the role of ambient thermal pressure at collimating the flow, to see whether collimation depends on the initial ambient temperature (20 K), but this is beyond the scope of the present work.

9. We have assessed the misalignment between disks, outflows and core-scale magnetic fields. Disks orientation appears to be set by the initial angular momentum at scales $\lesssim 10^4$ AU only, in agreement with Machida et al. (2019). Meanwhile, the streamers are located in a plane perpendicular to the magnetic field in all runs, but do not influence the disk formation process.

10. We do not find preferential outflow-magnetic fields alignment. Outflows are first launched nearly perpendicular to the disk plane. Even though streamers do not influence disk formation, they carry an additional ram pressure. Hence, outflows tend to avoid them to propagate along a path of least resistance. This explains a relative decrease between the disk-magnetic field misalignment ($\sim$50 deg in runs M05 and M05B2) and the outflow-magnetic field misalignment ($20 - 40$ deg). These results predict a random misalignment if $\mathcal{M}_\mathrm{A} > 1$ and a better alignment for $\mathcal{M}_\mathrm{A} < 1$ (because of the streamers).

To summarize, these results show that the magnetic tower flow process is a good candidate regarding the outflow mass, mass ejection rate and mass momentum rate of massive protostellar outflows. On the contrary, they also show that the effect of the ambient gas of the outflow collimation is poorly known, and that, in the present study, magnetic tower flows cannot reproduce the opening angles obtained from observations. Although the radiative acceleration dominates close to the star, it seems insufficient to perturb the magnetic field topology enough to prevent MHD outflows from being launched. Our high-resolution simulations are still running, and we will further address this question when the central star is more massive (*i.e.* more luminous) to confirm these results. Therefore, the only candidate (so far) to disrupt the field geometry is photoionization, as pointed out by Peters et al. (2011), and should occur at later times than those considered here.

This work has confirmed that disk formation does not occur preferentially perpendicularly to the core-scale magnetic fields, but its orientation is likely driven by turbulence (even sub-alfvenic). Following this trend, outflows preferentially develop perpendicularly to the disk,

but their orientation is highly-dependent on the ambient gas ram pressure. Moreover, multiplicity may be linked to the medium turbulence. Depending on the models, one may expect this turbulence to be higher in massive star-forming regions (due to radiative outflows and photoionization from other stars, and inflow from large scales), ending up in a higher stellar multiplicity than for low-mass stars.

Let us now discuss some of the limitations of our approach. First, we have used a gray hybrid scheme to treat separately the stellar irradiation from the ambient radiation. As discussed in Kuiper et al. (2010c), such a gray treatment would under- or overestimate the effect of radiative pressure depending on the stellar spectrum, compared to a frequency-dependent (multigroup) scheme. Nonetheless, this is a second-order effect, while we have determined regions where radiative acceleration and Lorentz acceleration differ by more than one order of magnitude (Fig. 5.12). Therefore, our conclusions should not be affected by the gray approximation.

We have enforced gas-radiation decoupling within the sink volume. This has permitted us to assess accurately the effect of the radiative force regarding the outflow physics. Meanwhile, the star has exerted a stronger radiative force onto the gas at the first absorption region, *i.e.* at the sink accretion radius ($\sim$20 AU). This has possibly shifted the disk inner edge (*i.e.* the edge at 20 AU received a direct stellar radiative force, perturbing the gravitation-centrifugal equilibrium) and therefore our disk sizes should be interpreted as higher limits.

Finally, we have chosen to follow self-consistently the collapse of a massive pre-stellar core. The price to pay is that we are not able to capture high-velocity ($\sim 300\,\mathrm{km\,s^{-1}}$) MHD jets launched in the vicinity of the star, which would be too expensive because of the very-high resolution required. They may be necessary though, to reproduce the well-collimated outflows we have mentioned (see *e.g.*, Moscadelli et al. 2005), while radiative force could contribute to their partial de-collimation. Actually, they may entrain the ambient gas and fit the outflow momentum rate observed in CO (Arce et al., 2006). In that regard, the development of a subgrid model for such jets is a first step (Kuiper et al. 2015, Rosen & Krumholz 2020). On this topic, a collaboration work (led by A. Verliat, PhD student at AIM) is under progress and will allow us to improve our understanding of outflows around massive protostars.

CHAPTER 6
Conclusions and Perspectives

This work has been dedicated to the study of the formation of massive stars with numerical simulations. Understanding this process requires dedicated observational strategies, since massive stars are rare and form in dense regions. Hence, progress has been made thanks to complementary observational, theoretical and numerical astrophysics. Due to the many physical processes involved (gravity, hydrodynamics, magnetic fields, radiation), it is a fantastic playground for astrophysicists, but it also requires high-performance numerical simulations. The major part of my contribution involves the improvement of the radiative transfer modelling, which is of paramount importance in the vicinity of such luminous stars. Aided by this development, we have tackled three specific questions: How do massive protostars accrete material? What are the mechanisms at the source of the outflows we observe? What determines the multiplicity of a massive stellar system? To make progress on these enigmas, we have focused on the multi-physics character of massive star-forming regions by considering a radiation-magneto-hydrodynamical framework, in order to relax the assumptions regarding either the presence of magnetic fields or the treatment of stellar radiation. While working on this project oriented towards the first two questions, I discovered challenging and exciting questions such as the third one. Consequently, we have developed a collaboration with the Massive Star Formation group of the University of Tübingen aiming at understanding the formation and multiple stellar systems via disk fragmentation. In this short review, I will summarize the main steps of the work presented in this manuscript and focus on the major results.

In Chapter 1, I review the state of the art of massive star formation, using the formation of low-mass stars as a reference frame. I highlight the role of radiative transfer in that context, and in Chapter 2 I introduce the two radiative transfer methods I have used - the FLD and M1 methods -, and coupled into a hybrid approach, in their "gray" (frequency-averaged) form. This hybrid method relies on the M1 method to model stellar radiation because it is well-suited for anisotropic radiation fields, and on the FLD method for the radiation emitted everywhere else, which does not have a preferential direction. Our method is built to model stellar radiation in highly non-isotropic conditions, typical of (massive) star-forming regions.

In Chapter 3, I present the Eulerian code RAMSES (Teyssier, 2002), which is characterized by its adaptive-mesh refinement grid. I describe the implicit FLD module and RAMSES-RT which solves explicitly the M1 equations under the reduced-speed-of-light approximation, implemented by Benoît Commerçon and Joakim Rosdahl, respectively. The newly developed hybrid radiative transfer method, which is the very heart of this thesis, is presented, focusing on the parts of the code where both modules communicate. Finally, the validation of this method is assessed in pure radiative transfer tests of a disk irradiated by a central star. We show that the hybrid method shows big improvements at computing the temperature profile of an optically-thin, or moderately optically-thick disk, compared to the FLD method used in star-formation calculations so far. We observe the limitation of the hybrid method when the

disk is very optically thick (an optical depth $\tau > 10^3$) because, first, stellar radiation (where most of the modelling improvement is done) is absorbed, and second, the photon mean free path becomes very short and is hardly resolved. The stellar radiative force, a major source of feedback from massive (proto-)stars, is no longer underestimated by a factor $\sim$100, as it was with a gray FLD method.

The first application of the hybrid method in a radiation-hydrodynamical context is the first and main topic of Chapter 4. We follow the collapse of a massive pre-stellar core until a star (modelled by a subgrid "sink particle" method) has formed and reached $\sim$20 $M_\odot$. For comparison, we use the same numerical setup as Rosen et al. (2016), and we run the same simulation with the FLD method. The hybrid method leads to a slightly less massive star (17.6 $M_\odot$) than the FLD (23.3 $M_\odot$) and to more extended and massive radiative cavities, because of the stronger radiative force modelled. Performing a refinement strategy focused on the cavity edges, we obtain the absence of radiative Rayleigh-Taylor instabilities, a possible and debated complementary accretion mechanism to disk-mediated accretion (Krumholz et al., 2009), because the gas is advected on a time scale shorter than the instability growth time scale. To date, this is the unique proof of their absence which combines high-resolution and hybrid radiative transfer, and it brings a solid argument to the debate. We identify disk-mediated accretion as the unique mechanism by which massive stars gain their mass.

In the second part of Chapter 4, we present the preliminary results of the on-going collaboration with A. Mercado-Oliva and R. Kuiper, from the University of Tübingen, regarding the numerical modelling of accretion disk fragmentation around massive protostars. We operate a comparison study between the AMR, Cartesian RAMSES code and the spherical-grid PLUTO code, aiming at investigating the fragmentation process, the use of sink particles, and how stellar multiplicity is affected. Strikingly, with and without sink particles (in addition to the primary one), we obtain the formation of a long-lived multiple system, while they obtain a single star. Moreover, we found that the density profile and the stellar mass history were strongly dependent of the accretion scheme. When a sink becomes massive enough to dominate the dynamics, both approaches lead to Keplerian disks with roughly similar temperature profiles.

In Chapter 5, we include realistic physics consistent with massive star-forming regions: magnetic fields (in the non-ideal MHD framework) and turbulence. Our first motivation is to identify the launching mechanism of massive protostellar outflows, among three candidates: a magnetic tower flow, a magnetocentrifugal jet, and a radiative outflow. The first one appears to be the dominant effect in our simulation, while the second occurs at scales smaller than our resolution, and the third one only dominates close to the central star and is, so far ($M \sim 14\,M_\odot$, $L \sim 10^4\,L_\odot$ at high-resolution), not strong enough to affect negatively the magnetic tower flow. The simulations are running and will provide a more robust answer to the latter point when the star luminosity reaches typically $L \sim 10^5\,L_\odot$. Our second objective is to extend the frame of disk-mediated accretion studied in Chapter 4 to magnetized and turbulent regions. Due to magnetic braking, magnetized disks are smaller than in the pure hydrodynamical case, and superalfvenic turbulence helps the formation of binary systems. Finally, we compare outflows properties and disk-outflow-magnetic fields orientations with observations. We show that a high level of turbulence can lead to a monopolar outflow, preventing its launching on the other side of the disk. Disk orientation appears to be set only by the initial rotation, in agreement with previous numerical studies. We find that outflows do not align with core-scale magnetic fields, because they develop mainly perpendicularly to the disk and therefore depend strongly on the disk orientation. This is consistent with the random distribution of outflow-magnetic fields angles recently observed.

Several medium- and long-term exciting leads exist to follow the present work and improve our knowledge on the formation of high-mass stars. First, the high-angular resolution provided

by ALMA and NOEMA will keep on providing us precious clues on the physics at the disk scales. With large statistical samples, we will be able to identify the fragmentation level of these objects, compare their radius to pure hydrodynamical ($\sim$1000 AU) or magnetically-regulated ($\sim 100 - 200$ AU) disks and subsequently determine the role of magnetic fields. Similarly, it will set constraints on the formation of multiple stellar systems around massive protostars (core or disk fragmentation?). Moreover, polarimetry measurements will help us constraining the outflow mechanism, because, for instance, a (dominant) poloidal field is expected in magneto-centrifugal outflows while a toroidal field would be consistent with a magnetic tower flow. Here are a few numerical developments or leads that would complement the advances previously mentioned.

Dust abundances

We have used a constant dust-to-gas ratio (1%) within the simulated volume throughout this thesis. Nonetheless, dust is the main contributor to the medium opacity. Grain growth and sedimentation are expected to occur, affecting this dust-to-gas ratio and therefore the opacities which couple the dust-gas mixture and radiation. This would impact the temperature structure of the disk and of the cavities. Furthermore, dust grains are charge carriers, so the ionization degree would vary and the non-ideal MHD resistivities together with it. Hence, we plan to include dust dynamics (Lebreuilly et al., 2019) to obtain a dust size distribution that varies dynamically during the collapse. One may expect a strong radiation field to exert a differential force onto dust grains and gas particles and to locally influence the dust size distribution consequently.

Multigroup radiative transfer

Frequency-dependent radiation transport is of main importance for the physical structure of irradiated disks. A gray approximation overestimates the absorption of infrared photons, which can then diffuse through the disk and heat the midplane. Hence, the disk self-shielding is only partially captured. In some problems, the precise disk temperature structure has to be determined. This is the case for protoplanetary disks evolution and for dedicated studies of (circum-)binary disks. Throughout this work, we have used a gray approximation for both the stellar irradiation (treated with the M1 module of RAMSES-RT, Rosdahl et al. 2013) and the ambiant radiation (with the Flux-Limited Diffusion, Commerçon et al. 2011b). While both approaches were used in their gray form, we have presented in Chapter 3 the simple frame for a multigroup treatment of one of them, or both.

Ionizing radiation

We have not included photoionization, which is already found to be responsible of perturbing the magnetic fields geometry (Peters et al., 2011). Their simulations were performed on larger scales than ours (a resolution of 100 AU), and have shown the disturbance of the magnetic tower flow by the development of an HII region. Going to a finer, $\sim$ AU resolution, would provide insights on both the magneto-centrifugal outflows and on the effect of photoionization on them, in order to understand why protostars tend to have less collimated jets as they evolve (Arce et al., 2006).

More than that, (Kuiper & Hosokawa, 2018) have shown that massive ($> 25\,M_\odot$) protostars could photoevaporate partially their accretion disk, before radiative forces finishes to suppress it. While they have used a spherical grid, which may not be adapted to multiple systems (as discussed in Sect. 4.2.6), we may study this phenomenon during binary formation, with the RAMSES AMR Cartesian grid.

For the reasons mentioned above, the inclusion of photoionizing radiation in the hybrid method is promising. More than that, it is already implemented in RAMSES-RT, hence it should be tested first within the hybrid approach but does not need to be developed from scratch.

Initial conditions

The initial conditions of massive star formation are poorly constrained. Throughout this work, we have chosen to use a simple setup to begin with, progressively increasing the complexity in order to identify the key mechanisms at each step. Nevertheless, this setup relies on the existence of massive pre-stellar cores. They appear to be far too rare (see the discussion in Motte et al., 2018) to be the main progenitors of massive stars. In the last few years, several models based on large-scale interactions have emerged (see Sect. 1.5), *e.g.* the Global Hierarchical Collapse (Vázquez-Semadeni et al., 2016) and the Inertial-Inflow (Padoan et al., 2019) models. The growing popularity of these models comes initially from the lack of massive pre-stellar core candidates. Regarding the Global Hierarchical Collapse model, several studies have indeed detected global infall motions (see *e.g.* Schneider et al. 2010). Large-scale simulations are commonly used, aiming in general at answering questions in a statistical manner (*e.g.* the origin of the Initial Mass Function of stars), but include several subgrid recipes to account for various feedback processes (ionization, supernovæ...). These global models call for numerical experiments to test their ability to form massive protostars with properties consistent with observations, regarding their environment, their accretion/ejection mechanisms... Since these models are intrinsically global, they require the simulation of an entire molecular cloud or subregions, instead of a single massive pre-stellar core as usually done in the literature and in this work. To make these calculations tractable, zoom-in methods are to be used. A 8-weeks collaboration with S. Geen, at the University of Amsterdam, has been founded by the HPC-Europa programm in order to lead this project and to build the bridge between large-scale and small-scale numerical simulations of massive star formation.

Accretion luminosity

As mentioned in this manuscript, we have not included the accretion luminosity in this work because of the lack of theoretical and observational constraints regarding it. We have chosen to avoid the use of an additional subgrid model whose parameters are poorly constrained. Indeed, the efficiency of this mechanism at converting gravitational into radiative energy is usually kept constant throughout a simulation and the value chosen differs from one study to another (3/4 in Rosen et al. 2016, 1 in Kuiper & Yorke 2013). Nevertheless, this process may dominate the total stellar luminosity before $10\,M_\odot$. Hence, as discussed in Sect. 4.2.5, the observational constraints on the temperature of protostellar cavities could be used as a constraint for its efficiency, while theoretical studies should be performed to identify the conditions under which it occurs.

Appendices

APPENDIX A
Basics of Virial theorem

In this appendix, we derive Eq. 1.11. from basic principles. Let us assume a homogenous, self-gravitating cloud of adiabatic gas with no external pressure force, and derive the Virial theorem. The Fundamental Principle of Dynamics applied to a local parcel of gas reads

$$\rho \frac{\mathrm{d}\mathbf{v}}{\mathrm{d}t} = -\rho \nabla \phi \tag{A.1}$$

where ρ is the local density, $\mathbf{v}$ is the velocity and ϕ is the gravitational potential. We multiply A.1 with $\mathbf{r}$ and obtain

$$\rho\, \mathbf{r} \frac{\mathrm{d}\mathbf{v}}{\mathrm{d}t} = \rho \left(\frac{1}{2} \frac{\mathrm{d}^2 \mathbf{r}^2}{\mathrm{d}t^2} - \left(\frac{\mathrm{d}\mathbf{r}}{\mathrm{d}t} \right)^2 \right) = -\rho\, \mathbf{r} \cdot \nabla \phi. \tag{A.2}$$

By integrating A.2 over the cloud volume V it leads to

$$\frac{1}{2} \iiint_V \rho \frac{\mathrm{d}^2 \mathbf{r}^2}{\mathrm{d}t^2} \mathrm{d}\tau = \iiint_V \rho \left(\frac{\mathrm{d}\mathbf{r}}{\mathrm{d}t} \right)^2 \mathrm{d}\tau - \iiint_V \rho\, \mathbf{r}\, \nabla \phi \, \mathrm{d}\tau, \tag{A.3}$$

which corresponds to

$$\frac{1}{2} \ddot{I} = 2\Gamma + \Omega_\mathrm{g}, \tag{A.4}$$

where I is the momentum of inertia of the system, Γ is the kinetic energy (which accounts for macroscopic motions) and Ω_g is the gravitational energy. Therefore, a system at rest is characterized by the following relation:

$$2\Gamma + \Omega_\mathrm{g} = 0. \tag{A.5}$$

Now, let us consider also the thermal pressure and the Lorentz force which act on the gas, on the right-hand side of A.1:

$$\begin{aligned} \rho \frac{\mathrm{d}\mathbf{v}}{\mathrm{d}t} &= -\nabla P + (\nabla \times \mathbf{B}) \times \mathbf{B} - \rho \nabla \phi \\ &= -\nabla \left(P + \frac{B^2}{2} \right) + (\mathbf{B} \cdot \nabla)\mathbf{B} - \rho \nabla \phi, \end{aligned} \tag{A.6}$$

where the Lorentz force has been decomposed into the *magnetic pressure* (which adds to the thermal pressure) and *magnetic tension* forces. We take the first-order moment of this equation (*i.e.*, $\iiint_V \mathbf{r}[...]\mathrm{d}\tau$). The total pressure term (the first right-hand side term) becomes

$$\begin{aligned} \iiint_V \mathbf{r}\, \nabla P_\mathrm{tot}\, \mathrm{d}\tau &= \iiint_V \nabla \cdot (P_\mathrm{tot}\, \mathbf{r})\, \mathrm{d}\tau - 3 \iiint_V \nabla P_\mathrm{tot}\, \mathrm{d}\tau \\ &= \oiint_S P_\mathrm{tot}\, \mathbf{r} \cdot \mathrm{d}\mathbf{S} - 3 \iiint_V P_\mathrm{tot}\, \mathrm{d}\tau, \end{aligned} \tag{A.7}$$

using Green-Ostrogradski's theorem to obtain a surface integral. The thermal pressure of an ideal gas verifies $P = (\gamma - 1)\rho e$ where γ is the adiabatic index and e is the internal energy given by $e = \frac{1}{\gamma - 1}\frac{k_B T}{\mu m_H}$, where k_B is Boltzmann's constant, μ is the mean molecular weight and m_H is the atomic hydrogen mass. It leads to

$$\iiint_V P \mathrm{d}\tau = (\gamma - 1) \iiint_V \rho\, e\, \mathrm{d}\tau = (\gamma - 1)\, U, \tag{A.8}$$

where U is the total internal energy of the cloud. Similarly, a total magnetic energy M can be defined as

$$\iiint_V \frac{B^2}{2} \mathrm{d}\tau = M. \tag{A.9}$$

It can be shown that the first-order moment of the second right-hand side term of A.6 reads

$$\begin{aligned} \iiint_V \mathbf{r} \cdot (\mathbf{B} \cdot \nabla)\, \mathbf{B} \mathrm{d}\tau &= \iiint_V \nabla \cdot ((\mathbf{r} \cdot \mathbf{B})\, \mathbf{B})\, \mathrm{d}\tau - \iiint_V B^2 \mathrm{d}\tau \\ &= \oiint_S (\mathbf{r} \cdot \mathbf{B})\, \mathbf{B} \cdot \mathrm{d}\mathbf{S} - 2M, \end{aligned} \tag{A.10}$$

using once again Green-Ostrogradski's theorem. Putting it altogether, one obtains the Virial theorem for a magnetized cloud

$$\frac{1}{2}\ddot{I} = 3(\gamma - 1)U + M + 2\Gamma + \Omega_g + \oiint_S (\mathbf{r} \cdot \mathbf{B})\, \mathbf{B} \mathrm{d}\mathbf{S} - \oiint_S P_{tot} \mathbf{r}\, \mathrm{d}\mathbf{S}, \tag{A.11}$$

corresponding to Eq. 1.11.

APPENDIX B
Core gravitational and rotational energy

In this appendix, we detail the calculation for a core gravitational and rotational energy for density and rotation profiles following power-laws of respective indices β_ρ and β_Ω. Eventually, we apply it to the setup presented in Sect. 4.2.2 to obtain the core rotational to gravitational energy ratio.

The mass contained in a sphere of radius R_c, for a density profile given by

$$\rho(r) = \rho_0 \left(\frac{r}{r_0}\right)^{\beta_\rho}, \tag{B.1}$$

is

$$\begin{aligned} M_\mathrm{c} = M(R_\mathrm{c}) &= 4\pi \int_0^R \rho(r) r^2 dr = 4\pi \int_0^R \rho_0 \left(\frac{r}{r_0}\right)^{\beta_\rho} r^2 dr \\ &= 4\pi \frac{\rho_0}{r_0^{\beta_\rho}} \int_0^R r^{2+\beta_\rho} dr = 4\pi \frac{\rho_0}{r_0^{\beta_\rho}} \frac{1}{3+\beta_\rho} R^{3+\beta_\rho}. \end{aligned} \tag{B.2}$$

The total gravitational energy within the core radius R_c is therefore

$$\begin{aligned} E_\mathrm{grav} = \int_0^{R_\mathrm{c}} dU &= -\int_0^{R_\mathrm{c}} \frac{GM(r)dm}{r} \\ &= -\int_0^{R_\mathrm{c}} G\rho_0 4\pi r_0^3 \frac{1}{3+\beta_\rho} \left(\frac{r}{r_0}\right)^{3+\beta_\rho} \rho_0 \left(\frac{r}{r_0}\right)^{\beta_\rho} 4\pi \frac{r^2}{r} dr \\ &= -\int_0^{R_\mathrm{c}/r_0} G\rho_0^2 16\pi^2 r_0^3 \frac{1}{3+\beta_\rho} u^{3+2\beta_\rho} r_0^2 u du \\ &= -\int_0^{R_\mathrm{c}/r_0} G\rho_0^2 16\pi^2 r_0^5 \frac{1}{3+\beta_\rho} u^{4+2\beta_\rho} du \\ &= -G\rho_0^2 16\pi^2 \frac{r_0^5}{3+\beta_\rho} \frac{1}{5+2\beta_\rho} \left(\frac{R_\mathrm{c}}{r_0}\right)^{5+2\beta_\rho} \\ &= -G\rho_0^2 16\pi^2 \frac{r_0^6}{r_0} \frac{3+\beta_\rho}{(3+\beta_\rho)^2} \frac{1}{5+2\beta_\rho} \frac{R}{r_0}^{6+2\beta_\rho} \frac{r_0}{R_\mathrm{c}} \\ &= -\frac{3+\beta_\rho}{5+2\beta_\rho} \frac{GM_\mathrm{c}^2}{R_\mathrm{c}} \end{aligned} \tag{B.3}$$

To compute the rotational energy, let us first re-write the speed as

$$\begin{aligned} v(r) &= R_{\rm cyl}\Omega_0 \left(\frac{R_{\rm cyl}}{r_0}\right)^{\beta_\Omega} \\ &= r\sin\theta\Omega_0 \left(\frac{r\sin\theta}{r_0}\right)^{\beta_\Omega} \\ &= r^{1+\beta_\Omega}\frac{\Omega_0}{r_0^{\beta_\Omega}}\sin\theta^{\beta_\Omega}, \end{aligned} \tag{B.4}$$

hence the rotational energy within a radius R is

$$\begin{aligned} E_{\rm rot}(R) &= 2\pi \int_0^\pi \int_0^R \frac{1}{2}\rho(r)v(r)^2 \sin\theta r^2 dr d\theta \\ &= \frac{2\pi}{2}\int_0^\pi \int_0^R \frac{\rho_0 r^{\beta_\rho}}{r_0^{\beta_\rho}} r^{2+2\beta_\Omega+2}\sin\theta^{2+2\beta_\Omega+1}\frac{\Omega_0^2}{r_0^{2\beta_\Omega}} dr d\theta \\ &= \pi\int_0^R \rho_0 \frac{\Omega_0^2}{r_0^{2\beta_\Omega}}\frac{r^{4+2\beta_\Omega+\beta_\rho}}{r_0^{\beta_\rho}} dr \int_0^\pi \sin\theta^{3+2\beta_\Omega} d\theta \\ &= \pi\rho_0\frac{\Omega_0^2}{r_0^{2\beta_\Omega}}\frac{1}{5+2\beta_\Omega+\beta_\rho}\frac{R^{5+2\beta_\Omega+\beta_\rho}}{r_0^{\beta_\rho}}\int_0^\pi \sin\theta^{3+2\beta_\Omega} d\theta \\ &= \frac{\beta_\rho+3}{\beta_\rho+2\beta_\Omega+5}\frac{\Omega_0^2 M_{\rm c} R^{2(1+\beta_\Omega)}}{4 r_0^{2\beta_\Omega}}\int_0^\pi \sin\theta^{3+2\beta_\Omega} d\theta \end{aligned} \tag{B.5}$$

using Eq. B.2. Depending on β_Ω, the final integral has to be integrated numerically.

Applying formula B.3 to the numerical setup of Oliva & Kuiper (Sect. 4.2.2) with $\beta_\rho = -3/2$, $M_{\rm c} = 200\,{\rm M}_\odot$ and $R_{\rm c} = 20625$ AU gives a core gravitational energy $E_{\rm grav} = 2.6 \times 10^{46}$ erg. We use Eq. B.5 to compute the rotational energy, with $\Omega_0 = 9.84 \times 10^{-11}$ s and $\beta_\Omega = -3/4$. We obtain a rotational energy $E_{\rm rot} = 1.25 \times 10^{45}$ erg, hence the ratio of the rotational to the gravitational energy is $E_{\rm grav}/E_{\rm rot} \approx 5\%$.

Appendix C

Luminosity injection in the sink particle volume

In this appendix, we investigate the impact of the radiative transfer method and of the kernel function to deposit the luminosity within the sink volume, on the outflows and on the disk size at early times. This is motivated by the fact that part of the sink sits onto the inner disk region, hence a portion of the stellar radiation (which depends on the disk density, the resolution, the luminosity and the opacities) is locally absorbed before it has time to escape the sink volume. This is a limitation of the hybrid approach, because the re-emitted radiation is treated with the FLD method instead of the M1. Since the FLD method does not model properly stellar radiation in such anisotropic geometries and underestimates the radiative force, if one is interested in the temperature or dynamics of the outflows, one may want to circumvent this limitation so that stellar radiation can effectively escape from the sink volume.

The simulations are similar to run M0 presented in Chapter 5, hence they include non-ideal MHD (ambipolar diffusion) but no turbulence, and the outflow is originally launched from a magnetic tower flow process. We run four simulations: two with the Flux-Limited Diffusion ("FLD"), two with the hybrid radiative transfer approach ("HY"). For each method, we test two injection kernels: either the luminosity is deposited uniformly over the sink volume ("uniform"), or only over the central oct ("peaked").

Figure C.1 shows the density slices perpendicularly to the disk and in the disk plane, for each run, when the central star mass is $\approx 5\,M_\odot$. Comparing the left and right columns, the outflows are larger with the hybrid method than with the FLD, as expected from the pure radiative transfer tests (Sect. 3.5.1). They also appear less symmetric (with respect to the disk

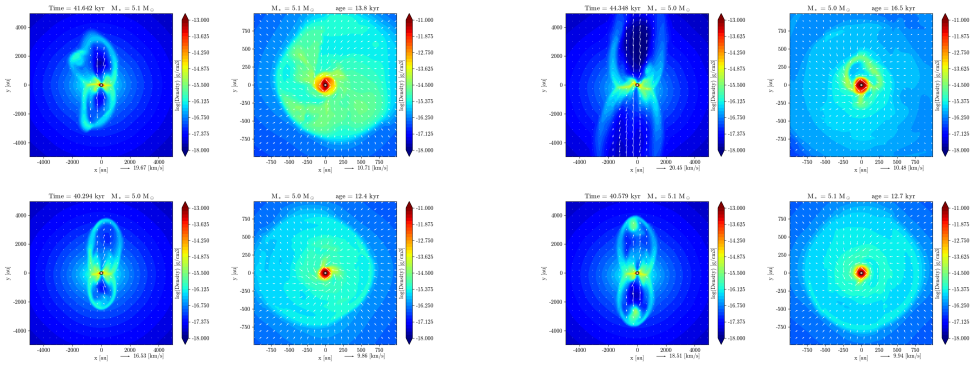

Figure C.1: Density slices perpendicular (left) and parallel to the disk plane (right). Left column: FLD method ; right column: hybrid method. Top row: uniform; bottom row: peaked.

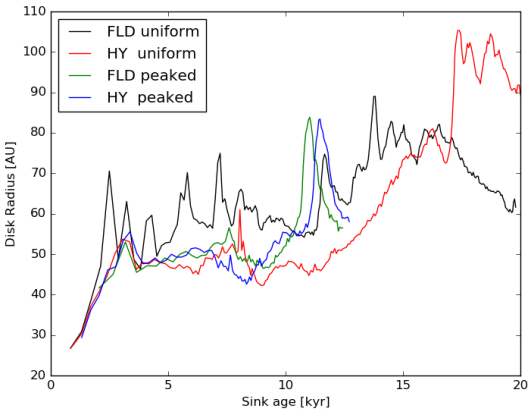

Figure C.2: Disk radius as a function of the sink age, for the four runs.

plane) in the FLD runs. We note the presence of high-density "clumps" at the outflow front in the HY runs. These are likely due to the greater acceleration by the stellar radiative force, compared to the FLD runs, which shocks with the outer medium.

Let us compare the top and bottom rows of Fig. C.1 to estimate the influence of the luminosity injection function. For both radiative transfer methods, the "peaked" run leads to smaller outflows than the "uniform" run. The difference in outflow size is even more obvious for the HY runs, because, as mentioned above, the M1 radiative force is significantly larger than the FLD radiative force. Indeed, when all the luminosity is injected in the central oct, part of the radiation is absorbed and re-emitted with the FLD method, thus the outflow and disk properties can resemble that of the FLD runs. On the opposite, the sink volume is larger than the local disk scale height, hence among the cells where luminosity has been injected uniformly there are some cells located outside the disk, so that stellar radiation can directly escape without being absorbed.

As shown in Fig. C.2, we obtain similar disk sizes in all runs, except in run HY uniform where the disk radius is larger by $\sim$20 AU. This corresponds to the sink accretion (and luminosity injection) radius. When the luminosity is deposited uniformly up to a radius of 20 AU, this leads to an additional repulsive force (the direct stellar radiative force) exerted onto the gas over a radius equal to the sink luminosity injection radius, which is 20 AU. Hence, a uniform luminosity injection with the hybrid method likely shifts the disk towards a slightly larger radius.

Nevertheless, a uniform injection of luminosity within the sink volume is not physically satisfying. In fact, the M1 radiative flux which powers the radiative force indirectly depends on the local radiative energy gradient (Eq. 3.39). If the injection is uniform over the sink volume, radiative energy is more absorbed in the central cells (which sit onto dense gas) than above and below the disk plane (where lower-density gas is located). This results in a radiative flux oriented towards the central cells and consequently in a spurious radiative force oriented towards the central cells. For this reason, we do not adopt a uniform luminosity injection function in Chapter 5 but rather set the sink volume as entirely optically-thin.

Bibliography

Adams, F. C. & Shu, F. H. 1986, The Astrophysical Journal, 308, 836 10

Aharonian, F., Yang, R., & Wilhelmi, E. d. O. 2019, arXiv:1804.02331 [astro-ph], arXiv: 1804.02331 3

Ahmadi, A., Kuiper, R., & Beuther, H. 2019, arXiv:1909.04051 [astro-ph], arXiv: 1909.04051 99

Ali, A. A. & Harries, T. J. 2019, Monthly Notices of the Royal Astronomical Society, 487, 4890, arXiv: 1906.05858 3

Andre, P. 2002, EAS Publications Series, 3, 1 xvii, 8, 9

Andre, P., Men'shchikov, A., Bontemps, S., et al. 2010, Astronomy and Astrophysics, 518, L102 3

Andre, P., Ward-Thompson, D., & Barsony, M. 1993, The Astrophysical Journal, 406, 122 8

Anglada, G., Rodriguez, L. F., Canto, J., Estalella, R., & Torrelles, J. M. 1992, The Astrophysical Journal, 395, 494 16

Anglada, G., Rodriguez, L. F., & Carrasco-Gonzalez, C. 2018, Astron Astrophys Rev, 26, 3, arXiv: 1806.06444 17

Arce, C., Louvet, F., Cortes, P., et al. 2020, arXiv:2005.12921 [astro-ph], arXiv: 2005.12921 158

Arce, H. G., Shepherd, D., Gueth, F., et al. 2006, arXiv:astro-ph/0603071, arXiv: astro-ph/0603071 155, 159, 161, 166

Aubert, D. & Teyssier, R. 2008, Monthly Notices of the Royal Astronomical Society, 387, 295 20, 45, 65

Ballesteros-Paredes, J., Hartmann, L. W., Vázquez-Semadeni, E., Heitsch, F., & Zamora-Avilés, M. A. 2011, Monthly Notices of the Royal Astronomical Society, 411, 65 16

Banerjee, R. & Pudritz, R. E. 2006, The Astrophysical Journal, 641, 949 119

Banerjee, R. & Pudritz, R. E. 2007, The Astrophysical Journal, 660, 479 21, 34, 119, 141, 147

Bate, M. R., Bonnell, I. A., & Price, N. M. 1995, Monthly Notices of the Royal Astronomical Society, 277, 362 52

Beltrán, M. 2020, arXiv:2005.06912 [astro-ph], arXiv: 2005.06912 18, 120

Beltrán, M. T. & de Wit, W. J. 2016, Astron Astrophys Rev, 24, 6, arXiv: 1509.08335 18

Beltrán, M. T., Padovani, M., Girart, J. M., et al. 2019, arXiv:1908.01597 [astro-ph], arXiv: 1908.01597 18

Berger, M. J. & Oliger, J. 1984, Journal of Computational Physics, 53, 484 52

Beuther, H., Ahmadi, A., Mottram, J. C., et al. 2019, Astronomy & Astrophysics, 621, A122 18

Beuther, H., Schilke, P., Sridharan, T. K., et al. 2002, Astronomy & Astrophysics, 383, 892 16, 152, 153, 155, 156

Blandford, R. D. & Payne, D. G. 1982, Monthly Notices of the Royal Astronomical Society, 199, 883 33, 118, 145, 146

Bleuler, A. & Teyssier, R. 2014, Monthly Notices of the Royal Astronomical Society, 445, 4015 67, 68, 87, 88, 123, 138

Bonanos, A. Z., Stanek, K. Z., Udalski, A., et al. 2004, The Astrophysical Journal, 611, L33 4

Bonnell, I. A., Bate, M. R., Clarke, C. J., & Pringle, J. E. 2001, Monthly Notices of the Royal Astronomical Society, 323, 785 13

Bonnell, I. A., Bate, M. R., & Vine, S. G. 2003, Monthly Notices of the Royal Astronomical Society, 343, 413 14

Bonnell, I. A., Bate, M. R., & Zinnecker, H. 1998, Monthly Notices of the Royal Astronomical Society, 298, 93 13

Bonnell, I. A. & Davies, M. B. 1998, Monthly Notices of the Royal Astronomical Society, 295, 691 13

Bonnell, I. A., Vine, S. G., & Bate, M. R. 2004, Monthly Notices of the Royal Astronomical Society, 349, 735 13

Bontemps, S., André, P., Kaas, A. A., et al. 2001, Astronomy & Astrophysics, 372, 173 3

Bontemps, S., Motte, F., Csengeri, T., & Schneider, N. 2010, Astronomy & Astrophysics, 524, A18 16, 117

Bosco, F., Beuther, H., Ahmadi, A., et al. 2019, arXiv:1907.04225 [astro-ph], arXiv: 1907.04225 18

Bromm, V., Coppi, P. S., & Larson, R. B. 1999, The Astrophysical Journal, 527, L5 4

Bruston, P., Audouze, J., Madjar, A. V., & Laurent, C. 1981, The Astrophysical Journal, 243, 161 7

Cabrit, S. & Bertout, C. 1990, The Astrophysical Journal, 348, 530 17

Cabrit, S. & Bertout, C. 1992, A&A, 261, 274 16, 33, 120, 125

Cabrit, S., Edwards, S., Strom, S. E., & Strom, K. M. 1990, The Astrophysical Journal, 354, 687 17

Caratti o Garatti, A., Stecklum, B., Garcia Lopez, R., et al. 2017, Nature Physics, 13, 276 18, 108

Castor, J. I. 2004, Radiation hydrodynamics (Cambridge, UK ; New York: Cambridge University Press) 39

Castor, J. I., Abbott, D. C., & Klein, R. I. 1975, The Astrophysical Journal, 195, 157 3

Cesaroni, R., Neri, R., Olmi, L., et al. 2005, Astronomy & Astrophysics, 434, 1039 118

Cesaroni, R., Sánchez-Monge, Á., Beltrán, M. T., et al. 2017, Astronomy & Astrophysics, 602, A59 156

Chabrier, G. 2005, in The Initial Mass Function 50 Years Later, ed. E. Corbelli, F. Palla, & H. Zinnecker, Vol. 327 (Dordrecht: Springer Netherlands), 41–50 3

Chandrasekhar, S. & Fermi, E. 1953, The Astrophysical Journal, 118, 113 19

Chapman, N. L., Davidson, J. A., Goldsmith, P. F., et al. 2013, The Astrophysical Journal, 770, 151 157, 158

Chini, R., Hoffmeister, V. H., Nasseri, A., Stahl, O., & Zinnecker, H. 2012, Monthly Notices of the Royal Astronomical Society, 424, 1925 5

Churchwell, E. 2002, Annual Review of Astronomy and Astrophysics, 40, 27 15

Ciardi, A. & Hennebelle, P. 2010, Monthly Notices of the Royal Astronomical Society: Letters, 409, L39 151

Commerçon, B., Debout, V., & Teyssier, R. 2014, Astronomy & Astrophysics, 563, A11 64, 70

Commerçon, B., Hennebelle, P., Audit, E., Chabrier, G., & Teyssier, R. 2008, Astronomy & Astrophysics, 482, 371 21

Commerçon, B., Hennebelle, P., & Henning, T. 2011a, The Astrophysical Journal, 742, L9 13, 18, 21, 45, 61, 114, 120, 123

Commerçon, B., Teyssier, R., Audit, E., Hennebelle, P., & Chabrier, G. 2011b, Astronomy & Astrophysics, 529, A35 47, 61, 62, 63, 70, 121, 166

Courant, R. & Friedrichs, K. 1928, Mathematische Annalen, 43 57

Crowther, P. A., Schnurr, O., Hirschi, R., et al. 2010, Monthly Notices of the Royal Astronomical Society, 408, 731 4, 12

Csengeri, T., Bontemps, S., Schneider, N., Motte, F., & Dib, S. 2011, Astronomy & Astrophysics, 527, A135 14

Davis, S. W., Stone, J. M., & Jiang, Y.-F. 2012, The Astrophysical Journal Supplement Series, 199, 9 45

de Valon, A., Dougados, C., Cabrit, S., et al. 2020, arXiv:2001.09776 [astro-ph, physics:physics], arXiv: 2001.09776 17

Dekel, A. & Silk, J. 1986, The Astrophysical Journal, 303, 39 3

Draine, B. T. 2003, The Astrophysical Journal, 598, 1026 87

Draine, B. T. & Lee, H. M. 1984, The Astrophysical Journal, 285, 89 xix, 73, 78

Dubroca, B. & Feugeas, J. L. 1999, Etude théorique et numérique d'une hiérarchie de modèles aux moments pour le transfert radiatif 46

Duchêne, G. & Kraus, A. 2013, Annual Review of Astronomy and Astrophysics, 51, 269 99

Dullemond, C. P., Juhasz, A., Pohl, A., et al. 2012, Astrophysics Source Code Library, ascl:1202.015 71

Eggleton, P. P. & Tokovinin, A. A. 2008, Monthly Notices of the Royal Astronomical Society, 389, 869 5

Ekström, S., Georgy, C., Eggenberger, P., et al. 2012, Astronomy & Astrophysics, 537, A146 xvii, 4

Elmegreen, B. G. & Scalo, J. 2004, Annual Review of Astronomy and Astrophysics, 42, 211 1

Emerson, J. P., Jennings, R. E., & Moorwood, A. F. M. 1973, The Astrophysical Journal, 184, 401 19

Evans, C. R. & Hawley, J. F. 1988, The Astrophysical Journal, 332, 659 58

Falgarone, E., Troland, T. H., Crutcher, R. M., & Paubert, G. 2008, Astronomy & Astrophysics, 487, 247 19

Federrath, C., Banerjee, R., Clark, P. C., & Klessen, R. S. 2010, The Astrophysical Journal, 713, 269 88

Fernández-López, M., Curiel, S., Girart, J. M., et al. 2011a, The Astrophysical Journal, 141, 72 17

Fernández-López, M., Girart, J. M., Curiel, S., et al. 2011b, The Astrophysical Journal, 142, 97 18

Fernández-López, M., Girart, J. M., Curiel, S., et al. 2013, The Astrophysical Journal, 778, 72 17

Flock, M., Fromang, S., González, M., & Commerçon, B. 2013, Astronomy & Astrophysics, 560, A43 119

Foglizzo, T., Scheck, L., & Janka, H.-T. 2006, The Astrophysical Journal, 652, 1436 96, 132

Fontani, F., Commerçon, B., Giannetti, A., et al. 2016, Astronomy & Astrophysics, 593, L14 19

Fromang, S., Hennebelle, P., & Teyssier, R. 2006, Astronomy & Astrophysics, 457, 371 58, 59, 61, 118, 121

Fuksman, J. D. M., Klahr, H., Flock, M., & Mignone, A. 2020, arXiv:2005.01785 [astro-ph], arXiv: 2005.01785 20, 120

Fuller, G. A., Williams, S. J., & Sridharan, T. K. 2005, Astronomy & Astrophysics, 442, 949 16

Galametz, M., Maury, A., Girart, J. M., et al. 2018, Astronomy & Astrophysics, 616, A139 157, 158

Galli, D., Walmsley, M., & Gonçalves, J. 2002, Astronomy & Astrophysics, 394, 275 7

Gaudel, M., Maury, A. J., Belloche, A., et al. 2020, arXiv:2001.10004 [astro-ph], arXiv: 2001.10004 132

Gies, D. R. & Bolton, C. T. 1986, The Astrophysical Journal Supplement Series, 61, 419 5

Girart, J. M., Beltran, M. T., Zhang, Q., Rao, R., & Estalella, R. 2009, Science, 324, 1408 19, 21

Girart, J. M., Estalella, R., Fernández-López, M., et al. 2017, The Astrophysical Journal, 847, 58 17, 18, 99

Girart, J. M., Fernandez-López, M., Li, Z.-Y., et al. 2018, The Astrophysical Journal, 856, L27 18, 137

Girart, J. M., Frau, P., Zhang, Q., et al. 2013, The Astrophysical Journal, 772, 69 19

Gnedin, N. Y. & Abel, T. 2001, New Astronomy, 6, 437 67

González, M., Audit, E., & Huynh, P. 2007, Astronomy & Astrophysics, 464, 429 xviii, 20, 45, 65, 76

González, M., Vaytet, N., Commerçon, B., & Masson, J. 2015, Astronomy & Astrophysics, 578, A12 43, 47, 80

Goodman, A. A., Benson, P. J., Fuller, G. A., & Myers, P. C. 1993, The Astrophysical Journal, 406, 528 88

Gressel, O., Ramsey, J. P., Brinch, C., et al. 2020, arXiv:2005.03431 [astro-ph], arXiv: 2005.03431 119

Harries, T. J., Douglas, T. A., & Ali, A. 2017, Monthly Notices of the Royal Astronomical Society, 471, 4111 20

Harten, A., Lax, P. D., & Leer, B. v. 1983, SIAM Review, 25, 35 56, 65

Haworth, T. J. & Harries, T. J. 2012, Monthly Notices of the Royal Astronomical Society, 420, 562 20

Hennebelle, P. & Ciardi, A. 2009, Astronomy & Astrophysics, 506, L29 21

Hennebelle, P., Commerçon, B., Chabrier, G., & Marchand, P. 2016, The Astrophysical Journal, 830, L8 22, 118, 137

Hennebelle, P., Commerçon, B., Joos, M., et al. 2011, Astronomy & Astrophysics, 528, A72 119, 137

Hennebelle, P., Commerçon, B., Lee, Y.-N., & Charnoz, S. 2020, Astronomy & Astrophysics, 635, A67 105

Hennebelle, P. & Fromang, S. 2008, Astronomy & Astrophysics, 477, 9 118, 119

Hennebelle, P., Lee, Y.-N., & Chabrier, G. 2019, The Astrophysical Journal, 883, 140 4

Hirota, T. 2018, arXiv:1806.10837 [astro-ph], arXiv: 1806.10837 34

Hirota, T., Machida, M. N., Matsushita, Y., et al. 2017, Nature Astronomy, 1 120, 156

Hirota, T., Plambeck, R. L., Wright, M. C. H., et al. 2020, arXiv:2005.13077 [astro-ph], arXiv: 2005.13077 158

Hoang, T., Tram, L. N., Lee, H., & Ahn, S.-H. 2018, arXiv:1810.05557 [astro-ph], arXiv: 1810.05557 3

Hosokawa, T., Hirano, S., Kuiper, R., et al. 2016, The Astrophysical Journal, 824, 119 4

Hosokawa, T. & Omukai, K. 2009, The Astrophysical Journal, 691, 823 7, 8, 111

Hosokawa, T., Yorke, H. W., & Omukai, K. 2010, The Astrophysical Journal, 721, 478 8, 103

Hull, C. L. H., Plambeck, R. L., Bolatto, A. D., et al. 2013, The Astrophysical Journal, 768, 159 157, 158

Hull, C. L. H., Plambeck, R. L., Kwon, W., et al. 2014, The Astrophysical Journal Supplement Series, 213, 13 157, 158

Ilee, J. D., Cyganowski, C. J., Brogan, C. L., et al. 2018, The Astrophysical Journal, 869, L24 99

Isella, A. & Natta, A. 2005, Astronomy & Astrophysics, 438, 899 87

Jacquet, E. & Krumholz, M. R. 2011, The Astrophysical Journal, 730, 116 21, 95, 96

Jeans, J. H. 1902, Proceedings of the Royal Society of London Series I, 71, 136 26

Johnston, K. G., Hoare, M. G., Beuther, H., et al. 2020, Astronomy & Astrophysics, 634, L11 93

Johnston, K. G., Robitaille, T. P., Beuther, H., et al. 2015, The Astrophysical Journal, 813, L19 93, 105, 107, 137

Joos, M., Hennebelle, P., & Ciardi, A. 2012, Astronomy & Astrophysics, 543, A128 89, 118, 124, 131

Joos, M., Hennebelle, P., Ciardi, A., & Fromang, S. 2013, Astronomy & Astrophysics, 554, A17 21, 118, 131, 151, 157

Kaisig, M., Tajima, T., & Lovelace, R. V. E. 1992, The Astrophysical Journal, 386, 83 132

Kannan, R., Vogelsberger, M., Marinacci, F., et al. 2019, Monthly Notices of the Royal Astronomical Society, 485, 117 20

Kato, Y., Mineshige, S., & Shibata, K. 2004, The Astrophysical Journal, 605, 307 145, 147

Kee, N. D. & Kuiper, R. 2019, Monthly Notices of the Royal Astronomical Society, arXiv: 1811.10521 3

Keto, E. 2007, Monthly Notices of the Royal Astronomical Society, 666, 976 15, 22

Keto, E. & Klaassen, P. 2008, The Astrophysical Journal Letters, 678, L109 22

Khokhlov, A. 1998, Journal of Computational Physics, 143, 519 52

Kim, J.-G., Kim, W.-T., Ostriker, E. C., & Skinner, M. A. 2017, The Astrophysical Journal, 851, 93 20

Klassen, M., Pudritz, R. E., Kuiper, R., Peters, T., & Banerjee, R. 2016, The Astrophysical Journal, 823, 28 20, 21, 87, 90, 91, 93

Kölligan, A. & Kuiper, R. 2018, A&A, 620, A182, arXiv: 1811.07009 33, 119, 147, 151

Krasnopolsky, R., Li, Z.-Y., Shang, H., & Zhao, B. 2012, The Astrophysical Journal, 757, 77 126, 134

Kraus, S., Hofmann, K.-H., Menten, K. M., et al. 2010, Nature, 466, 339 18

Kroupa, P. 2001, Monthly Notices of the Royal Astronomical Society, 322, 231 xvii, 3, 4

Krumholz, M. R. 2017, Notes on Star Formation (The Open Astrophysics Bookshelf) 12

Krumholz, M. R., Klein, R. I., McKee, C. F., & Bolstad, J. 2007, The Astrophysical Journal, 667, 626 43

Krumholz, M. R., Klein, R. I., McKee, C. F., Offner, S. S. R., & Cunningham, A. J. 2009, Science, 323, 754 20, 45, 87, 95, 114, 164

Krumholz, M. R. & Matzner, C. D. 2009, The Astrophysical Journal, 703, 1352 137

Krumholz, M. R., McKee, C. F., & Klein, R. I. 2005, The Astrophysical Journal, 618, L33 147

Kuiper, R. & Hosokawa, T. 2018, Astronomy & Astrophysics, 616, A101 22, 66, 86, 166

Kuiper, R., Klahr, H., Beuther, H., & Henning, T. 2010a, The Astrophysical Journal, 722, 1556 20, 87, 93, 118

Kuiper, R., Klahr, H., Beuther, H., & Henning, T. 2010b, Proceedings of the International Astronomical Union, 6, 215 xvii, 11, 12, 19, 87

Kuiper, R., Klahr, H., Beuther, H., & Henning, T. 2011, The Astrophysical Journal, 732, 20 xviii, 22, 93, 137

Kuiper, R., Klahr, H., Beuther, H., & Henning, T. 2012, Astronomy & Astrophysics, 537, A122 20, 87, 147

Kuiper, R., Klahr, H., Beuther, H., & Henning, T. 2014, in The Labyrinth of Star Formation, ed. D. Stamatellos, S. Goodwin, & D. Ward-Thompson, Astrophysics and Space Science Proceedings (Springer International Publishing), 379–383 87

Kuiper, R., Klahr, H., Dullemond, C., Kley, W., & Henning, T. 2010c, Astronomy & Astrophysics, 511, A81 20, 43, 99, 119, 160

Kuiper, R. & Yorke, H. W. 2013, The Astrophysical Journal, 772, 61 8, 88, 167

Kuiper, R., Yorke, H. W., & Turner, N. J. 2015, The Astrophysical Journal, 800, 86 21, 120, 161

Lada, C. J. 1985, Annual Review of Astronomy and Astrophysics, 23, 267 xvii, 17, 120, 151, 153

Lada, C. J. 1987, IAU Symposium, 115, 1 8

Lada, C. J. & Lada, E. A. 2003, Annu. Rev. Astron. Astrophys., 41, 57, arXiv: astro-ph/0301540 5

Lam, K. H., Li, Z.-Y., Chen, C.-Y., Tomida, K., & Zhao, B. 2019, Monthly Notices of the Royal Astronomical Society, stz2436, arXiv: 1908.11806 22, 118

Larson, R. B. 1969, MNRAS, 145, 271 xvii, 6

Larson, R. B. 1974, MNRAS, 169, 229 3

Larson, R. B. & Starrfield, S. 1971, Astronomy & Astrophysics, 13, 190 12, 118, 119

Lebreuilly, U., Commerçon, B., & Laibe, G. 2019, Astronomy & Astrophysics, 626, A96 165

Leitherer, C., Schaerer, D., Goldader, J. D., et al. 1999, The Astrophysical Journal Supplement Series, 123, 3 3

Leung, K.-C., Moffat, A. F. J., & Seggewiss, W. 1979, The Astrophysical Journal, 231, 742 5

Levermore, C. D. 1984, JQSRT, 31, 149 20, 46

Levermore, C. D. & Pomraning, G. C. 1981, The Astrophysical Journal, 248, 321 20, 44, 119

Li, H.-b., Yuen, K. H., Otto, F., et al. 2015, Nature, 520, 518 19

Li, Z.-Y., Krasnopolsky, R., & Shang, H. 2013, The Astrophysical Journal, 774, 82 21

Lovelace, R. V. E. & Scott, H. A. 1981, Plasma Astrophysics, Course and Workshop, 1981, p.215 132

Lynden-Bell, D. 1996, Monthly Notices of the Royal Astronomical Society, 279, 389 34, 119, 145, 159

Lynden-Bell, D. 2003, Monthly Notices of the Royal Astronomical Society, 341, 1360 34, 119, 145

Machida, M. N., Hirano, S., & Kitta, H. 2019, Monthly Notices of the Royal Astronomical Society 131, 160

Machida, M. N., Inutsuka, S.-i., & Matsumoto, T. 2008, The Astrophysical Journal, 676, 1088 xviii, 21, 22

Marchand, P., Masson, J., Chabrier, G., et al. 2016, Astronomy & Astrophysics, 592, A18 61

Martins, F., Hillier, D. J., Paumard, T., et al. 2008, Astronomy & Astrophysics, 478, 219 4

Masson, J., Chabrier, G., Hennebelle, P., Vaytet, N., & Commerçon, B. 2016, Astronomy & Astrophysics, 587, A32 22, 118, 126, 138

Masson, J., Teyssier, R., Mulet-Marquis, C., Hennebelle, P., & Chabrier, G. 2012, The Astrophysical Journal Supplement Series, 201, 24 58, 61, 121

Masunaga, H. & Inutsuka, S.-i. 2000, The Astrophysical Journal, 531, 350 xvii, 6

Matsushita, Y., Machida, M. N., Sakurai, Y., & Hosokawa, T. 2017, Monthly Notices of the Royal Astronomical Society, 470, 1026 119, 151, 152, 153

Maury, A. J., Girart, J. M., Zhang, Q., et al. 2018, Monthly Notices of the Royal Astronomical Society 18, 141

McKee, C. F. & Ostriker, J. P. 1977, The Astrophysical Journal, 218, 148 1

McKee, C. F. & Tan, J. C. 2002, Nature, 416, 59 14

McKee, C. F. & Tan, J. C. 2003, The Astrophysical Journal, 585, 850 14, 16, 29

Mestel, L. & Spitzer, L. 1956, Monthly Notices of the Royal Astronomical Society, 116, 503 60

Meyer, D. M.-A., Kuiper, R., Kley, W., Johnston, K. G., & Vorobyov, E. 2018, Monthly Notices of the Royal Astronomical Society, 473, 3615 101

Meyer, D. M.-A., Vorobyov, E. I., Kuiper, R., & Kley, W. 2017, Monthly Notices of the Royal Astronomical Society: Letters, 464, L90 101

Mignon-Risse, R., González, M., Commerçon, B., & Rosdahl, J. 2020, Astronomy & Astrophysics, 635, A42 119, 120, 121, 144, 147

Mignone, A., Bodo, G., Massaglia, S., et al. 2007, The Astrophysical Journal Supplement Series, 170, 228 99

Mihalas, B. W. & Mihalas, D. 1984, Foundations of radiation hydrodynamics (Oxford University Press) 36, 49, 91

Miyoshi, T. & Kusano, K. 2005, Journal of Computational Physics, 208, 315 60, 101

Moscadelli, L., Cesaroni, R., & Rioja, M. J. 2005, Astronomy & Astrophysics, 438, 889 156, 161

Motte, F., André, P., Ward-Thompson, D., & Bontemps, S. 2001, Astronomy & Astrophysics, 372, L41 3

Motte, F., Bontemps, S., & Louvet, F. 2018, The Annual Review of Astronomy and Astrophysics, 56, 41 16, 90, 93, 134, 151, 166

Motte, F., Bontemps, S., Schilke, P., et al. 2007, Astronomy & Astrophysics, 476, 1243 16

Mouschovias, T. C. 1991, The Astrophysical Journal, 373, 169 2

Mouschovias, T. C. & Spitzer, Jr., L. 1976, The Astrophysical Journal, 210, 326 29, 122

Myers, A. T., McKee, C. F., Cunningham, A. J., Klein, R. I., & Krumholz, M. R. 2013, The Astrophysical Journal, 766, 97 13, 18, 120, 135

Myers, P. C. 2009, The Astrophysical Journal, 700, 1609 15

Naab, T. & Ostriker, J. P. 2017, Annu. Rev. Astron. Astrophys., 55, 59, arXiv: 1612.06891 3

Neupane, S., Garay, G., Contreras, Y., Guzmán, A., & Rodríguez, L. F. 2020, arXiv:2001.02227 [astro-ph], arXiv: 2001.02227 14

Nomoto, K., Kobayashi, C., & Tominaga, N. 2013, Annual Review of Astronomy and Astrophysics, 51, 457 3

Nony, T., Louvet, F., Motte, F., et al. 2018, Astronomy & Astrophysics, 618, L5 14, 16, 86

Nony, T., Motte, F., Louvet, F., et al. 2020, arXiv:2002.05720 [astro-ph], arXiv: 2002.05720 16, 151

Offner, S. S. R., Lee, E. J., Goodman, A. A., & Arce, H. 2011, The Astrophysical Journal, 743, 91 155

Ogilvie, G. I. 2016, Journal of Plasma Physics, 82 30, 146

Oster, L. 1963, The Astrophysical Journal, 138, 761 39

Owen, J. E., Ercolano, B., & Clarke, C. J. 2014, in The Labyrinth of Star Formation, ed. D. Stamatellos, S. Goodwin, & D. Ward-Thompson, Vol. 36, 127 20, 77, 118, 147

Padoan, P., Nordlund, A., & Jones, B. J. T. 1997, Monthly Notices of the Royal Astronomical Society, 288, 145 3, 4, 14

Padoan, P., Pan, L., Juvela, M., Haugbolle, T., & Nordlund, A. 2019, arXiv:1911.04465 [astro-ph], arXiv: 1911.04465 14, 166

Palau, A., Fuente, A., Girart, J. M., et al. 2013, The Astrophysical Journal, 762, 120 19

Palla, F. & Stahler, S. W. 1990, The Astrophysical Journal, 360, L47 xvii, 9

Pascucci, I., Wolf, S., Steinacker, J., et al. 2004, Astronomy & Astrophysics, 417, 793 xix, 72, 73, 74, 75, 76, 77, 78, 79, 81, 82, 105

Patel, N. A., Curiel, S., Sridharan, T. K., et al. 2005, Nature, 437, 109 18

Pelletier, G. & Pudritz, R. E. 1992, The Astrophysical Journal, 394, 117 31, 33, 119

Penston, M. V. 1969, Monthly Notices of the Royal Astronomical Society, 144, 425 6

Peretto, N. & Fuller, G. A. 2010, The Astrophysical Journal, 723, 555 15

Peters, T., Banerjee, R., Klessen, R. S., & Low, M.-M. M. 2011, The Astrophysical Journal, 729, 72 18, 21, 22, 120, 150, 160, 166

Peters, T., Klaassen, P. D., Seifried, D., Banerjee, R., & Klessen, R. S. 2014, Monthly Notices of the Royal Astronomical Society, 437, 2901 120

Pety, J., Gueth, F., Guilloteau, S., & Dutrey, A. 2006, Astronomy & Astrophysics, 458, 841 156

Pillai, T., Kauffmann, J., Tan, J. C., et al. 2015, The Astrophysical Journal, 799, 74 19

Pillai, T., Kauffmann, J., Wiesemeyer, H., & Menten, K. M. 2016, Astronomy & Astrophysics, 591, A19 19

Pinte, C., Harries, T. J., Min, M., et al. 2009, Astronomy & Astrophysics, 498, 967 xix, 72, 77, 78, 79, 105

Pinte, C., Ménard, F., Duchêne, G., & Bastien, P. 2006, Astronomy & Astrophysics, 459, 797 39, 71

Pomraning, G. C. 1968, The Astrophysical Journal, 153, 321 39

Pudritz, R. E. & Norman, C. A. 1983, The Astrophysical Journal, 274, 677 119

Pudritz, R. E., Ouyed, R., Fendt, C., & Brandenburg, A. 2006, arXiv:astro-ph/0603592, arXiv: astro-ph/0603592 31, 119, 147

Pudritz, R. E. & Ray, T. P. 2019, Front. Astron. Space Sci., 6, 54, arXiv: 1912.05605 10, 33, 34, 119, 147, 151

Qiu, K., Zhang, Q., & Menten, K. M. 2011, The Astrophysical Journal, 728, 6 16

Ramsey, J. P. & Dullemond, C. P. 2015, Astronomy & Astrophysics, 574, A81 74, 79, 80, 119

Rebolledo, D., Guzmán, A. E., Contreras, Y., et al. 2020, arXiv:2001.06969 [astro-ph], arXiv: 2001.06969 3

Rodriguez, L. F., Garay, G., Brooks, K. J., & Mardones, D. 2005, The Astrophysical Journal, 626, 953 156

Rosdahl, J., Blaizot, J., Aubert, D., Stranex, T., & Teyssier, R. 2013, Monthly Notices of the Royal Astronomical Society, 436, 2188 20, 45, 47, 64, 65, 67, 70, 74, 121, 166

Rosdahl, J. & Teyssier, R. 2015, Monthly Notices of the Royal Astronomical Society, 449, 4380 66, 70, 121

Rosen, A., Krumholz, M., Oishi, J., Lee, A., & Klein, R. 2017, Journal of Computational Physics, 330, 924 20, 119

Rosen, A. L. & Krumholz, M. R. 2020, arXiv:2006.04829 [astro-ph], arXiv: 2006.04829 120, 161

Rosen, A. L., Krumholz, M. R., McKee, C. F., & Klein, R. I. 2016, Monthly Notices of the Royal Astronomical Society, 463, 2553 xx, 20, 86, 87, 88, 90, 95, 99, 100, 120, 144, 164, 167

Rosen, A. L., Li, P. S., Zhang, Q., & Burkhart, B. 2019, arXiv:1902.10153 [astro-ph], arXiv: 1902.10153 95, 150

Salaris, M. & Cassisi, S. 2005, Evolution of stars and stellar populations (Chichester, West Sussex, England ; Hoboken, NJ, USA: J. Wiley) 2

Salpeter, E. E. 1955, The Astrophysical Journal, 121, 161 3

Sana, H., de Mink, S. E., de Koter, A., et al. 2012, Science, 337, 444 5

Sanna, A., Kölligan, A., Moscadelli, L., et al. 2019, Astronomy & Astrophysics, 623, A77 105, 107

Schneider, F. R. N., Ramírez-Agudelo, O. H., Tramper, F., et al. 2018, Astronomy & Astrophysics, 618, A73 4

Schneider, N., Csengeri, T., Bontemps, S., et al. 2010, Astronomy and Astrophysics, 520, A49 14, 166

Seifried, D., Banerjee, R., Klessen, R. S., Duffin, D., & Pudritz, R. E. 2011, Monthly Notices of the Royal Astronomical Society, 417, 1054 118

Seifried, D., Banerjee, R., Pudritz, R. E., & Klessen, R. S. 2012a, Monthly Notices of the Royal Astronomical Society: Letters, 423, L40 21, 118

Seifried, D., Pudritz, R. E., Banerjee, R., Duffin, D., & Klessen, R. S. 2012b, Monthly Notices of the Royal Astronomical Society, 422, 347 xxiii, 119, 145, 146, 147, 148, 153

Semenov, D., Henning, T., Helling, C., Ilgner, M., & Sedlmayr, E. 2003, Astronomy & Astrophysics, 410, 611 87

Shu, F. H. 1977, The Astrophysical Journal, 214, 488 6, 14, 122, 137

Shu, F. H. & Adams, F. C. 1987, in IAU Symposium, Vol. 122, Circumstellar Matter, ed. I. Appenzeller & C. Jordan, 7–22 8

Shu, F. H., Adams, F. C., & Lizano, S. 1987, Annual Review of Astronomy and Astrophysics, 25, 23 60

Silva, M. D. V. & Napiwotzki, R. 2011, Monthly Notices of the Royal Astronomical Society, 411, 2596 5

Smith, R. J., Longmore, S., & Bonnell, I. 2009, Monthly Notices of the Royal Astronomical Society, 400, 1775 13

Spruit, H. C. 1996, arXiv:astro-ph/9602022, arXiv: astro-ph/9602022 xviii, 30, 32, 145, 146

Stahler, S., ed. 2018, Astrophysics and Space Science Library, Vol. 424, The Birth of Star Clusters (Cham: Springer International Publishing) 5

Stahler, S. W. 1988, The Astrophysical Journal, 332, 804 7

Stone, J. M. & Norman, M. L. 1992, The Astrophysical Journal Supplement Series, 80, 753 52

Tan, J. C. & McKee, C. F. 2002, arXiv:astro-ph/0203072, arXiv: astro-ph/0203072 16

Tang, Y.-W., Ho, P. T. P., Girart, J. M., et al. 2009, The Astrophysical Journal, 695, 1399 19

Teyssier, R. 2002, Astronomy & Astrophysics, 385, 337 ix, 43, 52, 87, 99, 121, 163

Teyssier, R., Fromang, S., & Dormy, E. 2006, Journal of Computational Physics, 218, 44 58, 61

Truelove, J. K., Klein, R. I., McKee, C. F., et al. 1997, The Astrophysical Journal, 489, L179 88, 123

Vaidya, B., Fendt, C., Beuther, H., & Porth, O. 2011, The Astrophysical Journal, 742, 56 21, 120, 142

van Leer, B. 1979, Journal of Computational Physics, 32, 101 56

Vaytet, N., Chabrier, G., Audit, E., et al. 2013, Astronomy & Astrophysics, 557, A90 35, 87, 122

Vaytet, N., Commerçon, B., Masson, J., González, M., & Chabrier, G. 2018, Astronomy & Astrophysics, 615, A5 61, 123

Vázquez-Semadeni, E., Gonzalez-Samaniego, A., & Colin, P. 2016, Monthly Notices of the Royal Astronomical Society, stw3229, arXiv: 1611.00088 13, 18, 166

Vázquez-Semadeni, E., Palau, A., Ballesteros-Paredes, J., Gómez, G. C., & Zamora-Avilés, M. 2019, arXiv:1903.11247 [astro-ph], arXiv: 1903.11247 13

Wang, K., Zhang, Q., Testi, L., et al. 2014, Monthly Notices of the Royal Astronomical Society, 439, 3275 16

Ward-Thompson, D., Scott, P. F., Hills, R. E., & Andre, P. 1994, Monthly Notices of the Royal Astronomical Society, 268, 276 8

Watkins, E. J., Peretto, N., Marsh, K., & Fuller, G. A. 2019, arXiv:1906.09275 [astro-ph], arXiv: 1906.09275 3

Weingartner, J. C. & Draine, B. T. 2001, The Astrophysical Journal, 548, 296 78

Wu, Y., Wei, Y., Zhao, M., et al. 2004, Astronomy & Astrophysics, 426, 503 119, 127, 151, 152, 153, 155, 156, 159

Wu, Y., Zhang, Q., Chen, H., et al. 2005, The Astronomical Journal, 129, 330 152, 153

Wurster, J. & Lewis, B. T. 2020, arXiv:2005.05348 [astro-ph], arXiv: 2005.05348 118

Wynn-Williams, C. G. & Becklin, E. E. 1974, Publications of the Astronomical Society of the Pacific, 86, 5 15

Wyrowski, F., Güsten, R., Menten, K. M., et al. 2016, Astronomy & Astrophysics, 585, A149 16

Yorke, H. W. & Sonnhalter, C. 2002, The Astrophysical Journal, 569, 846 12, 13, 19, 20, 36, 45, 97, 118

Zhang, Q., Hunter, T. R., Brand, J., et al. 2005, The Astrophysical Journal, 625, 864 152, 155

Zhang, Q., Qiu, K., Girart, J. M., et al. 2014, The Astrophysical Journal, 792, 116 18, 117

Zhang, Y., Arce, H. G., Mardones, D., et al. 2016, The Astrophysical Journal, 832, 158 17

Zhang, Y., Tanaka, K. E. I., Rosero, V., et al. 2019, arXiv:1910.04271 [astro-ph], arXiv: 1910.04271 19